Universidade de São Paulo
Instituto de Física

Investigação da influência da iluminação (com luz vermelha ou infravermelha) em propriedades mecânicas de células: Fotobiomodulação

Ana Carolina de Magalhães

Orientadora: Prof.ª Dra. Elisabeth M. Yoshimura

Tese de doutorado apresentada ao Instituto de Física para a obtenção do título de Doutor em Ciências

Banca examinadora:

Profª. Dra. Elisabeth M. Yoshimura – orientadora (IFUSP)
Prof. Dr. Adriano Mesquita Alencar (IFUSP)
Prof. Dr. Zwinglio de Oliveira Guimarães Filho (IFUSP)
Profª. Dra. Ana Campa (FCF/USP)
Profª. Dra. Maria Cristina Chavantes (Uninove)

São Paulo
2016

FICHA CATALOGRÁFICA
Preparada pelo Serviço de Biblioteca e Informação
do Instituto de Física da Universidade de São Paulo

Magalhães, Ana Carolina de

Investigação da influência da iluminação (com luz vermelha ou Infravermelha) em propriedades mecânicas de células: fotobiomodulação. São Paulo, 2016.

Tese (Doutorado) – Universidade de São Paulo. Instituto de Física. Depto. de Física Nuclear.

Orientador: Profa. Dra. Elisabeth Mateus Yoshimura

Área de Concentração: Física Médica.

Unitermos: 1.Terapia à laser; 2. Células epiteliais; 3. Fibroblastos; 4. Eritrócitos; 5. Fotobiomodulação.

USP/IF/SBI-101/2016

University of São Paulo
Institute of Physics

Investigation of the influence of red and infrared illumination on mechanical properties of cells: Photobiomodulation

Ana Carolina de Magalhães

Advisor: Prof. Dr. Elisabeth M. Yoshimura

Thesis submitted to the Institute of Physics of the University of Sao Paulo for the PhD degree in Sciences

Examination Committee:

Prof. Dr. Elisabeth M. Yoshimura – advisor (IFUSP)
Prof. Dr. Adriano Mesquita Alencar (IFUSP)
Prof. Dr. Zwinglio de Oliveira Guimarães Filho (IFUSP)
Prof. Dr. Ana Campa (FCF/USP)
Prof. Dr. Maria Cristina Chavantes (Uninove)

São Paulo
2016

“A scientist in his laboratory is not only a technician: he is also a child placed before natural phenomena which impress him like a fairy tale.”

Marie Curie

To my parents, Rosangela and Hermes.

To my husband, Fábio.

Acknowledgments

I would like to thank God, for the opportunity to be here. I would also like to thank my family and friends, who give me all the support and help. In particular, my parents, Rosangela and Hermes, for all the love and support that made me what I am today. And my husband, Fábio, for the love, patience and support for all those years. No words can express my gratitude towards them!

I deeply thank my advisor Elisabeth, for the patience, teaching, guidance and for being a great example of scientist.

I would like to thank Lothar Lilge, who opened his laboratory to me and helped me during the time I was in Toronto, with precious teachings and tips. I also would like to thank his family, in particular Brenda, for the reception and friendship.

I thank Adriano Alencar and Oscar Mesquita for the help and for opening their laboratories to me.

I also would like to thank Marcia Z. J. Ferreira, Lívia Siman, Paula M. Roma, Carl Fisher and Layla Pires for their help with the experiments.

I thank all my colleagues, in particular from the *Grupo de Dosimetria das Radiações e Física Médica* and from the *Department of Medical Biophysics of the University of Toronto*, for the friendship, the talks, ideas and everything else.

I specially thank Maria Cristina Chavantes, who is always available to help me.

I thank CNPq and CAPES for the financial support.

I would also like to thank all the people that I did not cite, but who contributed for the realization of this work.

Resumo

A terapia por fotobiomodulação tem muitas aplicações na área de Saúde devido a sua ação anti-inflamatória e de reparação tecidual. O objetivo geral desse trabalho é verificar se a terapia por fotobiomodulação provoca mudanças nas propriedades mecânicas de células, em particular em hemácias, células epiteliais e fibroblastos. Além de contribuir com o conhecimento dos mecanismos de ação da terapia por fotobiomodulação, este estudo pretende subsidiar aplicações da terapia por fotobiomodulação durante procedimentos mais invasivos, como a iluminação direta do sangue em procedimentos cirúrgicos com circulação extracorpórea, sob o ponto de vista da segurança quanto à integridade celular. Para essa análise foram utilizadas três técnicas experimentais: citometria óptica magnética de oscilação (OMTC), microscopia de desfocalização e microscopia confocal. Com a técnica de OMTC foram avaliadas células epiteliais brônquicas humanas em cultura, foto-tratadas com laser vermelho (λ=660 nm), com potência e tempo fixos (densidade de potência de 153 mW/cm^2, tempo 300 s). Não foi possível constatar diferenças significativas entre as células epiteliais foto-tratadas e as células controle, para a histerisividade (razão entre os módulos viscoso e elástico das células). Com a técnica de microscopia de desfocalização, semelhante a uma microscopia de contraste de fase, foram estudadas hemácias humanas de sangue recém coletado. As hemácias foram tratadas com laser vermelho (λ=660 nm), com potências e tempos variados (densidade de potência de 0 a 510 mW/cm^2, tempo de 0 a 180 s). Foram avaliadas algumas características morfológicas e mecânicas das hemácias individualmente, como o volume, perfil radial de espessura, flutuações lateral e vertical da membrana, tanto para hemácias foto-tratadas quanto para hemácias controle. Não foi possível detectar diferenças entre as hemácias foto-tratadas e controle para nenhum dos parâmetros avaliados. Para ambas as técnicas, a falta de mudanças observáveis poderia ser devida a diversos fatores, como a não ação da terapia por fotobiomodulação nas células epiteliais e nas hemácias, com os parâmetros aqui empregados, ou à falta de sensibilidade de cada uma das técnicas usadas. A microscopia confocal foi utilizada para avaliar os filamentos de actina de fibroblastos de camundongo em cultura, os quais foram foto-tratados com luz vermelha (λ=625 nm) ou infravermelha (λ=808 nm) e potência e tempo fixos (densidade de potência de 113 a 158 mW/cm^2, tempo 300 s). Foi possível constatar

ligeiro aumento nas áreas nuclear e celular das células foto-tratadas em relação aos fibroblastos controle. Também foi possível verificar a diminuição da quantidade total de actina, densidade de actina e do número de filamentos de actina nos fibroblastos foto-tratados. Essas mudanças são detectadas para tempos curtos após o tratamento, sendo que depois de $24\,\mathrm{h}$ elas desaparecem. O tamanho total dos filamentos parece não sofrer alterações. A partir dos dados coletados com as três técnicas, foi possível constatar que a terapia por fotobiomodulação, com os parâmetros utilizados, não consegue provocar mudanças perceptíveis em hemácias e em células epiteliais, *in vitro*. Porém, causa mudanças nos filamentos de actina de fibroblastos, *in vitro*, em particular a diminuição da densidade de actina total.

Palavras-chave: terapia à laser; células epiteliais; fibroblastos; eritrócitos; fotobiomodulação.

Abstract

The photobiomodulation therapy (PBMT) has many demonstrated applications in the health area including anti-inflammatory and wound healing effects. The main objective of this work is to verify if the PBMT causes measurable changes in the mechanical properties of cells, specifically in red blood cells, epithelial cells and fibroblasts. In addition, to contribute to the knowledge of the action mechanisms of the PBMT, this study intends to support applications of the PBMT during invasive procedures, such as the direct photo-treatment of the blood in surgical procedures with cardiopulmonary bypass, regarding security of the cellular integrity. For this analysis, three experimental techniques were used: optical magnetic twisting cytometry (OMTC), defocusing microscopy and confocal laser-scanning microscopy. Human bronchial epithelial cells were evaluated with OMTC. The epithelial cell culture was either photo-treated or not, with red laser (λ=660 nm), and fixed power and time (power density of 153 $\mathrm{mW/cm^2}$, time 300 s). It was not possible to observe significant differences between photo-treated and control epithelial cells, for the hysteresivity (ratio between the cell loss and elastic shear moduli). The defocusing microscopy, similar to a phase contrast microscopy, was used to study human red blood cells from fresh blood. The red blood cells were either photo-treated or not, with red laser (λ=660 nm), and different powers and times (power densities from 0 to 510 $\mathrm{mW/cm^2}$, times from 0 to 180 s). Some morphological and mechanical characteristics of individual red blood cells were evaluated, such as volume, radial profile of cell thickness, lateral and vertical membrane fluctuations, for the photo-treated and control red blood cells. It was not possible to detect differences between the two groups, for any of the parameters analyzed. For both techniques, the absence of detectable differences might be due to several factors, such as the non-action of the PBMT, with the parameters used, in the epithelial cells and red blood cells or to the small sensitivity of each technique. Confocal laser-scanning microscopy was used to evaluate the actin filaments of mouse fibroblasts. The fibroblast cell culture was either photo-treated or not, with red (λ=625 nm) or infrared (λ=808 nm) light and fixed power and time (power density from 113 to 158 $\mathrm{mW/cm^2}$, time 300 s). The nucleus and cell areas increased slightly when comparing photo-treated and control cells. On the other hand, the total actin, total actin density and the number of filaments decreased. These changes were detected for a short time after treatment, however,

after 24 h they are not anymore detectable. The total branch length does not seem to suffer any modifications. In summary, with the data acquired with the three techniques, it was found that the PBMT, in the red range, with the parameters used, could not cause noticeable changes in red blood cells and epithelial cells, *in vitro*. On the other hand, the PBMT in the red and near-infrared range, with the power and times used, cause changes in actin filaments of fibroblasts, *in vitro*, in particular the decrease of the total actin density.

Keywords: laser therapy; epithelial cells; fibroblasts; erythrocytes; photobiomodulation.

List of figures

Figure 1.1: Viscosity of two blood samples diluted under the same conditions used in the cardiopulmonary bypass surgery, one of the samples was photo-treated, on the right, and the other was not, on the left. Figure adapted from [19]. 46

Figure 1.2: On the left, the representation of the junctional complex, which connects the spectrin molecules. Small actin filaments and other molecules form this complex. In the center, the network formed by spectrin and the junctional complex, which form the RBC cytoskeleton. On the right, the spectrin molecule. Figure adapted from *Biologia molecular da célula* [24].....50

Figure 2.1: On the left, the microscope used for OMTC measurements. The left arrow shows the solenoids responsible for magnetic field generation. The right arrow shows the CCD camera attached to the microscope, which is responsible for the image capture. On the right, a detailed image of the solenoids responsible for the magnetic field generation required for the experiment. The central hole is the place for the wells with cells.....70

Figure 2.2: Flowchart of the experimental protocol, from the preparation of epithelial cells to photo-treatment and measurement. The slashed intervals represent epithelial cell incubation. The two timelines were performed in parallel. Twelve wells were used in each timeline, four for each group. 72

Figure 2.3: Hysteresivity histograms for the photo-treated group. On the left, the histogram for η and on the right the histogram for ln(η). Although data seem to have a lognormal distribution, according to Lilliefors test they do not have.....74

Figure 2.4: Histogram of micro bead displacement for the bench control group. On the left, the histogram for $|d^*|$ and on the right, the histogram for ln($|d^*|$). Although data seem to have a lognormal distribution, according to Lilliefors test they do not have. 74

Figure 2.5: Results for the three OMTC experiments. The two graphs show the same data but grouped differently. On the left, data were grouped by experiments (1, 2 and 3) and on the right by epithelial cell group (*ic*, *bc* and *tr*). The data boxplots are also shown. The numbers 1, 2 and 3 in the horizontal axis label refer to the experiment. The

acronym *ic* refers to the control group whose wells stayed all the time in the incubator, *bc* refers to the control group whose wells stayed part of the time outside the incubator, on the bench, and *tr* denotes the photo-treated group. 75

Figure 2.6: Diagrams with p-values obtained with the two-sample rank sum test comparing the hysteresivity η of different groups in the same experiment. The groups were considered different when $p < 5\%$. On the left, experiment 1 (*e1*), on the center, experiment 2 (*e2*), and on the right, experiment 3 (*e3*). The acronym *ic* refers to the control group whose wells stayed all the time in the incubator, *bc* refers to the control group whose wells stayed part of the time outside the incubator, on the bench, and *tr* denotes the photo-treated group. The red arrows indicate groups with values not compatible, for the same experiment. 76

Figure 2.7: Diagrams with p-values obtained with the two-sample rank sum test comparing the hysteresivity η of different experiments for the same group. The groups were considered different when $p < 5\%$. On the left, the control group whose wells stayed all the time in the incubator (*ic*), on the center, the control group whose wells stayed part of the time outside the incubator (*bc*), and on the right, the photo-treated group (*tr*). The acronym refers to experiment 1 (*e1*), experiment 2 (*e2*) and experiment 3 (*e3*). The red arrows indicate groups with values not compatible, for the same group. 76

Figure 2.8: Comparison between the measurements 1 and 2 for each setup. The percentages in the graph indicate the p-values for the comparison between the measurement 1 and 2, for Student's *t*-test. The error bars represent the uncertainty of the measurements.....77

Figure 2.9: Comparison between the different setups: measurement 1 (on the left) and measurement 2 (on the right). The p-values for the Student's *t*-test are shown in Figure 2.10. The error bars represent the uncertainty of the measurements. 77

Figure 2.10: Diagrams with the comparison between the different setups, for measurement 1 (on the left) and measurement 2 (on the right). The percentages represent the p-value, for the Student's *t*-test, for the comparison between the wells

with that specific number of epithelial cells (zero, 15 thousand and 45 thousand epithelial cells). Averages were considered incompatible when $p < 5\%$. 78

Figure 2.11: Graph for transmittance and absorbance of L929 fibroblast cells in culture media. Data were measured with a spectrophotometer. The red data shown represent the wavelengths used in this work: 625 nm, 660 nm and 808 nm. These results were provided by D. F. T. Silva (personal communication, December 1, 2015).....78

Figure 3.1: RBC images obtained with a bright field microscope. On the left, the image is focused and on the right, the image is slightly defocused.....80

Figure 3.2: Image of the two types of sample holders used in the experiments. The O-ring (on the left) or the acrylic bucket (on the right) were bonded with silicone on the cover slip. 84

Figure 3.3: On the left, an image of the experimental setup used for the photo-treatment of the samples. In this case the Eppendorf tube, which is indicated by the left arrow, was used to centralize the beam (the laser output head is indicated by the right arrow). On the right, the experimental sketch, in which the sample was photo-treated in the Eppendorf tube and then measured. There is also a timeline of the experiment.....86

Figure 3.4: Image of the experimental setup used for the sample photo-treatment. The microscope illumination system was raised in order to give space to the laser, which was centered with the objective lens. 89

Figure 3.5: Experimental sketch for the experiments in which the sample was photo-treated in the microscope stage and then measured (experiments 2, 3 and 4). There is also a timeline with the three different experiments described in the text.....90

Figure 3.6: On the left are shown the lines in which the lateral fluctuation of RBCs was evaluated. On the right is shown the radial profile of gray levels to line 1. The arrows indicate the distances between maxima (on top of the graph) and between minima (on bottom of the graph). 92

Figure 3.7: RBC thickness profile, in 3D view (top left graph); view from top (top right graph), where the color scale represents the RBC thickness in μm; 3D view with zoom

in the background area (bottom left graph); and lateral view with zoom in the background area (bottom right graph). For this case, the background was homogeneous and the reconstruction has good quality with very few and small artifacts in the background. 95

Figure 3.8: RBC thickness profile, in 3D view (top left graph); view from top (top right graph), where the color scale represents the RBC thickness in μm; 3D view with zoom in the background area (bottom left graph); and lateral view with zoom in the background area (bottom right graph). For this case, the background was not homogeneous and the reconstruction does not have such a good quality with a few artifacts in the background. 96

Figure 3.9: RBC thickness profile, in 3D view (top left graph); view from top (top right graph), where the color scale represents the RBC thickness in μm; 3D view with zoom in the background area (bottom left graph); and lateral view with zoom in the background area (bottom right graph). For this case, the background was heterogeneous and the reconstruction has poor quality with massive artifacts in the background. 97

Figure 3.10: Background thickness profile, in a 3D view. The RBC region had the thickness set to zero to evaluate the background contribution to the RBC volume. The background represented here refers to the RBC shown in Figure 3.9. 98

Figure 3.11: Volumes for RBCs photo-treated with $10\ mW$ for $60\ s$, either in the Eppendorf tube, from experiment 1, or in the microscope stage, from experiment 2. On the left, all RBC volumes are presented. Filled symbols represent reconstructions with good quality, and empty symbols represent reconstructions with poor quality. On the right, the average volumes, calculated using all data, and the standard deviations (represented by the error bars) are displayed. The blue interval represents the range of values found in literature obtained with the same technique used here $93 \pm 19\ \mu m^3$ (average $\pm\ 1$ standard deviation) [91]. 100

Figure 3.12: Volumes for RBCs from experiment 1 with times and powers described in Table 3.4. On the left, all RBC volumes are presented. Filled symbols represent reconstructions with good quality, and empty symbols represent reconstructions with

poor quality. On the right, the average volumes are displayed; the average was calculated using all data, and error bars represent the standard deviations. The blue interval represents the range of values found in literature obtained with the same technique used here $93 \pm 19\ \mu m^3$ (average $\pm$ 1 standard deviation) [91]. 101

Figure 3.13: Volumes for RBCs from experiment 2. On the left, all RBC volumes are presented. Filled symbols represent reconstructions with good quality, and empty symbols represent reconstructions with poor quality. On the right, the average volumes are displayed, the average was calculated using all data and error bars represent the standard deviations. The blue interval represents the range of values found in literature obtained with the same technique used here $93 \pm 19\ \mu m^3$ (average $\pm$ 1 standard deviation) [91].....102

Figure 3.14: Behavior of RBC volume as a function of time after photo-treatment obtained for experiment 3, for the $30\ mW$ photo-treated sample. The first point in time is negative because it refers to the measurement that was completed prior to photo-treatment, before starting timing. The legend refers to the two RBCs that were monitored over time. Filled symbols represent reconstructions with good quality and empty symbols represent reconstructions with poor quality. 103

Figure 3.15: Behavior of RBC volume as a function of time after photo-treatment obtained for experiment 3, for the $100\ mW$ photo-treated sample. The first point in time is negative because it refers to the measurement that was completed prior to photo-treatment, before starting timing. The legend refers to the three RBCs that were monitored over time. Filled symbols represent reconstructions with good quality and empty symbols represent reconstructions with poor quality. 103

Figure 3.16: Behavior of RBC volume as a function of time obtained for experiment 3, for the control samples, that were not photo-treated. The legend refers to the two RBCs that were monitored over time. Filled symbols represent reconstructions with good quality and empty symbols represent reconstructions with poor quality. 104

Figure 3.17: Behavior of RBC volume as a function of time after photo-treatment obtained for experiment 3, for all samples. Some points in time are negative because they refer to the measurement that was completed prior to photo-treatment, before

starting timing. The legend refers to the power used for each sample; the control group was not photo-treated. Filled symbols represent reconstructions with good quality, and empty symbols represent reconstructions with poor quality. The blue interval represents the range of values found in literature obtained with the same technique used here $93 \pm 19\ \mu m^3$ (average $\pm$ 1 standard deviation) [91].....104

Figure 3.18: Volumes obtained for experiment 4, for the $30\ mW$ photo-treated sample. The legend refers to the two RBC that were monitored. Filled symbols represent reconstructions with good quality and empty symbols represent reconstructions with poor quality.....106

Figure 3.19: Volumes obtained for experiment 4, for the $100\ mW$ photo-treated sample. The legend refers to the two RBC that were monitored. Filled symbols represent reconstructions with good quality and empty symbols represent reconstructions with poor quality.....107

Figure 3.20: Volumes obtained for experiment 4, for all samples. On the left, volume as a function of the accumulated photo-treatment time. On the right, volume as a function of the accumulated energy delivered to the sample. The legend refers to the power used for each sample and the RBC that was monitored. Filled symbols represent reconstructions with good quality and empty symbols represent reconstructions with poor quality. The blue interval represents the range of values found in literature obtained with the same technique used here $93 \pm 19\ \mu m^3$ (average $\pm$ 1 standard deviation) [91].....107

Figure 3.21: On the left, the radial profile of cell thickness for RBCs photo-treated with $30\ mW$ for $10\ s$. On the right, the radial profile of cell thickness for RBCs photo-treated with $10\ mW$ for $60\ s$, both from experiment 1. The legend refers to good (GD) or poor quality (PR) reconstructions and RBC identification. Each curve refers to a different RBC.....109

Figure 3.22: Radial profile of cell thickness for samples photo-treated either in the Eppendorf tube (from experiment 1) or in the microscope stage (from experiment 2), with $10\ mW$ for $60\ s$. The values represented are the averages for all data, for each

radial distance. On the left, the error bars represent data standard deviation and on the right, the standard deviation of the mean. 110

Figure 3.23: Radial profile of cell thickness for samples from experiment 1. The values represented are the averages for all data. On the left, the error bars represent data standard deviation and on the right, the standard deviation of the mean. 111

Figure 3.24: Radial profile of cell thickness for samples photo-treated from experiment 2. The values represented are the averages for all data. On the left, the error bars represent data standard deviation and on the right, the standard deviation of the mean. 112

Figure 3.25: Comparison between the $10\ \mathrm{mW}$, $180\ \mathrm{s}$ ($1.8\ \mathrm{J}$) photo-treated sample and its respective control, using Student's *t*-test. The error bars represent data standard deviation. The points presented in orange represent incompatible averages when comparing photo-treated and control samples. 113

Figure 3.26: Comparison between the $30\ \mathrm{mW}$, $180\ \mathrm{s}$ ($5.4\ \mathrm{J}$) photo-treated sample and its respective control, using Student's *t*-test. The error bars represent data standard deviation. The points presented in orange represent incompatible averages when comparing photo-treated and control samples. 114

Figure 3.27: Comparison between the $50\ \mathrm{mW}$, $180\ \mathrm{s}$ ($9.0\ \mathrm{J}$) photo-treated sample and its respective control, using Student's *t*-test. The error bars represent data standard deviation. The points presented in orange represent incompatible averages when comparing photo-treated and control samples. 114

Figure 3.28: Comparison between the $70\ \mathrm{mW}$, $180\ \mathrm{s}$ ($12.6\ \mathrm{J}$) photo-treated sample and its respective control, using Student's *t*-test. The error bars represent data standard deviation. The points presented in orange represent incompatible averages when comparing photo-treated and control samples. 115

Figure 3.29: Comparison between the $90\ \mathrm{mW}$, $180\ \mathrm{s}$ ($16.2\ \mathrm{J}$) photo-treated sample and its respective control, using Student's *t*-test. The error bars represent data standard deviation. The points presented in orange represent incompatible averages when comparing photo-treated and control samples. 115

Figure 3.30: Radial profile of cell thickness obtained for one RBC photo-treated with $100\ \mathrm{mW}$ for $180\ \mathrm{s}$ ($18\ \mathrm{J}$), for experiment 3. The legend refers to time after photo-treatment, except for *Control* that refers to the measurement before photo-treatment. All curves refer to the same RBC. 116

Figure 3.31: Radial profile of cell thickness obtained for one RBC photo-treated with $100\ \mathrm{mW}$, for experiment 4. The legend refers to accumulated photo-treatment time. All curves refer to the same RBC. 117

Figure 3.32: RBC lateral fluctuation. These data are for the distance between maxima, however, data for the distances between minima have this same profile but with lower amplitude values. The separation of the distances along the four fluctuations directions indicates the RBC asymmetry. The numbers in the legend refer to the four central lines traced as seen in Figure 3.6. 118

Figure 3.33: Fourier transform obtained for the experimental data. 119

Figure 3.34: Coefficients of variation for distances between maxima (max) and minima (min), referring to the lateral fluctuation for RBCs photo-treated with $10\ \mathrm{mW}$ for $60\ \mathrm{s}$, either in the Eppendorf tube or in the microscope stage, from experiments 1 and 2, respectively. All measurement lines are represented, but without symbol distinction. 120

Figure 3.35: Coefficients of variation for distances between maxima (on the left) and minima (on the right), referring to the lateral fluctuation for RBCs from experiment 1. All measurement lines are represented, but without symbol distinction. Data are shown in increasing order of energy, but the horizontal axis is not in scale. 121

Figure 3.36: Coefficients of variation of distances between maxima (on the left) and minima (on the right), referring to the lateral fluctuation for RBCs from experiment 2. All measurement lines are represented, but without symbol distinction. Data are shown in increasing order of power and energy, but the horizontal axis is not in scale. Each color represent one power, with one set of data for the photo-treated group (with the energy) and another for its respective control group (*ctr*). 123

Figure 3.37: Coefficients of variation of RBCs for distances between maxima (on the left) and minima (on the right), referring to the lateral fluctuation for experiment 3..124

Figure 3.38: Coefficients of variation of RBCs for distances between maxima (on the left) and minima (on the right), referring to the lateral fluctuation for experiment 4..125

Figure 3.39: Vertical fluctuation for RBCs from experiment 1. On the left, data for all radial distances. On the right, only the region of interest in the center of the RBC, away from the region where there is diffraction due to the edges.....125

Figure 4.1: Images from the confocal microscope from the original patent. On the top, there are two lenses and on the bottom just one. The principle is the same, the focal point *D* in the specimen is illuminated by 10 and a pinhole *G* is put in a confocal plane with this focal point, thus, most of the light detected by 28 will come direct from the focal point and the pinhole. The specimen scan might be done by either moving the specimen holder or the light source. Images from the Microscope apparatus patent from M. Minsky [99]. 128

Figure 4.2: LED module used for fibroblast photo-treatment. On the left, the whole equipment, with the diffusing paper used to homogenize the light and the well plate on top of it. On the right, the detail of the LED module for 96 well plate, $625\ \mathrm{nm}$, image from top. The red outline in the left image indicates the LED module, detailed in the image on the right. 132

Figure 4.3: Flowchart of the experimental protocol, from the coverslip preparation to fibroblast photo-treatment and measurement.....135

Figure 4.4: Example of fibroblast image. On the left, the original image in grey levels, for both channels, green for AF488 (actin filaments) and blue for DAPI (cell nucleus), this image is a MIP. On the right, the same image after threshold and conversion to black and white, only for the AF488 channel. 139

Figure 4.5: Example of nucleus counting. On the left, the image after threshold and conversion to black and white, only for the DAPI channel. The original image was a MIP. On the right, the outline of the counted particles is shown. Note that small black particles were not counted, because the minimum size was set to $60\ \mu\mathrm{m}^2$.....139

Figure 4.6: Example of filament analysis. On the left, the image after the filter application used only in the AF488 channel. On the right, the same image after threshold and conversion to black and white. Both images are from a central optical section of the image. The small inlet image on the top center is the MIP presented in Figure 4.4. 142

Figure 4.7: Example of filament analysis. On the left, the image after the application of the *ImageJ Skeletonize 3D* plugin. On the right, the same image after the application of the *ImageJ Analyze skeleton 3D* plugin. Blue pixels represent *end-point*s, which are pixels with less than two neighbors; orange pixels represent *slab*s, which are pixels with exactly two neighbors; and purple pixels represent *junction*s, which are pixels with more than two neighbors. Both images are from a central optical section of the image. 143

Figure 4.8: Threshold study for cell area, on the left, and total actin, on the right. Just control groups were tested, from two different imaging days of experiment 14.1. The names in the horizontal axis represent the confocal imaging *day*, the *experiment* and, the last two digits, the *threshold used* (2, 4, 6, 8 and 10). 146

Figure 4.9: Threshold study for the number of filaments, on the left, and total branch length, on the right. Just control groups were tested, from two different imaging days of experiment 14.1. The names in the horizontal axis represent the confocal imaging *day*, the *experiment* and the *threshold used* (last two digits: 75, 80, 85, 90 and 95). 146

Figure 4.10: Example of images obtained with confocal microscopy. Fibroblasts from the negative control group are on the top left, DMSO "$10\ \mu mol/dm^3$" group, on the top right and cytochalasin D $10\ \mu mol/dm^3$ on the bottom. All images are MIP for both channels, from experiment 14.1, first confocal imaging day. 148

Figure 4.11: Boxplot for the nucleus area, on the left, and cell area, on the right, for the experiment 14.1. Experimental parameters are shown in Table 4.2. Data represented in the graph are data of fibroblasts from different images. Each graph was divided into regions that represent different imaging days. The label on top of each region describes the only replication 14.1 and the numbers before it represent the confocal imaging day. In the horizontal axis label, *con_00uM* refers to the negative control group; *DMS_10uM*

refers to the DMSO "10 μmol/dm³" group; *DMS_30uM* refers to the DMSO "30 μmol/dm³" group; *CcD_10uM* refers to the cytochalasin D 10 μmol/dm³ group; and *CcD_30uM* refers to the cytochalasin D 30 μmol/dm³ group. 149

Figure 4.12: Boxplot for the total actin, on the left, and total actin density, on the right, for the experiment 14.1. Experimental parameters are shown in Table 4.2. Data represented in the graph are data of fibroblasts from different images. Each graph was divided into regions that represent different imaging days. The label on top of each region describes the only replication 14.1 and the numbers before it represent the confocal imaging day. In the horizontal axis label, *con_00uM* refers to the negative control group; *DMS_10uM* refers to the DMSO "10 μmol/dm³" group; *DMS_30uM* refers to the DMSO "30 μmol/dm³" group; *CcD_10uM* refers to the cytochalasin D 10 μmol/dm³ group; and *CcD_30uM* refers to the cytochalasin D 30 μmol/dm³ group. 150

Figure 4.13: Boxplot for the experiment 14.1, for the total branch length (TBL) on the top, and the number of filaments, on the bottom. Experimental parameters are shown in Table 4.2. Data represented in the graph are data of multiple images, for total branch length and for fibroblasts from different images, for the number of filaments. On the top left graph, the vertical axis was compressed after 5 μm to facilitate the visualization of the boxes. Thus, data above 5 μm are compressed and not in scale. On the top right graph, the vertical axis has a logarithmic scale. Each graph was divided into regions that represent different imaging days, the label on top of each region describes the only replication 14.1 and the numbers before it represents the confocal imaging day. In the horizontal axis label, *con_00uM* refers to the negative control group; *DMS_10uM* refers to the DMSO "10 μmol/dm³" group; *DMS_30uM* refers to the DMSO "30 μmol/dm³" group; *CcD_10uM* refers to the cytochalasin D 10 μmol/dm³ group; and *CcD_30uM* refers to the cytochalasin D 30 μmol/dm³ group. 151

Figure 4.14: Correlation coefficient, on the left, and coefficient of determination, on the right, for experiment 14.1. In the horizontal axis, the initials refer to the parameters correlated, so, TA means total actin, Ar means cell area, NF means the number of filaments and BL means total branch length. In the legend, *con_00uM* refers to the negative control group; *DMS_10uM* refers to the DMSO "10 μmol/dm³" group; *DMS_30uM* refers to the DMSO "30 μmol/dm³" group; *CcD_10uM* refers to the

cytochalasin D $10\ \mu mol/dm^3$ group; and *CcD_30uM* refers to the cytochalasin D $30\ \mu mol/dm^3$ group. The numbers before the experiment replication refers to the confocal imaging day.....153

Figure 4.15: Graphs of the slopes of linear fittings for experiment 14.1. On the top left, cell area versus total actin correlation; on the top right, cell area versus the number of filaments; and on the bottom, the number of filaments versus total actin. The legend describes the confocal imaging date (year, month and day). In the horizontal axis label, *con_00uM* refers to the negative control group; *DMS_10uM* refers to the DMSO "$10\ \mu mol/dm^3$" group; *DMS_30uM* refers to the DMSO "$30\ \mu mol/dm^3$" group; *CcD_10uM* refers to the cytochalasin D $10\ \mu mol/dm^3$ group; and *CcD_30uM* refers to the cytochalasin D $30\ \mu mol/dm^3$ group. The error bars represent two times the slope uncertainty, thus, if the error bars overlap, the slopes were considered as compatible. Otherwise, they were considered incompatible. The lines are drawn just as a guide for the eyes.....154

Figure 4.16: Correlation graph between cell area and the number of filaments. In the legend, *con_00uM* refers to the negative control group; *DMS_10uM* refers to the DMSO "$10\ \mu mol/dm^3$" group; *DMS_30uM* refers to the DMSO "$30\ \mu mol/dm^3$" group; *CcD_10uM* refers to the cytochalasin D $10\ \mu mol/dm^3$ group; and *CcD_30uM* refers to the cytochalasin D $30\ \mu mol/dm^3$ group. The numbers before the experiment replication refers to the confocal imaging day.....155

Figure 4.17: Example of images obtained with the confocal microscopy. Fibroblasts from the control group are on the left, and from the photo-treated group are on the right. All images are MIP for both channels, from experiment 1.1. 156

Figure 4.18: Boxplot of the nucleus area for the three replications of experiment 1. Experimental parameters for this experiment are shown in Table 4.2. Data represented in the graph are from fibroblasts, from different images. The graph was divided into regions that represent different imaging days, the label on top of each region describes the three replications 1.1, 1.2 and 1.3, and the numbers before it represent the confocal imaging date (month and day). In the horizontal axis label, *control* refers to the control group, and *illumin* refers to the photo-treated group, the "+" signal indicates that the photo-treated group median is larger than the control group median. The red color

indicates that the control and photo-treated sample data are not compatible according to the two-sample rank sum test and $p < 5\%$, otherwise, the green color indicate that the control and photo-treated sample data are compatible according to the two-sample rank sum test. Graphs from others experiments are in Appendix E. 157

Figure 4.19: Boxplot of the total branch length for the three replications of experiment 1. Experimental parameters for this experiment are shown in Table 4.2. Data represented in the graph are data of each image, for all images of the specific group and experiment, because for this parameter there is not one value for each fibroblast. Each graph was divided into regions that represent different imaging days, the label on top of each region describes the three replications 1.1, 1.2 and 1.3, and the numbers before it represent the confocal imaging date (month and day). In the horizontal axis label, *control* refers to the control group, and *illumin* refers to the photo-treated group, the "-" signal indicates that the photo-treated group median is smaller than the control group median. The "=" signal indicates that the medians from both groups are equal. The red color indicates that the control and photo-treated sample data are not compatible according to the two-sample rank sum test and $p < 5\%$. On the left, the vertical axis was compressed after $5\ \mu m$ to facilitate the visualization of the boxes, thus, data above $5\ \mu m$ are compressed and not in scale. On the right, the vertical axis has a logarithmic scale. Graphs from others experiments are in Appendix E. 158

Figure 4.20: Comparison between all experiments in a 3D graph, for the relative nucleus area. The relative nucleus area is the ratio between the photo-treated group median and the control group median for the nucleus area. The axis *time after treatment* is not in scale. 159

Figure 4.21: Comparison between all experiments in projections of the 3D graph shown in Figure 4.20, for the relative nucleus area. The relative nucleus area is the ratio between the photo-treated group median and the control group median, for the nucleus area. On the left, the horizontal axis shows the *time after treatment* (not in scale), the symbols represent the different gel stiffness, and the color represents the photo-treatment wavelength. On the right, the horizontal axis shows the *gel stiffness:* the symbols represent the different times after treatment, and the color represents the photo-treatment wavelength. Green outlined symbols represent samples in which the

photo-treated and control group data were compatible according to the two-sample rank sum test and a confidence interval of 95%.....159

Figure 4.22: Comparison between all experiments. Nucleus area is on the left, and cell area on the right. Each graph was separated into three regions, related to the time after treatment. The colors represent the photo-treatment wavelengths. The horizontal axis and color shades represent the gel stiffness. The parameter represented is the difference between the photo-treated group median and the control group median, divided by the control group median.....163

Figure 4.23: Comparison between all experiments. Total actin is on the left and total actin density on the right. Each graph was separated into three regions, related to the time after treatment. The colors represent the photo-treatment wavelengths. The horizontal axis and color shades represent the gel stiffness. The parameter represented is the difference between the photo-treated group median and the control group median, divided by the control group median.....165

Figure 4.24: Comparison between all experiments. The number of filaments is on the left and total branch length on the right. Each graph was separated into three regions, related to the time after treatment. The colors represent the photo-treatment wavelengths. The horizontal axis and color shades represent the gel stiffness. The parameter represented is the difference between the photo-treated group median and the control group median, divided by the control group median. 167

Figure 4.25: Correlation coefficient, on the left, and coefficient of determination, on the right, for experiment 1 replications. Experimental parameters, for this experiment, are shown in Table 4.2. In the horizontal axis, the initials refer to the parameters correlated, so, TA means total actin, Ar means cell area, NF means the number of filaments and BL means total branch length. In the legend, *control* refers to the control group, and *illumin* refers to the photo-treated group, the numbers before the experiment replication refers to the imaging day (month and day).....171

Figure 4.26: Graph of the cell area versus total actin slope for the three replications of experiment 1. Experimental parameters, for this experiment, are shown in Table 4.2. The legend represents the three replications 1.1, 1.2 and 1.3, and the numbers before

it represent the confocal imaging date (month and day). The error bars represent two times the slope uncertainty, thus, if the error bars overlap, the slopes were considered as compatible. Otherwise, they were considered as incompatible. The lines are guides for the eyes.....171

Figure 4.27: Comparison between all experiments. On the top left, the comparison for the correlation coefficient of the cell area versus total actin graph. On the top right, for the coefficient of determination, and on the bottom, for the linear fit slope. Each graph was separated into three regions, related to the time after treatment. The colors represent the photo-treatment wavelengths. The horizontal axis and color shades represent the gel stiffness. The parameter represented is the difference between the photo-treated group value and the control group value, divided by the control group value.....172

Figure 4.28: Comparison between all experiments. On the top left, the comparison for the correlation coefficient of the cell area versus the number of filaments graph. On the top right, for the coefficient of determination, and on the bottom, for the linear fit slope. Each graph was separated into three regions, related to the time after treatment. The colors represent the photo-treatment wavelengths. The horizontal axis and color shades represent the gel stiffness. The parameter represented is the difference between the photo-treated group value and the control group value, divided by the control group value.....173

Figure 4.29: Comparison between all experiments. On the top left, the comparison for the correlation coefficient of the number of filaments versus total actin graph. On the top right, for the coefficient of determination, and on the bottom, for the linear fit slope. Each graph was separated into three regions, related to the time after treatment. The colors represent the photo-treatment wavelengths. The horizontal axis and color shades represent the gel stiffness. The parameter represented is the difference between the photo-treated group value and the control group value, divided by the control group value.....174

List of tables

Table 1.1 – Summary of papers related to the effects of PBMT in blood. Data shown in grey were not presented in the paper, but calculated based on the parameters presented. The sign "?" alone means that data do not appear in the paper and could not be calculated based on the provided parameters. Data followed by the sign "?" are not clear in the paper. CW means continuous wave, ϕ and *A* mean beam diameter and area, respectively, SEM means scanning electron microscopy and *HCT* means hematocrit.....58

Table 1.2 – Summary of papers related to the effects of PBMT in the cytoskeleton. Data shown in grey were not presented in the paper, but calculated based on the parameters presented. The sign "?" alone means that data do not appear in the paper and could not be calculated based on the provided parameters. Data followed by the sign "?" are not clear in the paper. CW means continuous wave, ϕ and *A* mean beam diameter and area, respectively, and AF, MT and IF mean actin filaments, microtubules and intermediate filaments, respectively. 62

Table 2.1 – Light source parameters used in the epithelial cell photo-treatment for the OMTC experiment. The beam area was evaluated experimentally, and we got a value very different from the nominal one. For the sake of completeness, we show both values (nominal in the first line and experimental in the second line). Accordingly, power density and energy density were calculated with both area values. The number displayed in parentheses is the uncertainty, the digits are in the last decimals of the number, for example, $0.14(5)$ represents a quantity of 0.14 with uncertainly of 0.05 and $11.3(21)$ a quantity of 11.3 with uncertainty of 2.1. 69

Table 2.2 – Results of Lilliefors test. The test was performed to verify if the epithelial cell hysteresivity η or bead displacement $|d^*|$ have a lognormal distribution. Experiments named with zero as prefix are experiments to familiarize with the OMTC technique, and to test some parameters of the final experiments, such as the number of epithelial cells per well. Data presented in columns η and $|d^*|$ represent the number of groups whose analyzed data (for each parameter) can have a lognormal distribution. 75

Table 3.1 – Light source parameters used in the defocusing microscopy experiments, for the RBC photo-treatment. The quantities radiant power, power density, radiant energy, energy density and photo-treatment time were variable according to the experiment and are shown below. The beam area was evaluated experimentally, and we got a value very different from the nominal one. For the sake of completeness, we show both values (nominal in the first line and experimental in the second line). The number displayed in parentheses is the uncertainty of the beam area, the digits are in the last decimals of the number, thus, $0.196(20)\ \mathrm{cm}^2$ represents an area of $0.196\ \mathrm{cm}^2$ and $0.020\ \mathrm{cm}^2$ uncertainty. 84

Table 3.2 – Characteristics of the microscopes used in the experiments. 85

Table 3.3 – Characteristics of the electronic cameras used for image capture. The calibration shown is for the $100\times$ lens used in the experiments. 85

Table 3.4 – Light source parameters used to photo-treat different samples used in the experiments. When the parameter has two values, the first one was obtained with the nominal beam area; and the second one with the experimental beam area, and respective uncertainty. The number displayed in parentheses is the uncertainty, the digits are in the number last decimals, for example, $0.14(5)$ represents a quantity of 0.14 with uncertainly of 0.05 and $11.3(21)$ a quantity of 11.3 with uncertainty of 2.1. ...87

Table 3.5 – Statistical tests that were used for each experiment for each parameter evaluated. The difference between “none” and “-” is that none statistical test was performed in the first case, and the RBC parameter was not analyzed for the second case.....94

Table 3.6 – Average volume compatibilities for samples from experiment 2. The filled positions indicate incompatibility between the listed samples. Values were considered incompatible when $p < 5\%$ in the Z test. 102

Table 3.7 – Values of χ^2 and number of degrees of freedom (*ndf*) for linear and constant functions for experiment 3. The quality of the fitting is also presented, considering two tails and $p < 5\%$. The last column shows the slope of the linear fit and the number displayed in parentheses is the uncertainty in the last digits of the number.

For example, $0.14(5)$ represents a quantity of 0.14 with uncertainly of 0.05 and $11.3(21)$ a quantity of 11.3 with uncertainty of 2.1. 105

Table 3.8 – Values of χ^2 and number of degrees of freedom (*ndf*) for linear and constant functions for experiment 4. The quality of the fitting is also presented, considering two tails and $p < 5\%$. The last column shows the slope of the linear fit and the number displayed in parentheses is the uncertainty in the last digits of the number. For example, $0.14(5)$ represents a quantity of 0.14 with uncertainly of 0.05 and $11.3(21)$ a quantity of 11.3 with uncertainty of 2.1. 108

Table 3.9 – Results of the Student's *t*-test comparing the RBC average thickness, for samples from experiment 1. The comparison was performed for each radial distance and the table shows the compatibilities and incompatibilities by regions. The table is symmetric, thus, the positions below the diagonal are empty.....111

Table 3.10 – Results of the Student's *t*-test comparing the RBC average thickness, for the photo-treated samples from experiment 2. The comparison was performed for each radial distance and the table shows the compatibilities and incompatibilities by regions. The table is symmetric, thus, the positions below the diagonal are empty. 112

Table 3.11 – Result of the two-sample rank sum test comparing the values of the coefficient of variation from the RBC lateral fluctuation, from experiment 1. The test was performed separately for each measurement line. Data above the grey diagonal refers to the UNIQ camera, and data below the grey diagonal refers to the CMOS camera. The acronyms *Dmin* and *Dmax* refer to the distances between minima and maxima, respectively; the numbers refer to the lines where the lateral fluctuation was evaluated and there was incompatibility. The filled table positions bring information about the incompatibility between sample data, specifying the situation in which it occurred. Unfilled table positions correspond to compatibility of the compared samples. 122

Table 3.12 – Result of the two-sample rank sum test comparing the values of the coefficient of variation for RBC lateral fluctuation, from experiment 2. The test was performed separately for each measurement line. Data above the grey diagonal refers to the comparison between photo-treated samples for distance between maxima, and

data below the grey diagonal refers to the distance between minima. Finally, the grey diagonal refers to the comparison between photo-treated samples and its respective control (RBCs before photo-treatment). The acronyms *Dmin* and *Dmax* refer to the distances between minima and maxima, respectively; the numbers refer to the lines where the lateral fluctuation data were incompatible. The filled table positions refer to tests where there was incompatibility between sample data. 123

Table 4.1 – Light source parameters used in the fibroblast photo-treatment for the confocal microscopy experiment. The area considered to calculate the power and energy was the coverslip area ($1.13\ \mathrm{cm}^2$), as the module has several LEDs and is not a point source. Because of this reason, some values are not unique, but are represented by a range of values measured along the whole module. 131

Table 4.2 – Experimental configuration. For all experiments, there was always a photo-treatment group and a control group. The experiment replications mean experiments performed with the same parameters, but on different days. This was done to verify reproducibility. Experiment 13 was a cytochalasin D experiment with fixation after $1\ \mathrm{h}$, but the fibroblasts were not in good conditions, so it was discarded. 135

Table 4.3 – Matrix that represents the enhancement filter applied to the image for the number of filaments and total branch length analysis.....142

Table 4.4 – Results of the comparison between the negative and positive control groups with the two-sample rank sum test, for all parameters analyzed. The symbols “+”, “=” and “-” indicate that the positive control group median is larger, equal or smaller when compared to the negative control group median, respectively. The numbers represent the p-values, in percentage, the sample data were considered incompatible when $p < 5\%$. Incompatibility is represented in red, and compatibility in green. 152

Table 4.5 – Interpretation map for Table 4.6, Table 4.7, Table 4.9, Table 4.10, Table 4.12 and Table 4.13. Experiments are represented in each table position. The letters *A* and *B* after the experiment replication represent the imaging day, *A* refers to the first confocal imaging day of that replication and *B* the second. Experiments that do not have a letter were imaged in only one day. 161

Table 4.6 – Results of the comparison between the control and photo-treated groups with the two-sample rank sum test, for the nucleus area. The symbols “+” and “-” indicate that the photo-treated group median is larger or smaller than the control group median, respectively. The numbers represent the p-values, in percentage, sample data were considered incompatible when $p < 5\%$ and are represented in red, compatible sample data are represented in green. The experiment replication of each table position is shown in the equivalent position in Table 4.5. 162

Table 4.7 – Results of the comparison between the control and photo-treated groups with the two-sample rank sum test, for the cell area. The symbols “+” and “-” indicate that the photo-treated group median is larger or smaller than the control group median, respectively. The numbers represent the p-values, in percentage, sample data were considered incompatible when $p < 5\%$ and are represented in red, compatible sample data are represented in green. The experiment replication of each table position is shown in the equivalent position in Table 4.5. 162

Table 4.8 – Summary table with the results of the two-sample rank sum test for nucleus area and cell area. The symbols “+” and “-” indicate that for all experiments with that specific configuration, the photo-treated group median was larger or smaller, respectively, than the control group median. The symbol “+-“ indicates that for some experiments the photo-treated group median was larger than the control group median, but for other experiments, it was smaller. The red and green colors indicate that for all experiments with that specific configuration, the photo-treated and control group data were incompatible or compatible, respectively, according to the two-sample rank sum test and confidence interval of 95%. The yellow color indicates that, for some experiments, sample data were compatible, but for others they were incompatible. 163

Table 4.9 – Results of the comparison between the control and photo-treated groups with the two-sample rank sum test, for the total actin. The symbols “+” and “-” indicate that the photo-treated group median is larger or smaller than the control group median, respectively. The numbers represent the p-values, in percentage, sample data were considered incompatible when $p < 5\%$ and are represented in red, compatible sample

data are represented in green. The experiment replication of each table position is shown in the equivalent position in Table 4.5. 164

Table 4.10 – Results of the comparison between the control and photo-treated groups with the two-sample rank sum test, for the total actin density. The symbols “+” and “-” indicate that the photo-treated group median is larger or smaller than the control group median, respectively. The numbers represent the p-values, in percentage, sample data were considered incompatible when $p < 5\%$ and are represented in red, compatible sample data are represented in green. The experiment replication of each table position is shown in the equivalent position in Table 4.5. 164

Table 4.11 – Summary table with the results of the two-sample rank sum test for total actin and total actin density. The symbols “+” and “-” indicate that for all experiments with that specific configuration, the photo-treated group median was larger or smaller, respectively, than the control group median. The symbol “+-“ indicates that for some experiments the photo-treated group median was larger than the control group median, but for other experiments, it was smaller. The red and green colors indicate that for all experiments with that specific configuration, the photo-treated and control group data were incompatible or compatible, respectively, according to the two-sample rank sum test and confidence interval of 95%. The yellow color indicates that, for some experiments, sample data were compatible, but for others they were incompatible. 165

Table 4.12 – Results of the comparison between the control and photo-treated groups with the two-sample rank sum test, for the number of filaments. The symbols “+” and “-” indicate that the photo-treated group median is larger or smaller than the control group median, respectively. The numbers represent the p-values, in percentage, sample data were considered incompatible when $p < 5\%$ and are represented in red, compatible sample data are represented in green. The experiment replication of each table position is shown in the equivalent position in Table 4.5. 166

Table 4.13 – Results of the comparison between the control and photo-treated groups with the two-sample rank sum test, for the total branch length. The symbols “+”, “=” and “-” indicate that the photo-treated group median is larger, equal or smaller when compared to the control group median, respectively. The numbers represent the p-

values, in percentage, sample data were considered incompatible when $p < 5\%$ and are represented in red, compatible sample data are represented in green. The experiment replication of each table position is shown in the equivalent position in Table 4.5. 166

Table 4.14 – Summary table with the results of the two-sample rank sum test for the number of filaments and total branch length. The symbols “+”, “=” and “-” indicate that for all experiments with that specific configuration, the photo-treated group median was larger, or equal, or smaller, respectively, than the control group median. The symbol “+-“ indicates that for some experiments the photo-treated group median was larger than the control group median, but for other experiments, it was smaller. Analogous interpretation can be used for the other symbol combinations “+=”, “=-“ and “+=-“. The red and green colors indicate that for all experiments with that specific configuration, the photo-treated and control group data are incompatible or compatible, respectively, according to the two-sample rank sum test and confidence interval of 95%. The yellow color indicates that, for some experiments, sample data were compatible, but for others they were incompatible. 167

Table 4.15 – Results of the Student’s *t*-test, for comparison between the relative variation data with zero, for all parameters. The numbers represent the p-values, in percentage, sample data were considered incompatible when $p < 5\%$ and are represented in red, compatible data are represented in green. 168

Table 4.16 – Results of the Kruskal-Wallis test, for comparison between the relative variation data for each experimental variable: wavelength, time after treatment and gel stiffness, for all parameters. The numbers represent the p-values, in percentage, sample data were considered incompatible when $p < 5\%$ and are represented in red, compatible data are represented in green. 169

Table 4.17 – Results of the Student’s *t*-test, for comparison between the relative variation data with zero, for the correlation coefficients, coefficients of determination and slopes. The numbers represent the p-values, in percentage, sample data were considered incompatible when $p < 5\%$ and are represented in red, compatible data are represented in green. 175

Table 4.18 – Results of the Kruskal-Wallis test, for comparison between the relative variation data for each experiment variable: wavelength, time after treatment and gel stiffness, for the correlation coefficients, coefficients of determination and slopes. The numbers represent the p-values, in percentage, sample data were considered incompatible when $p < 5\%$, compatible data are represented in green.....176

Table 5.1 – Summary of the experiments used in this work and their respective conditions and parameters. 179

List of abbreviations, acronyms, symbols and units

Abbreviations and acronyms

In alphabetic order.

2D	Two-dimensional
3D	Three-dimensional
3T3	Mouse embryonic fibroblast cell line
AChE	Acetylcholinesterase
Ad12SV40	Adenovirus 12-SV40 hybrid virus
AF	Actin filaments
AF488	Alexa fluor 488 phalloidin
AFM	Atomic force microscopy
APS	Ammonium persulfate
Ar	Cell area
ATP	Adenosine triphosphate
bc	Bench control group
BEAS-2B	Human bronchial epithelial cell line
BL	Total Branch length
BSA	Bovine serum albumin
BSR	Blood sedimentation rate
C2C12	Murine myoblast cell line
CBC	Complete blood count
CCD	Charge-coupled device – electronic camera
CcD_10uM	Cytochalasin D $10\ \mu\ mol/dm^3$ group
CcD_30uM	Cytochalasin D $30\ \mu\ mol/dm^3$ group
CHO K-1	Chinese hamster ovary cell line
CMOS	Complementary metal oxide semiconductor – electronic camera
con_00uM	Control group
COX-2	Ciclooxygenase-2
CPB	Cardiopulmonary bypass
ctr	Control group
CW	Continuous wave
DAPI	4',6-Diamidino-2-Phenylindole, Dihydrochloride
Dmax	Distance between maxima
DMEM	Cell culture media
DMF	Dimethylformamide
Dmin	Distance between minima
DMS_10uM	DMSO "$10\ \mu\ mol/dm^3$" group
DMS_30uM	DMSO "$30\ \mu\ mol/dm^3$" group
DMSO	Dimethyl sulfoxide
DNA	Deoxyribonucleic acid
e1	OMTC experiment 1

e2	OMTC experiment 2
e3	OMTC experiment 3
EEI	Erythrocyte elongation rate
Eq.	Equation
ESR	Erythrocyte sedimentation rate
exp	Experiment
FBS	Fetal bovine serum
FFR	Filter filtration rate
GD	Good reconstruction quality
hi-j	Red blood cell code. i varies from 1 to 5, referring to the original image and j varies from 1 to 3, referring to the RCB in the image
HCT	Hematocrit
He-Ne	Helium Neon
HepG2	Human hepatocellular carcinoma cell line
ic	Incubator control group
IF	Intermediate filaments
Illumin	Photo-treated group
IQR	Interquartile range
J-5	Human hepatocellular carcinoma cell line
L929	Mouse fibroblast cell line
LED	Light emitting diode
LHC-9	Cell culture media
LLLT	Low-level laser/light therapy
MCV	Mean cell volume
MIP	Maximum intensity projection
MT	Microtubules
NF	Number of filaments
NRK	Normal rat kidney epithelial cell line
OMTC	Optical magnetic twisting cytometry
PBMT	Photobiomodulation therapy
PBS	Phosphate buffered saline
PC-12	Rat neuron cells
PFA	Paraformaldehyde
PFS	Perfect Focus System
PGE-2	Prostaglandin E2
pH	Decimal logarithm of the reciprocal of the hydrogen ion activity in a solution
PR	Poor reconstruction quality
PZT	Piezoelectric nano dislocator
RAW264.7	Mouse monocyte/macrophage cell line
RBC	Red blood cell
RBCi	Red blood cell studied. i varies from 1 to 3 and refers to the number of the RBC
RGD	Arginylglycylaspartic acid
RO	Reverse osmosis

ROS	Reactive oxygen species
RSC	Rat neuron cells
SEM	Scanning electron microscopy
SIRS	Systemic inflammatory response syndrome
TA	Total actin
TBL	Total Branch length
tr	Photo-treated group
UHN	University Health Network
UNIQ	Brand of a CCD camera used
UV	Ultraviolet
vs	Versus
WS1	Human skin fibroblast cell line

Quantities and symbols

In order of appearance in the text, separated by chapters.

ϕ	Beam diameter	Chapter 1
A	Beam area	
d	Bead displacement	Chapter 2
T	Specific torque	
g'	Cellular elastic shear modulus	
g''	Cellular loss modulus	
i	Imaginary unit (i^2=-1)	
G'	Elastic shear modulus	
G''	Loss modulus	
η	Hysteresivity	
G	Rigidity	
$\|d^*\|$	Bead displacement modulus	
χ^2	Chi-squared	
ln	Natural logarithm	
p	p-value	
n_0	Objective immersion oil refractive index	Chapter 3
f_1	Focal distance of the microscope objective lens	
δ	Space between lenses	
f_2	Focal distance of the microscope tube lens	
A_0	Angular spectrum	
z_f	Microscope defocusing length	
$\vec{k}$	Wave vector	
$\vec{q}$	Wave vector in the transverse plane of propagation direction	
$\vec{\rho}$	Position vector in the transverse plane of propagation direction	
$E(\vec{\rho},z)$	Electric field	
$h(\vec{\rho})$	Height profile of the phase object	

Δn	Difference between the phase object and objective immersion oil refraction indexes	
$C(\vec{\rho})$	Image contrast	
κ	Phase object local curvature	
h_1	Red blood cell upper membrane	
h_2	Red blood cell lower membrane	
$\mathcal{F}$	Fourier transform	
$\mathcal{F}^{-1}$	Inverse Fourier transform	
ndf	Number of degrees of freedom	
$\|Y(t)\|$	Amplitude spectrum from Fourier transformed signal	
$H(x,y,t)$	Red blood cell thickness map	
rms	Root mean square	
D	Distance between maxima or minima	
N	Data number (number of frames in the red blood cell video)	
σ_{Ar}	Cell area uncertainty	Chapter 4
$Ar_{\max}$	Maximum cell area	
$Ar_{\min}$	Minimum cell area	
σ_{TA}	Total actin uncertainty	
$TA_{\max}$	Maximum total actin	
$TA_{\min}$	Minimum total actin	
σ_{NF}	Number of filaments uncertainty	
$NF_{\max}$	Maximum number of filaments	
$NF_{\min}$	Minimum number of filaments	
IQR	Interquartile range	
ρ	Correlation coefficient	
ρ^2	Coefficient of determination	
$F_0(x)$	Reference cumulative distribution function	Appendix A
$F_e(x)$	Experimental cumulative distribution function	
KS	Kolmogorov-Smirnov test value	
m	Number of observations lower than *x*	
M	Total number of observations	
n	Standard sample size	Appendix B
P_{H_0}	Probability to find a sample more extreme than the standard sample, given the null hypothesis	
r	Standard sample rank sum	
R	Drawn sample rank sum	

Units

In alphabetic order.

μg/mL	Microgram per milliliter
μL	Microliter
μm	Micrometer
μm/px	Micrometer per pixel

μm^2	Square micrometer
μm^3	Cubic micrometer
$\mu m^3/min$	Cubic micrometer per minute
$\mu m^3/s$	Cubic micrometer per second
$\mu mol/dm^3$	Micromole per cubic decimeter
°	Degrees
°C	Celsius degrees
AU	Arbitrary unit
A.U.	Airy unit
cm	Centimeter
cm^2	Square centimeter
Da	Dalton
g	Gram
GPa	Gigapascal
h	Hour
Hz	Hertz
J	Joule
J/cm^2	Joule per square centimeter
J/mm^2	Joule per square millimeter
kHz	Kilohertz
kJ/cm^2	Kilojoule per square centimeter
kPa	Kilopascal
L	Liter
$mmol/dm^3$	Millimole per cubic decimeter
mg	Milligram
mg/mL	Milligram per milliliter
min	Minute
mJ	Millijoule
mL	Milliliter
mm	Millimeter
mm^2	Square millimeter
mol/dm^3	Mole per cubic decimeter
mOsm/kg	Milliosmol per kilogram
MPa	Megapascal
mW	Milliwatt
mW/cm^2	Milliwatt per square centimeter
mW/mm^2	Milliwatt per square millimeter
$mW/\mu m^2$	Milliwatt per square micrometer
$nmol/dm^3$	Nanomole per cubic decimeter
nm	Nanometer
px	Pixel
s	Second
W	Watt
W/cm^2	Watt per square centimeter

Contents

Resumo 7

Abstract 9

List of figures 11

List of tables 26

List of abbreviations, acronyms, symbols and units 34

Abbreviations and acronyms 34

Quantities and symbols 36

Units 37

Contents 39

1. Introduction 45

1.1 Objectives 47

1.2 Thesis structure 48

1.3 Literature review 48

1.3.1 Cell structure and mechanical properties 48

1.3.1.1 Blood and red blood cells (RBCs) 49

1.3.1.2 Cytoskeleton 50

1.3.1.3 Cell culture 51

1.3.2 Photobiomodulation therapy 54

1.3.2.1 Effects of PBMT in blood 56

1.3.2.2 Effects of PBMT in cytoskeleton 61

1.3.2.3 Summary 65

2. Optical Magnetic Twisting Cytometry 66

2.1 Material and Methods 67

2.1.1 Materials 67

2.1.2 Methods 70

2.1.2.1 Statistical analysis 73

2.2 Results 73

2.2.1 Summary 78

3. Defocusing Microscopy 80

3.1 Materials and Methods 83

3.1.1 Materials 83

3.1.2 Methods 85

3.1.2.1 Data acquisition 85

3.1.2.1.1 Photo-treatment in the Eppendorf tube with variable power (experiment 1) 86

3.1.2.1.2 Photo-treatment in the stage of microscope (experiments 2, 3, and 4) 88

3.1.2.2 Analysis 90

3.1.2.2.1 Volume 91

3.1.2.2.2 Radial profile of cell thickness 91

3.1.2.2.3 Lateral fluctuation 92

3.1.2.2.4 Vertical fluctuation 93

3.1.2.2.5 Statistical analysis 93

3.2 Results....94

3.2.1 Volume....99

3.2.1.1 Comparison between photo-treatments in the Eppendorf tube and microscope stage....99

3.2.1.2 Photo-treatment in the Eppendorf tube with variable power (experiment 1)....100

3.2.1.3 Photo-treatment in the microscope stage with variable power (experiment 2)....101

3.2.1.4 Photo-treatment in the microscope stage and fractional acquisition (experiment 3)....102

3.2.1.5 Photo-treatment in the microscope stage and fractional photo-treatment (experiment 4)....106

3.2.2 Radial profile of cell thickness....109

3.2.2.1 Comparison between photo-treatments in the Eppendorf tube and microscope stage....110

3.2.2.2 Photo-treatment in the Eppendorf tube with variable power (experiment 1)....111

3.2.2.3 Photo-treatment in the microscope stage with variable power (experiment 2)....112

3.2.2.4 Photo-treatment in the microscope stage and fractional acquisition (experiment 3)....115

3.2.2.5 Photo-treatment in the microscope stage and fractional photo-treatment (experiment 4)....116

3.2.3 Lateral fluctuation....117

3.2.3.1 Comparison between photo-treatments in the Eppendorf tube and microscope stage....120

3.2.3.2 Photo-treatment in the Eppendorf tube with variable power (experiment 1) 120

3.2.3.3 Photo-treatment in the microscope stage with variable power (experiment 2) 122

3.2.3.4 Photo-treatment in the microscope stage and fractional acquisition (experiment 3) 124

3.2.3.5 Photo-treatment in the microscope stage and fractional photo-treatment (experiment 4) 124

3.2.4 Vertical fluctuation 125

3.2.5 Summary 125

4. Confocal laser-scanning microscopy 127

4.1 Materials and methods 130

4.1.1 Materials 130

4.1.2 Methods 134

4.1.2.1 Analysis 136

4.2 Results 145

4.2.1 Cytochalasin D positive control experiments 147

4.2.1.1 Correlation analysis 152

4.2.2 PBMT experiments 155

4.2.2.1 Relative parameter and relative variation analysis 158

4.2.2.2 Correlation analysis 170

4.2.3 Summary 176

5. Final Discussion 178

6. Conclusion 186

References 188

Appendix A – Kolmogorov-Smirnov test and Lilliefors test 199

Appendix B – Two-sample rank sum test 201

Appendix C – Polyacrylamide gel substrate full protocol 203

Piranha acid cleaning 203

Activation 203

Making polyacrylamide gel substrate 205

Cross-linking gels 207

Matrigel solution 209

Appendix D – Cell fixation, permeabilization and staining 210

Cell fixation with formaldehyde 210

Permeabilization 210

Staining with fluorescence markers (AF488 and DAPI) and slide mounting 211

Formaldehyde 4% 213

AF488 stock solution 214

DAPI stock solution 214

Appendix E – Result graphs 216

Nucleus area 218

Cell area 221

Total actin 224

Total actin density 227

Number of filaments 229

Total branch length 231

Correlation coefficients between the parameters total actin, cell area, the number of filaments and total branch length 235

Coefficients of determination between the parameters total actin, cell area, the number of filaments and total branch length 237

Ar vs TA slope 239

Ar vs NF slope 241

NF vs TA slope 243

Comparison between relative parameters for all experiments 245

1. Introduction

The photobiomodulation therapy (PBMT), also known as low level laser therapy or low level light therapy is widely used in the health area, such as Medicine [1]–[3], Odontology [4]–[7] and Physiotherapy [8]. The best-known effects of the PBMT, which applies red and infrared lasers or LEDs in the treatments, are the reduction of inflammatory processes [9], improvement of wound healing [10], and reduction of pain [11].

The majority of papers approach the problem through the biochemical aspect to explain the PBMT mechanisms [12]–[18]. Regarding cell mechanical properties, which might have a major role in the PBMT mechanisms, the literature is scarce. We were motivated by a preliminary study where we observed changes in mechanical properties of blood. Therefore, we intend to research about changes in the mechanical properties of cells. In that preliminary study, measurements of viscosity of blood indicated that blood viscosity decreases for samples photo-treated with red light [19]. Those results were obtained with a rotational rheometer, which can measure the dynamic viscosity coefficient, shear rate, shear stress and torque. As the rheological properties vary greatly with temperature, the equipment has a rigid temperature control. Thus the measurements were performed at a constant temperature.

Figure 1.1 shows the results of this experiment. The samples that were not photo-treated and measured at $20\ °C$ and $30\ °C$ have similar viscosity values when the shear rate is increased and when it is reduced back to the initial value. For samples measured at $36\ °C$, the viscosity values do not return to the initial values when the shear rate is decreased. In the case of photo-treated samples, seen on the right in Figure 1.1, none of them has viscosity values returning to the initial values when the shear rate is decreased. The results of these measurements indicate that hemolysis might be happening in the photo-treated samples but not in the control samples.

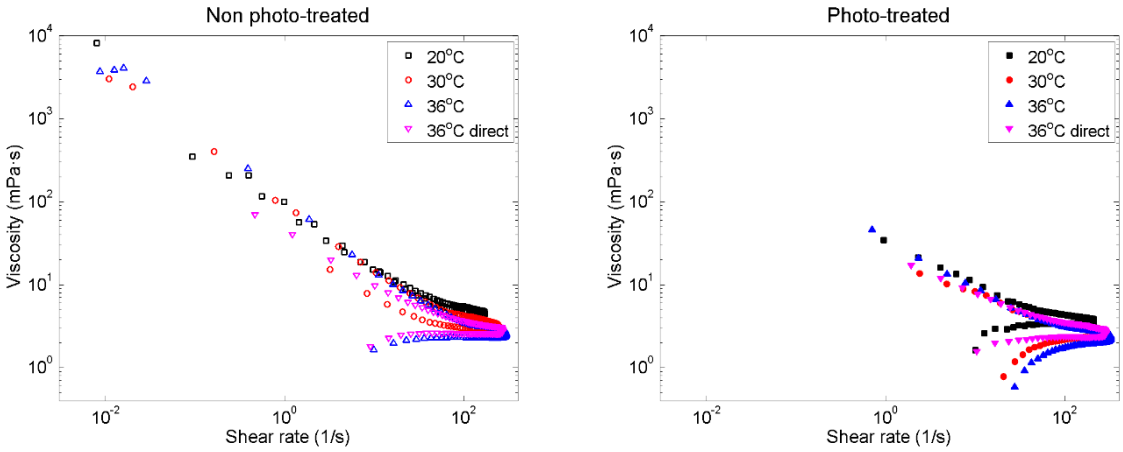

Figure 1.1: Viscosity of two blood samples diluted under the same conditions used in the cardiopulmonary bypass surgery, one of the samples was photo-treated, on the right, and the other was not, on the left. Figure adapted from [19].

Blood viscosity is highly dependent on the red blood cells (RBCs), because they compose nearly half the blood volume, they can deform and they have mechanical properties that influence primarily blood viscosity. Given that, a study of the photo-treatment action on mechanical properties of RBCs is essential.

One of the potentially interesting areas for PBMT application is in heart surgeries that use cardiopulmonary bypass (CPB). The development of this surgical procedure meant a breakthrough for heart surgery [20]. However, it is not free of risks and complications [21], [22]. The method triggers a series of physiological changes in the patients' body, due to blood diversion through a bypass circuit, and to the use of continuous flow. Furthermore, blood has contact with non-endothelial biocompatible surfaces. Due to these factors, a large number of patients develops the systemic inflammatory response syndrome (SIRS) or even sepsis, and many of them might even die because of that [20]. Besides, some technical procedures such as hemodilution (the CPB machine circuits are filled with saline solution, diluting the blood), and hypothermia are also responsible for causing physiological changes in the patient [22]. The CPB process affects largely the blood cells, especially the RBCs. The contact with non-endothelial surfaces and filters present in the CPB circuit increases the mechanical stress suffered by the RBCs. Thus, many of them undergo disruption [23]. The PBMT application during the CPB surgery, with photo-treatment of all the blood volume, would be a non-invasive option to reduce the inflammatory process. However, this is a delicate procedure, with the patient in a critical condition. This requires prior

assessment of potential effects of photo-treatment on blood cells before its use in procedures with humans.

As PBMT can also be applied to patients in various conditions, with transcutaneous application, as a non-invasive procedure, we also intend to assess the effects of photo-treatment on mechanical properties of epithelial cells and fibroblasts, which would be illuminated in the photo-treatment process. Furthermore, epithelial cells and fibroblasts are also very important in the wound healing processes, for which PBMT is largely used [12]. Besides, this study can help in collecting knowledge on cellular mechanisms involved in the photo-treatment.

1.1 Objectives

The general objective of this study is to investigate the changes that the photobiomodulation therapy (PBMT) causes in the mechanical properties of cells and cytoskeletons. It is an experimental study, using cells in vitro. It intends to contribute to the understanding of the PBMT action mechanisms in inflammatory processes and wound healing, through the knowledge acquired about light effects in cells.

The specific objectives of this study are:

- To verify if PBMT can change the elastic shear and loss moduli, or their ratio, for human epithelial cells. To reach this objective, the optical magnetic twisting cytometry was used in those cells, either or not submitted to photo-treatment, with red light and fixed power and photo-treatment time.
- To verify if PBMT can change morphological or mechanical characteristics, such as volume, radial profile cell thickness, lateral fluctuation or vertical fluctuation of human red blood cells. To reach this objective, the defocusing microscopy was used to evaluate those cells, either or not submitted to photo-treatment, with red light and different powers and photo-treatment times; and
- To verify if PBMT can change morphological or mechanical characteristics, such as nucleus area, cell area, total actin, total actin density, the number of filaments, total branch length and the correlation between some of these parameters, for mouse fibroblast cells. To reach this objective, the confocal laser-scanning microscopy was used to evaluate those cells, either or not

submitted to photo-treatment, with different wavelengths and grown on substrates with different Young's modulus.

1.2 Thesis structure

This thesis was divided into six chapters. This first chapter contains the thesis structure, besides providing the motivation, the objectives and a literature review necessary for the understanding of the work developed. Chapters 2, 3 and 4 contain the theory, materials and methods, results and a brief discussion about the experiments, for each technique used: Chapter 2 presents optical magnetic twisting cytometry; Chapter 3 shows defocusing microscopy; and Chapter 4 presents confocal laser-scanning microscopy. At last, Chapters 5 and 6 contain the final discussion of the results obtained with all techniques and the general conclusion of this work, respectively.

1.3 Literature review

The literature review refers to two subjects: the first deals with the cell structure and mechanical properties, highlighting the cytoskeleton; the second part refers to PBMT and biological effects of light.

1.3.1 Cell structure and mechanical properties

The cytoskeleton is responsible for tasks such as cell shape and movement coordination [24]. Basically, it is responsible for the structure and the mechanical properties of cells.

The cells respond to external stimuli, which can cause changes in their movement and/or shape. Many fundamental cellular functions are dependent on the cell ability to change its shape in response to external mechanical stress; indeed, the cytoskeleton is the primary responsible for these changes. Cells might present either liquid or elastic solid behaviors; both are possible and necessary in response to different external stimuli. What determines the type of behavior that the cell will present are the type of cell function and timescale [25]. Functions like contraction, migration, wound healing and division are related to the liquid behavior of the cell. On the other hand, when cells are subjected to mechanical stress, they need to preserve their structure to

counterbalance the forces to which they were subject, in those cases, cell behavior is elastic solid. These characteristics make the study of cell rheology very complex.

1.3.1.1 Blood and red blood cells (RBCs)

The blood is the liquid present in the circulatory system, which has the function of transporting, among other substances, nutrients, hormones, electrolytes, water, cell metabolism residues and, in particular, oxygen and carbon dioxide. The blood is also responsible for water balance, pH and temperature regulation. The main components of blood are cells and plasma (liquid portion). The three main kinds of cells that compose blood are RBCs, leucocytes and platelets. The plasma is formed basically by water; among others, the solid elements in plasma are proteins, lipids, electrolytes, hormones, glycose, enzymes, vitamins. The hematocrit, which is the proportion of the RBC volume and the total blood volume is in average around 45% [26].

Blood viscosity depends on the behavior of cells and plasma, and on interactions between them. More specifically, blood viscosity depends on plasma viscosity, hematocrit, RBC aggregation and deformation, being this last factor the most important [27]. RBC deformation is what determines the vessels they can reach, thus, their ability to provide tissue oxygenation and their lifetime in circulation. RBCs with reduced deformation capacity give rise to increased blood viscosity and limit the perfusion in small diameter vessels, what may cause poor tissue oxygenation.

The RBCs, also known as erythrocytes, are the most abundant blood cells and their function is oxygen and carbon dioxide transport [26]. RBC shape is a biconcave disk with a diameter around $8\ \mu\mathrm{m}$. This shape provides a high ratio between surface area and volume, facilitating gas diffusion and cell deformation for the passage through small blood vessels. It is worth mentioning that the RBC deformation is related to membrane flexibility, cell inner content viscosity and cell geometry (basically, the relationship between surface area and volume). [27]

Most animal cells have their cytoskeleton consisting of three essential filaments, which will be described following. However, RBC cytoskeleton is simpler and formed basically by spectrin. It forms a two-dimensional flexible network that covers the entire cell inner surface.

Two loosely braided chains compose spectrin molecules (see Figure 1.2, right), which are connected by junctional complexes (see Figure 1.2, left). Small actin filaments and some other proteins compose these complexes. Two membrane proteins connect this network with the RBC membrane (see Figure 1.2, center). The network that composes the RBC cytoskeleton originates a rigid cell cortex, responsible for maintaining the cell membrane structure, and allows the RBC to return to its original shape after being deformed to pass through small vessels such as capillaries. [24]

It is worth mentioning that the membrane-cytoskeleton connection determines the RBC mechanical properties.

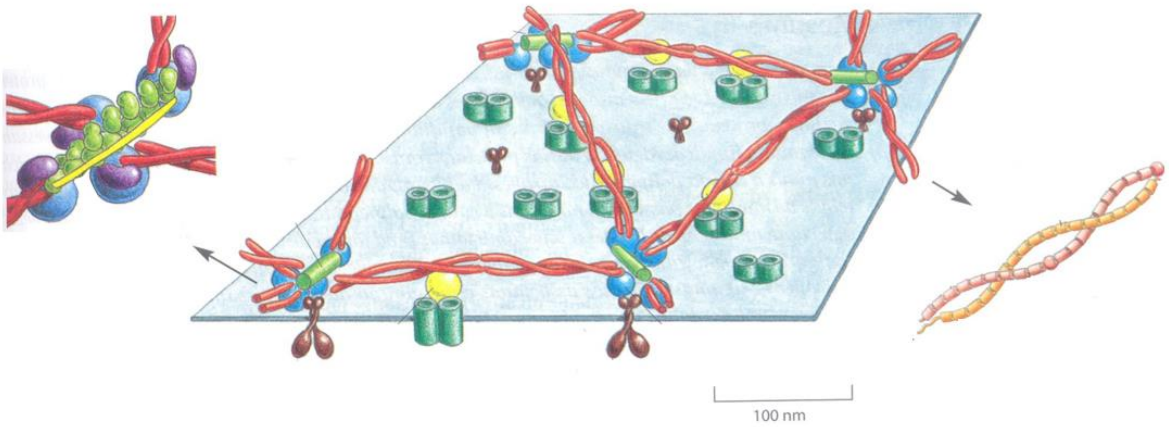

Figure 1.2: On the left, the representation of the junctional complex, which connects the spectrin molecules. Small actin filaments and other molecules form this complex. In the center, the network formed by spectrin and the junctional complex, which form the RBC cytoskeleton. On the right, the spectrin molecule. Figure adapted from *Biologia molecular da célula* [24].

1.3.1.2 Cytoskeleton

The cytoskeleton is a filament network composed by different fibers. It is responsible for the cell structure and movement, and for the transport of cytoplasm organelles, among other functions. The cytoskeleton is a dynamic structure, which reorganizes due to external stimuli or to cell division, for example. The cytoskeleton monomers form linear filaments and thus, the cytoskeleton filaments. These filaments connect protein complexes and organelles in different cell regions and transport the structures between different cytoplasm regions. Other proteins that are bound to filaments and cell components assist the roles that the cytoskeleton plays. [24]

Three types of filaments compose the cytoskeleton [24]:

- *Actin filaments or microfilaments* are formed by G-actin monomers, which are globular proteins that can bind to several types of proteins and perform different functions within the cell. Their largest concentration is just below the cell membrane, forming either a mesh or parallel bundles. Proteins bind the actin filaments to the membrane and form the cell cortex. As the cell membrane is not rigid, the cell cortex is responsible for maintaining the cell shape and the majority of movements over surfaces or within the tissue structure. The actin filament Young's modulus was estimated to be 2.6 GPa [28].

- *Microtubules* are hollow filaments formed by tubulin, which is also a globular protein. One of the microtubule ends connects to a common center, the centrosome; the other end is loose in the cytoplasm. Their main function is the location of organelles and other cell components. The microtubule Young's modulus was estimated to be around 1.2 GPa [28].

- *Intermediate filaments* are formed by a family of fibrous and elongated proteins. Their composition depends on the cell to which they belong. For example, keratin forms the epithelial cell intermediate filaments. The intermediate filaments are responsible for cell mechanical strength and resistance to mechanical stress. Therefore, they are frequent in cells that are subject to tension, such as skin and muscle cells. Due to their structure, the intermediate filaments deform but do not break. For this reason, they can withstand forces of much higher amplitudes than actin filaments and microtubules.

As said before, the cytoskeleton filaments connect to various proteins. One of these proteins, which plays a very important role, is spectrin. This long, thin and flexible protein binds to actin and form networks. [24]

1.3.1.3 Cell culture

Cell cultures are widely used nowadays in many types of research. A search for the term "*cell culture*", in the *Web of Science* results in more than 40 thousand entries, only for 2015. Despite the broad database presently, the cell culture development is recent. Only in 1885, Wilhelm Roux discovered the possibility of keeping cells alive, for a few days, out of an animal body [29]. In 1907, Ross Granville Harrison grew a nerve from a fragment of an embryonic frog tissue in lymphatic fluid and showed its

development [30]. In the early 1910, scientists showed that cells could be grown for a long time, as far as they were properly fed and kept in a sterile environment [31]. At that time, explants of various adult animals could be cultivated, and the first cell line was established, extracted from a chicken embryo, and propagated for over 30 years [29].

In 1951, the first cancer cell line was established, it was and still is widely used today. The HeLa cells were obtained from an aggressive cervical cancer of a 30-year old black woman, named Henrietta Lacks, hence the name HeLa. Typically, cervix cancer takes long to develop. However, this was not Henrietta's case, who died eight months after the cancer was diagnosed. Her cancer did not respond to treatment with radiation and was a rare type of adenocarcinoma. Possibly, these characteristics were responsible for the cell good adjustment to culture. [32], [33]

The main applications of cell culture are the production of monoclonal antibodies, such as the ones used in immunoassays or the ones associated with radioactive markers. Furthermore, some other types of protein are produced by cell cultures. The production of some vaccines, such as measles and polio, uses cell cultures, since viruses need a host, and the cultured cells play this role. At last, there is the cell therapy, which uses cells to restore tissue function or structure. An example is some degenerative disease cases, for which stem cells are used in the treatment. [34]

There are basically three types of cultured cells [34]:

- *Primary cells* are cells that grow from a piece of tissue from a living individual, so the cells that survive to the process will give rise to the culture. These cells can live in culture for a certain period. The original tissue characteristics are maintained, so they are frequently used to study the behavior of that cell type *in vitro*.

- *Established cells* are primary cells that were grown for some time. As the primary cell culture is replicated, the more resistant cells will proliferate. Despite the high proliferation rate, established cells still have the original tissue characteristics. They are widely used in research, especially in the development of vaccines, because they maintain the original tissue features and grow for much longer than the primary cells.

- *Transformed cells* are cells with their genome modified somehow, so they no longer have all the original tissue characteristics. The DNA of these cells can be modified due to multiple agents, such as chemicals, viruses or physical agents (ultraviolet radiation, for example). Usually, the genetic alteration is done in genes responsible for cell cycle control, which control the number of cell divisions so that, after a certain number of divisions, the cell would stop proliferating and would die. In transformed or cancer cells that division control process does not happen properly, and the cells divide indefinitely. For this reason, some transformed cells are obtained directly from cancer or other mutated tissue. This type of cell is often used in researches about cytotoxicity and quality control, among others.

The culture media is the source of essential substances for the cell growth. Some substances needed for metabolism and energy supply are added to the medium: minerals, carbohydrates, amino acids, vitamins, proteins, peptides, lipids and fatty acids. Many times serums, buffers, antibiotics, fungicides and pH indicators are also added. The fetal bovine serum is widely used, with concentrations ranging from 5% to 20%. It is responsible for providing growth factors, hormones and proteins, among others. Buffers help to control the culture pH. Antibiotics and fungicides are added to control the microbial contamination. The composition and complexity of the culture medium depend on the cell type and use. [34]

The epithelial cells are among the most studied cell cultures. All tissues that cover body's external structures, such as our skin, or internal parts of organs, secreting ducts and channels are called epithelium. This kind of tissue is often found in interfaces between organism and environment or between organs and fluid spaces. Its main functions are regulation of the substance permeability and protection, working either as a total barrier, in skin, or as a regulatory barrier, in intestine and lung, for example. Epithelial cells are widely studied, due to their interesting characteristics, like the fact that epithelium is usually renewable. This means that they are a good model for studies of differentiation and regulation of cell proliferation. For this same reason, epithelial cells are very subject to mutations, including those that originate the more common malignant cancers. Epithelial cells are also important in organ transplant studies, such as skin and cornea. [35]

The most studied epithelial cells are the mammary, oral, bronchial, alveolar, intestinal, cervical and prostate. Nevertheless, some studies use several other less common cell types, such as the ones from the pancreas, thyroid, kidney, endometrial, cornea and gastric mucosa [35], generating a wide range of applications for this type of cell.

Fibroblasts are the most available mammalian cell type, being found in most organs, and are very responsive to culture *in vitro*. Fibroblasts play a major role in organ development and structural tissues. Furthermore, in adult individuals, their main function is to help wound healing of skin and other complex organs. Besides, they are responsible for the synthesis of extracellular matrix in connective tissues. In culture, they present elongated spindle-shaped morphology and adherence to plastic tissue culture dishes. [36], [37]

1.3.2 Photobiomodulation therapy

Light is used as therapy since antiquity. Ancient civilizations, such as Indian, Chinese and Greek, knew about the sunlight curative effects and used it as a therapeutic agent for a variety of diseases. At the 19^{th} century, light started to be better understood, with Maxwell formulating the electromagnetic wave theory, and Lord Rayleigh explaining light scattering. The controlled phototherapy was also used at this time. Niels Finsen used it for dermatosis treatments. In the first and second wars, sunlight was used to help healing processes. However, with the antibiotic advent, the method was abandoned until recently, with the establishment of PBMT, which uses a light source (usually a laser) mainly for wound healing. [13], [38], [39]

The PBMT (also known as low-level laser therapy or low-level light therapy – LLLT) is used in many health areas, such as medicine, dentistry, physiotherapy, nursing and veterinary. It has wound healing, anti-inflammatory, anti-edematous and new angiogenesis effects. It is an effective treatment; furthermore, it is non-invasive and practically does not have collateral effects. This therapy uses a light source, usually a laser. The radiant powers used are below $1\ \mathrm{W}$ [13], this condition should not cause temperature increase greater than $1\ ^{\circ}\mathrm{C}$ in the photo-treated tissue. The PBMT action on tissue is not of a thermal nature, macroscopically: it is due to physical and chemical effects. Thus, the photoacceptors, which are certain molecules present in cells, absorb the incident photons and use its energy in chemical cell processes. Light absorption

helps the biomodulation of cell processes, such as ATP synthesis [13], [14]. The photoacceptors do not require light to perform its function. Nonetheless, this helps to perform the task. The wavelengths used in PBMT are in the red and near-infrared ranges (between $600\,\mathrm{nm}$ and $1000\,\mathrm{nm}$). Due to characteristics of photoacceptors present in biological tissue, these wavelengths are poorly absorbed by the tissue. Thus, they are used to provide a greater extent of treatment. Therefore, light penetrates far into tissue and is absorbed by skin deeper layers (dermis), not only superficial layers [40]. Light sources vary, laser is not strictly necessary. However, its advantages are the narrow wavelength range and simple coupling to optical fibers [14]. LED devices are becoming more common in PBMT, with good results in treatments [12]. Some advantages are the low cost and the possibility to couple many LED's into a large source and reduce photo-treatment times.

It is important to note that the biological effect occurs only if the light is absorbed. This is known as the first law of photochemistry: "light must be absorbed for photochemistry occur" [41]. It is also important to note that light behaves like the usual pharmaceutical drugs, it might have beneficial or harmful effects, depending on how much and where light is absorbed [38].

It is known that mitochondria absorb light photons in the range used in PBMT, causing physical and/or chemical changes in the photoacceptor molecules. This will influence the biochemical process cascades that these molecules mediate. The increase of mitochondrial activity is observed for cells that were treated with light [12], [42], [43]. The main effect is in a component of the respiratory chain, the cytochrome C oxidase, which is the primary photon absorber, leading to electron transfer. This causes changes in membrane potentials and in sodium-potassium pumps and calcium channels. These processes generate an increase in the intracellular ATP synthesis, therefore, facilitate cell division, which is essential to the healing process [13], [14]. Furthermore, the cell concentration of reactive oxygen species (ROS), mainly hydrogen peroxide (H_2O_2), increases due to photon absorption in the mitochondria. Hydrogen peroxide is a molecule that has an important role in cell signaling: it can activate transcription factors responsible for gene activation or deactivation, and it can act into calcium channels [16]. Related to the anti-inflammatory processes, PBMT is known to help their modulation [17], [44], however, in this case, the mechanism of action is not well known. Possibly, prostaglandin E2 (PGE-2) levels are reduced by

inhibition of cyclo-oxygenase-2 (COX-2), and leukocyte migration decreases [44]. Another factor still unknown is the ideal dosimetry for different kinds of photo-treatments. The best powers, energies, and densities, as well as the photo-treatment times that produce the desired biological effect, are unknown.

Few data is available regarding phototoxicity in tissue. A recent paper shows that light in the near infrared range might cause cell damage, *in vitro* and *in vivo*, and the damage is related to the temperature increase [45]. Thus, inhibition occurs if the tissue/cell has its temperature increased to around 45 °C. Also according to this study, the effect is mediated by ROS production. However, there is not induction of DNA damage.

Although the light absorption by the cytochrome C oxidase is a well stablished mechanism for the PBMT, not all the effects might be explained through the absorption by cell chromophores [46]. In this paper, Amat and colleagues suggest that some of these effects could be explained by a direct effect of the light electric field in cell components [46]. According to the authors, the incident light induces an electric field and a transmembrane potential that replaces the ATP energy, which is usually used in this process, through the ATPase pump enzyme. This mechanism could explain the maintenance of the Na^+/K^+ gradient in RBCs caused by a photo-treatment with $632.8\ nm$, as for this wavelength, there are not chromophores in the pump [46]. Other references also mention light effects in the plasmatic membrane through the Na^+/K^+ pumps [47], including in RBCs [14]. Furthermore, there are also references to effects of PBMT in calcium channels [16] and in the increase of the membrane permeability [48].

1.3.2.1 Effects of PBMT in blood

In the literature, there is a few papers about PBMT effects in blood, some related to physical and mechanical RBC characteristics and some to blood rheological characteristics. Table 1.1 shows a summary of papers found on this topic. As far as the mechanical characteristics are concerned, all papers analyze macroscopic parameters of the sample that are related to the blood rheological properties or to the RBC mechanical properties. There is some conflicting information, related to hemolysis, as Luo and colleagues [49] detected that hemolysis is increasing with laser power and Kujawa and colleagues [50], [51] did not find that PBMT causes hemolysis.

However, in Luo's paper [49], the power density used was not clear. Thus, a very high power density might be the responsible for the hemolysis outcome. Furthermore, there is not an agreement related to changes in RBC membrane. Siposan and Lukacs [52], [53] did not find changes in the membrane. Luo and colleagues [49] found that PBMT turns membrane fragile. On the other hand, Kujawa and colleagues [50], [51], and Musawi and colleagues [54] found that PBMT changes the membrane structure and the ion pumps. In addition, some authors report that PBMT has a protective effect on blood and RBCs [52], [53], [55]. Some other authors say that PBMT modulates RBC deformability and some rheological parameters [53], [56], [57].

Cen and Chen [58] report in their paper that He-Ne laser-treatment causes hemolysis and they analyze the influence of the power density used to that effect. In the study, the authors focus the laser on a RBC and measure the time that the membrane takes to break; they tested a few power densities. The hemolysis time varies from $10\ \mathrm{s}$ to $120\ \mathrm{s}$ ($2\ \mathrm{min}$) for power densities in the range of a few $\mathrm{mW}/\mu\mathrm{m}^2$. These times seem small but it is important to note that the power densities used were very high. If the units were converted, power densities would be around $10^5\ \mathrm{W}/\mathrm{cm}^2$, far above those used in PBMT. Thus, we conclude, from this paper, that photo-treatment, with the commonly used power densities are safe regarding hemolysis, at least in the red spectral range.

Table 1.1 – Summary of papers related to the effects of PBMT in blood. Data shown in grey were not presented in the paper, but calculated based on the parameters presented. The sign "?" alone means that data do not appear in the paper and could not be calculated based on the provided parameters. Data followed by the sign "?" are not clear in the paper. CW means continuous wave, ϕ and *A* mean beam diameter and area, respectively, SEM means scanning electron microscopy and *HCT* means hematocrit.

Experimental parameters	Iijima et al., 1993 [56]	Itoh et al., 2000 [55]	Siposan & Lukacs, 2000 [52]	Luo et al., 2002 [49]
Wavelength (nm) / mode	632.8	632.8	632.8 / CW	632.8
Beam size	A=0.026 mm^2	ϕ=4 mm	ϕ =2 mm	?
Radiant power (mW)	8.5	8.5	1	(1, 2, 3, 4, 5, 6, 7, 8)
Power density	32.5 W/cm^2	67.6 mW/cm^2	30 mW/cm^2	?
Time	(0, 1, 3, 5, 10, 15, 30) min	(0, 60, 120, 240) min	(57 to 132) min	40 min
Radiant energy (J)	(0, 0.5, 1.5, 2.6, 5.1, 7.6, 15)	(0, 31, 61, 122)	(3.4 to 7.9)	(2.4, 4.8, 7.2, 9.6, 12, 14.4, 16.8, 19.2)
Energy density (J/cm^2)	(0, 2, 6, 10, 19.5, 29, 59) 10^3	(0, 243, 487, 973)	(103 to 238)	?
Sample type	RBCs	Blood	RBCs	Blood
Sample condition	Diluted in 0.9% NaCl solution to 30%.	Diluted in saline solution to 25%, stored at 4 °C for 48 h, then used in a heart-lung machine	RBCs were photo-treated, then mixed again with original plasma	Diluted in physiological solution
Type of photo-treatment	Either one or two (12 h or 24 h interval) photo-treatment sections	During circulation in heart-lung machine	One photo-treatment section	One photo-treatment section
Time interval treatment-measurement	Immediate	Immediate	Immediate	24 h incubation at 37 °C
Parameters analyzed	Filter filtration rate (FFR)	Deformability, hemolysis, filtration rate, morphology with SEM	Complete blood count (CBC), blood sedimentation rate (BSR)	Hemolysis
What did change?	FFR decreases with storage time. Laser samples have higher FFR than control samples, but not as high as the fresh sample FFR.	Deformability reduces over time, but laser group has higher deformability. Laser group has more discocytes (normal shape) than control.	Some CBC changed, but others did not. BSR oscillates with dose, close to normal values	Hemolysis increases with laser power.
What does that mean?	PBMT increases deformability of damaged RBCs and helps to maintain homeostasis.	PBMT protects RBCs in whole blood from damage caused in perfusion in a heart-lung machine.	PBMT does not affect membrane stability. PBMT could help blood preservation.	PBMT turns membrane fragile.

Table 1.1 – (continuation) Summary of papers related to the effects of PBMT in blood. Data shown in grey were not presented in the paper, but calculated based on the parameters presented. The sign "?" alone means that data do not appear in the paper and could not be calculated based on the provided parameters. Data followed by the sign "?" are not clear in the paper. CW means continuous wave, ϕ and *A* mean beam diameter and area, respectively, SEM means scanning electron microscopy and *HCT* means hematocrit.

Experimental parameters	Siposan & Lukacs, 2003 [53]	Cen & Chen, 2004 [58]	Kujawa et al. 2004 [50]	Mi et al., 2004 [59]
Wavelength (nm) / mode	632.8	632.8	810	632.8 or 532
Beam size	ϕ =2mm or A=0.033cm^2	ϕ =(4, 4, 2) μm	A=0.8 cm^2	ϕ =5 mm
Radiant power (mW)	(1 or 6)	(6.5, 17, 17)	(10, 200, 400)	30
Power density	(30 or 180) mW/cm^2	(0.52, 1.35, 5.41) mW/μm^2	(12.5, 250, 500) mW/cm^2	1.5 mW/mm^2
Time	?	Variable	?	(3.6 or 1.2) s
Radiant energy (J)	?	Variable	(3, 6, 9, 12, 15, 20)	(108 or 36)
Energy density (J/cm^2)	?	Variable	(3.75, 7.5, 11.25, 15, 18.75, 25)	(5.4 or 1.8) 10^2
Sample type	Blood (?)	RBCs	RBCs	Blood
Sample condition	Whole blood (?)	In PBS	*HCT*=10% or just membranes, in PBS	Whole within 2 days after collection
Type of photo-treatment	One photo-treatment section	Continuously until the RBC membrane breaks	Either one or two photo-treatment sections	One photo-treatment section
Time interval treatment-measurement	?	Immediate	?	?
Parameters analyzed	CBC, fragility, viscosity, morphology, other indirect parameters for morpho-functional alterations.	Tolerance duration with direct light from photo-treatment	Hemolysis and membrane fluorescence and oxidation	*HCT*, erythrocyte sedimentation rate (ESR), viscosity, deformability
What did change?	Some parameters changed but others did not.	For lower power densities, tolerance duration is longer than for higher power densities.	No hemolysis; changes in membrane ion pumps.	ESR was reduced, the viscosity was reduced, and deformability was increased for laser groups. Green was better than red.
What does that mean?	PBMT modulates blood rheological parameters, does not damage membrane and helps to maintain cell shape for long storage periods.	RBCs have long tolerance duration for power densities used in PBMT.	Long-term conformational transitions of the cell membrane. Changes in membrane structure of proteins and lipid bilayer.	PBMT modulates some blood rheological parameters. Probably hemoglobin is the target of light.

Table 1.1 – (continuation) Summary of papers related to the effects of PBMT in blood. Data shown in grey were not presented in the paper, but calculated based on the parameters presented. The sign "?" alone means that data do not appear in the paper and could not be calculated based on the provided parameters. Data followed by the sign "?" are not clear in the paper. CW means continuous wave, ϕ and *A* mean beam diameter and area, respectively, SEM means scanning electron microscopy and *HCT* means hematocrit.

Experimental parameters	Luo et al., 2012 [57]	Kujawa et al. 2014 [51]	Musawi et al., 2016 [54]
Wavelength (nm) / mode	632.8 / CW	808 / CW + 905 / pulsed (1 kHz or 2 kHz)	405
Beam size	ϕ =12 mm	*A*=3.18 cm^2	*A*=0.332 cm^2
Radiant power (mW)	(1.0, 2.0, 3.0, 5.0)	620 (1 kHz) or 731 (2 kHz)	10
Power density	(0.9, 1.8, 2.7, 4.4) mW/cm^2	195 mW/cm^2 (1 kHz) or 230 mW/cm^2 (2 kHz)	30 mW/cm^2
Time	(0, 5, 15, 30) min	?	(20, 30, 40, 50) min
Radiant energy (J)	(0 to 8.9)	(0, 1.5, 3, 6, 9, 12, 15)	(12, 18, 24, 30)
Energy density (J/cm^2)	(0 to 7.9)	(0.46 to 4.9)	(36, 54, 72, 90)
Sample type	Blood	RBCs	Blood or RBCs
Sample condition	Diluted in isotonic or hypertonic solution to 5%	Diluted in PBS to 10%	Whole or in physiological solution
Type of photo-treatment	One photo-treatment section	One photo-treatment section	One photo-treatment section
Time interval treatment-measurement	?	Immediate	Immediate
Parameters analyzed	Contact area, perimeter, roundness and erythrocyte elongation index (EEI)	Hemolysis; membrane acetylcholinesterase (AChE) activity	Mean cell volume (MCV), cell count
What did change?	Increase of contact area and perimeter for almost all doses and roundness and EEI for specific doses.	No hemolysis. Dose dependent effect in membrane AChE activity. Increase in the anti-oxidative capacity of RBCs.	MCV for laser group was smaller than for control group.
What does that mean?	PBMT modulates deformability for non-homeostatic RBCs.	Changes in membrane structure and stability.	Changes in the membrane and ion pumps.

Most authors used He-Ne lasers, in the red range for their experiments and found positive results, such as modulation of deformability or rheological parameters. Authors from the same research group, reported in two papers, the use of an infrared laser with positive results [50], [51]. Furthermore, authors from two different research groups, reported in two papers the use of green (532 nm) [59] and violet (405 nm) [54] light for

their experiments, also with positive results. In the first one, Mi and colleagues compared the results for red and green wavelengths and found that the green was more efficient to modulate the blood's rheological parameters. They suggest that the photoacceptor in blood and RBCs is hemoglobin, which has much higher absorption in green wavelengths than in the red and near-infrared ranges [60]. Thus, these wavelengths are more effective, but their light penetration in tissue is reduced. Both facts have to be considered when choosing the wavelength to be used in blood photo-treatment, to balance light penetration, light absorption, and effect *in vivo*.

These papers show the relevance of executing well-controlled studies about the PBMT effects in blood and its rheological properties, showing that PBMT has a substantial effect on the regulation of these properties.

1.3.2.2 Effects of PBMT in cytoskeleton

Papers about PBMT effects in cytoskeleton are rare in literature. Furthermore, some of them report unreliable results. Table 1.2 shows a summary of the papers found on this topic. The main difference between papers about PBMT effects in blood and cytoskeleton is the scale. Usually, papers using blood samples, measured macroscopic blood parameters, which are related to blood mechanical properties, as viscosity. On the other hand, cytoskeleton studies typically look microscopically to the cytoskeleton and its organization and how this is affected by photo-treatment.

Table 1.2 – Summary of papers related to the effects of PBMT in the cytoskeleton. Data shown in grey were not presented in the paper, but calculated based on the parameters presented. The sign "?" alone means that data do not appear in the paper and could not be calculated based on the provided parameters. Data followed by the sign "?" are not clear in the paper. CW means continuous wave, ϕ and *A* mean beam diameter and area, respectively, and AF, MT and IF mean actin filaments, microtubules and intermediate filaments, respectively.

Experimental parameters	Carnevalli et al., 2003 [43]	Liu et al., 2006 [61]	Chow et al., 2007 [62]	Oliveira et al., 2009 [63]
Wavelength (nm) / mode	830	808 / CW	830 / CW	904 / pulsed
Beam size	ϕ =0.8 mm	ϕ =16 mm *A*=2.009 cm^2	*A*=1.4 cm^2	*A*=0.01 cm^2
Radiant power (mW)	?	130	400	(0; 0.25; 1.67)
Power density (mW/cm^2)	?	65	300	(0; 25; 167)
Time	?	(0; 30; 60; 90; 120; 150; 180) s	(0; 5; 30; 60; 120) s	(0; 2; 36) s
Radiant energy (J)	(0; 0.01)	(0; 3.9; 7.8; 11.7; 15.6; 19.5; 23.4)	(0; 1.5; 9; 18; 36)	(0; 0.5; 60) 10^{-3}
Energy density (J/cm^2)	(0; 2)	(0; 1.95; 3.9; 5.85; 7.8; 9.75; 11.7)	(0; 1.4; 8.3; 16.7; 33.3)	(0; 0.05; 6)
Cell type	Chinese hamster ovary	Human hepatocellular carcinoma	Rat dorsal root ganglion	Mouse fibroblast cell
Lineage	CHO K-1	HepG2 and J-5	Primary cells	L929
Cytoskeleton filament	IF	AF, MT and IF	MT	AF
Cell condition	Nutritional stress	Healthy cells	Healthy cells	Healthy cells
Wells	24-well plate	24-well plate	24-well plate	96-well plate
Type of photo-treatment	?	One photo-treatment section	One photo-treatment section	Fractional with 24 h intervals
Time interval treatment-measurement	?	24 h	(1, 4 and 24) h	(24, 48 and 72) h
What did change?	A little disturbance on the organization of the parallel bundles of IF was observed. IF also presented depolarization of their proteins.	AF – expression did not change IF and MT – collapsed and became fragmented and irregular to form aggregated lattices. Organization of cytoskeleton destructed	Formation of intensely β-tubulin positive axonal varicosities that are resolved by 24 h.	Photo-treated cells showed greater distribution and organization of the AF.
What does that mean?	Cell division, which is preceded by depolarization and disarrangement of the cytoskeleton.	Cell adaptation or damage. Inhibitory effect.	β-tubulin positive varicosities are an indicative of MT disruption.	Biomodulatory effects with cell proliferation

Table 1.2 – (Continuation) Summary of papers related to the effects of PBMT in the cytoskeleton. Data shown in grey were not presented in the paper, but calculated based on the parameters presented. The sign "?" alone means that data do not appear in the paper and could not be calculated based on the provided parameters. Data followed by the sign "?" are not clear in the paper. CW means continuous wave, ϕ and *A* mean beam diameter and area, respectively, and AF, MT and IF mean actin filaments, microtubules and intermediate filaments, respectively.

Experimental parameters	Ricci et al., 2009 [64]	Monici et al., 2013 [65]	Houreld et al., 2014 [66]	Lim et al., 2014 [67]
Wavelength (nm) / mode	685	(808, 905) / pulsed	660 / CW	635
Beam size	*A*=1.8 cm^2	ϕ =13 mm	*A*=9.1 cm^2	ϕ =5 mm
Radiant power (mW)	20	550, variable	100	0.4
Power density (mW/cm^2)	11.1	?	11	2
Time	0; 1440 s (24 min)	(0; 20 or 60) s (?)	0 s; 455 s (7 min 35 s)	72 h
Radiant energy (J)	(0; 28.8)	68	45.5	102
Energy density (J/cm^2)	(0; 16)	?	5	518
Cell type	Rabbit aorta endothelial cell	Murine myoblast (skeletal muscle cell)	Human skin fibroblast cells	Mouse monocyte/ macrophage
Lineage	RAEC	C2C12	WS1	RAW264.7
Cytoskeleton filament	AF	AF, MT and IF	Genes related to the cytoskeleton	Actin ring and genes related to it
Cell condition	Media with 0, 5 or 10% fetal bovine serum (FBS)	Healthy cells	Healthy cells	Healthy cells
Wells	24-well plate	24-well plate	6-well plate	96-well plate
Type of photo-treatment	Four sections with 12 h intervals	Sections once a day for 3 days	One photo-treatment section	One photo-treatment section
Time interval treatment-measurement	144 h (6 days)	Immediate	48 h	?
What did change?	Reorganization of AF and increase in the number of stress fibers across the cytoplasm. AF organization is similar to non-treated healthy cells.	Redistribution of the filaments. Elongated shapes, alignment and fusion to form structures with nuclei and between cells. Proteins related to cytoskeleton changed.	76 of 84 genes had their expression changed. 5 were related to cytoskeleton: 2 genes up-regulated 3 genes down-regulated	Disorganization of actin rings in the cell periphery. Fewer cells with actin rings. Smaller cells with actin rings. Always comparing photo-treated with control groups.
What does that mean?	Reestablishment of cellular homeostasis, in the period without growing factors.	Differentiation process. Cytoskeleton network remodeling.	Cell motility, structure and integrity, cytoskeleton reorganization.	Inhibition of bone matrix resorption Regulation of bone remodeling.

Some of the papers about PBMT action in cytoskeleton present some issues. For example the paper of Carnevalli and colleagues [43], does not present all the parameters used in the cell photo-treatment. They present only wavelength, beam diameter and energy density, data that are not enough to calculate the other parameters. This prevents the comparison to data obtained in other papers. The authors do not define the nutritional deficiency that the cells were subjected to. Another problem found in two papers is related to the pulsed laser: in the paper of Oliveira and colleagues [63], the authors did not explain important parameters, such as pulse duration, frequency, and pulse form. Furthermore, it is not clear whether the laser energy density values refer to the average over time, or to the peak values. This means that the calculated values for energy, power, and their densities might be incorrect. In the paper of Monici and colleagues [65], the authors present more information about the pulsed-mode, but how the cell photo-treatment was performed is unclear. At last, in the paper of Liu and colleagues [61], the authors show images of stained cells either to intermediate filaments or microtubules, for cells that were either photo-treated or not. For those cells and the parameters used, they found that PBMT might induce cell damage and might have an inhibitory effect. However, the photo-treated cell shapes are very different from each other, even considering that the cells were stained with different markers. If they have gone through the same procedure, they should present similar shapes. This may indicate a problem with the samples, which could mean that the inhibitory effect was caused by another factor, and not the photo-treatment.

The other papers seem to have relevant data regarding the PBMT effect in the cytoskeleton. Chow and colleagues [62] indicate that the PBMT might have an effect on axons, causing temporary conformational changes in microtubules, modulating the nerve impulse transmission and inhibiting pain. Ricci and colleagues [64] show that the PBMT may lead cells to homeostasis when the cells were restricted of growth factors. According to the authors, the PBMT causes actin filament changes in the deprived cells so that their organization becomes similar to the organization of the cytoskeleton of healthy cells. Houreld and colleagues [66] evaluated gene expression from healthy cells either or not subjected to PBMT. The result showed that from the 84 genes assessed (5 related to cytoskeleton), 76 (including the 5 cytoskeleton-related genes) had their expression changed. Two of the cytoskeleton-related genes had decreased expression, and three genes had increased expression. These genes are related to

mobility, cell structure and integrity, and cytoskeletal reorganization. However, it is not possible to determine the specific effects of PBMT in the cytoskeleton, in particular, if their function was modified. At last, Lim and colleagues, [67] found a PBMT inhibitory effect. Actually, the authors' objective was to inhibit the cells. Because of that, they used low powers and power densities with long photo-treatment times, resulting in very high energy and energy densities, and thus the inhibitory effect.

Again, these papers show the relevance of doing well-controlled studies about the PBMT effects in the cytoskeleton, showing that PBMT has an important effect, promoting the cytoskeleton regulation. With this in mind, we proposed and executed a series of experimental studies to aggregate knowledge on the effects of PBMT on the mechanical properties of various cell types, regarding changes in their cytoskeleton.

1.3.2.3 Summary

The most accepted mechanism of the PBMT is the photon absorption by the cytochrome C oxidase, in the mitochondria. However, there are some effects that cannot be explained by this mechanism, thus, there are other possible mechanisms that might not involve the light absorption by chromophores, such as the preservation of the Na^+/K^+ pump activity in the cell membrane due to induction of electric fields in the membrane.

Regarding the effects of the PBMT in blood, for the light power ranges used for PBMT, the light does not cause hemolysis. Furthermore, PBMT modulates some blood rheological parameters, such as deformability and cell shape, which helps to preserve RBCs in stress situations.

Regarding the effects of the PBMT in the cytoskeleton, the main effects reported are in actin filaments and microtubules, mainly in the filament organization, which might be related to some cell functions as cell division or migration.

2. Optical Magnetic Twisting Cytometry

Optical magnetic twisting cytometry (OMTC) is a technique used to investigate rheological and mechanical properties of cells in culture. [25], [68]–[75]

The technique consists in binding ferrimagnetic microbeads, to the cytoskeleton. The beads are previously treated with a peptide that bind to the integrin receptors on the cell surface. The beads, already adhered to cells, are horizontally magnetized with a strong magnetic pulse; after that, an oscillatory vertical magnetic field is applied to the sample. This field creates a torque that makes the beads twist, trying to align their magnetic dipole moment with the direction of the oscillating field. The bead rotation is limited as they are tied to the cell. Thus, the beads tend to move laterally. Furthermore, the cells react by creating an internal tension to resist the movement. The registration of the bead motion under the influence of the oscillatory magnetic field and posterior analysis allows the determination of the complex viscoelastic moduli of the cytoskeletal structure of the cells.

Through the relation of the bead displacement (d) and the specific torque (T) is possible to obtain the cellular elastic (g') and loss (g'') moduli, as shown in Eq. 2.1. The symbol * indicates the Fourier transform and $i^2 = -1$. The elastic shear G' and loss G'' moduli are obtained multiplying g' and g'', respectively, by a geometric factor related to cell shape and thickness, and to the degree of bead embedding in the cell membrane. [70], [75]

$$g = g' + i\,g'' = \frac{T^*}{d^*} \qquad \text{Eq. 2.1}$$

With this methodology, G' and G'' may vary up to three orders of magnitude [76], even when comparing cells from the same lineage cultured in the same well. These variations might be caused by several factors, such as differences in properties of cell elements; or differences in cell structures to which the microbeads are bound; or even, by geometry differences between cells, such as thickness, contact area between cell and bead, among others. Although the differences in cell elements or structures to which the beads are bound are interesting to the experiment results, it is not trivial to separate these types of contribution from the geometrical differences between cells. The parameter called hysteresivity η is often used in order to avoid this kind of issue and to eliminate undesirable contributions; it is defined as the ratio between G'' and

G' [76]. It might be related to the solid-liquid behavior of the cell [77], thus, for high values of η the cell behaves like a dissipative liquid, for small values of η the cell behaves like an elastic solid. An alternative to this approach is to use each cell as its own control. This means to compare the moduli before and after the action of some substance that causes changes in the cell mechanical properties; for example, histamine which can increase cell stiffness [72]. Nevertheless, some studies compare absolute values of the moduli measured. For example, Dinardo and colleagues [78] use OMTC to detect differences between cells of the same type, in this case arterial vascular smooth muscle cells, but from different sources: abdominal or thoracic aorta, renal, femoral, among others. They could differentiate these cells through their mechanical properties. In another paper, from Dinardo and colleagues [79], the authors also used vascular smooth muscle cells, to verify differences in rigidity G and hysteresivity η for multiple passages of this cell culture. They showed that G decreases with the passage while η increases.

The exact process by which the beads bind to cells is not known; the exact cell element to which they bind is also unknown. Nevertheless, OMTC is sensitive to changes caused in many processes or cellular components, such as actin filaments, myosin motors, cell spreading, cell stretching, cytoskeletal tension, among others [80].

In this work, optical magnetic twisting cytometry was used to evaluate human bronchial epithelial cells, either or not submitted to photo-treatment with red light and fixed power and photo-treatment time. The effects of the PBMT in the ratio between the loss and elastic shear moduli, the hysteresivity η, of those cells were studied.

2.1 Material and Methods

The optical magnetic twisting cytometry experiments were performed in the Laboratory of Micro-Rheology and Molecular Physiology, at the Institute of Physics of University of São Paulo.

2.1.1 Materials

Cells of human bronchial epithelial cell culture, lineage *BEAS-2B*, were used. It is transformed by adenovirus *12-SV40*, hybrid virus (*Ad12SV40*). The epithelial cells were grown either in plastic bottles of $25\ \mathrm{cm}^2$ area or in cylindrical wells with $0.32\ \mathrm{cm}^2$

area, present in 96 well plates. The bottom of the bottles and wells was covered with Matrix Matrigel (*BD* Medical Technology). Containers were kept at 5 °C overnight after Matrigel application, washed with phosphate buffered saline solution (PBS), and then used for cell culture. As the Matrigel is a thin layer, the Young's modulus of the growing cells was determined by the tissue culture plastic (> 1 MPa).

The *LHC-9* culture media used was supplemented with penicillin and streptomycin, L-glutamine, sodium pyruvate, nonessential amino acids and 10% fetal bovine serum (FBS). The epithelial cells were grown in bottles and cultured in the incubator at 37 °C and 5% carbon dioxide. The media was replaced every 48 h. The epithelial cells were sub-cultured when reaching 90% confluence, according to standard protocols.

One day before the OMTC experiment, samples were prepared for the experiments. The epithelial cells were separated from the culture bottle with trypsin, centrifuged, resuspended in culture media, counted and placed in culture wells. After that, they were kept in the incubator under the same conditions described above, for 24 h. The media placed in wells was not supplemented with FBS. Each well received approximately 15 thousand cells.

The magnetic microbeads used have approximately 4.5 μm diameter and were coated with a synthetic peptide that attaches to the cytoskeleton. The peptide has an Arginylglycylaspartic acid (RGD) sequence that binds to integrin, on the cell's surface [76]. A carbonate buffer solution with pH 9.4 and 1 mg/mL bead concentration was prepared and added to the wells.

A red laser Twin Flex Evolution, from MMOptics, was used for the epithelial cell photo-treatment. Table 2.1 presents the parameters used in the experiment.

Table 2.1 – Light source parameters used in the epithelial cell photo-treatment for the OMTC experiment. The beam area was evaluated experimentally, and we got a value very different from the nominal one. For the sake of completeness, we show both values (nominal in the first line and experimental in the second line). Accordingly, power density and energy density were calculated with both area values. The number displayed in parentheses is the uncertainty, the digits are in the last decimals of the number, for example, $0.14(5)$ represents a quantity of 0.14 with uncertainly of 0.05 and $11.3(21)$ a quantity of 11.3 with uncertainty of 2.1.

Light source	Laser (InGaAlP)
Wavelength	660 nm
Beam area	0.04 cm^2 0.196(20) cm^2
Opening angle	4°
Nominal radiant power	30 mW
Power density	750 mW/cm^2 153(16) mW/cm^2
Time of photo-treatment	300 s
Radiant energy	9 J
Energy density	225 J/cm^2 46(5) J/cm^2
Distance between the laser and the sample	18.00(10) cm

An inverted microscope*, Leica DMI 4000 B*, was used, with a $10\times$ magnification objective and 0.3 numerical aperture, see Figure 2.1, left. Solenoids are attached to the microscope to generate the magnetic field to magnetize the microbeads (vertical direction) and the oscillatory magnetic field (horizontal direction), see Figure 2.1, right. An image capture system, composed of a *CCD camera Allied pike F100B ASG16* is also attached to the microscope. Both systems (magnetic and image capturing) are connected to a computer and are controlled by a specific software.

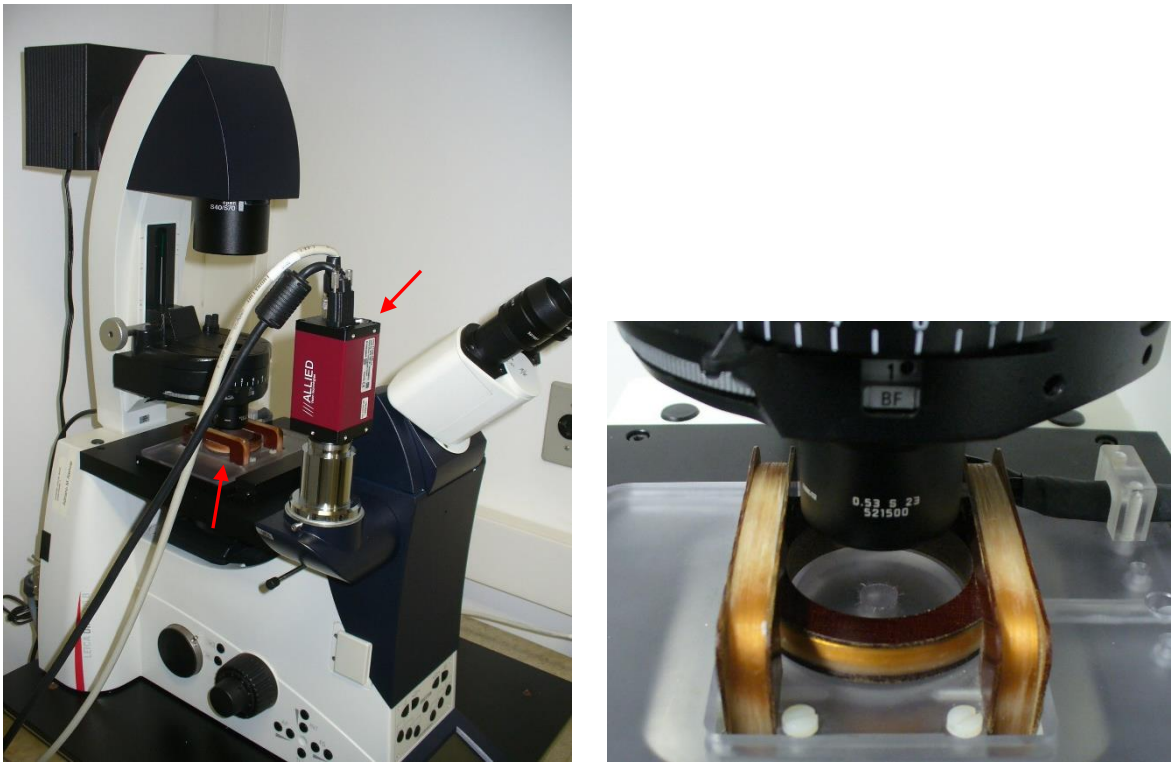

Figure 2.1: On the left, the microscope used for OMTC measurements. The left arrow shows the solenoids responsible for magnetic field generation. The right arrow shows the CCD camera attached to the microscope, which is responsible for the image capture. On the right, a detailed image of the solenoids responsible for the magnetic field generation required for the experiment. The central hole is the place for the wells with cells.

2.1.2 Methods

The experiment was executed in triplicate, using the same parameters for each experiment. The three experiments were conducted in the same manner, with epithelial cells with similar characteristics. The only difference is that they were done in different days, and were performed as biological repeats to verify the reproducibility of results.

The epithelial cell samples were divided into three groups, each one with eight wells:

- *Group 1* – incubator control (*ic*) – epithelial cells that were not photo-treated and were kept inside the incubator while the group 3 was photo-treated;
- *Group 2* – bench control (*bc*) – epithelial cells that were not photo-treated, but remained on the bench during the group 3 photo-treatment. This group was planned to verify the effects of the non-suitable environment on the epithelial cells. The incubator is considered a suitable environment for cells because it has controlled temperature (37 °C) and atmosphere (air with 5% of carbon dioxide concentration). Groups 1 and 2 (*ic* and *bc*) passed through the same

steps, except for the photo-treatment interval, in which group 1 (*ic*) was inside the incubator and group 2 (*bc*) remained on the bench;

- *Group 3* – photo-treated (*tr*) – epithelial cells that were treated with PBMT.

The epithelial cells were photo-treated before adding the magnetic microbeads. Thus, beads would not influence in any way the light distribution or the light interaction with the epithelial cells. The laser was positioned perpendicularly above the wells. Figure 2.2 shows the experiment protocol schematized. The photo-treatment was performed in two stages, in four wells at a time. As a result, the time that epithelial cells were outside the incubator was just the necessary for the photo-treatment, around $20\ \mathrm{min}$. In Figure 2.2, the two timelines represent these two stages. Furthermore, these timelines were performed in parallel, because there were many waiting intervals. The photo-treatment in the second set of wells started when the first set of wells was being incubated for the first time. Right after the photo-treatment, the wells were washed with PBS and incubated for $10\ \mathrm{min}$ (in Figure 2.2, the slashed intervals represent incubation). After that, $10\ \mu\mathrm{L}$ of the magnetic micro bead solution was added to each well. Then, wells were incubated for $20\ \mathrm{min}$. Thus, the beads could decant and bind to the epithelial cells. After that, wells were washed again with PBS, to remove loose beads, following a $10\ \mathrm{min}$ incubation and OMTC measurements. Epithelial cells were always incubated in media without FBS.

For the OMTC measurement itself, the wells were removed one by one from the incubator and passed through the measuring process. Wells that were not being measured were kept inside the incubator, to preserve the epithelial cells. The camera capture frame rate was $15\ \mathrm{Hz}$ and data were collected for $60\ \mathrm{s}$, during which the oscillatory magnetic field was applied. The data acquisition software identifies the beads in each image and records their individual positions in a text file.

The data analysis software uses the individual bead positions to calculate bead displacement and then the epithelial cells' mechanical parameters using Eq. 2.1 presented previously, in the technique description section 2.

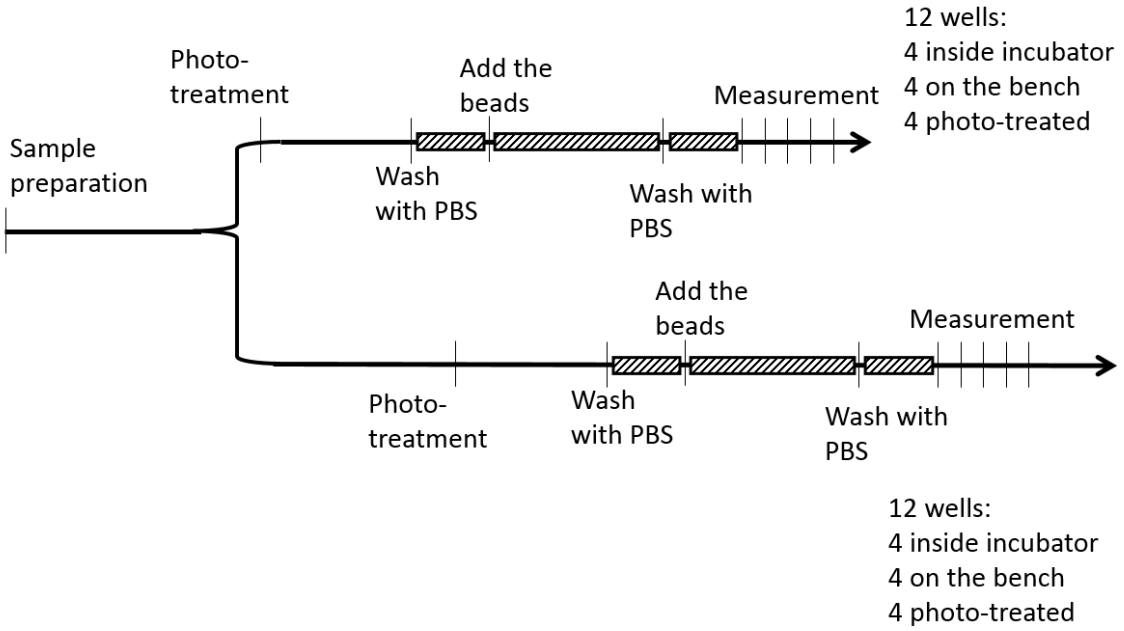

Figure 2.2: Flowchart of the experimental protocol, from the preparation of epithelial cells to photo-treatment and measurement. The slashed intervals represent epithelial cell incubation. The two timelines were performed in parallel. Twelve wells were used in each timeline, four for each group.

An experiment was performed to estimate the energy absorption by the sample. For that, incident (laser only) and transmitted (laser through sample) power were measured in three setups:

1. The sample was the culture well coated with matrigel and $200\ \mu L$ of culture media. This setup was done to verify the power transmitted through an arrangement that was composed by all the elements except for the epithelial cells.

2. The sample was the culture well with 15 thousand epithelial cells, prepared in the same manner used for OMTC experiments.

3. The sample was the culture well with 45 thousand epithelial cells. This sample was used to verify if a larger amount of epithelial cells would absorb more, and if this difference could be detected by the experimental system.

For each setup, eight wells were used; for each one, the measurements were duplicated.

2.1.2.1 Statistical analysis

Two statistical analysis were performed: the first one, to verify the lognormality of the hysteresivity η and bead displacement $|d^*|$ distributions. This distribution was chosen because data seem to be lognormally distributed, also because Fabry and colleagues suggest this [81]. For that, Lilliefors test was used [82], this test is described in more detail in Appendix A. For each group of each experiment the Lilliefors test was performed to verify if the natural logarithm of cell hysteresivity η or bead displacement $|d^*|$ had a normal distribution, which means data with a lognormal distribution. This test was chosen because it is more accurate than the χ^2 test [83].

The second statistical analysis was performed to compare the hysteresivity η of different groups among themselves, within a single experiment and to compare different experiments, within the same group. For that, the two-sample rank sum test was used [84], it is detailed in Appendix B. This test was chosen because it can be utilized for any data distribution. Moreover, it is useful when there are outliers as the test is not much affected by them. [84]

2.2 Results

Histograms from Figure 2.3 show hysteresivity η for experiment 1 for photo-treated epithelial cells: on the left, the histogram for η, on the right, the histogram for $\ln(\eta)$. This one seems to approximate a normal distribution, which would mean that η would have approximately a lognormal distribution. Figure 2.4 shows similar histograms for bead displacement, $|d^*|$, in the same experiment, for the bench control group.

The results for Lilliefors test, for η and $|d^*|$ data, for many OMTC experiments, are shown in Table 2.2. The null hypothesis, data having a lognormal distribution, was rejected when $p < 5\%$. None of the analyzed groups might have η data with a lognormal distribution. Thus, it suggests that data is not lognormally distributed. Besides, for bead displacement, 25% of groups might have lognormal distribution data, which also suggests that this is not the overall data distribution. According to a paper from Fabry and colleagues [81], bead displacement seems to have a lognormal distribution, but in that paper, they did not mention statistical tests performed to corroborate the affirmation.

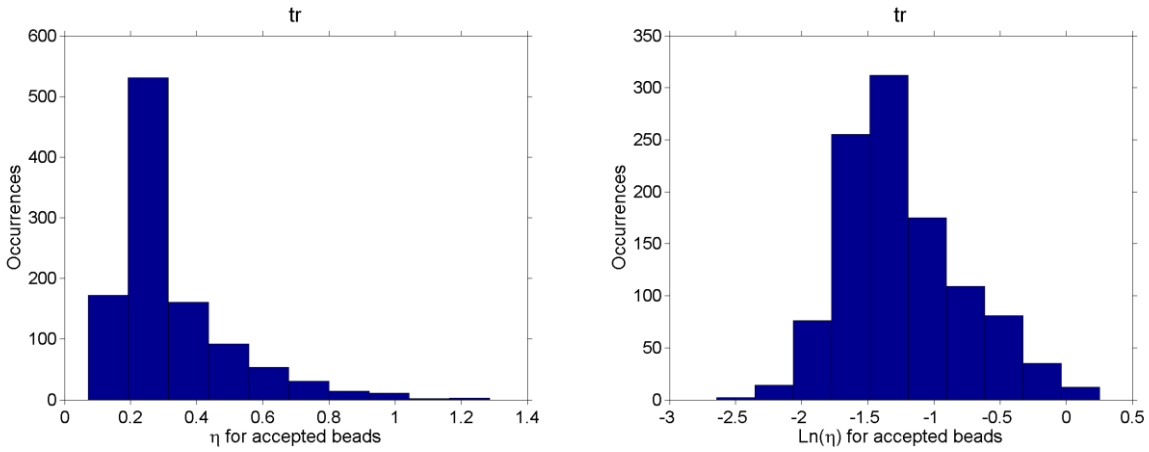

Figure 2.3: Hysteresivity histograms for the photo-treated group. On the left, the histogram for η and on the right the histogram for ln(η). Although data seem to have a lognormal distribution, according to Lilliefors test they do not have.

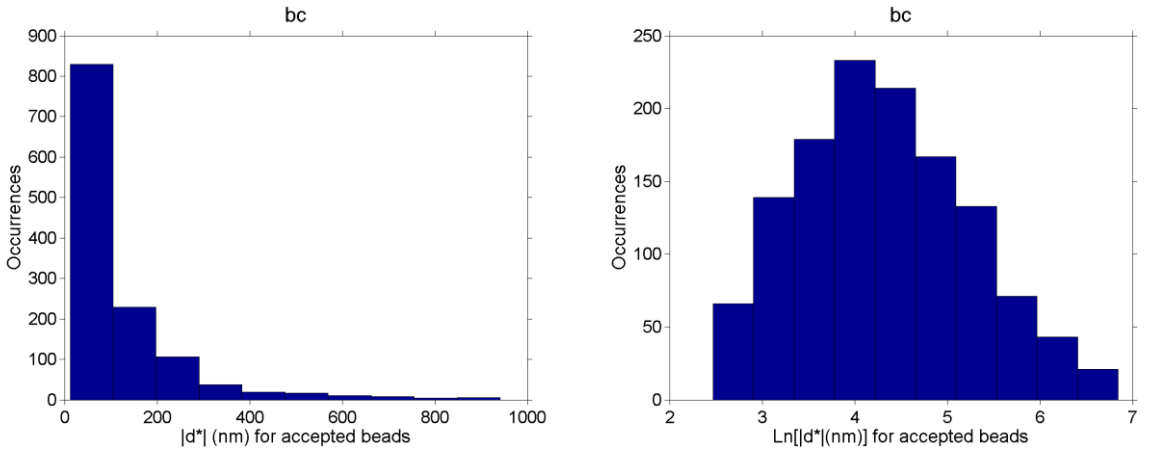

Figure 2.4: Histogram of micro bead displacement for the bench control group. On the left, the histogram for |d^*| and on the right, the histogram for ln(|d^*|). Although data seem to have a lognormal distribution, according to Lilliefors test they do not have.

Figure 2.5 shows the results for OMTC experiments 1, 2 and 3. The amplitude of η is similar between days and groups, without very strong variations. Data from different groups and experiments were tested with the two-sample rank sum test, whose results are shown in diagrams of Figure 2.6 and Figure 2.7. From these diagrams, it is possible to conclude that the technique cannot differentiate between macro environmental changes (such as day, climate, culture media, cell passage, etc.), effects of the microenvironment (such as the non-suitable environment for cells – epithelial cells remaining $20\ \mathrm{min}$ outside the incubator) and the photo-treatment.

Table 2.2 – Results of Lilliefors test. The test was performed to verify if the epithelial cell hysteresivity η or bead displacement $|d^*|$ have a lognormal distribution. Experiments named with zero as prefix are experiments to familiarize with the OMTC technique, and to test some parameters of the final experiments, such as the number of epithelial cells per well. Data presented in columns η and $|d^*|$ represent the number of groups whose analyzed data (for each parameter) can have a lognormal distribution.

Experiment	η	$\|d^*\|$	Total of analyzed groups
0.1	0	3	3
0.2	0	1	1
0.3	0	0	2
0.4	0	0	1
1	0	0	3
2	0	0	3
3	0	0	3
Total	0	4	16

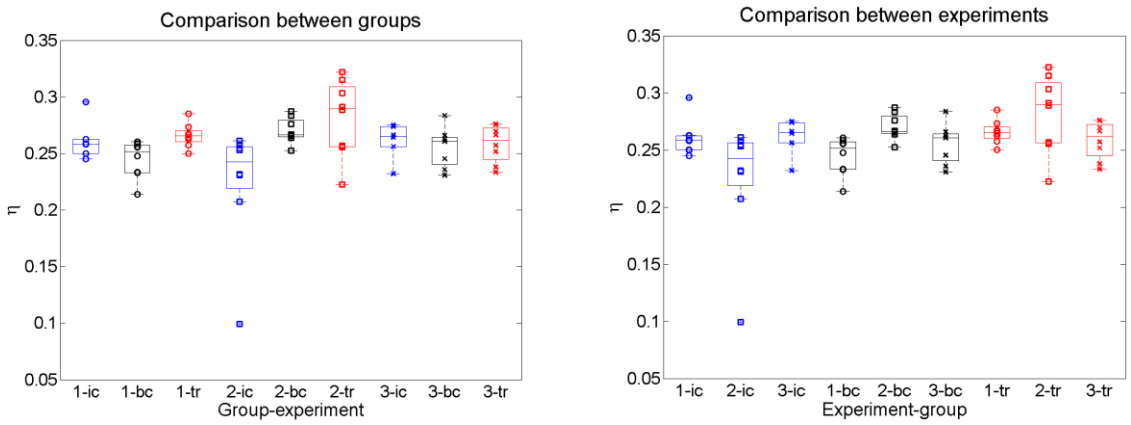

Figure 2.5: Results for the three OMTC experiments. The two graphs show the same data but grouped differently. On the left, data were grouped by experiments (1, 2 and 3) and on the right by epithelial cell group (*ic*, *bc* and *tr*). The data boxplots† are also shown. The numbers 1, 2 and 3 in the horizontal axis label refer to the experiment. The acronym *ic* refers to the control group whose wells stayed all the time in the incubator, *bc* refers to the control group whose wells stayed part of the time outside the incubator, on the bench, and *tr* denotes the photo-treated group.

† In the boxplots used here, the central line shows the median; the bottom and top box edges show the first and third quartiles, respectively; the whiskers represent 1.5×IQR (interquartile range); and individual points represent outliers.

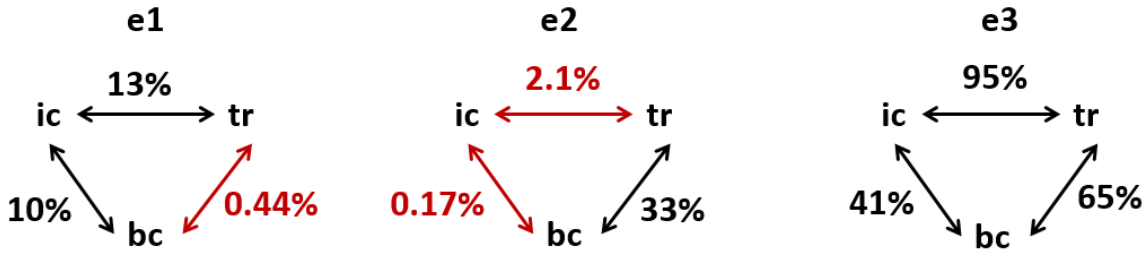

Figure 2.6: Diagrams with p-values obtained with the two-sample rank sum test comparing the hysteresivity η of different groups in the same experiment. The groups were considered different when $p < 5\%$. On the left, experiment 1 (*e1*), on the center, experiment 2 (*e2*), and on the right, experiment 3 (*e3*). The acronym *ic* refers to the control group whose wells stayed all the time in the incubator, *bc* refers to the control group whose wells stayed part of the time outside the incubator, on the bench, and *tr* denotes the photo-treated group. The red arrows indicate groups with values not compatible, for the same experiment.

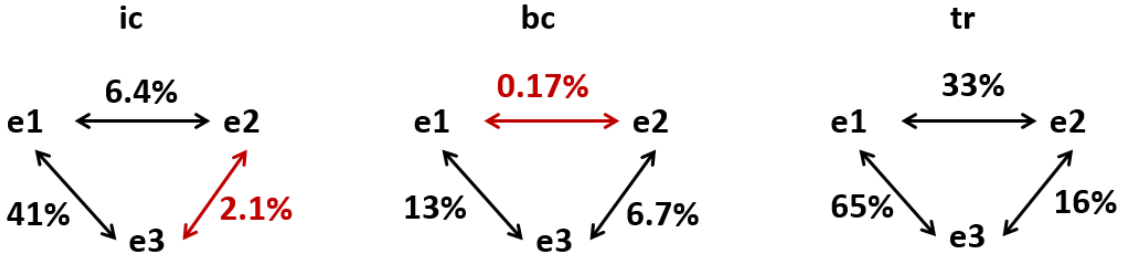

Figure 2.7: Diagrams with p-values obtained with the two-sample rank sum test comparing the hysteresivity η of different experiments for the same group. The groups were considered different when $p < 5\%$. On the left, the control group whose wells stayed all the time in the incubator (*ic*), on the center, the control group whose wells stayed part of the time outside the incubator (*bc*), and on the right, the photo-treated group (*tr*). The acronym refers to experiment 1 (*e1*), experiment 2 (*e2*) and experiment 3 (*e3*). The red arrows indicate groups with values not compatible, for the same group.

Finally, there is the evaluation of light absorption by epithelial cells. Figure 2.8 shows the comparison between the first and second evaluations of transmitted light of each setup (measurements 1 and 2). Student's *t*-test was done to compare both measurements of each setup. As the samples are statistically dependent within a setup and well, the difference between the measurements 1 and 2 of each well was tested with zero, if compatible, the samples are considered similar, otherwise, the samples are considered different. The numbers in the graph indicate the p-values, for the Student's *t*-test. Figure 2.9 shows, for each measurement, the comparison between the three setups, which means the comparison between samples with a different number of epithelial cells. Student's *t*-tests were executed, and p-values are shown in Figure 2.10. Here, as the measurements are statistically independent, it was not necessary to take the difference between their results. The red color indicates the

setups that have averages incompatible between them, considering $p < 5\%$. In the case of measurement 1, the three setups have incompatible averages, and the average transmission in setup 1 is smaller than in setups 2 and 3, which refer to wells containing epithelial cells. For the second measurement, setups 2 and 3 have compatible averages but, again, the setup 1 has a smaller average than those of setups 2 and 3. Therefore, the absorption estimation was not possible, because with this experimental setup, the variations caused by other factors are too large compared to epithelial cell absorption.

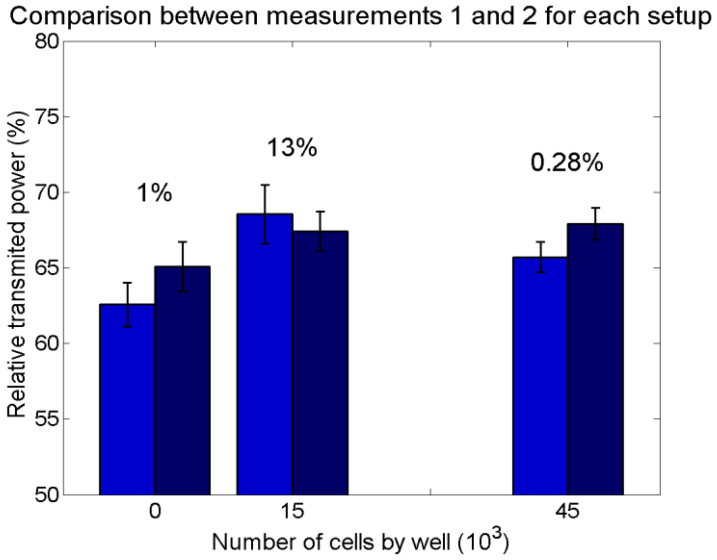

Figure 2.8: Comparison between the measurements 1 and 2 for each setup. The percentages in the graph indicate the p-values for the comparison between the measurement 1 and 2, for Student's *t*-test. The error bars represent the uncertainty of the measurements.

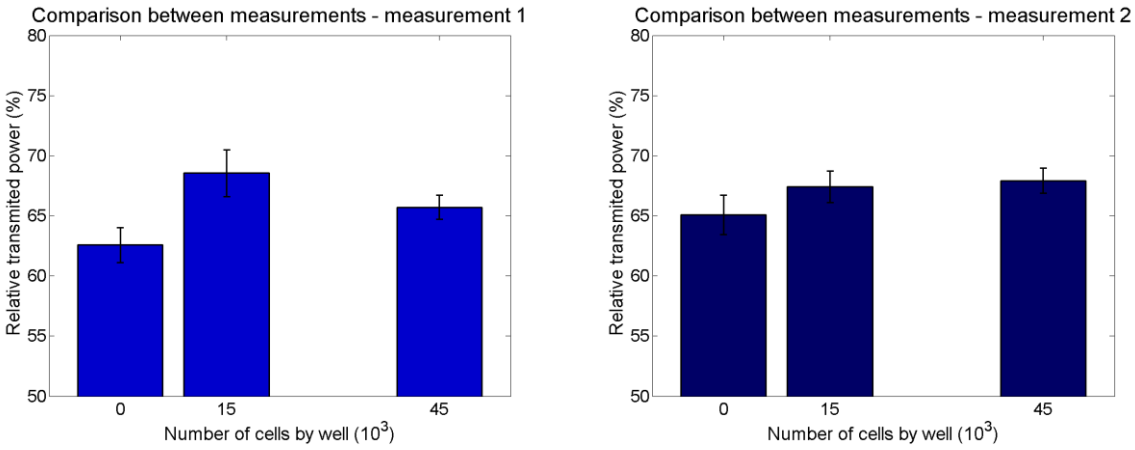

Figure 2.9: Comparison between the different setups: measurement 1 (on the left) and measurement 2 (on the right). The p-values for the Student's *t*-test are shown in Figure 2.10. The error bars represent the uncertainty of the measurements.

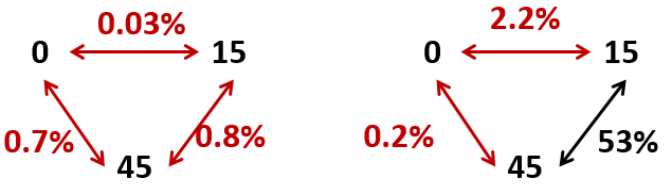

Figure 2.10: Diagrams with the comparison between the different setups, for measurement 1 (on the left) and measurement 2 (on the right). The percentages represent the p-value, for the Student's *t*-test, for the comparison between the wells with that specific number of epithelial cells (zero, 15 thousand and 45 thousand epithelial cells). Averages were considered incompatible when $p < 5\%$.

An experiment performed with a spectrophotometer and L929 fibroblast cells in culture media resulted in the graph shown in Figure 2.11. According to this experiment, the fibroblasts absorb 5% to 6% of the incident power, depending on the wavelength used in the red – near infrared range.

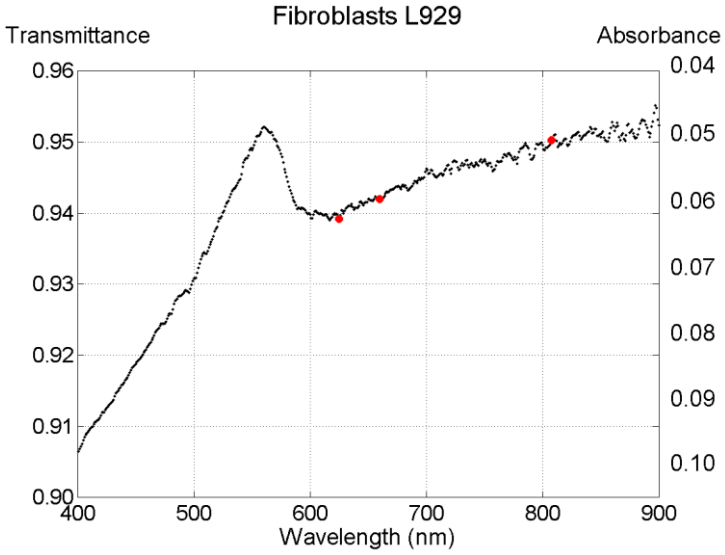

Figure 2.11: Graph for transmittance and absorbance of L929 fibroblast cells in culture media. Data were measured with a spectrophotometer. The red data shown represent the wavelengths used in this work: 625 nm, 660 nm and 808 nm. These results were provided by D. F. T. Silva (personal communication, December 1, 2015).

2.2.1 Summary

For the OMTC experiments, no changes were observed in the mechanical properties of epithelial cells, in the studied conditions. The constant behavior of the ratio between the loss and elastic shear moduli (cell hysteresivity η) evidenced this result. Furthermore, both bead displacement and hysteresivity did not present a lognormal distribution. Thus, with high probability, these parameters are not lognormally

distributed. At last, it was not possible to estimate experimentally the light absorption by the epithelial cells.

3. Defocusing Microscopy

The defocusing microscopy is a technique used to observe a phase object in a bright field microscope. The result is similar to a phase contrast microscopy. This technique was developed and is being improved by the Laboratory of Physics of Biological Systems, at the Federal University of Minas Gerais, Belo Horizonte, for over 10 years, [85]–[92].

A phase objective is an object that does not change the amplitude of the incident electric field, but changes its phase; therefore, it is not visible under a bright field microscope. The observation of this type of object becomes possible if the microscope is slightly defocused. Through the analysis of the defocused image, the results are similar to a phase contrast microscope. Figure 3.1 shows images of two red blood cells (RBCs), obtained with a bright field microscope. On the left, the image is focused and on the right, the RBC is the same, but the image is slightly defocused. Note that the RBC is visible under the microscope, despite being a phase object, because it is thick, so it is not possible to maintain the whole RBC volume simultaneously focused.

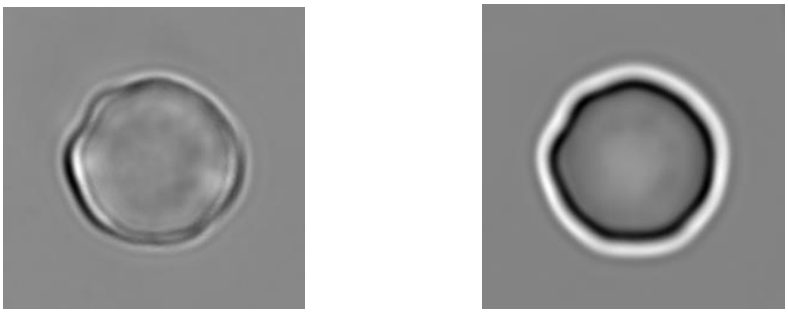

Figure 3.1: RBC images obtained with a bright field microscope. On the left, the image is focused and on the right, the image is slightly defocused.

The theoretical treatment for defocusing microscopy consists in the propagation of the incident electric field in each element of the bright field inverted microscope, with infinity corrected optics, to the image plane. In order to make the math easier, the propagation is completed for the angular spectrum, which is the Fourier transform of the electric field. Then, the propagation is made through all the microscope components:

- Phase object (the object that is being observed), thin and flat;
- Immersion oil with refractive index n_0;

- Objective lens with focal length f_1;
- Distance δ between lenses;
- Tube lens with focal length f_2;
- Distance between the lens and the image plane.

After that, the angular spectrum propagated is Fourier transformed back to obtain the electric field in the image plane. This field is shown in Eq. 3.1, where A_0 is the angular spectrum, z_f represents the microscope defocusing, $\vec{k}$ represents the wave vector, $\vec{q}$ and $\vec{\rho}$ represent, respectively, the wave and position vectors in the transverse plane of the propagation direction, and the factor $k_0 f_1/k f_2$ represents the microscope magnification.

$$E(\vec{\rho},z) = \frac{1}{i(2\pi)^3}\sqrt{\frac{k_0 f_1}{k f_2}}\, e^{i\beta} e^{i\alpha\frac{f_2^2 k^2}{f_1^2 k_0^2}\rho^2} \int A_0(\vec{q},0) e^{i\frac{q^2}{2k}z_f} e^{i(\vec{\rho}\cdot\vec{q})} d\vec{q} \qquad \text{Eq. 3.1}$$

where $\alpha = \frac{k_0^2}{2f_2^2}\left(\frac{f_1}{k} - \frac{\delta}{k_0} + \frac{f_2}{k_0}\right)$ and $\beta = k\left(f_1 - z_f\right) + k_0\delta + k_0 f_2$

Eq. 3.2 gives the image contrast, where $h(\vec{\rho})$ represents the height profile of the phase object and Δn represents the difference between the phase object and the immersion oil refractive indices. Note that the factor z_f, which refers to the defocusing, is in the sine argument, this means that if there is no defocusing, the sine argument is null and there is no contrast, thus the phase objects are not visible in bright field microscopes, unless the image is defocused.

$$C(\vec{\rho}) = -2\Delta n k_0 \sum_{\vec{q}} \left[h(\vec{q})\sin(\vec{q}\cdot\vec{\rho})\sin\left(\frac{z_f}{2k}q^2\right)\right] \qquad \text{Eq. 3.2}$$

Eq. 3.3 represents the propagated electric field for a thick and curved phase object. The difference to the electric field from Eq. 3.1 is the extra phase term $h(\vec{\rho})$, at the exponential argument, which represents the phase object profile.

$$E(\vec{\rho},z)=\frac{1}{i(2\pi)^3}\sqrt{\frac{k_0 f_1}{k f_2}}e^{i\beta}e^{i\alpha\frac{f_2^2k^2}{f_1^2k_0^2}\rho^2}\int A_0(\vec{q},0)e^{i\frac{z_f-h(\vec{\rho})}{2k}q^2}e^{i(\vec{\rho}\cdot\vec{q})}d\vec{q} \quad \text{Eq. 3.3}$$

In this case, the contrast, represented by Eq. 3.4, is also changed. It takes into account the object thickness, $h(\vec{\rho})$ that appears in the sine argument. If the object thickness is expanded into Fourier series and if small defocusing is also considered, the approximation $\sin(x)\sim x$ is valid, and the contrast equation is obtained as in Eq. 3.5. The factor n_0 represents the immersion oil refractive index, and κ is the object's local curvature. Hence, the contrast brings information about the phase object's curvature.

$$C(\vec{\rho})=-2\Delta n k_0\sum_{\vec{q}}\left[h(\vec{q})\sin(\vec{q}\cdot\vec{\rho})\sin\left(\frac{z_f-h(\vec{\rho})}{2k}q^2\right)\right] \quad \text{Eq. 3.4}$$

$$C(\vec{\rho})=\left[z_f-h(\vec{\rho})\right]\frac{\Delta n}{n_0}\nabla^2h(\vec{\rho})=\left[z_f-h(\vec{\rho})\right]\frac{\Delta n}{n_0}\kappa\vec{\rho} \quad \text{Eq. 3.5}$$

RBCs can be considered thick objects and, in addition, they have two membranes in the light path. Their refractive index can be assumed as practically homogeneous because in effect they have no organelles inside. Eq. 3.6 gives the contrast to RBCs: wherein each membrane appears separately represented by h_1 and h_2, which corresponds to the free membrane and the membrane in contact with the base, respectively.

$$C(\vec{\rho})=\frac{\Delta n}{n_0}\left[\left(z_f-h_1\right)\nabla^2h_1(\vec{\rho})-\left(z_f-h_2\right)\nabla^2h_2(\vec{\rho})\right] \quad \text{Eq. 3.6}$$

A more detailed derivation of the defocusing microscopy theory can be found in Livia S. Gomes' thesis [91] and a full deduction of each step to obtain these equations can be found in Giuseppe Glionna's thesis [90].

Two sets of images of the RBCs along time (videos), at two different known focuses are used to enable reconstruction of the RBC thickness profile, the radial thickness profile and the RBC volume. Moreover, the subtraction of the time-averaged contrast of each video gives Eq. 3.7. The RBC thickness profile can be calculated by Fourier

transforms, as shown in Eq. 3.8, where $\mathcal{F}$ and $\mathcal{F}^{-1}$ represents the Fourier transform and inverse transform, respectively. [91]

$$\langle C_2 \rangle - \langle C_1 \rangle = \frac{\Delta n}{n_0}\left(z_{f_2} - z_{f_1}\right)\nabla^2\langle h_1 - h_2 \rangle \qquad \text{Eq. 3.7}$$

$$H = (h_1 - h_2) = \frac{n_0}{\Delta n\left(z_{f_1} - z_{f_2}\right)}\mathcal{F}^{-1}\left\{\frac{\mathcal{F}\{\langle C_2 \rangle - \langle C_1 \rangle\}}{q^2}\right\} \qquad \text{Eq. 3.8}$$

In this work, the defocusing microscopy was used to evaluate human RBCs, either or not submitted to photo-treatment with red light and different powers and photo-treatment times. The effects of PBMT in morphological or mechanical characteristics such as volume, radial profile of cell thickness, lateral fluctuation or vertical fluctuation of these RBCs were verified.

3.1 Materials and Methods

The defocusing microscopy experiments were performed in the Laboratory of Physics of Biological Systems, at Federal University of Minas Gerais.

3.1.1 Materials

Human RBCs were obtained from peripheral venous blood, right before the experiment. The blood was collected with a pipette and dissolved in a BSA (bovine serum albumin) solution in PBS at a 0.1% concentration and approximately $300\ \mathrm{mOsm/kg}$. The blood concentration varied between 0.002% and 0.005%.

PBS is an isotonic solution, thus, osmosis will not occur significantly between RBCs and dilution media. The BSA function is to keep the RBCs with a discoid shape during the experiment.

The BSA solution in PBS was placed in Eppendorf tubes and right after sample collection, the blood was added to these containers.

For the measurements, the samples were placed in sample holders, as shown in Figure 3.2. An O-ring (on the left) or an acrylic bucket (on the right), glued with silicone

in a cover slip composed the sample holders. The sample is placed on them and covered with another cover slip to prevent liquid loss.

A red laser Twin Flex Evolution, from MMOptics, was used for the RBC photo-treatment. Table 3.1 presents some of the parameters used in the experiment.

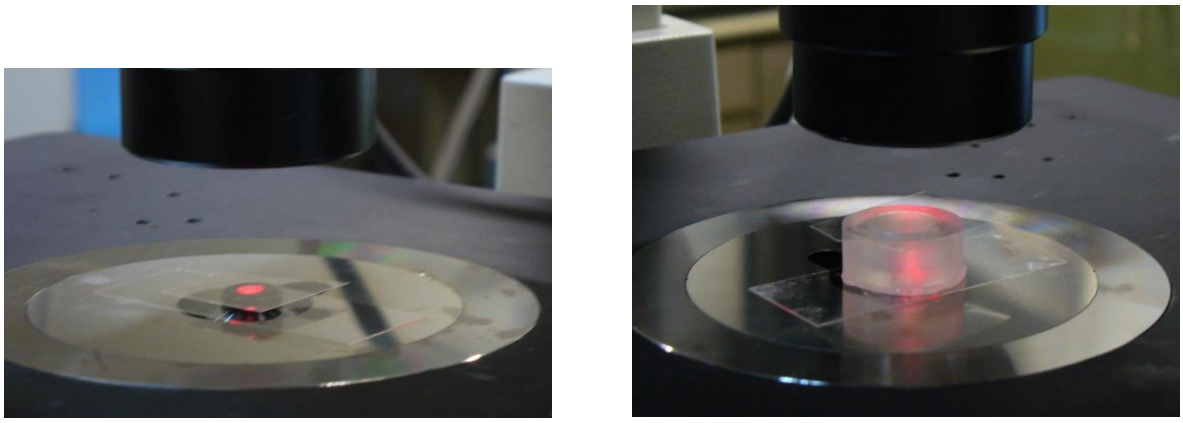

Figure 3.2: Image of the two types of sample holders used in the experiments. The O-ring (on the left) or the acrylic bucket (on the right) were bonded with silicone on the cover slip.

Table 3.1 – Light source parameters used in the defocusing microscopy experiments, for the RBC photo-treatment. The quantities radiant power, power density, radiant energy, energy density and photo-treatment time were variable according to the experiment and are shown below. The beam area was evaluated experimentally, and we got a value very different from the nominal one. For the sake of completeness, we show both values (nominal in the first line and experimental in the second line). The number displayed in parentheses is the uncertainty of the beam area, the digits are in the last decimals of the number, thus, $0.196(20)\ \mathrm{cm}^2$ represents an area of $0.196\ \mathrm{cm}^2$ and $0.020\ \mathrm{cm}^2$ uncertainty.

Light source	Laser (InGaAlP)
Wavelength	660 nm
Beam area	$0.04\ \mathrm{cm}^2$ $0.196(20)\ \mathrm{cm}^2$
Opening angle	4°

Two inverted microscopes were used in the experiments (*Nikon Eclipse TE300* and *Nikon TI-E*), both with oil immersion objectives from Nikon with $100\times$ magnification. They were operating in bright field mode with infinity corrected optics. In order to ensure that the light reaching the sample was monochromatic, a filter was employed. Table 3.2 shows other characteristics of the microscopes.

Table 3.2 – Characteristics of the microscopes used in the experiments.

Microscope	Objective magnification (numerical aperture)	Focus control	Filter
TI-E	100× (1.3)	Perfect Focus System (PFS)	Red
TE300	100× (1.4)	Piezoelectric nano shifter (PZT)	Green

The objective immersion oil has refractive index $n_0 = 1.51$ and the difference between the RBC and immersion oil refractive indices was $\Delta n = 0.058$ [91].

Two electronic cameras were used for image capture; both attached to a microscope. The main difference between the cameras is temporal and spatial resolution: *UNIQ UP1800 CL*, a CCD camera, has good spatial resolution, but low capture rate; on the other hand, *CMOS SILICON VIDEO 642M*, has low spatial resolution, but high capture rate. Table 3.3 shows the camera characteristics.

Table 3.3 – Characteristics of the electronic cameras used for image capture. The calibration shown is for the 100× lens used in the experiments.

Camera	Acquisition rate (Hz)	Calibration (μm/px)	Acquired image size (px×px)	Analyzed image size (px×px)
UNIQ (CCD)	15	0.064	1372×1034	256×256
CMOS	>300	0.098	256×256	128×128

3.1.2 Methods

The methods are divided into data acquisition methods and analysis methods.

3.1.2.1 Data acquisition

Sample preparation was the same for all measurement modes; the difference was the moment when the RBCs were photo-treated. In this subsection, the general procedure

will be described here. In the following subsections we describe the timeline and details of the photo-treatment performed.

Initially the blood was collected and placed in a BSA solution in PBS in an Eppendorf tube. After that, the sample was placed on the sample holder. The sample rested for $15\ \text{min}$ to $20\ \text{min}$ on the stage of the microscope, so the RBCs could decant and reach the bottom at the cover slip. After this time, the measurement was executed, the image capture of each region took $30\ \text{s}$, with an acquisition rate depending on the camera. The videos were obtained in two known focusing situations: one of the videos was obtained in focus ($0\ \mu\text{m}$ defocusing) and the other $2\ \mu\text{m}$ above the focus ($+2\ \mu\text{m}$ defocusing).

3.1.2.1.1 Photo-treatment in the Eppendorf tube with variable power (experiment 1)

After preparation, the sample was photo-treated within the Eppendorf tube, which was placed on a holder, see Figure 3.3, on the left. The light reached the liquid surface perpendicularly, and different photo-treatment times and laser powers were employed, as shown in the first group of lines in Table 3.4. The Figure 3.3, on the right, shows the experiment protocol schematized.

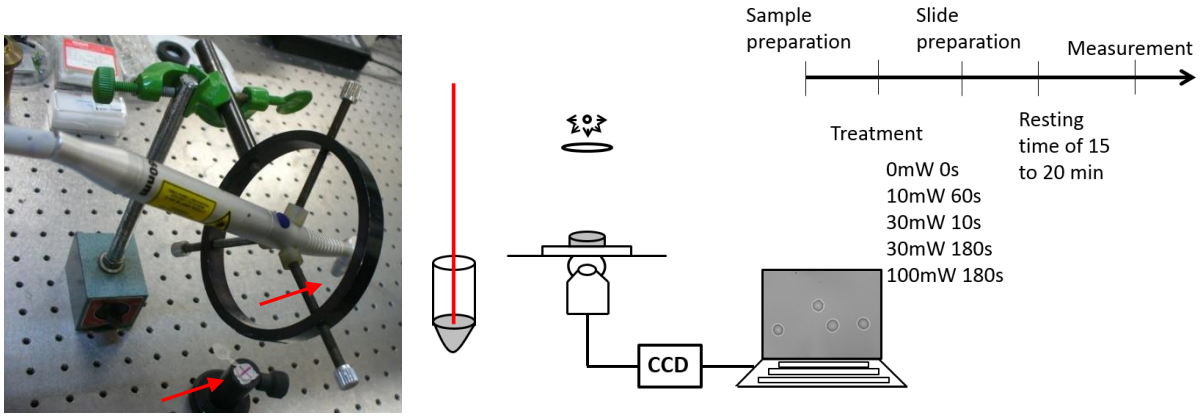

Figure 3.3: On the left, an image of the experimental setup used for the photo-treatment of the samples. In this case the Eppendorf tube, which is indicated by the left arrow, was used to centralize the beam (the laser output head is indicated by the right arrow). On the right, the experimental sketch, in which the sample was photo-treated in the Eppendorf tube and then measured. There is also a timeline of the experiment.

Table 3.4 – Light source parameters used to photo-treat different samples used in the experiments. When the parameter has two values, the first one was obtained with the nominal beam area; and the second one with the experimental beam area, and respective uncertainty. The number displayed in parentheses is the uncertainty, the digits are in the number last decimals, for example, 0.14(5) represents a quantity of 0.14 with uncertainly of 0.05 and 11.3(21) a quantity of 11.3 with uncertainty of 2.1.

Experiment	Radiant power (mW)	Power density (mW/cm^2)	Time (s)	Radiant energy (J)	Energy density (J/cm^2)
Photo-treatment in the Eppendorf tube with variable power (Experiment 1)	100	2500 510(52)	180	18	450 92(9)
	30	750 153(16)	180	5.4	135 27.6(28)
	10	250 51(5)	60	0.6	15 3.1(3)
	30	750 153(16)	10	0.3	7.5 1.53(16)
	0	0	0	0	0
Photo-treatment in the microscope stage with variable power (Experiment 2)	90	2250 459(47)	180	16.2	405 83(8)
	70	1750 357(36)	180	12.6	315 64(7)
	50	1250 255(26)	180	9.0	225 46(5)
	30	750 153(16)	180	5.4	135 27.6(28)
	10	250 51(5)	180	1.8	45 9.2(9)

Table 3.4 – (continuation) Light source parameters used to photo-treat different samples used in the experiments. When the parameter has two values, the first one was obtained with the nominal beam area; and the second one with the experimental beam area, and respective uncertainty. The number displayed in parentheses is the uncertainty, the digits are in the number last decimals, for example, 0.14(5) represents a quantity of 0.14 with uncertainly of 0.05 and 11.3(21) a quantity of 11.3 with uncertainty of 2.1.

Experiment	Radiant power (mW)	Power density (mW/cm^2)	Time (s)	Radiant energy (J)	Energy density (J/cm^2)
Fractional acquisition (Experiment 3)	100	2500 510(52)	180	18	450 92(9)
	30	750 153(16)	180	5.4	135 27.6(28)
	0	0	180	0	0
Fractional photo-treatment (Experiment 4)	100	2500 510(52)	6×30	6×3.0	6×75 6×15.3(16)
	30	750 153(16)	6×30	6×0.9	6×22.5 6×4.6(5)

3.1.2.1.2 Photo-treatment in the stage of microscope (experiments 2, 3, and 4)

In this second protocol, the samples were photo-treated directly on the microscope stage with one of three different application forms. The initial procedure was the same for all the three possibilities: the sample and the slide were prepared and allowed to rest for the RBCs decant; and a reference measurement (pre-treatment) was performed. After these first steps, the laser beam was centered with the objective lens of the microscope and the application was performed, as seen in Figure 3.4. Five minutes after the photo-treatment, a new measurement was performed, according to the respective pre-determined acquisition mode.

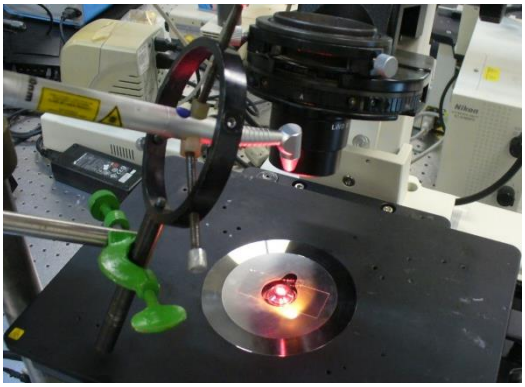

Figure 3.4: Image of the experimental setup used for the sample photo-treatment. The microscope illumination system was raised in order to give space to the laser, which was centered with the objective lens.

The laser beam was centered on the middle of the objective's field of view to ensure that the measured RBCs were photo-treated. However, this procedure added a systematic error for the photo-treatment time, which we tried to keep as short as possible: during the first few seconds of photo-treatment, the illumination was used to make the fine adjustment of the beam centralization with the objective lens. It is worth mentioning that this time was less than $5\,\mathrm{s}$. Another important fact is that, during the measurement, the laser could not remain aligned with the sample, because the application head was in the microscope's optical pathway, which means that the measurement could not be performed with the laser centered, so it had to be aligned only during the photo-treatment.

The three experiments performed using this mode of photo-treatment are described below. Figure 3.5 shows the experiment protocol schematized, and Table 3.4 shows the photo-treatment parameters:

- *Variable power* (experiment 2) – a group of RBCs was imaged. After this reference measurement, the photo-treatment was performed in a single step, followed by another imaging of these RBCs. A few more RBCs around them were also measured. Only RBCs that were very near to the initial RBCs were chosen to ensure that all measurements were performed on photo-treated RBCs. The photo-treatment time was fixed at $180\,\mathrm{s}$ and the laser parameters used in this experiment are presented in Table 3.4.
- *Fractional acquisition* (experiment 3) – each sample was photo-treated in a single step of $180\,\mathrm{s}$. After the photo-treatment several images were acquired over time, with $6\,\mathrm{min}$ interval between them. The RBCs were tracked up to

60 min after the photo-treatment. A non-treated sample was also tracked in the microscope field of view over time and, in this case, the measurements were performed with intervals of around 20 min up to 140 min.

- *Fractional photo-treatment* (experiment 4) –the photo-treatment was performed in six steps of 30 s each, totalizing 180 s. Five minutes after each application step, a measurement was performed. The interval between each measurement and a new photo-treatment step was around 3 min. This procedure was carried out until the end of the sixth step, when the cumulative photo-treatment time was 180 s. The laser parameters used in this experiment are presented in Table 3.4.

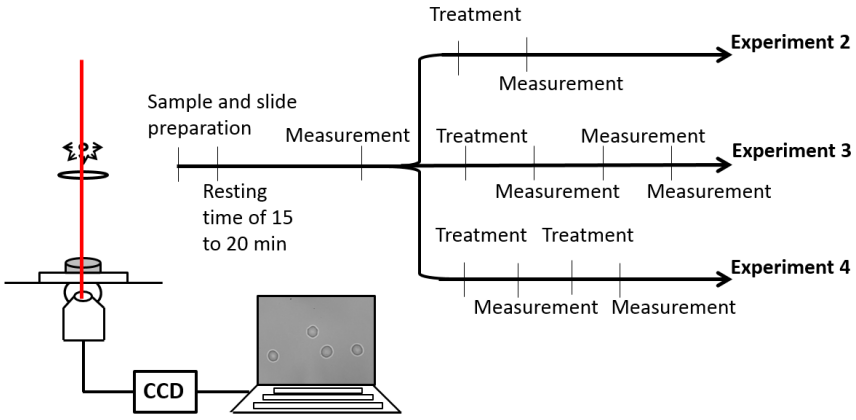

Figure 3.5: Experimental sketch for the experiments in which the sample was photo-treated in the microscope stage and then measured (experiments 2, 3 and 4). There is also a timeline with the three different experiments described in the text.

3.1.2.2 Analysis

Data obtained are videos of RBCs of 30 s length. The analysis was performed with the *ImageJ* program. The initial steps were:

1. To identify the appropriate RBCs for the measurement, which means to find isolated RBCs.
2. To verify the absence of biological contamination.
3. To crop the image with the selected RBC centered;
4. To correct the Noise and/or background:
    - To take the temporal average of the background video grey levels, pixel by pixel, resulting in an image (background image);

- To divide the image grey levels of the temporal average of the RBC video by the grey levels of the background image, pixel by pixel, resulting in another image (RBC image);
- To multiply the RBC image grey levels by the spatial average of the background image. Each pixel was multiplied by the same number, which is the spatial average of the grey levels, to return the pixels to the original values;
- To adjust the contrast. This resulting image was used in the following protocols.

These initial steps were performed for all videos. After that, specific protocols were used, depending on the RBC parameter to be analyzed (volume, the radial profile of cell thickness, lateral fluctuation, and vertical fluctuation), as described. A more detailed description of the defocusing microscopy analysis can be found in Paula M. R. Lapa's thesis [92].

3.1.2.2.1 Volume

For the determination of the RBC volume, a temporal averaging was done with the video grey levels, pixel by pixel, resulting in a new image that was used for the reconstruction of the RBC thickness profile. This reconstruction was performed using a *MATLAB* program, with Eq. 3.7 and Eq. 3.8, presented previously. Both images (focused and defocused) were used in this program.

The reconstruction outcome is the RBC thickness for each position, in this case, for each pixel. Thus, the sum of each pixel thickness, multiplied by the pixel area results in the volume.

This analysis was done for each experiment, with the data obtained with the UNIQ camera.

3.1.2.2.2 Radial profile of cell thickness

The radial profile of the RBC thickness was calculated through the angular average of the RBC thickness, for each radial position, from the center of the image to the edge, all around ($360°$) the RBC. The radial profile was also obtained using the reconstruction thickness profile and an *ImageJ* plugin.

This analysis was done for each experiment, with the data obtained with the UNIQ camera.

3.1.2.2.3 Lateral fluctuation

The defocused image presents diffraction at the object's edge. If a line is drawn through the center of the RBC image, its grey level profile is similar to the one presented in Figure 3.6 graph (on the right). The distances between the minima and the maxima were identified for each profile. This was executed for four lines in the image, numbered according to Figure 3.6, on the left. The distances were obtained for each video frame, and the variation of these values in time was called lateral fluctuation. With these data two analysis were performed: time Fourier transform, to identify any dominant oscillation frequency; and evaluation of the standard deviation of the distances, for each one of the four lines. Furthermore, the coefficient of variation (ratio between the standard deviation and the mean value) of the lateral fluctuation was calculated for each line, for each RBC.

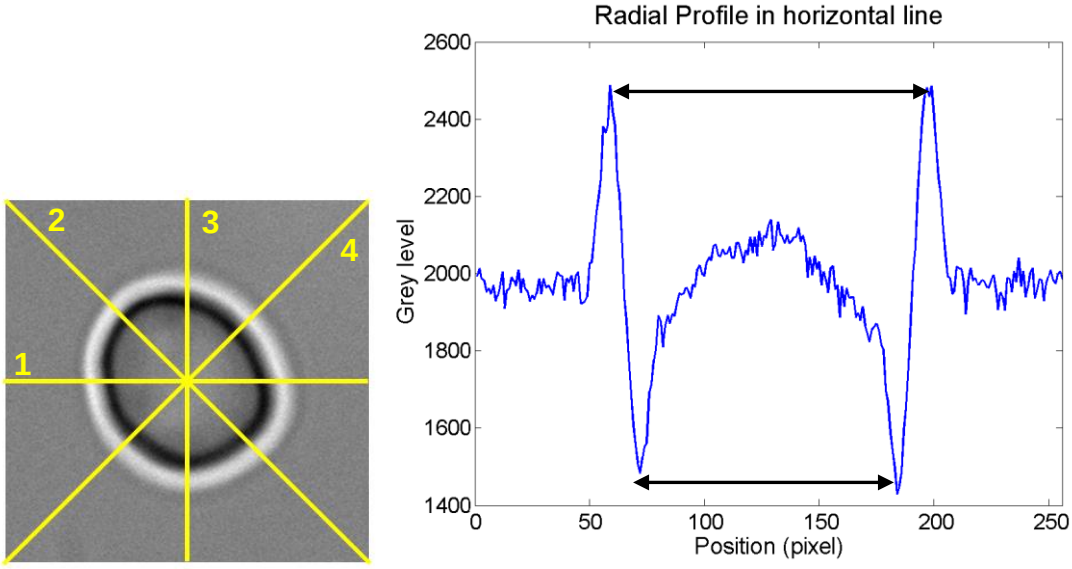

Figure 3.6: On the left are shown the lines in which the lateral fluctuation of RBCs was evaluated. On the right is shown the radial profile of gray levels to line 1. The arrows indicate the distances between maxima (on top of the graph) and between minima (on bottom of the graph).

The analysis for the lateral fluctuation was done using the RBC with defocusing of $2\ \mu m$ using *MATLAB* programs. This analysis was done for all experiments, with data obtained with both cameras.

3.1.2.2.4 Vertical fluctuation

The contrast provides information about the membrane curvature, as shown above. Thus, the mean-squared fluctuation of contrast provides information on the membrane curvature fluctuation. The mean-squared fluctuation of contrast is the square of the difference between contrast at time *t* and time average of contrast. [91]

The $2\ \mu m$ defocused image of the RBC and an *ImageJ* plugin were used to determine the vertical fluctuation. This analysis was done just for RBCs that were photo-treated in the Eppendorf tube, with data obtained with the CMOS camera.

3.1.2.2.5 Statistical analysis

Three statistical tests were used, the Student's *t*-test, the two-sample rank sum test [84] (for more details see Appendix B) and the chi-square χ^2 goodness of fit test. The samples were considered different when $p < 5\%$ for all tests. Table 3.5 shows the statistical test that was used for each experiment and analysis.

Table 3.5 – Statistical tests that were used for each experiment for each parameter evaluated. The difference between “none” and “-” is that none statistical test was performed in the first case, and the RBC parameter was not analyzed for the second case.

Experiment or analysis	Volume	Radial profile	Lateral fluctuation	Vertical fluctuation
Photo-treatment in the Eppendorf tube with variable power (Experiment 1)	Student’s *t*-test	Student’s *t*-test	Two-sample rank sum test	Student’s *t*-test
Photo-treatment in the microscope stage with variable power (Experiment 2)	Student’s *t*-test	Student’s *t*-test	Two-sample rank sum test	-
Comparison between photo-treatments in the Eppendorf tube and microscope stage	Student’s *t*-test	Student’s *t*-test	Two-sample rank sum test	-
Fractional acquisition (Experiment 3)	Curve fitting and χ^2	None	None	-
Fractional photo-treatment (Experiment 4)	Curve fitting and χ^2	None	None	-

3.2 Results

The reconstruction of the RBC thickness profile was done for all data obtained. This reconstruction was used to derive the RBC volume and the radial profile of cell thickness. Figure 3.7, Figure 3.8 and Figure 3.9 show three typical reconstructions. Note that, in the vertical axis, what is represented in each position is the *thickness* of the RBC, starting from a flat base. Figure 3.7 shows the case of a reconstruction from

a homogeneous image background, in grey levels. Thus, an effective correction of this background was possible, resulting in a high quality reconstruction, in which practically no artifacts appear in the background. On the other hand, in the case presented in Figure 3.8, the image background was not homogeneous. Therefore, the correction was not satisfactory, resulting in a low quality reconstruction. There are a few artifacts in the background, as seen in the bottom left and right graphs of the images in Figure 3.8. At last, in Figure 3.9, the image background was very heterogeneous, the correction was very poor, and so was the reconstruction. Consequently, the background presents massive artifacts.

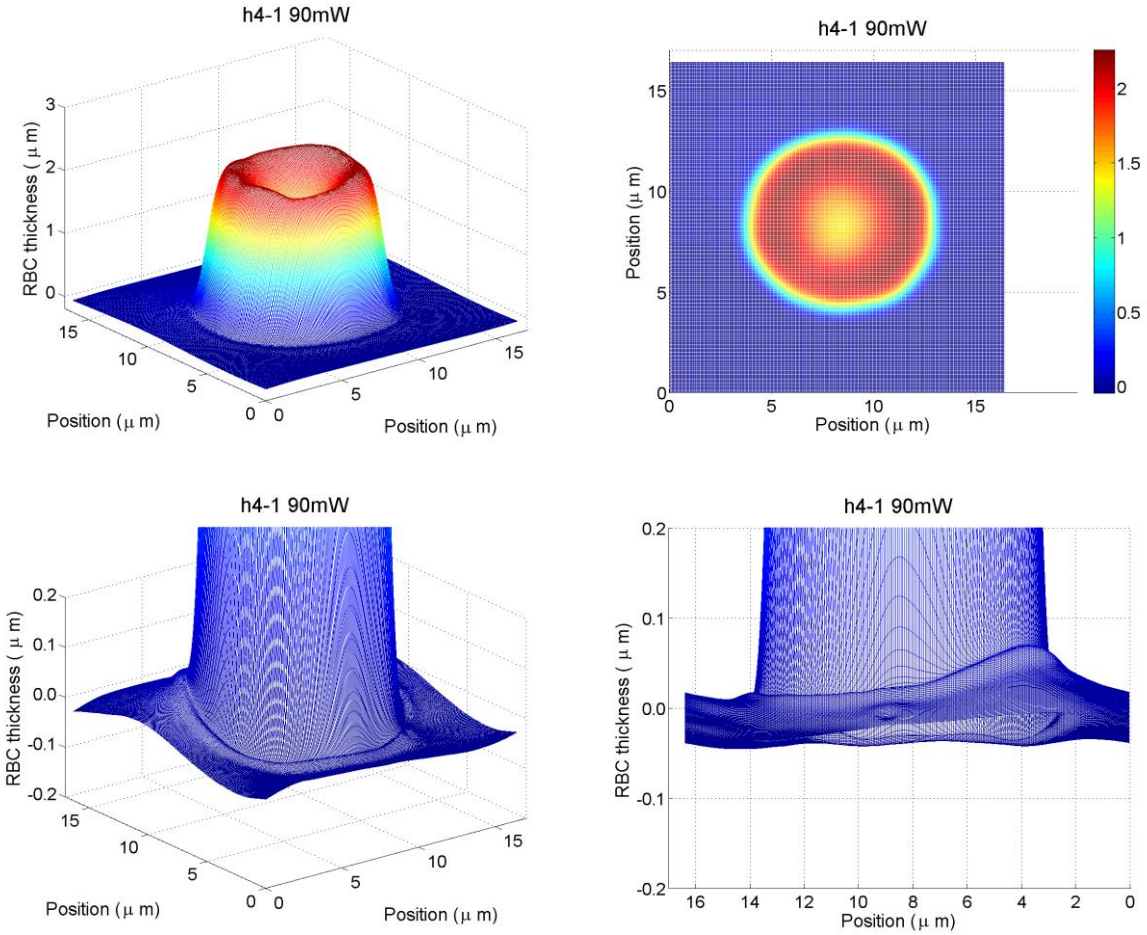

Figure 3.7: RBC thickness profile, in 3D view (top left graph); view from top (top right graph), where the color scale represents the RBC thickness in μm; 3D view with zoom in the background area (bottom left graph); and lateral view with zoom in the background area (bottom right graph). For this case, the background was homogeneous and the reconstruction has good quality with very few and small artifacts in the background.

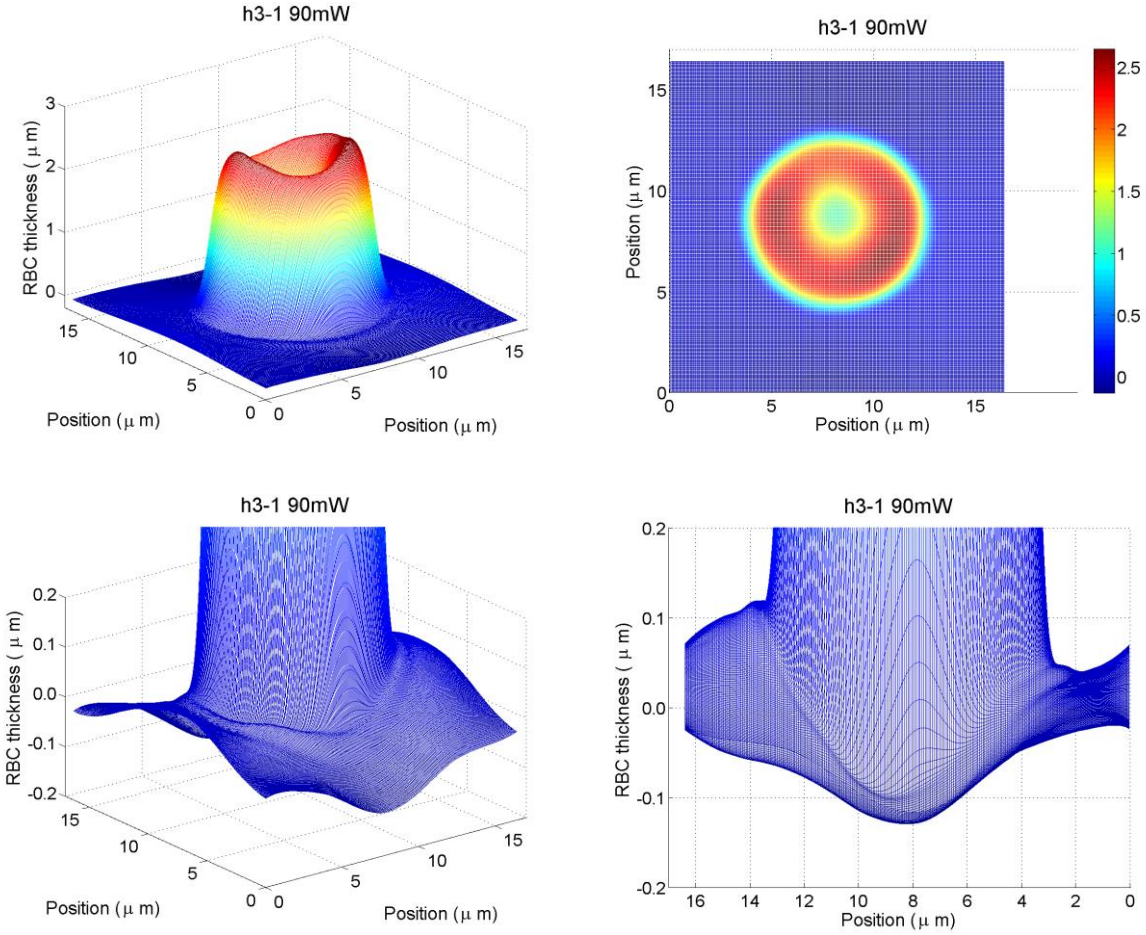

Figure 3.8: RBC thickness profile, in 3D view (top left graph); view from top (top right graph), where the color scale represents the RBC thickness in μm; 3D view with zoom in the background area (bottom left graph); and lateral view with zoom in the background area (bottom right graph). For this case, the background was not homogeneous and the reconstruction does not have such a good quality with a few artifacts in the background.

As the RBC reconstructions were not always of good quality, a study was completed to evaluate the error made in the volume calculation and then, estimate the uncertainty, due to a poor quality reconstruction. For each RBC reconstruction the following analysis was done:

- Identification of the background area, that is, the image region where there were no RBCs. For ideal conditions, the thicknesses should be zero for each pixel in the background region.
- Calculation of the background contribution to the volume by summing the thickness of the pixels in that region;
- Comparison of the background contribution to the total volume of that reconstruction.

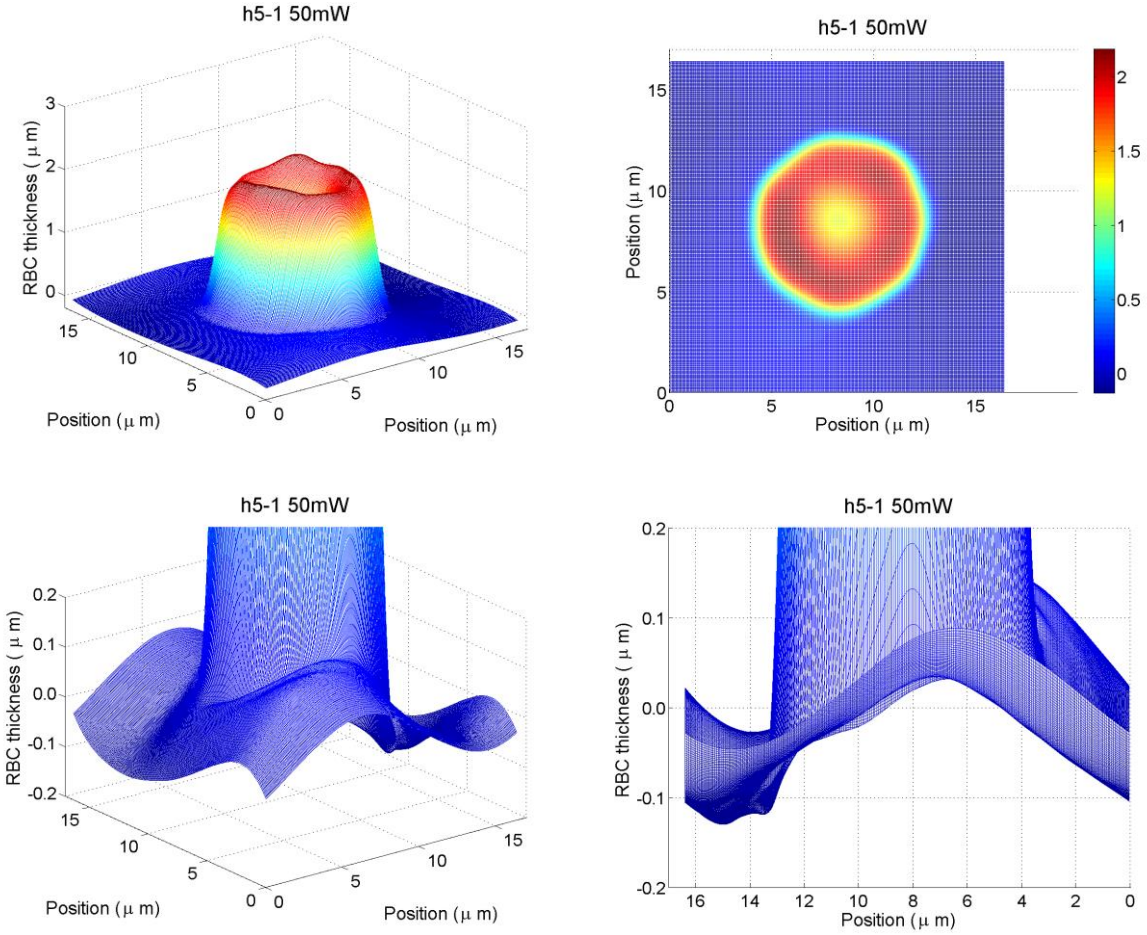

Figure 3.9: RBC thickness profile, in 3D view (top left graph); view from top (top right graph), where the color scale represents the RBC thickness in μm; 3D view with zoom in the background area (bottom left graph); and lateral view with zoom in the background area (bottom right graph). For this case, the background was heterogeneous and the reconstruction has poor quality with massive artifacts in the background.

The background area was identified through the radial profile of cell thickness. The thickness variation between each pair of pixels of the radius was evaluated. When this variation was small (around 10^{-3} μm), that radius was considered on the edge of the RBC. As the radial profile of cell thickness is the angular average of the radius, with this procedure, we get the average radius that the RBC occupy. The threshold variation was set to eliminate the whole RBC from the image. The region with a radius greater than the edge was considered the background region. For radius smaller than the edge, the thickness was set to zero to eliminate the RBC from the image, and complete the calculations with the background region. In the background region, the original thickness value was maintained. Figure 3.10 represents the resulting reconstruction, after the background region identification.

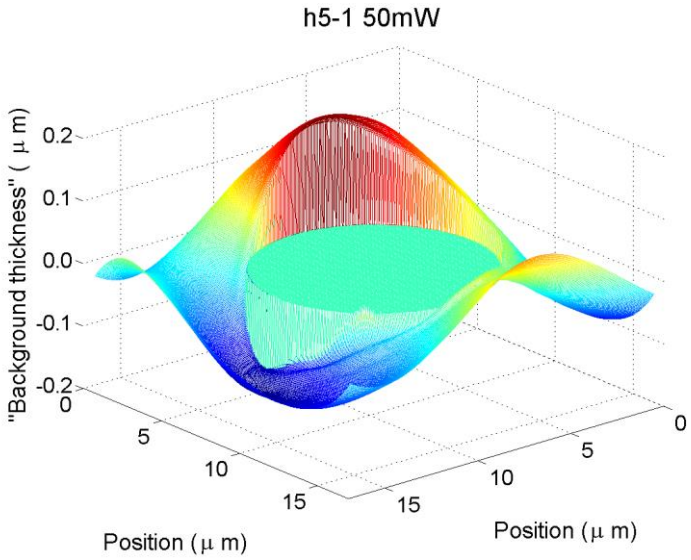

Figure 3.10: Background thickness profile, in a 3D view. The RBC region had the thickness set to zero to evaluate the background contribution to the RBC volume. The background represented here refers to the RBC shown in Figure 3.9.

The information, resulting from this analysis, was:

- The kind of contribution of the background to the RBC volume. As the thickness of the background pixels should be null on average, it is possible to have positive and negative contributions to the thicknesses in this region, so the total contribution to the RBC volume from this region might be positive or negative. Through the analysis of the background contribution to the RBC volume it is possible to know if the volume of the RBC presented in that reconstruction was overestimated (positive contribution) or underestimated (negative contribution);

- The ratio between the background volume and the reconstruction total volume. With this, the magnitude of the error, due to reconstruction, might be estimated.

With this analysis, it is only possible to evaluate the error in volume in the background region, because this is the only region where the expected volume might be assumed (as zero). Furthermore, another assumption was done: that the error done in the RBC region is similar to the error evaluated in the background region. Once the background region occupies around 70% of the image, the error was normalized for the entire image and attributed to the RBC volume accordingly. This means that we extrapolated the error evaluated in the background region to the whole image, considering that the error is proportional to the image area.

From this study, it was possible to verify that the volume was underestimated in 85% of cases, while it was overestimated in only 15% of cases. Moreover, the maximum error was found to be less than 5% when the volume is underestimated and less than 0.5% when the volume is overestimated. Hence, all data were used for the analysis and when necessary 5% uncertainty was considered.

3.2.1 Volume

In the graphs presented in this section (from Figure 3.11 to Figure 3.20), regarding the RBC volumes, there are two types of symbols, which represent the reconstruction quality. The full symbols represent volumes obtained from good quality reconstructions, as shown in Figure 3.7. Alternatively, the empty symbols represent volumes obtained from poor quality reconstructions, like those shown in Figure 3.8 and Figure 3.9. The averages were calculated with all data, both good and poor quality reconstructions.

3.2.1.1 Comparison between photo-treatments in the Eppendorf tube and microscope stage

Samples photo-treated with the same power and energy ($10\ \mathrm{mW}$ for $60\ \mathrm{s}$) were compared; one of the samples was photo-treated in the Eppendorf tube, from experiment 1, and the other in the microscope stage, from experiment 2. The results for the volume are presented in Figure 3.11. The Student's *t*-test indicates that the averages of the two samples are compatible, which means that the two modes of photo-treatment may be equivalent regarding the RBC volume.

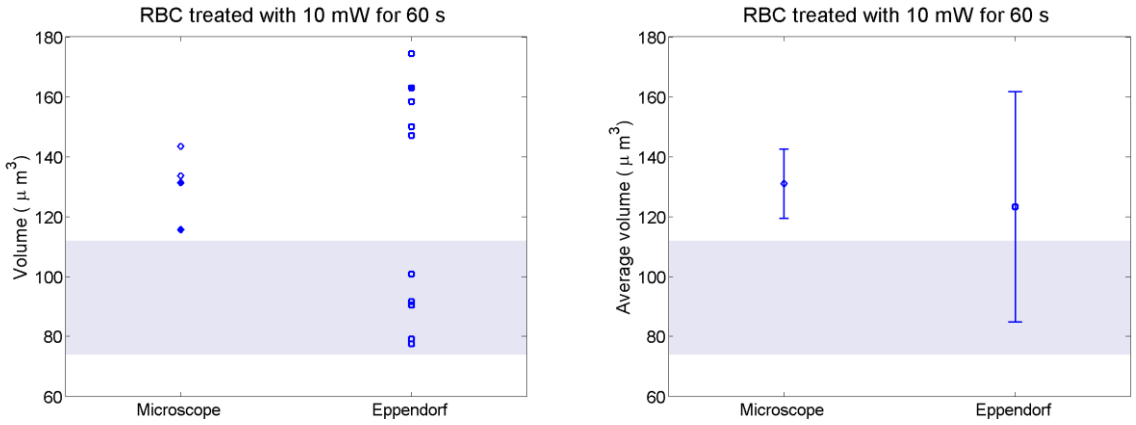

Figure 3.11: Volumes for RBCs photo-treated with $10\ \mathrm{mW}$ for $60\ \mathrm{s}$, either in the Eppendorf tube, from experiment 1, or in the microscope stage, from experiment 2. On the left, all RBC volumes are presented. Filled symbols represent reconstructions with good quality, and empty symbols represent reconstructions with poor quality. On the right, the average volumes, calculated using all data, and the standard deviations (represented by the error bars) are displayed. The blue interval represents the range of values found in literature obtained with the same technique used here $93 \pm 19\ \mu\mathrm{m}^3$ (average $\pm$ 1 standard deviation) [91].

3.2.1.2 Photo-treatment in the Eppendorf tube with variable power (experiment 1)

Figure 3.12 shows the results for the volume of RBCs from experiment 1, as a function of the delivered energy. The Student's *t*-test shows that the average volume of the $10\ \mathrm{mW}, 60\ \mathrm{s}$ photo-treated sample is not compatible with the average volumes of the other samples. Note that this sample is very heterogeneous, as is shown in Figure 3.11 and Figure 3.12. The same behavior was observed in the results for the radial profile. This heterogeneity might show a problem with the sample, in the blood sample collection or sample preparation, for example, since all the others did not show such heterogeneity.

The RBC volume values found in the literature are $93 \pm 19\ \mu\mathrm{m}^3$ [91], obtained with the same technique used here, $91 \pm 17\ \mu\mathrm{m}^3$, $83 \pm 14\ \mu\mathrm{m}^3$ [93], $89 \pm 18\ \mu\mathrm{m}^3$ [94] and in the range of $80\ \mu\mathrm{m}^3$ and $100\ \mu\mathrm{m}^3$ [95], all obtained with different techniques. All samples from this experiment have averages compatible with those values, except for the $10\ \mathrm{mW}, 60\ \mathrm{s}$ photo-treated sample, whose volume is incompatible with the value $83 \pm 14\ \mu\mathrm{m}^3$ [93], according to the *Z* test and $p < 5\%$.

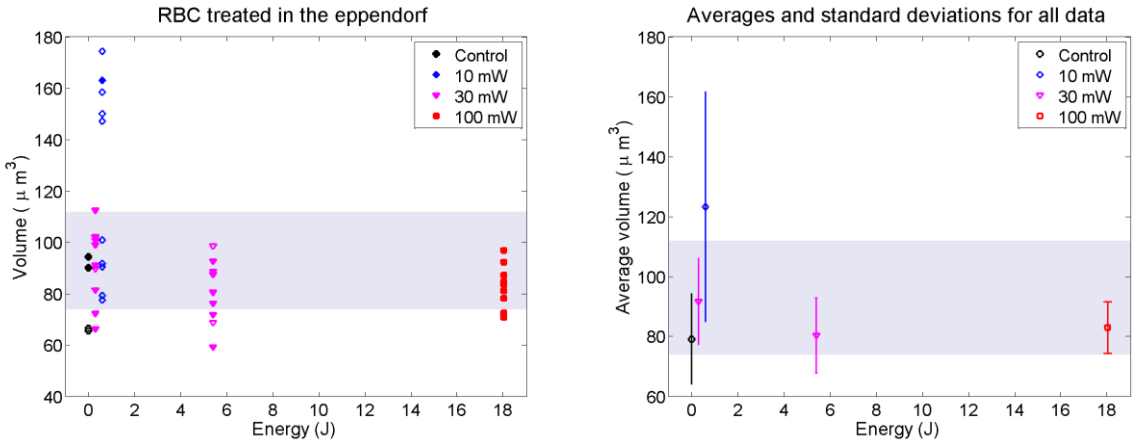

Figure 3.12: Volumes for RBCs from experiment 1 with times and powers described in Table 3.4. On the left, all RBC volumes are presented. Filled symbols represent reconstructions with good quality, and empty symbols represent reconstructions with poor quality. On the right, the average volumes are displayed; the average was calculated using all data, and error bars represent the standard deviations. The blue interval represents the range of values found in literature obtained with the same technique used here $93 \pm 19\ \mu m^3$ (average $\pm$ 1 standard deviation) [91].

3.2.1.3 Photo-treatment in the microscope stage with variable power (experiment 2)

Figure 3.13 shows data obtained for RBC volumes as a function of the light-energy delivered for the samples in experiment 2. The Student's *t*-test was used to compare the control group (0 mW, untreated group) with the photo-treated groups. The 90 mW photo-treated sample (16.2 J of energy delivered) has only one RBC in the control group. Thus, to perform the test, a 5% uncertainty was considered to the volume of this RBC and the photo-treated average was compared with this value. For all cases, the volumes of control and photo-treated groups are compatible. Furthermore, the test comparing the photo-treated samples between them, shows that there are basically two groups, one is composed of the 10 mW (1.8 J) and the 70 mW (12.6 J) photo-treated samples and the other by the 30 mW (5.4 J) and the 50 mW (9.0 J) photo-treated samples. The 90 mW photo-treated sample (16.2 J) does not fit into any of these two groups because its volume is incompatible with the volumes of the 30 mW (5.4 J) and the 70 mW (12.6 J) photo-treated samples. Despite the differences between the samples photo-treated with different powers, it is not possible to note any systematic behavior related to the power or the energy delivered on photo-treatment.

For the comparison of the average volumes with the literature values mentioned above (in the section related to experiment 1) the compatibilities are presented in Table 3.6.

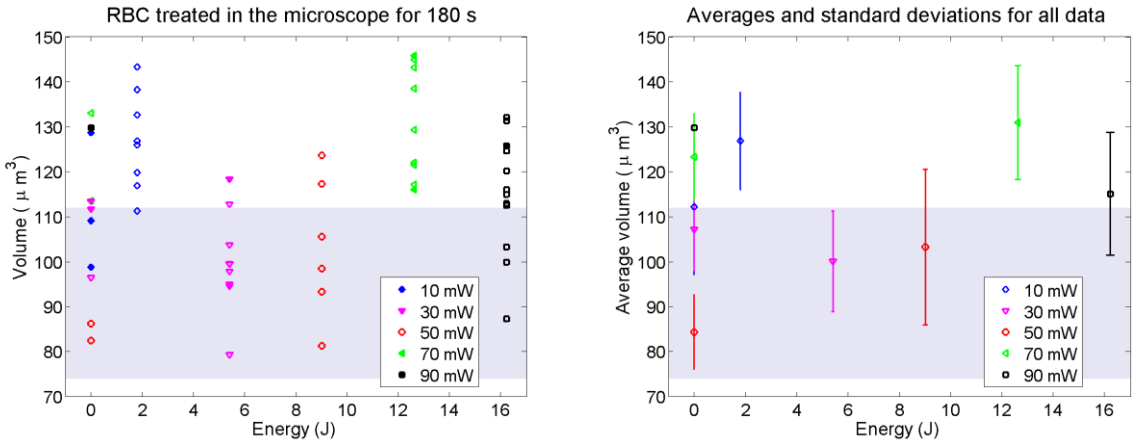

Figure 3.13: Volumes for RBCs from experiment 2. On the left, all RBC volumes are presented. Filled symbols represent reconstructions with good quality, and empty symbols represent reconstructions with poor quality. On the right, the average volumes are displayed, the average was calculated using all data and error bars represent the standard deviations. The blue interval represents the range of values found in literature obtained with the same technique used here $93 \pm 19\ \mu m^3$ (average $\pm$ 1 standard deviation) [91].

Table 3.6 – Average volume compatibilities for samples from experiment 2. The filled positions indicate incompatibility between the listed samples. Values were considered incompatible when $p < 5\%$ in the Z test.

Photo-treatment	Literature values			
	$83 \pm 14\ \mu m^3$ [93]	$89 \pm 18\ \mu m^3$ [94]	$91 \pm 17\ \mu m^3$ [93]	$93 \pm 19\ \mu m^3$ [91]
10 mW	Photo-treated	Photo-treated	Photo-treated	-
30 mW	-	-	-	-
50 mW	-	-	-	-
70 mW	Control; Photo-treated	Photo-treated	Photo-treated	-
90 mW	Control; Photo-treated	Control	Control	-

3.2.1.4 Photo-treatment in the microscope stage and fractional acquisition (experiment 3)

Figure 3.14 and Figure 3.15 show all volume values obtained for RBCs photo-treated either with 30 mW or 100 mW, respectively, as a function of time after photo-treatment,

for experiment 3. In addition, Figure 3.16 shows the same type of data, but for a non-treated sample. Figure 3.17 shows all data together.

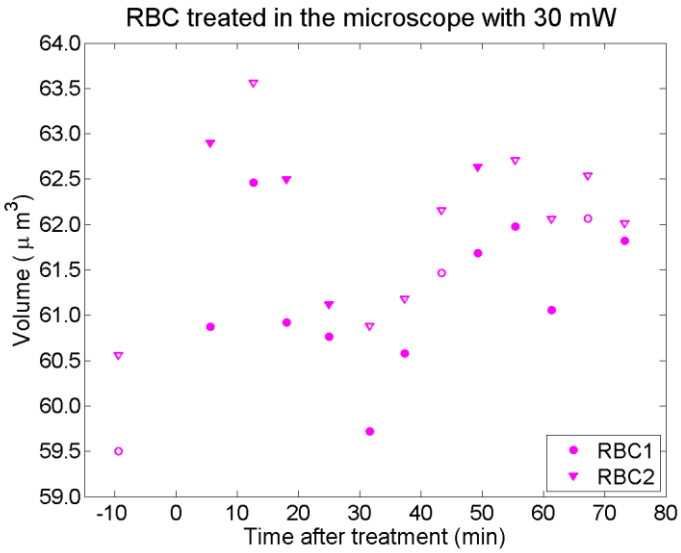

Figure 3.14: Behavior of RBC volume as a function of time after photo-treatment obtained for experiment 3, for the $30\ \mathrm{mW}$ photo-treated sample. The first point in time is negative because it refers to the measurement that was completed prior to photo-treatment, before starting timing. The legend refers to the two RBCs that were monitored over time. Filled symbols represent reconstructions with good quality and empty symbols represent reconstructions with poor quality.

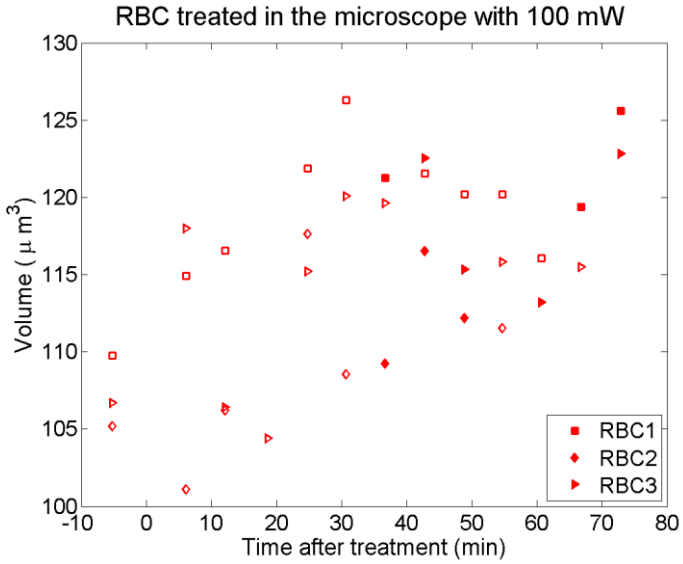

Figure 3.15: Behavior of RBC volume as a function of time after photo-treatment obtained for experiment 3, for the $100\ \mathrm{mW}$ photo-treated sample. The first point in time is negative because it refers to the measurement that was completed prior to photo-treatment, before starting timing. The legend refers to the three RBCs that were monitored over time. Filled symbols represent reconstructions with good quality and empty symbols represent reconstructions with poor quality.

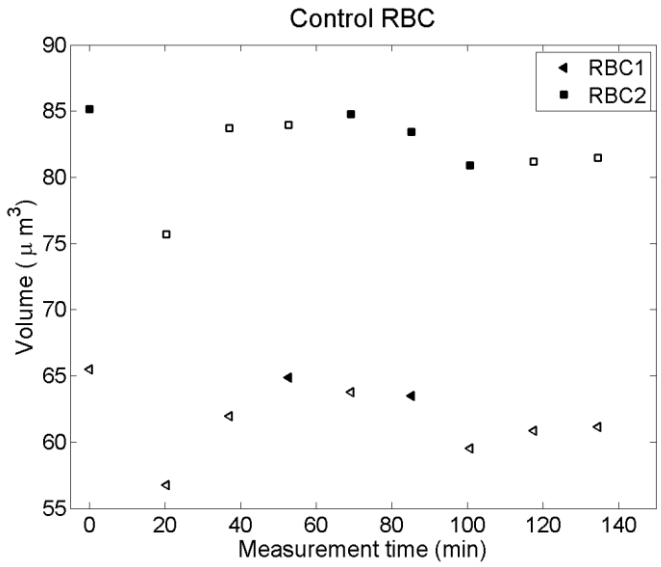

Figure 3.16: Behavior of RBC volume as a function of time obtained for experiment 3, for the control samples, that were not photo-treated. The legend refers to the two RBCs that were monitored over time. Filled symbols represent reconstructions with good quality and empty symbols represent reconstructions with poor quality.

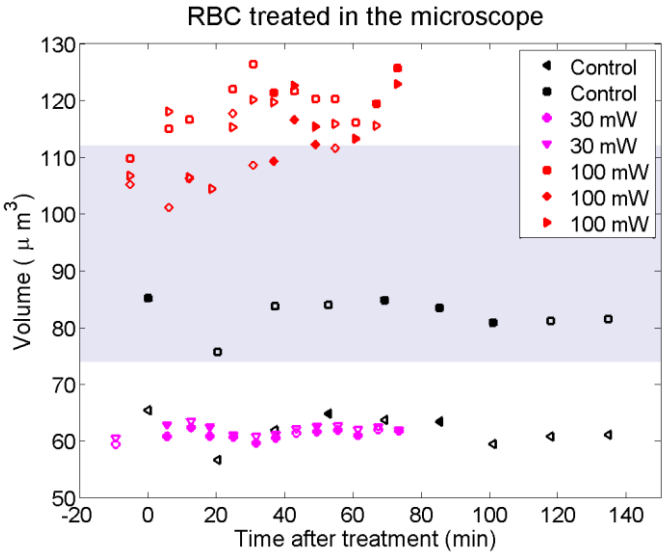

Figure 3.17: Behavior of RBC volume as a function of time after photo-treatment obtained for experiment 3, for all samples. Some points in time are negative because they refer to the measurement that was completed prior to photo-treatment, before starting timing. The legend refers to the power used for each sample; the control group was not photo-treated. Filled symbols represent reconstructions with good quality, and empty symbols represent reconstructions with poor quality. The blue interval represents the range of values found in literature obtained with the same technique used here $93 \pm 19\ \mu m^3$ (average $\pm$ 1 standard deviation) [91].

For each RBC, a constant and a linear function were fitted to data of volume as a function of time. The uncertainty was obtained through the quadratic sum of the reconstruction uncertainty (5% of volume) and the standard deviation of the control RBC volume. The results are presented in Table 3.7.

Table 3.7 – Values of χ^2 and number of degrees of freedom (*ndf*) for linear and constant functions for experiment 3. The quality of the fitting is also presented, considering two tails and $p < 5\%$. The last column shows the slope of the linear fit and the number displayed in parentheses is the uncertainty in the last digits of the number. For example, $0.14(5)$ represents a quantity of 0.14 with uncertainly of 0.05 and $11.3(21)$ a quantity of 11.3 with uncertainty of 2.1.

Sample	Constant function			Linear function			
	χ^2	*ndf*	Fitting quality	χ^2	*ndf*	Fitting quality	Slope (μm^3/min)
0 mW, 0 s, RBC1	3.90	9	Good	3.89	8	Good	-0.001(28)
0 mW, 0 s, RBC2	2.99	9	Good	2.98	8	Good	0.000(33)
30 mW, 180 s, RBC1	0.573	12	Poor	0.406	11	Poor	0.02(5)
30 mW, 180 s, RBC2	0.561	12	Poor	0.540	11	Poor	0.01(5)
100 mW, 180 s, RBC1	5.65	11	Good	3.63	10	Good	0.11(8)
100 mW, 180 s, RBC2	6.12	8	Good	3.33	7	Good	0.17(11)
100 mW, 180 s, RBC3	11.3	12	Good	7.72	11	Good	0.14(7)

For the control group it was not possible to decide which function fits better to data, based on the χ^2 goodness of fit analysis, because both functions fit satisfactorily. It is worth mentioning that the slope values are very low, being compatible with zero, for *Z* test ($p < 5\%$). Therefore, it is possible to conclude that the best function for these cases is the constant and consequently there are no trends in the RBC volume with respect to time after photo-treatment. For the 30 mW (5.4 J) photo-treated RBCs, it was neither possible to decide which function fits better to data. However, in this case both fits were not satisfactory, with too small χ^2 values. Finally, for 100 mW (18 J) photo-treated RBC volumes, also both functions fit to data. Here, again, the slopes are small, compatible with zero, for *Z* test ($p < 5\%$), which makes the constant function more adequate.

The average volume of each RBC was compared with the literature values mentioned above, using the *Z* test and $p < 5\%$. Only the RBC1 and RBC3, from the 100 mW

sample have their averages incompatible with the value $83 \pm 14\ \mu m^3$ [93]. All other averages are compatible with the values found in the literature.

3.2.1.5 Photo-treatment in the microscope stage and fractional photo-treatment (experiment 4)

Figure 3.18 and Figure 3.19 show all volumes obtained for RBCs photo-treated either with $30\ mW$ or $100\ mW$, respectively, as a function of accumulated photo-treatment time, for experiment 4. Figure 3.20 shows all data together.

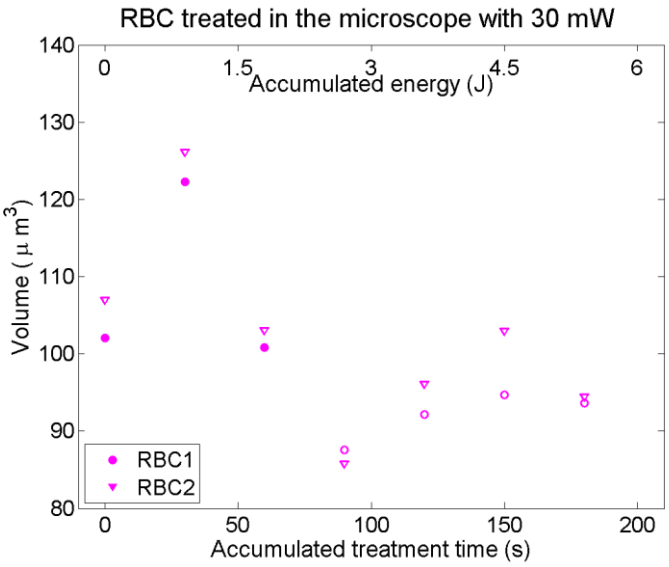

Figure 3.18: Volumes obtained for experiment 4, for the $30\ mW$ photo-treated sample. The legend refers to the two RBC that were monitored. Filled symbols represent reconstructions with good quality and empty symbols represent reconstructions with poor quality.

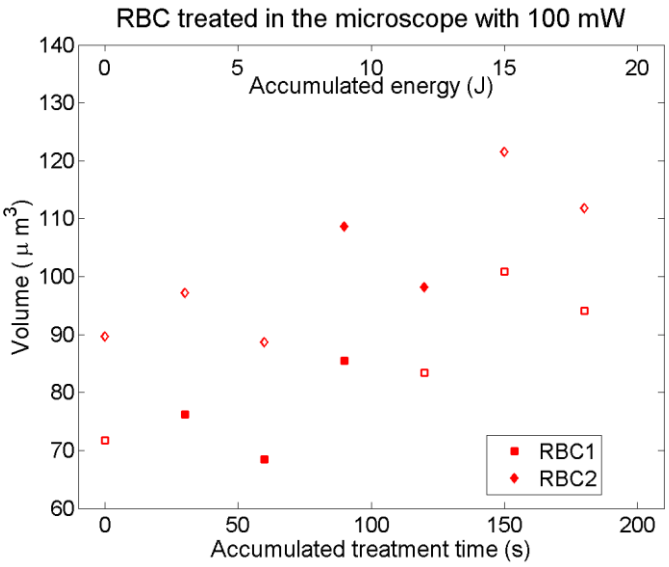

Figure 3.19: Volumes obtained for experiment 4, for the $100\,\mathrm{mW}$ photo-treated sample. The legend refers to the two RBC that were monitored. Filled symbols represent reconstructions with good quality and empty symbols represent reconstructions with poor quality.

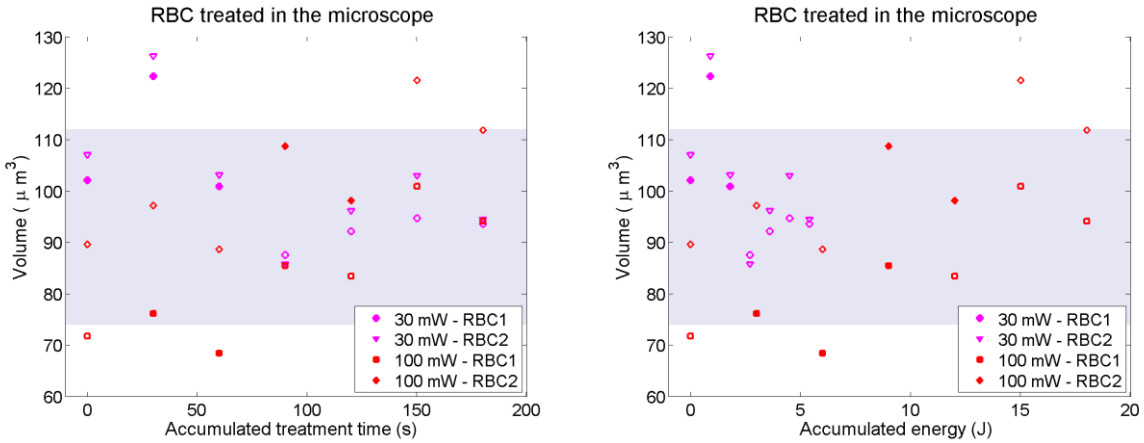

Figure 3.20: Volumes obtained for experiment 4, for all samples. On the left, volume as a function of the accumulated photo-treatment time. On the right, volume as a function of the accumulated energy delivered to the sample. The legend refers to the power used for each sample and the RBC that was monitored. Filled symbols represent reconstructions with good quality and empty symbols represent reconstructions with poor quality. The blue interval represents the range of values found in literature obtained with the same technique used here $93 \pm 19\ \mu\mathrm{m}^3$ (average $\pm$ 1 standard deviation) [91].

For data of volume as a function of accumulated photo-treatment time, for each RBC, a constant and a linear function were fitted. The uncertainty was obtained through the quadratic sum of the reconstruction uncertainty (5% of volume) and the standard deviation of the control RBC volume from experiment 3. The results are presented in Table 3.8.

Table 3.8 – Values of χ^2 and number of degrees of freedom (*ndf*) for linear and constant functions for experiment 4. The quality of the fitting is also presented, considering two tails and $p < 5\%$. The last column shows the slope of the linear fit and the number displayed in parentheses is the uncertainty in the last digits of the number. For example, $0.14(5)$ represents a quantity of 0.14 with uncertainly of 0.05 and $11.3(21)$ a quantity of 11.3 with uncertainty of 2.1.

Sample	Constant fit			Linear fit			
	χ^2	*ndf*	Fitting quality	χ^2	*ndf*	Fitting quality	Slope ($\mu m^3/s$)
30 mW RBC1	20.7	6	Poor	13.5	5	Poor	-0.093(36)
30 mW RBC2	26.6	6	Poor	19.3	5	Poor	-0.095(37)
100 mW RBC1	33.6	6	Poor	9.13	5	Good	0.152(31)
100 mW RBC2	25.9	6	Poor	9.72	5	Good	0.143(36)

For volumes of the 30 mW photo-treated RBCs, it was not possible to decide which function fits better to data, based on the χ^2 goodness of fit analysis, because both fits were unsatisfactory, with too large χ^2 values. Despite that, the χ^2 value of the linear fit is smaller than the χ^2 value of the constant fit. Furthermore, the slopes of the linear fits are not compatible with zero, for *Z* test ($p \sim 1\%$), which might show a decreasing volume as function of the accumulated photo-treatment time or accumulated photo-treatment energy. However, as the χ^2 values are not good, this conclusion might be inaccurate. On the other hand, the volumes of the 100 mW photo-treated RBCs are satisfactorily described by the increasing linear fitting, and the constant function does not, showing that there is an increasing behavior of volume with the accumulated photo-treatment time or accumulated photo-treatment energy. For this case, the slopes are also incompatible with zero, for *Z* test ($p \sim 10^{-6}$). This result could indicate a modulation effect of the RBC volume, as for the 30 mW photo-treated samples the volumes were slightly higher than the volumes found in the literature and the PBMT caused the decrease of this volume. Another possibility is that this trend is due to statistical fluctuation. On the other hand, for the 100 mW photo-treated samples, the volume increased. Another possible interpretation could be a biphasic effect. Thus, for lower doses, there is a stimulating effect and for higher doses, there is an inhibitory

effect, inducing the RBCs to increase the volume, to values above the normal values, which are found in the literature. However, for both cases, the slopes are small, indicating that there is a trend, but this trend is subtle. It has the order of $0.1\ \mu m^3/s$, which means a change lower than 0.2% of the RBC volume, for each second of photo-treatment.

Finally, despite the trends presented by the samples, the average volumes of each RBC was compared with the literature values mentioned above, using *Z* test and $p < 5\%$. All RBC volumes have their averages compatible with all literature values.

3.2.2 Radial profile of cell thickness

Figure 3.21 shows examples of radial profiles for RBC thickness obtained for two samples. In these graphs, the reconstruction quality is shown in the legend, thus GD refers to good quality reconstructions, as shown in Figure 3.7, and PR refers to poor quality reconstructions, as those shown in Figure 3.8 and Figure 3.9. The final part of the legend refers to the RBC identification. Each curve refers to the radial profile of cell thickness of a specific RBC. The averages presented in subsequent graphs were calculated with all data, from both good and poor quality reconstructions.

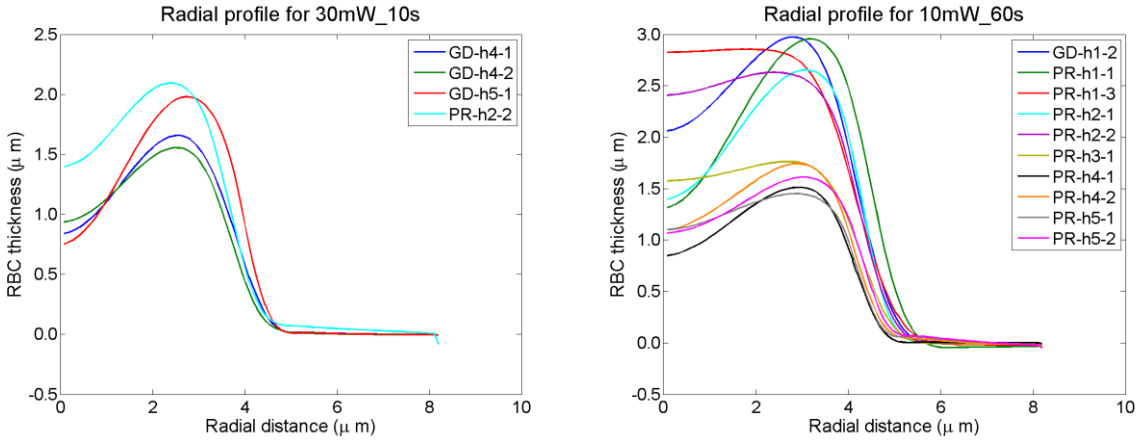

Figure 3.21: On the left, the radial profile of cell thickness for RBCs photo-treated with $30\ mW$ for $10\ s$. On the right, the radial profile of cell thickness for RBCs photo-treated with $10\ mW$ for $60\ s$, both from experiment 1. The legend refers to good (GD) or poor quality (PR) reconstructions and RBC identification. Each curve refers to a different RBC.

The left graph in Figure 3.21 shows the radial profile of cell thickness for RBCs photo-treated with $30\ mW$ for $10\ s$. The right graph shows RBCs photo-treated with $10\ mW$ for $60\ s$, both from experiment 1. Two kinds of radial profile for RBCs can be found in these graphs: biconcave (as expected for normal RBCs) and not biconcave. The cell format,

for most of the RBCs, is the expected biconcave with a huge increase of thickness from the RBC center to the edge. However, for many of them the center parts are very thick and the growth of thickness to the edge is more subtle. The biconcave shape is practically lost for some RBCs. Note that the RBC sample in the right graph is very heterogeneous regarding radial profile of cell thickness. It is worth to remember that this same sample is also very heterogeneous regarding the volume (see Figure 3.12). These RBCs with unusual profiles might have caused the difference of this sample related to others.

3.2.2.1 Comparison between photo-treatments in the Eppendorf tube and microscope stage

Figure 3.22 shows the average radial profile obtained with all data from all radial profile of cell thickness data from $10\,\mathrm{mW}$, $60\,\mathrm{s}$ photo-treated RBCs. The graphs compare photo-treatments done in the Eppendorf tube, from experiment 1, and in the microscope stage, from experiment 2. In the left graph, the error bars represent the sample standard deviation; in the right graph, the error bars represent the standard deviation of the mean. The comparison using Student's *t*-test, which was completed for each radial distance, indicates that the averages of the two samples are compatible with each other for all radial distances, which means that the two modes of photo-treatment may be equivalent also regarding the radial profile of cell thickness. As noticed for the volumes of the same RBCs, the standard deviations for the sample photo-treated at the microscope stage are very large.

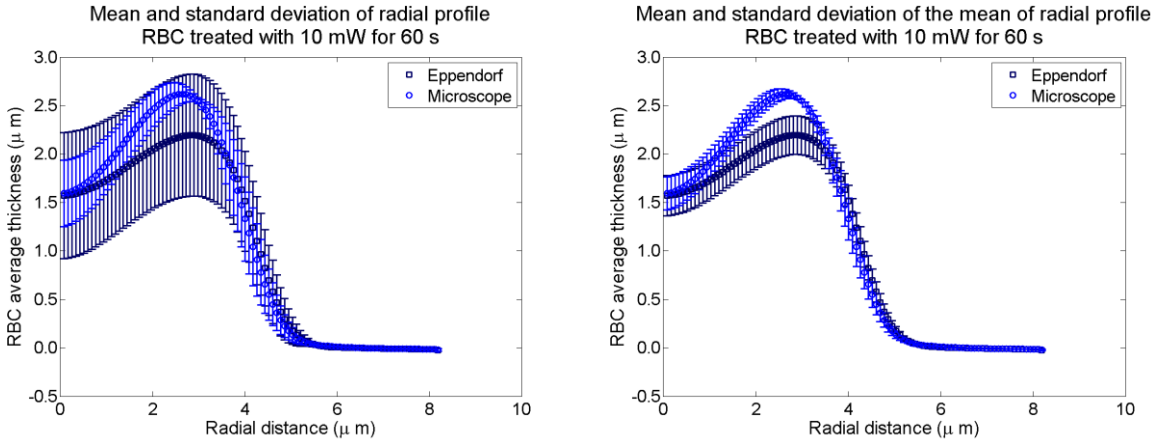

Figure 3.22: Radial profile of cell thickness for samples photo-treated either in the Eppendorf tube (from experiment 1) or in the microscope stage (from experiment 2), with $10\,\mathrm{mW}$ for $60\,\mathrm{s}$. The values represented are the averages for all data, for each radial distance. On the left, the error bars represent data standard deviation and on the right, the standard deviation of the mean.

3.2.2.2 Photo-treatment in the Eppendorf tube with variable power (experiment 1)

Figure 3.23 shows the averages for each radial position obtained with all radial profile of cell thickness data from RBCs from experiment 1. Table 3.9 shows the results of the Student's *t*-test for the comparison between samples.

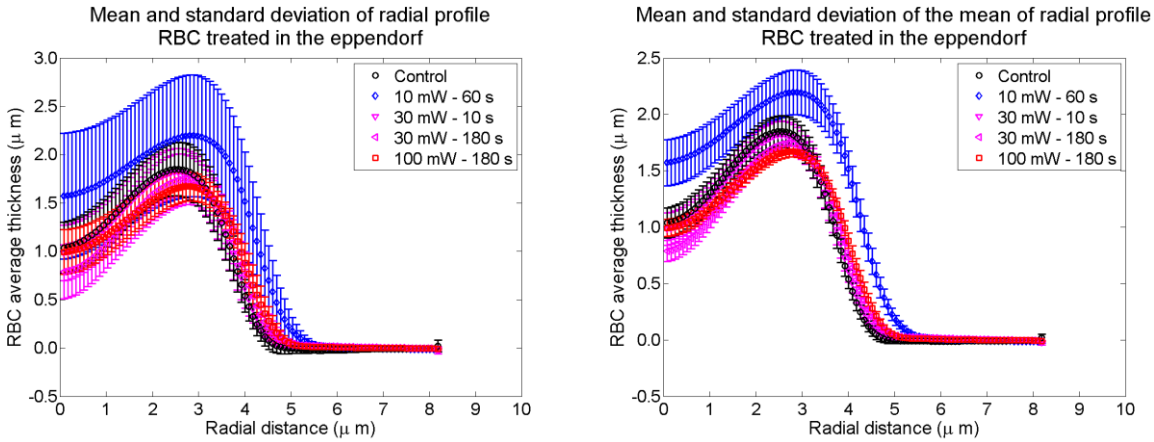

Figure 3.23: Radial profile of cell thickness for samples from experiment 1. The values represented are the averages for all data. On the left, the error bars represent data standard deviation and on the right, the standard deviation of the mean.

Table 3.9 – Results of the Student's *t*-test comparing the RBC average thickness, for samples from experiment 1. The comparison was performed for each radial distance and the table shows the compatibilities and incompatibilities by regions. The table is symmetric, thus, the positions below the diagonal are empty.

Compared samples	Control	10 mW, 60 s	30 mW, 10 s	30 mW, 180 s	100 mW, 180 s
Control		Incompatible 3.0 to 5.5 μm	Compatible whole RBC	Compatible whole RBC	Incompatible 3.8 to 4.9 μm
10 mW, 60 s			Incompatible 3.0 to 5.5 μm	Incompatible 3.0 to 5.5 μm	Incompatible whole RBC
30 mW, 10 s				Compatible whole RBC	Incompatible 3.8 to 4.9 μm
30 mW, 180 s					Compatible whole RBC
100 mW, 180 s					

3.2.2.3 Photo-treatment in the microscope stage with variable power (experiment 2)

Figure 3.24 shows the averages for each radial position obtained with all radial profile of cell thickness data from RBCs from experiment 2. Table 3.10 shows the results for the Student's *t*-test for the comparison of the photo-treated samples in pairs.

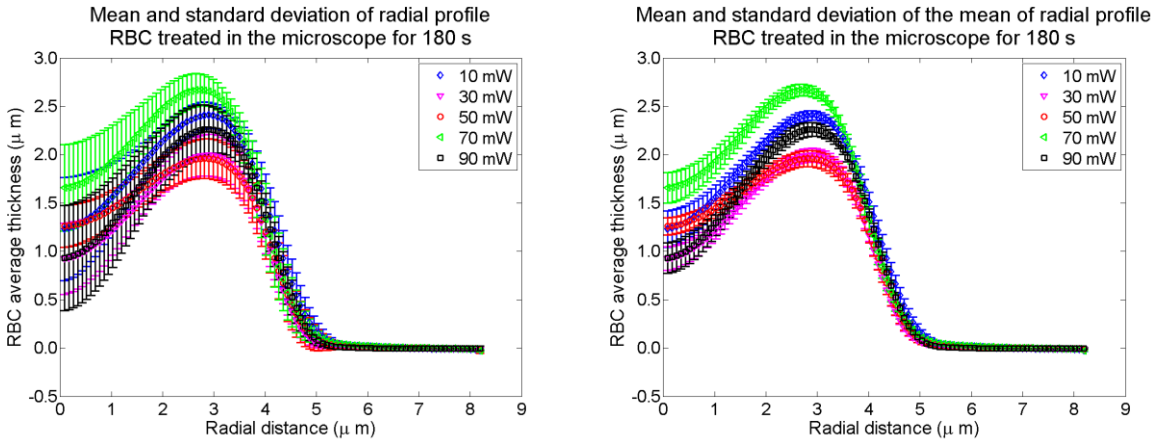

Figure 3.24: Radial profile of cell thickness for samples photo-treated from experiment 2. The values represented are the averages for all data. On the left, the error bars represent data standard deviation and on the right, the standard deviation of the mean.

Table 3.10 – Results of the Student's *t*-test comparing the RBC average thickness, for the photo-treated samples from experiment 2. The comparison was performed for each radial distance and the table shows the compatibilities and incompatibilities by regions. The table is symmetric, thus, the positions below the diagonal are empty.

Compared samples	10 mW	30 mW	50 mW	70 mW	90 mWs
10 mW		Incompatible whole RBC	Incompatible 1.0 to 4.5 μm	Incompatible 1.0 to 4.5 μm	Compatible whole RBC
30 mW			Compatible whole RBC	Incompatible 1.0 to 4.5 μm	Incompatible 1.0 to 4.5 μm
50 mW				Incompatible 1.0 to 4.5 μm	Incompatible 1.0 to 4.5 μm
70 mW					Incompatible 1.0 to 4.5 μm
90 mW					

Figure 3.25 to Figure 3.29 show Student's *t*-test results for the comparison between each photo-treated sample with its respective control sample. Data shown in orange represent regions with incompatibility between compared samples. Note that only the

90 mW (16.2 J) photo-treated sample has a large region of incompatibility. However, it is worth to remember that the control of this sample was composed by only one RBC and these samples were tested considering the control sample values as true values without uncertainty. An uncertainty estimation based on the other control samples is difficult as the standard deviations are very different between the various control samples. For the other cases, there are just some areas with incompatible averages. In addition, for almost all RBC regions the radial profiles of cell thickness averages are compatible, comparing control and photo-treated samples. Furthermore, there is no region in common where the incompatibility happens.

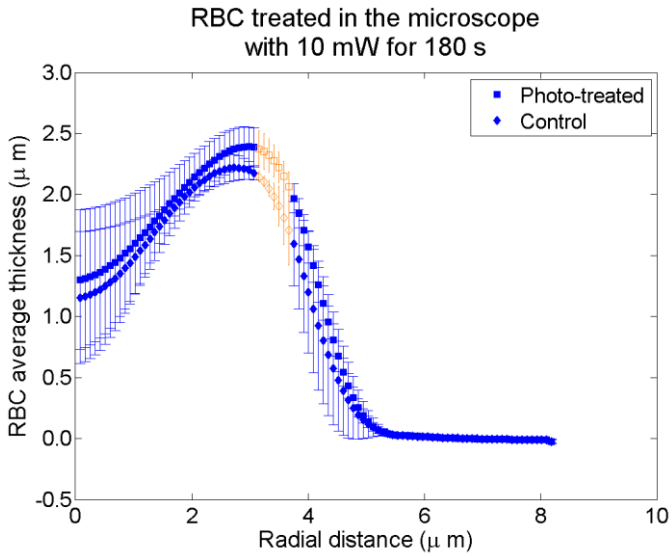

Figure 3.25: Comparison between the 10 mW, 180 s (1.8 J) photo-treated sample and its respective control, using Student's *t*-test. The error bars represent data standard deviation. The points presented in orange represent incompatible averages when comparing photo-treated and control samples.

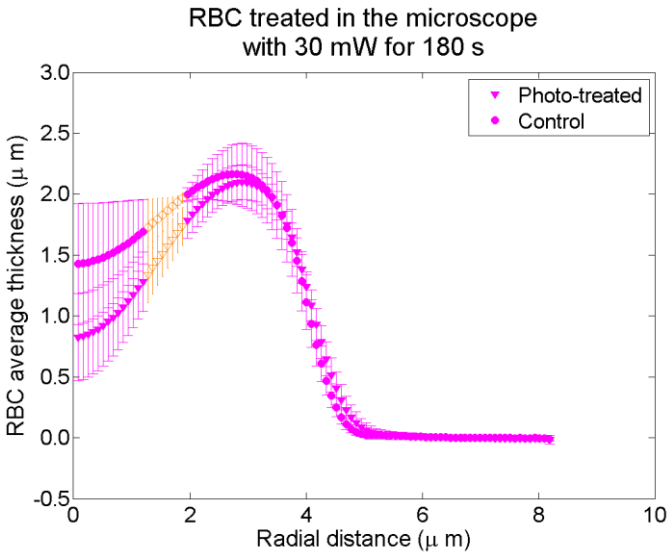

Figure 3.26: Comparison between the $30\ \mathrm{mW}$, $180\ \mathrm{s}$ ($5.4\ \mathrm{J}$) photo-treated sample and its respective control, using Student's *t*-test. The error bars represent data standard deviation. The points presented in orange represent incompatible averages when comparing photo-treated and control samples.

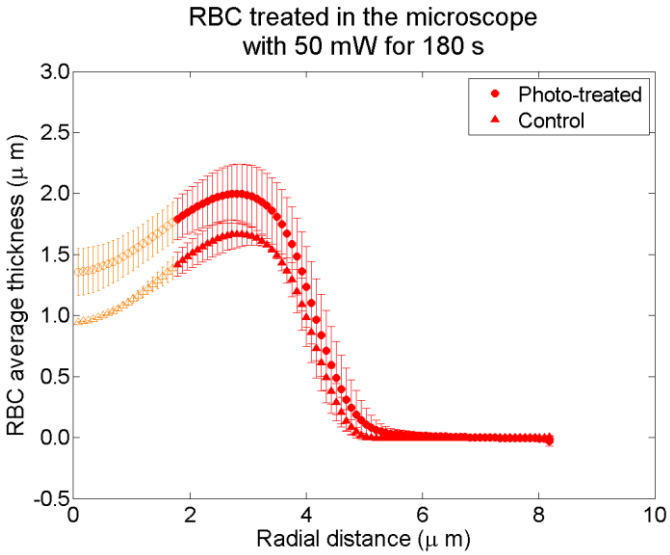

Figure 3.27: Comparison between the $50\ \mathrm{mW}$, $180\ \mathrm{s}$ ($9.0\ \mathrm{J}$) photo-treated sample and its respective control, using Student's *t*-test. The error bars represent data standard deviation. The points presented in orange represent incompatible averages when comparing photo-treated and control samples.

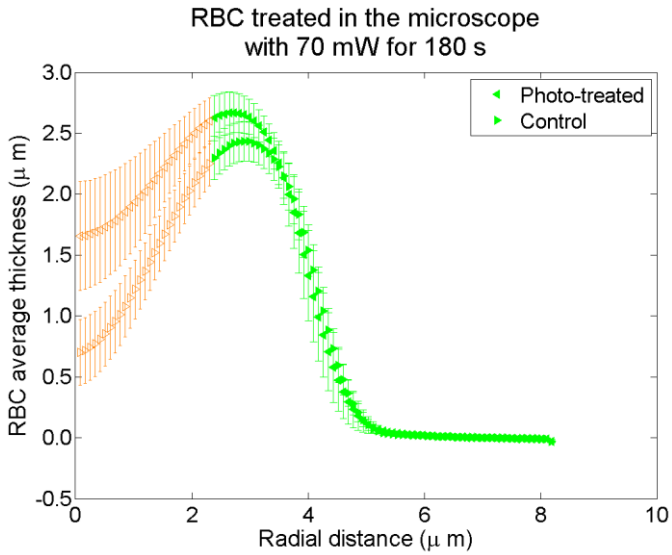

Figure 3.28: Comparison between the 70 mW, 180 s (12.6 J) photo-treated sample and its respective control, using Student's *t*-test. The error bars represent data standard deviation. The points presented in orange represent incompatible averages when comparing photo-treated and control samples.

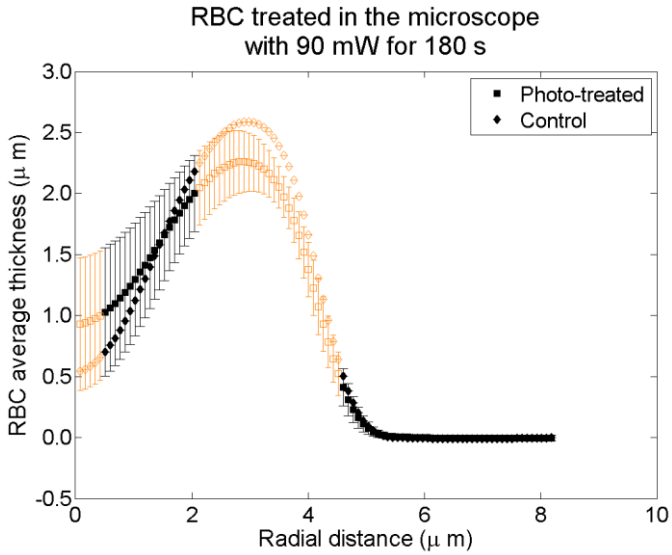

Figure 3.29: Comparison between the 90 mW, 180 s (16.2 J) photo-treated sample and its respective control, using Student's *t*-test. The error bars represent data standard deviation. The points presented in orange represent incompatible averages when comparing photo-treated and control samples.

3.2.2.4 Photo-treatment in the microscope stage and fractional acquisition (experiment 3)

Figure 3.30 shows radial profiles of cell thickness obtained for one RBC for experiment 3. The variation of the profiles is small, the thicknesses present small variation in all regions, and do not show increasing or decreasing systematic behaviors related to time after photo-treatment.

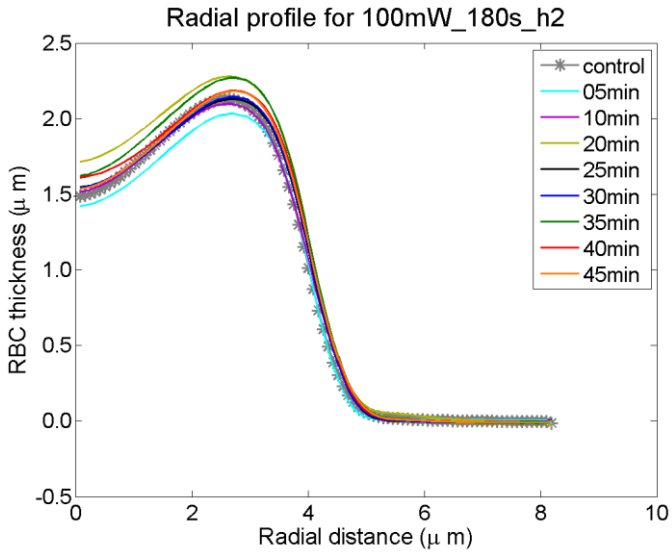

Figure 3.30: Radial profile of cell thickness obtained for one RBC photo-treated with $100\ \mathrm{mW}$ for $180\ \mathrm{s}$ ($18\ \mathrm{J}$), for experiment 3. The legend refers to time after photo-treatment, except for *Control* that refers to the measurement before photo-treatment. All curves refer to the same RBC.

3.2.2.5 Photo-treatment in the microscope stage and fractional photo-treatment (experiment 4)

Figure 3.31 shows radial profiles of cell thickness obtained for one RBC for experiment 4. Here, again, the profile variation is small and the same is observed for the thicknesses variation. Furthermore, there is a subtle systematic behavior related to the thickness of the RBC edge as a function of the accumulated photo-treatment time. This behavior is similar to the trend presented by the volume, for those samples (results shown in section 3.2.1.5).

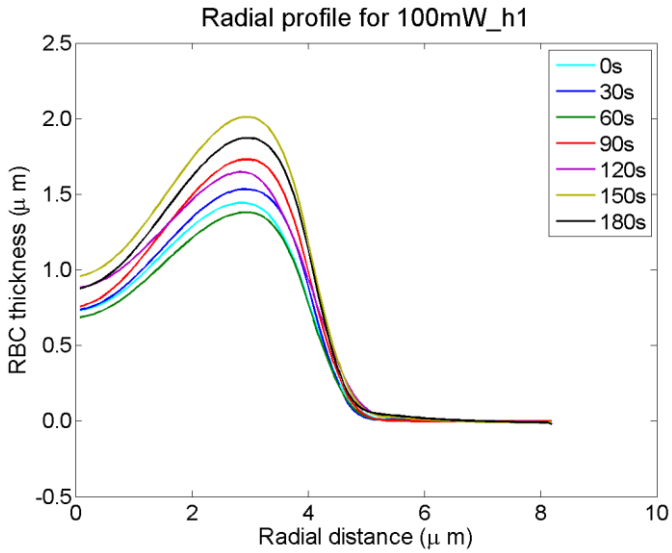

Figure 3.31: Radial profile of cell thickness obtained for one RBC photo-treated with $100\,\mathrm{mW}$, for experiment 4. The legend refers to accumulated photo-treatment time. All curves refer to the same RBC.

3.2.3 Lateral fluctuation

Figure 3.32 shows, as example, the results obtained for one RBC lateral fluctuation, for distances between maxima. For the distances between minima, the only difference is the distance amplitude, thus, the values are smaller due to image contrast characteristics. The separation of the distances along the four fluctuation directions seen in the graph indicates the RBC asymmetry; the more separated from each other, the greater the asymmetry.

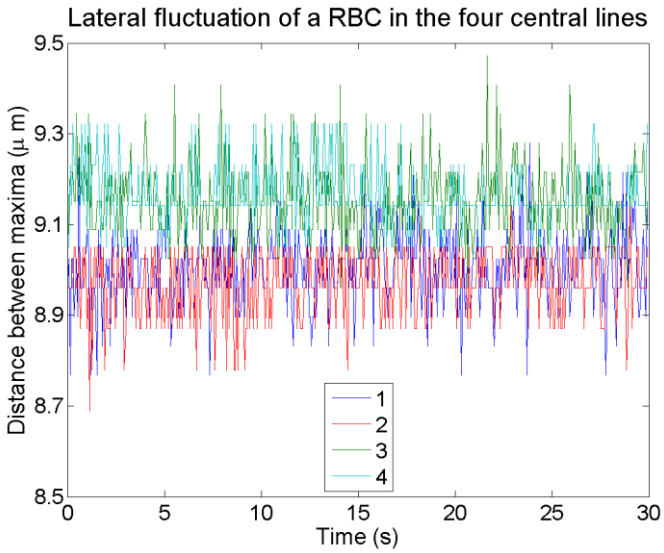

Figure 3.32: RBC lateral fluctuation. These data are for the distance between maxima, however, data for the distances between minima have this same profile but with lower amplitude values. The separation of the distances along the four fluctuations directions indicates the RBC asymmetry. The numbers in the legend refer to the four central lines traced as seen in Figure 3.6.

Figure 3.33 shows the typical Fourier transform for data obtained in the experiment, for UNIQ camera, $15\ \mathrm{Hz}$ capture rate. It is worth mentioning that the same structure of Fourier transform was obtained for a series of parameters that passed through the Fourier analysis: lateral fluctuation of distance between minima or maxima, grey level of a background pixel, grey level of a peak pixel, all these Fourier transforms presented the same behavior. The only difference between the graphs was the value $|Y(t)|$ where the curve "detaches" from the vertical axis, which is related to the amplitude of the transformed signal. The graphs show a high value $|Y(t)|$ for frequencies close to zero, and much smaller values (decreasing) for the highest frequencies, with a shape that is almost periodic. The troughs in the Fourier transform are equally spaced in frequency. The repetition frequency $0.23\ \mathrm{Hz}$ observed in case of Figure 3.33 was obtained in all the Fourier transforms, regardless of the signal that was transformed. Another important fact is that the Fourier transform of CMOS camera data, whose capture rate is around $300\ \mathrm{Hz}$, has the same shape, but the distance between the troughs is smaller, $0.0027\ \mathrm{Hz}$. This led to the conclusion that this Fourier transform shape is due to some factor related to the image acquisition and not with the behavior of the sample itself. Possibly if the RBCs have a natural oscillation frequency, this movement cannot be detected with capture rates employed in this experiment.

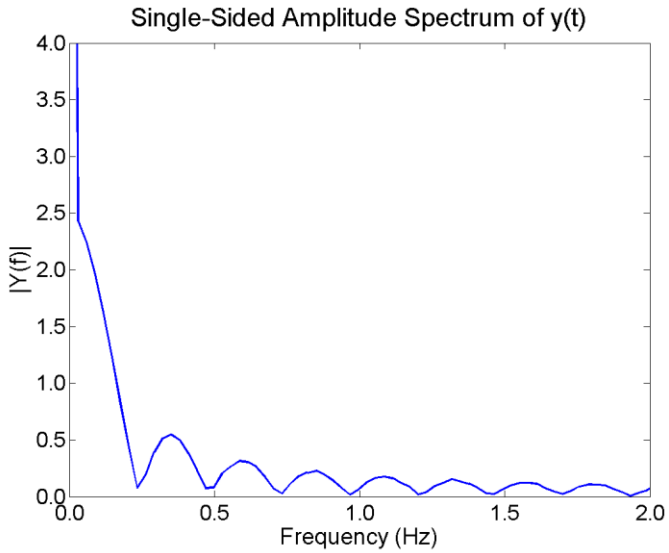

Figure 3.33: Fourier transform obtained for the experimental data.

The RBC fluctuation is obtained by Park and colleagues [96], [97]. They use the thickness map $H(x,y,t)$ to determine the fluctuation. For each time interval and position is calculated the deviation from average $\Delta H(x,y,t)=H(x,y,t)-\langle H(x,y)\rangle$, where $\langle H(x,y)\rangle$ represents the average thickness map over time. They calculate the *rms*, which is the root mean square, and consider this value as the membrane fluctuation. The square root of the time average of ΔH^2, or $\sqrt{\langle \Delta H^2 \rangle}$, the *rms*, represents the fluctuation. In our case, the standard deviation of the lateral fluctuation was obtained in a similar way, with only a small difference: if the distance between maxima or minima is called D, the standard deviation is the square root of the sum of ΔD^2 divided by N-1, where $\Delta D=D(t)-\langle D\rangle$ and N is the number of data. This expression is very close to the square root of the temporal average of ΔD^2, once N is a large number (it represents the number of frames in the RBC video, with 450 as a typical value) so $(N-1)\approx N$. Values obtained by Park were around $46\ \mathrm{nm}$ [97] and $60\ \mathrm{nm}$ [96]. The values obtained here are a little higher than these values, around $75\ \mathrm{nm}$ for the samples in general. There are two factors that might explain this difference, in Park's work, the fluctuation was obtained at the RBC center, which is more rigid than the edge [97]. Furthermore, in Park's work the fluctuation was obtained in the vertical direction, while here the fluctuation was obtained in the horizontal direction.

3.2.3.1 Comparison between photo-treatments in the Eppendorf tube and microscope stage

Figure 3.34 shows the comparison of the fluctuation data between the modes of photo-treatment in the Eppendorf tube and microscope stage, from experiments 1 and 2, respectively, for $10\,\mathrm{mW}$, $60\,\mathrm{s}$ photo-treated RBCs. All the four lines where the fluctuation was analyzed are shown in the graph, without symbol distinction. Each color represent one distance: either minima or maxima. Each box represent a distance and a method of photo-treatment, either in the Eppendorf tube or microscope stage. The two-sample rank sum test was done for each line separately (because lines from a single RBC are statistically dependent samples), comparing the different methods of photo-treatment, for each distance. It indicates that the samples have compatible data, for both distances (between maxima and between minima), in each line separately. This means that the two modes of photo-treatment may be equivalent as far as the lateral fluctuation data are concerned.

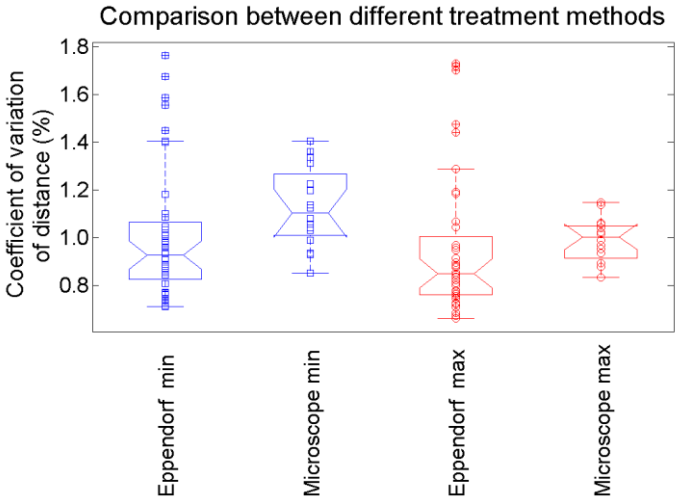

Figure 3.34: Coefficients of variation for distances between maxima (max) and minima (min), referring to the lateral fluctuation for RBCs photo-treated with $10\,\mathrm{mW}$ for $60\,\mathrm{s}$, either in the Eppendorf tube or in the microscope stage, from experiments 1 and 2, respectively. All measurement lines are represented, but without symbol distinction.

3.2.3.2 Photo-treatment in the Eppendorf tube with variable power (experiment 1)

Figure 3.35 shows the coefficients of variation for distances between maxima (on the left) and minima (on the right). The two-sample rank sum test was carried out to

compare the values of the coefficient of variation between different groups. The test was performed for each one of the lines in that analysis, separately, and also individually for each camera. According to the test, most samples have compatible data, except for a few cases (see Table 3.11), for both distances and both cameras. Within the 80 comparisons done, around 4% of the comparisons resulted in incompatibility between the coefficient of variation for data acquired with the UNIQ camera and 5% with the CMOS camera. Note that sample data were considered incompatible for $p < 5\%$.

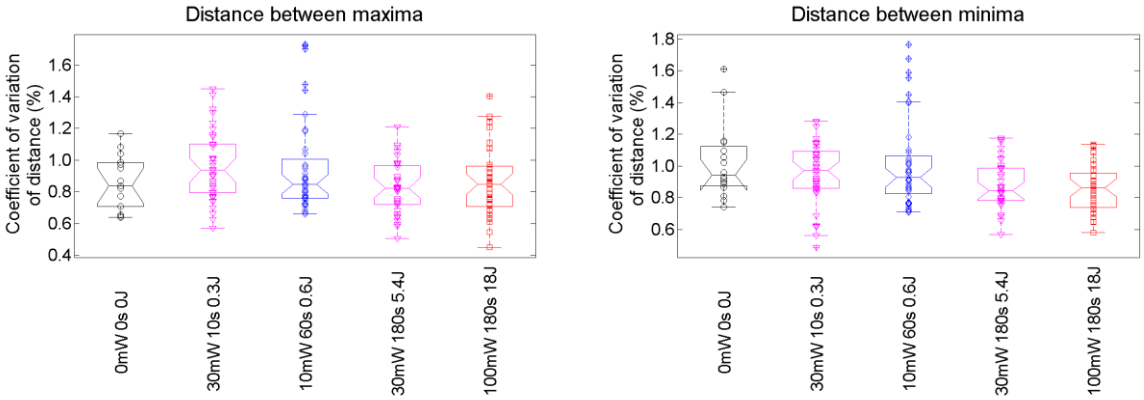

Figure 3.35: Coefficients of variation for distances between maxima (on the left) and minima (on the right), referring to the lateral fluctuation for RBCs from experiment 1. All measurement lines are represented, but without symbol distinction. Data are shown in increasing order of energy, but the horizontal axis is not in scale.

Table 3.11 – Result of the two-sample rank sum test comparing the values of the coefficient of variation from the RBC lateral fluctuation, from experiment 1. The test was performed separately for each measurement line. Data above the grey diagonal refers to the UNIQ camera, and data below the grey diagonal refers to the CMOS camera. The acronyms *Dmin* and *Dmax* refer to the distances between minima and maxima, respectively; the numbers refer to the lines where the lateral fluctuation was evaluated and there was incompatibility. The filled table positions bring information about the incompatibility between sample data, specifying the situation in which it occurred. Unfilled table positions correspond to compatibility of the compared samples.

Compared samples	0 mW, 0 s	30 mW, 10 s	10 mW, 60 s	30 mW, 180 s	100 mW, 180 s
0 mW, 0 s	-				
30 mW, 10 s		-		*Dmax* (1 and 2)	
10 mW, 60 s			-		*Dmax* 1
30 mW, 180 s				-	
100 mW, 180 s		(*Dmax* and *Dmin*) 4		(*Dmax* and *Dmin*) 4	-

3.2.3.3 Photo-treatment in the microscope stage with variable power (experiment 2)

Figure 3.36 shows the coefficients of variation for distances between maxima (on the left) and minima (on the right). The two-sample rank sum test was done to compare the coefficients of variation between samples. Furthermore, it was used to compare, within a sample, the photo-treated RBCs with their respective control RBCs. According to the test, most samples have compatible data for comparisons between the photo-treated samples and their respective control (only 8% of the 40 comparisons completed were incompatible). On the other hand, a larger amount of incompatibility was observed for comparisons between groups, around 29%, as it can be seen on Table 3.12. Note that there is not a clear relation between the sample data incompatibility and the photo-treatment power/energy used. As an example, data for the distance between minima for the 10 mW (1.8 J) photo-treated sample are not compatible with the 30 mW (5.4 J) photo-treated sample coefficients, but are compatible with the 70 mW (12.6 J) photo-treated sample data. Another example are the 50 mW (9.0 J) photo-treated sample coefficients that are not compatible with the 70 mW (12.6 J)

photo-treated sample data, but are compatible with the 90 mW (16.2 J) and 30 mW (5.4 J) photo-treated sample coefficients.

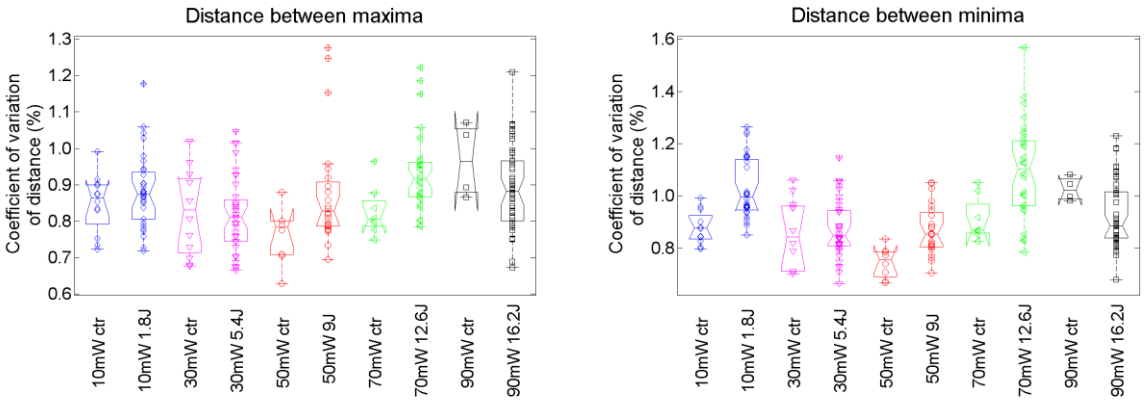

Figure 3.36: Coefficients of variation of distances between maxima (on the left) and minima (on the right), referring to the lateral fluctuation for RBCs from experiment 2. All measurement lines are represented, but without symbol distinction. Data are shown in increasing order of power and energy, but the horizontal axis is not in scale. Each color represent one power, with one set of data for the photo-treated group (with the energy) and another for its respective control group (*ctr*).

Table 3.12 – Result of the two-sample rank sum test comparing the values of the coefficient of variation for RBC lateral fluctuation, from experiment 2. The test was performed separately for each measurement line. Data above the grey diagonal refers to the comparison between photo-treated samples for distance between maxima, and data below the grey diagonal refers to the distance between minima. Finally, the grey diagonal refers to the comparison between photo-treated samples and its respective control (RBCs before photo-treatment). The acronyms *Dmin* and *Dmax* refer to the distances between minima and maxima, respectively; the numbers refer to the lines where the lateral fluctuation data were incompatible. The filled table positions refer to tests where there was incompatibility between sample data.

Compared samples	10 mW	30 mW	50 mW	70 mW	90 mW
10 mW	*Dmin* (1, 3)				
30 mW	1, 2, 3, 4			1, 2, 3	1
50 mW	3, 4			3	3
70 mW		1, 2, 4	1, 2, 3, 4	*Dmax* 3	
90 mW	1, 2			1, 2	

3.2.3.4 Photo-treatment in the microscope stage and fractional acquisition (experiment 3)

Figure 3.37 shows the coefficients of variation for the distances between maxima (on the left) and minima (on the right), for experiment 3. The coefficients of variation for the $100\ \mathrm{mW}$ ($18\ \mathrm{J}$) photo-treated sample are always greater than the coefficient of variation for the $30\ \mathrm{mW}$ ($5.4\ \mathrm{J}$) photo-treated sample, despite that, no trends of the lateral fluctuation regarding the time after photo-treatment were observed.

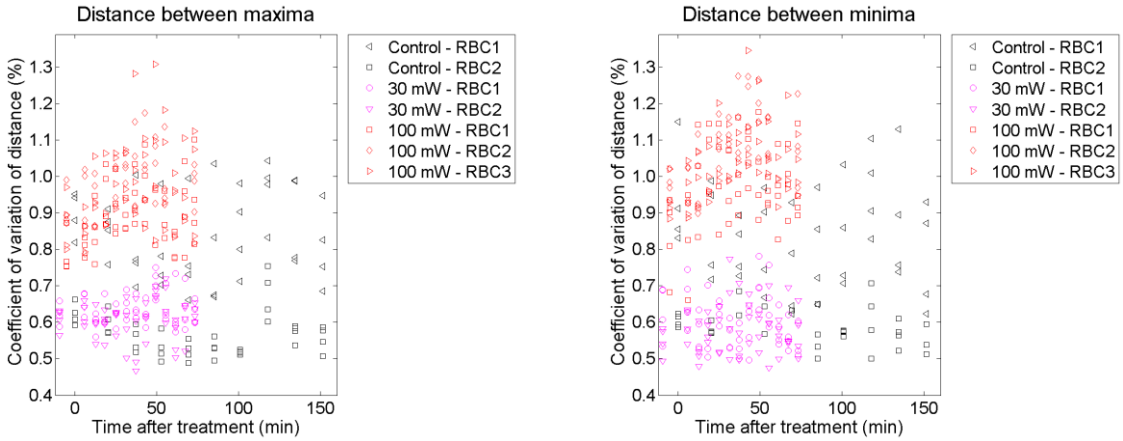

Figure 3.37: Coefficients of variation of RBCs for distances between maxima (on the left) and minima (on the right), referring to the lateral fluctuation for experiment 3.

3.2.3.5 Photo-treatment in the microscope stage and fractional photo-treatment (experiment 4)

Figure 3.38 shows the coefficients of variation for the distances between maxima (on the left) and minima (on the right), for experiment 4. The coefficients of variation for the $30\ \mathrm{mW}$ photo-treated sample is usually greater than the coefficients of variation for the $100\ \mathrm{mW}$ photo-treated samples. However, it is not possible to note trends of the lateral fluctuation regarding the accumulated photo-treatment time.

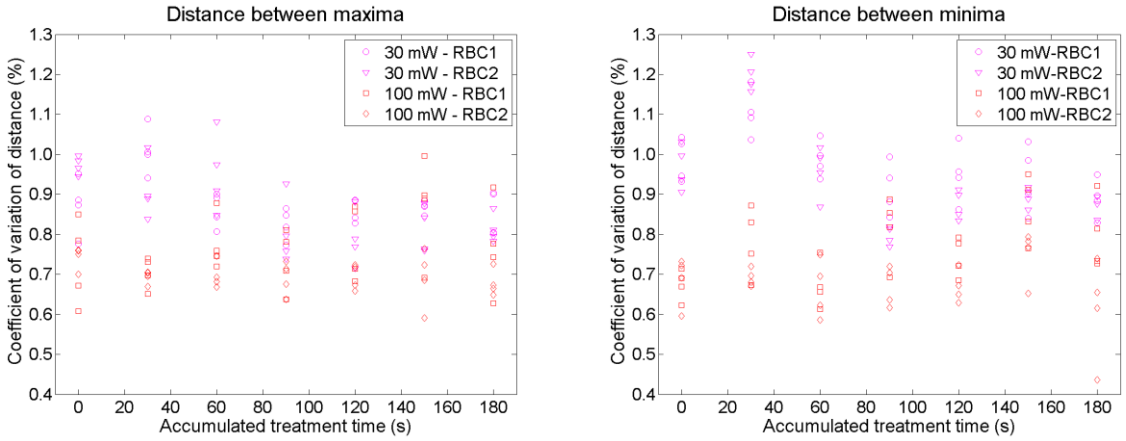

Figure 3.38: Coefficients of variation of RBCs for distances between maxima (on the left) and minima (on the right), referring to the lateral fluctuation for experiment 4.

3.2.4 Vertical fluctuation

Figure 3.39 shows the results obtained for the vertical fluctuation (contrast squared mean fluctuation) for RBCs from experiment 1. In the left graph, the region with large amplitude is due to the edge diffraction, so the region of interest is the RBC center, which is the region expanded for presentation in Figure 3.39 right graph. Student's *t*-test was performed in the region of interest, for each radial distance and it indicates that all samples have compatible averages.

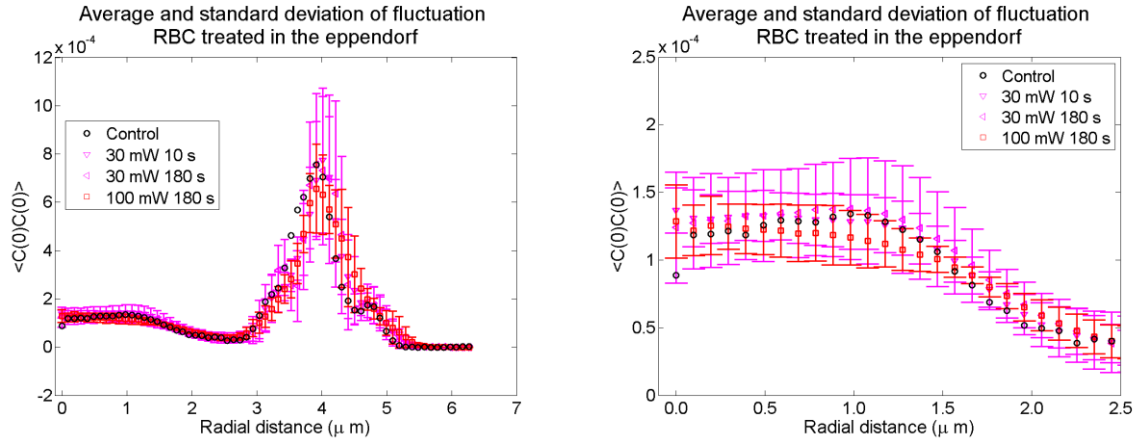

Figure 3.39: Vertical fluctuation for RBCs from experiment 1. On the left, data for all radial distances. On the right, only the region of interest in the center of the RBC, away from the region where there is diffraction due to the edges.

3.2.5 Summary

For the defocusing microscopy experiments, no significant changes were observed in the morphological or mechanical properties of red blood cells, due to PBMT, in the

studied conditions. No systematic changes were found in the parameters evaluated: volume, radial profile, lateral and vertical fluctuations, which evidenced this result. Subtle trends were observed for the fractional photo-treatment experiment, such as a modulation in the RBC volume and a change in the radial profile. Nevertheless, this result might be due to statistical fluctuation.

4. Confocal laser-scanning microscopy

Marvin Minsky invented the confocal microscope in the 1950's and patented it in 1957, however, this kind of microscope was commercially released only thirty years later [98]. In the confocal microscope, the incident light is focused to a specific spot in the specimen – the focal point; the objective lens collects the light from the specimen and focus it in a pinhole. As the pinhole is in a confocal plane with the focal point, almost all light passing through the pinhole will be originating from the focal point. The name confocal is because the pinhole is in a confocal plane with the focal point. Most of the light coming from other parts of the specimen, which are out-of-focus, will not pass through the pinhole, thus will not be detected. This reduces blurring and increases the spatial resolution. Furthermore, it increases signal to noise ratio; enables thick specimen scanning and *z*-scans; enables *xy*-scan of large areas in the specimen, as each point is scanned at once; enables electronic adjusted magnification and 3D reconstruction of thick specimens, among other advantages.

Figure 4.1 shows the images of the confocal microscope patent with its two different configurations. In the first one, on the top, there are two lenses (18 and 20) and two pinholes (*A* and *G*). The entrance pinhole *A* and the condenser lens 18 focus light into the focal point *D* where the specimen is located, the objective lens 20 focus light coming from the specimen focal point *D* in the exit pinhole *G*; this light is detected in 28. Most of the light coming from other parts of the specimen cannot pass through the pinhole *G* and does not blur the image. To scan the whole specimen, either the specimen holder or the light source is moved. In the second design, on the bottom of the figure, called epi-illuminated confocal microscope, there is only one lens (11), which works as condenser and objective lens. There is also a partial or dichromatic mirror (17). The specimen focal point *D* reflects light, which is focused in the pinhole *G*. The modern confocal microscopes are epi-illuminated, but the light source and detector have their places changed, so the partial mirror reflects the excitation light at a 90° angle, while transmits the light coming from the specimen to the detector.

After the patent, some improvements were done to the technique. In the 1970's, photomultiplier tubes started to be used for the detection and a new specimen holder was proposed with high positioning precision in the *z*-axis and faster *xy*-scan. In addition, due to the technique development, the image began to be displayed on a

monitor, and the scanned area was much larger than the conventional microscope scanned areas, these improvements remain until nowadays. Another advancement was the 3D reconstruction of the multiple optical sections, after the whole specimen scan. In the 1980's, the confocal microscope theory was revised and biological applications in cell biology were explored. With the rapid development of the video microscopy and imaging processing, the confocal laser-scanning microscope was developed, also for biological applications. After a few publications with the technique, it was commercially released in 1987. [98]

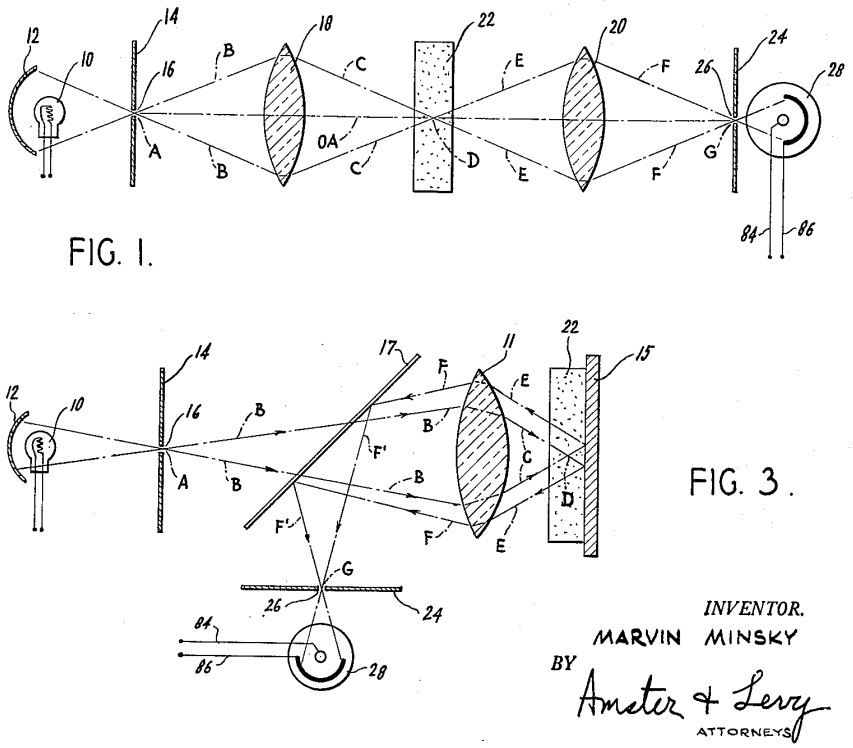

Figure 4.1: Images from the confocal microscope from the original patent. On the top, there are two lenses and on the bottom just one. The principle is the same, the focal point *D* in the specimen is illuminated by 10 and a pinhole *G* is put in a confocal plane with this focal point, thus, most of the light detected by 28 will come direct from the focal point and the pinhole. The specimen scan might be done by either moving the specimen holder or the light source. Images from the Microscope apparatus patent from M. Minsky [99].

Confocal microscopy might detect either reflected light or fluorescence. Usually, when monochromatic, high intensity, coherent and polarized light is needed, lasers are considered as the light source of choice [98]. This is the case of the fluorescence microscopy. Other advantages of the laser are the uniform illumination, stability, and long life.

The confocal fluorescence microscopy is widely used for biological applications because the fluorophores are very specific, binding to precise cell components. The use of fluorophores gives rise to an increase in the signal to noise ratio and generates high resolution and high contrast images [100]. In confocal fluorescence microscopy, the photons that matters are those that the specimen emits, instead of the excitation light, using epi-illumination as preferred configuration. Furthermore, the partial or dichroic mirror, is used to block the excitation light and to transmit the emitted fluorescent photons to the detector, which is a photomultiplier tube. The confocal laser-scanning microscope is very efficient to obtain fluorescence clear optical sections in 2D or 3D for thick specimens [98].

Fluorophores are molecules that emit photons when excited. The emission wavelength is longer than the excitation wavelength. The fluorophores are usually bound to biological macromolecules such as antibodies, proteins or other specific ligands, comprising a fluorescent probe. Thus, when the fluorescent probe is added to the cell or biological tissue, the macromolecule will bind to a specific cell component and the fluorescent molecule has to bind to it. When the fluorophore is excited, it will emit photons from a position that is related to that cell component. The fluorescent probes are very sensitive and specific for molecules of interest. Another possible mechanism are to use fluorescent probes whose fluorescent characteristics depend on the microenvironment where they are inserted, such as the pH. Many fluorescent probes are inert and do not interfere in the cell's metabolism. One disadvantage of fluorophores is that they are photo-bleachable, which means that their intensity fades when exposed long times to light [100]. The modern fluorophores are very stable and have low photobleaching rates. Reducing laser intensity and exposure times also helps to minimize photobleaching. Furthermore, the pinhole aperture regulation is an important factor because the pinhole reduces the scattered light responsible for blurring and the light intensity in the detector. If a too small pinhole was used, either the excitation light intensity or the exposure time would have to be increased to produce a clear image, and consequently the possibility of photobleaching would also be increased. Thus, it is necessary to consider also this factor when choosing the pinhole aperture. Using a larger pinhole aperture reduces spatial resolution, increasing out-of-focus light and consequently blurring, but increases the fluorescent signal, so usually, it is appropriate to use a bit larger aperture [98]. The recommended pinhole

aperture is around 1 A.U. (airy unit), which is related to the circular aperture diffraction image and the airy disk.

In this work, the confocal laser-scanning microscopy was used to evaluate mouse fibroblast cells, either or not submitted to photo-treatment with different wavelengths and grown on substrates with different Young's modulus. The effects of PBMT in morphological or mechanical characteristics such as nucleus area, cell area, total actin, total actin density, the number of filaments, total branch length and the correlation between some of these parameters were verified.

4.1 Materials and methods

The confocal microscopy experiments were performed in the Department of Medical Biophysics, at the University of Toronto. Several University Health Network (UHN) facilities were used, including the Microfabrication Centre and the Advanced Optical Microcopy Facility.

4.1.1 Materials

Cells of mouse embryonic fibroblast cell culture, lineage 3T3, a standard fibroblast cell line, were used. The fibroblasts were grown in either plastic petri dishes with $58\ \mathrm{cm}^2$ growing area or round glass coverslips with $1.13\ \mathrm{cm}^2$ area, covered with a polyacrylamide gel inside wells from a 24 well plate.

The DMEM culture media used was supplemented with penicillin and streptomycin, L-glutamine, sodium pyruvate and 10% fetal bovine serum (FBS). The fibroblasts were grown in dishes and cultured in the incubator at $37\ ^{\circ}\mathrm{C}$ and 10% carbon dioxide. The media was replaced every $48\ \mathrm{h}$. The fibroblasts were sub-cultured when reaching 90% confluence, according to standard protocols.

Before the photo-treatment, samples were prepared for the experiment. Fibroblasts were separated from the culture dish with the cell dissociation reagent Accutase, from Thermo Fisher Scientific, centrifuged, resuspended in culture media, counted and placed on the appropriate growth substrate. After that, they were kept in the incubator under the same conditions as described above. Each sample received approximately 10 thousand fibroblasts.

Coverslips used for cell growing were covered with a polyacrylamide gel substrate. This was initiated to try to reproduce the natural cell microenvironment, which is an important factor to cell behavior [101], as it affects various parameters including cell shape and the interaction between the cells. The polyacrylamide gel substrate protocol was adapted from the Fischer and colleagues protocol [102] and was used and tested by the Department of Medical Biophysics previously [101]. The full protocol for gel manufacturing takes two to three days, and is presented in Appendix C with more detail.

Two gel stiffness were used, either $4\ \mathrm{kPa}$ or $16\ \mathrm{kPa}$, representing soft tissues such as brain and connective tissue, but not cartilage and bone, which have higher stiffness or Young's modulus. The cell stiffness for 3T3 fibroblasts vary between 3 and $12\ \mathrm{kPa}$ [103], thus, we chose one value close to each extreme.

A LED module, from Theralase Inc., was used for the fibroblast photo-treatment, emitting light either in the red or in the infrared range. Table 4.1 presents the parameters used in the experiment. Originally, the module was projected for a 96 well plate (see Figure 4.2, on the right); therefore, a diffusing paper was used on top of the plate, to homogenize the light, for use with 24 well plate. Figure 4.2, on the left, shows the well plate on top of the diffusing paper.

Table 4.1 – Light source parameters used in the fibroblast photo-treatment for the confocal microscopy experiment. The area considered to calculate the power and energy was the coverslip area ($1.13\ \mathrm{cm}^2$), as the module has several LEDs and is not a point source. Because of this reason, some values are not unique, but are represented by a range of values measured along the whole module.

Light source	LED	LED
Wavelength (nm)	625	808
Power density ($\mathrm{mW/cm^2}$)	100 to 130	110 to 140
Radiant power per well (mW)	113 to 147	124 to 158
Time of photo-treatment (s)	300	300
Energy density ($\mathrm{J/cm^2}$)	30 to 39	33 to 42
Radiant energy per well (J)	34 to 44	37 to 47

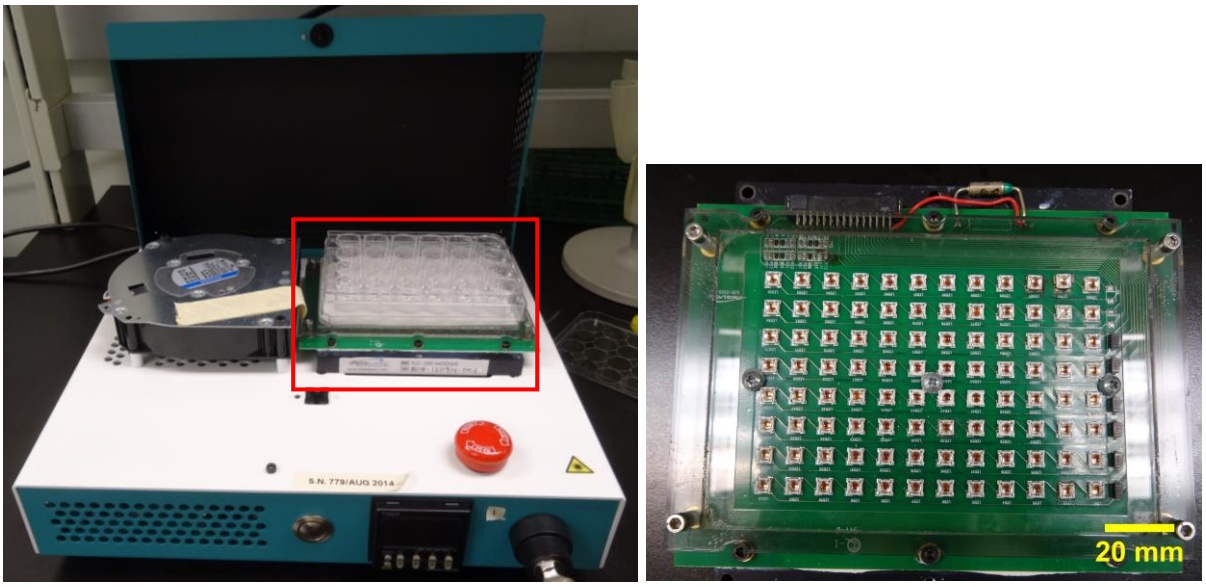

Figure 4.2: LED module used for fibroblast photo-treatment. On the left, the whole equipment, with the diffusing paper used to homogenize the light and the well plate on top of it. On the right, the detail of the LED module for 96 well plate, 625 nm, image from top. The red outline in the left image indicates the LED module, detailed in the image on the right.

A positive control experiment was executed to verify whether the technique used is sensitive to changes in the quantity and/or conformation of actin filaments. Here, by technique, we mean the process used in the experiment, from the fibroblast cell culture and treatment to the imaging. Cytochalasin D, from Sigma-Aldrich, was used as a positive control treatment, due to its known effects on actin filaments [104], [105].

There are many types of cytochalasins, usually originated from fungal metabolites, and with a molecular structure in common [106]. Cytochalasin binds to the fast-growing end of actin filaments, which stops association and dissociation of actin monomers in that end [105]. The effects range from interruption of the association/dissociation of filaments to disruption of actin filament and removal of stress fibers [105]. This might result in effects on cell function, such as inhibition of cell movements, of cell division and motility and changes in cell shape [104]. Some observable effects are rounding shape, inhibitions of membrane ruffling, formation of hairy structures, inhibition of actin filament elongation and decrease in viscosity of actin filaments, among others [104].

Rotsch and Radmacher [107] tested the effect of a few substances, including cytochalasin B and D, using various concentrations and treatment times, in 3T3 fibroblasts and NRK rat kidney epithelial cells. They show that for small concentrations ($< 2\ \mu mol/dm^3$), no effects are observed in the actin filaments up to $3\ h$ after the addition of the drug. For intermediate concentrations (from $5\ \mu mol/dm^3$ to $30\ \mu mol/dm^3$) the

stress fibers were disrupted in times ranging from $20\ \text{min}$ to $60\ \text{min}$. At last, for high concentrations ($> 50\ \mu\text{mol/dm}^3$) the cells detach from the substrate in less than $60\ \text{min}$. To evaluate the drug effect they used atomic force microscopy (AFM) measurements and fluorescence microscopy with fixed cells stained for actin. In other paper, Shen and colleagues [108] used fluorescence microscopy in fixed rat cardiac fibroblast cells to evaluate cell response to mechanical stretch and cytochalasin D to change cell condition.

The cytochalasin D formula is $C_{30}H_{37}NO_6$, weighting $507.62\ \text{Da}$ [106]. It is DMSO soluble at a concentration of $25\ \text{mg/mL}$ [109], thus, the $1\ \text{mg}$ vial content was dissolved in $40\ \mu\text{L}$ of DMSO, resulting a $49.25\ \text{mmol/dm}^3$ stock solution. A $1{:}100$ intermediate solution in DMEM was prepared and stored at $-20\ ^\circ\text{C}$, at dark. Final concentration used with fibroblasts were either $10\ \mu\text{mol/dm}^3$ or $30\ \mu\text{mol/dm}^3$, also diluted in DMEM. This does not exceed the 0.1% DMSO concentration in fibroblasts, otherwise, DMSO could affect the fibroblasts, instead of the cytochalasin D.

For all experiments, fibroblast fixation was completed with methanol-free 4% formaldehyde solution, after the specific times after treatment. Methanol-free solution was used to avoid actin filament disruption during the fixation process [110]. The fibroblast permeabilization was performed with Triton X-100 solution, from Sigma-Aldrich. Fibroblasts were stained with two different fluorescent probes: the *Alexa Fluor* 488 Phalloidin (AF488) for actin filaments and DAPI (4',6-Diamidino-2-Phenylindole, Dihydrochloride), for cell nucleus, both from ThermoFisher Scientific. Fluorescent probe stock solutions were dissolved in 1% BSA solution in PBS in order to reduce nonspecific background staining. The coverslips were mounted on glass slides using ProLong Gold antifade reagent, from ThermoFisher Scientific.

An inverted microscope, *Zeiss LSM700 confocal*, was used with a $40\times$ magnification objective, 1.4 numerical aperture and oil immersion. Solid-state lasers excited the samples with either $405\ \text{nm}$ (for DAPI) or $488\ \text{nm}$ (for AF488), and were collected in a different channel. Signal from the AF488, related to the actin filaments will be called as *AF488 channel* and signal from DAPI, related to the cell nuclei will be called as *DAPI channel*. The acquisition software was the *LSM Zen* 2012, which controls the acquisition parameters. The parameters used are presented bellow:

- Pinhole 1 A.U.;

- 488 nm channel gain: 400 for cytochalasin experiments, and 435 otherwise;
- 405 nm channel gain: from 700 to 800;
- Each pixel is the average of two measurements.

4.1.2 Methods

On the day of the experiment, the fibroblasts were seeded in coverslips with gels, which were placed in a 24 well plate. The photo-treatment was done either 6 h or 24 h after the plating process. This incubation time was chosen to control fibroblast proliferation and keep fibroblasts in a monolayer.

The experiments were numbered according to the parameters used, which are presented in Table 4.2. Some experiments were replicated and others were not. For each replication, the confocal images were acquired over one or two days, depending on the number of appropriate coverslips obtained. For each experiment, fibroblasts were divided into two groups: negative control (no PBMT) and photo-treatment (PBMT), with six coverslips in each group. Both groups passed through the same procedures, except for the photo-treatment, whose parameters are presented in Table 4.1. After photo-treatment, the fibroblasts were incubated during a specific period of time, 5 min, 1 h or 24 h. After that, the fibroblasts were fixed, permeabilized and stained. Appendix D shows the full protocols for this process. The coverslips were mounted on glass slides, kept at room temperature for 24 h to 72 h to dry and then stored in the refrigerator. The fibroblasts were imaged using the confocal microscope, with parameters shown above. For each coverslip 8 to 30 images were obtained with different fields of view. Figure 4.3 shows the experiment protocol schematized.

Table 4.2 – Experimental configuration. For all experiments, there was always a photo-treatment group and a control group. The experiment replications mean experiments performed with the same parameters, but on different days. This was done to verify reproducibility. Experiment 13 was a cytochalasin D experiment with fixation after 1 h, but the fibroblasts were not in good conditions, so it was discarded.

Experiment #	Gel (kPa)	Treatment	Time between cell seeding and treatment	Incubation time (between treatment and fixation)	Experiment replications
1	4	PBMT, 625 nm	24 h	5 min	3
2	4	PBMT, 625 nm	24 h	1 h	3
3	4	PBMT, 625 nm	6 h	24 h	1
4	16	PBMT, 625 nm	24 h	5 min	1
5	16	PBMT, 625 nm	24 h	1 h	1
6	16	PBMT, 625 nm	6 h	24 h	1
7	4	PBMT, 808 nm	24 h	5 min	1
8	4	PBMT, 808 nm	24 h	1 h	1
9	4	PBMT, 808 nm	6 h	24 h	2
10	16	PBMT, 808 nm	24 h	5 min	1
11	16	PBMT, 808 nm	24 h	1 h	1
12	16	PBMT, 808 nm	6 h	24 h	1
14	4	Cytochalasin D	24 h	40 min	1

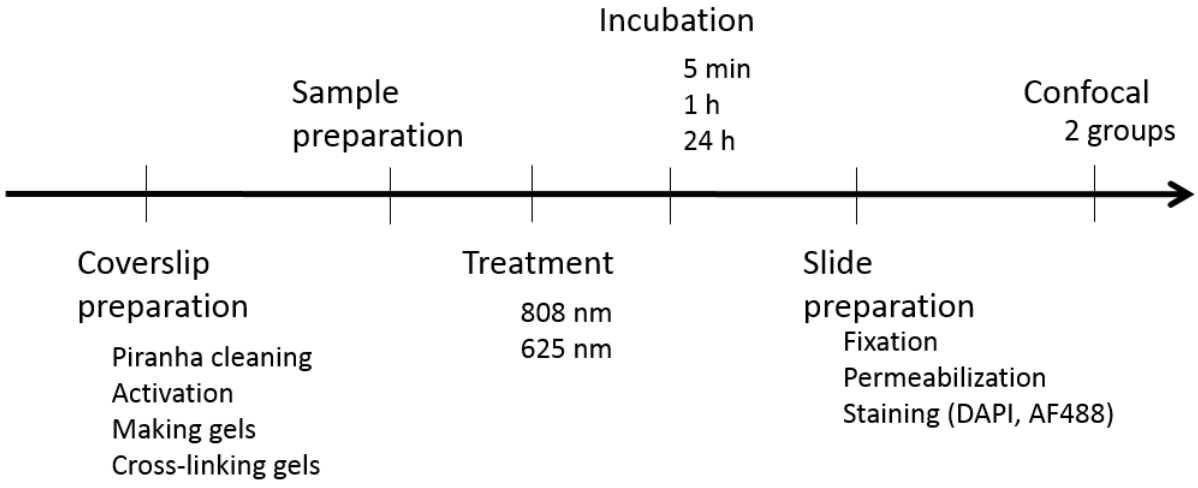

Figure 4.3: Flowchart of the experimental protocol, from the coverslip preparation to fibroblast photo-treatment and measurement.

For the positive control experiment, using cytochalasin D, only the $4\ \mathrm{kPa}$ gel was used and two cytochalasin concentrations ($10\ \mu\mathrm{mol/dm^3}$ and $30\ \mu\mathrm{mol/dm^3}$). As said before, those concentrations do not exceed the permitted solvent (DMSO) concentration in cells, nevertheless, to ensure the effect was not from DMSO, control samples were prepared with the corresponding amount of DMSO in substitution to the cytochalasin solution, for both concentrations. Thus, there were five groups: control (no treatment), DMSO "$10\ \mu\mathrm{mol/dm^3}$", DMSO "$30\ \mu\mathrm{mol/dm^3}$", cytochalasin D $10\ \mu\mathrm{mol/dm^3}$ and cytochalasin D $30\ \mu\mathrm{mol/dm^3}$, with two coverslips for each group.‡ The fibroblasts were fixed $40\ \mathrm{min}$ after addition of the drug. After that, the protocol followed was the same.

Around 2000 images were acquired with those experiments, considering all groups and all regions. The images are in 8-bit format, which means that each image pixel has grey levels ranging from 0 to 255. Each image has two channels, one for the actin filaments (AF488 channel) and the other for nuclei (DAPI channel). For each field of view in the image, a few data acquisitions were carried out in different depths of the sample. Thus, each image is composed of multiple optical sections of the sample, and each optical section corresponds to the image acquired in a different depth of the field of view.

4.1.2.1 Analysis

The data analysis is not trivial. Little is found in literature, and many of the identified papers provided insufficient detail on the analysis methods and hence could not be reproduced here. Some authors made the filament identification manually [111], [112]. Some papers refer to experiments with individual filaments, polymerized artificially, which changes the characteristics of the filament network and consequently its identification [28], [112], [113]. Other authors say that the analysis was done through program development [114] or the use of existing programs [115], but these programs refer to particular sample aspects, which are not present in our samples.

The software *ImageJ* (NIH) [116] is widely used for image analysis, as it is very powerful and a public domain program. In addition, it is open source, which enables people to develop tools for it and make them available to the scientific community.

‡ The DMSO groups have their concentration in quotes, because that is not the DMSO concentration, but the amount of DMSO in the cytochalasin samples with those concentrations.

Typically, these tools are in the form of plugins. A few plugins and programs available are designed for actin filament analysis:

- *Jfilament* [117] is an *ImageJ* plugin, which was developed for targeting and tracking filaments over time. This is not our case as we have static cell images.
- *FibrilTool* [118] is an *ImageJ* plugin, which was developed to determine anisotropy of the filaments, as well as its average orientation in cells. This plugin is ineffective for our case because there is no reason to believe that the photo-treatment causes a preferred orientation for filaments. Although there is evidence that this effect is possible in collagen [119] for example, in our study the light was not polarized, so it would not be possible to obtain this differentiation. Furthermore, this plugin requires manual selection of regions of interest, which is not feasible because of the amount of images we have. Also, the analysis is subjective, dependent on the person who chooses the regions of interest and we avoided that.
- *FiloDetect* [120] is a *MATLAB* program that was developed to detect filopodia, which are small filaments that are on the cell edge, growing away from the cell. This program requires individual cells, which means that the cells have to be segmented before analysis. We could not find an automated way to segment the cells and manual segmentation would be unviable.

Unfortunately, these plugins/programs are inadequate for our study; hence, other sets of *ImageJ* tools and plugins were used for the analysis. We selected tools/plugins that could be used in the whole image, without the need of regions of interest or cell segmentation, and adapted them for the acquisition of quantitative parameters related to the cells and their actin filaments. The parameters analyzed were: nucleus area, cell area, total actin, total actin density, the number of filaments and total branch length. The correlation between some of these parameters was also evaluated. The programs for analysis were developed using *ImageJ* tools/plugins within the *MATLAB* software, using *Miji* [121]; this combination works very well, because *ImageJ* has many useful tools/plugins and the steps can be automatized with *MATLAB* scripts. Furthermore, the results can be handled directly without great difficulty.

Before the analysis, all images were examined, just to remove fibroblasts in division and superposed fibroblasts from the image. Specific selection of regions of interest

was not necessary due to an important assumption that was made for the analysis. The assumption was that the "amount of cells entering" the image and the "amount of cells going out" of the image were the same. This means, for each cell in the image border and not completely inside the image it is assumed that there is another cell outside the image, which has an equal portion inside the image, compensating for the portion outside the image from the first cell.

Two tools were widely used in the analysis. The maximum intensity projection (MIP) is a tool used to turn a volumetric dataset into a 2D projection. The grey level of each resulting pixel corresponds to the maximum grey level found in all optical sections for that specific (*x*, *y*) pixel position. The other tool is the threshold, which is a grey level set at a limit, therefore, all pixels that have grey level values equal or greater than the threshold are considered valid, and all pixels that have grey level values smaller than the threshold are considered invalid. Usually, when a threshold is set, all valid pixels have their grey levels set to zero (black) and invalid pixels set to 255 (white). However, other possible use for the threshold tool is to maintain the grey level values for valid pixels and change only the grey levels of invalid pixels to zero.

The nucleus area and nucleus counting were determined using the DAPI channel. The sequence of steps used in this analysis were:

1. To apply MIP in the image, as the example seen in Figure 4.4, on the left;
2. To set the threshold using the *IsoData* [122] method and turning the image into black and white. Figure 4.5, on the left, shows an example of a nucleus image, after MIP and threshold;
3. To use the *ImageJ* tool *Analyze particles*. This tool finds the edges of all structures in the image and, for each structure, determines its area. Figure 4.5, on the right, shows the outlines of the structures found in Figure 4.5 left image.

The number of structures found was considered as the number of nuclei in the image and consequently the number of cells in the image. The area of each structure was considered as the **nucleus area**. Only structures larger than $60\ \mu m^2$ were considered nuclei. Smaller structures were not counted because usually, they are debris present in the image or a part of a nucleus in the edge of the image. Figure 4.5, on the right, shows the outlines of the counted structures; note that the small structures on the left figure were not considered. The nuclei in the image borders need a criterion to be

counted or not. A few different minimum sizes were tested and compared to manual nucleus count, for some images. The minimum size of $60\ \mu m^2$ resulted a good value to count all nuclei inside the image (with rare exceptions) and resulted in a good compromise for evaluating the true number of cells in the image.

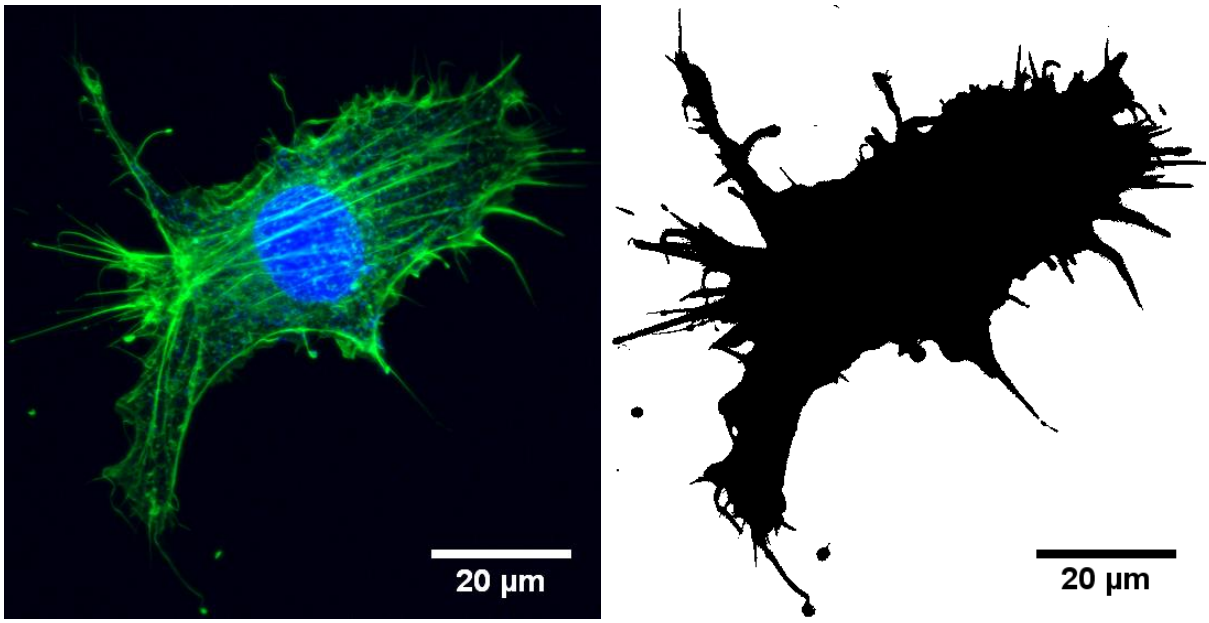

Figure 4.4: Example of fibroblast image. On the left, the original image in grey levels, for both channels, green for AF488 (actin filaments) and blue for DAPI (cell nucleus), this image is a MIP. On the right, the same image after threshold and conversion to black and white, only for the AF488 channel.

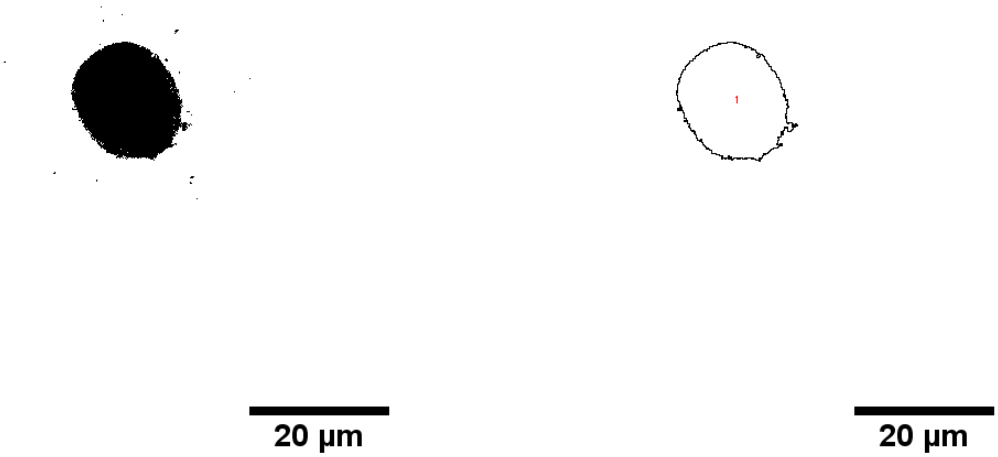

Figure 4.5: Example of nucleus counting. On the left, the image after threshold and conversion to black and white, only for the DAPI channel. The original image was a MIP. On the right, the outline of the counted particles is shown. Note that small black particles were not counted, because the minimum size was set to $60\ \mu m^2$.

For the analysis of cell area, it was assumed that the actin filaments are terminating on the cell surface [24], thus, if the cell area in which there are actin filaments is measured, the result will be very close to the cell area. Therefore, the AF488 channel was used to determine the cell area. The procedures used were:

1. To apply MIP in the image, as the example seen in Figure 4.4, on the left;
2. To set the threshold as 4 grey level units and turning the image into black and white. This threshold value was determined by testing a few different values across a few images collected. Figure 4.4, on the right, shows the image after threshold and conversion to black and white;
3. To use the *ImageJ* tool *Measure*: this tool returns the image area and the black area percentage (the area that cells occupy). The multiplication of these data results the area that cells occupy;
4. To calculate the average **area for the cells** in the image. This is the ratio between the total area that cells occupy and the number of cells in the image.

The area uncertainty was estimated by changing the threshold in 2 grey levels up and down, so the uncertainty was determined as the half of the difference between the maximum (Ar_{max}) and the minimum (Ar_{min}) area, thus $\sigma_{Ar} = (Ar_{max} - Ar_{min})/2$.

The total amount of actin was estimated by the fluorescence intensity, more precisely the image grey levels. Therefore, the AF488 channel was used to determine the total actin. The procedures used were:

1. To calculate the sum of the grey levels of all valid pixels according to threshold (the same value of threshold that was used for the cell area determination), for all optical sections;
2. To calculate the **total amount of actin** by cell, which means to divide the sum of the image grey levels by the number of cells in the image;

The uncertainty was estimated in a similar way as for the cell area. The threshold was changed in 2 grey levels up and down, and the uncertainty was determined as the half of the difference between the maximum (TA_{max}) and the minimum (TA_{min}) total actin, thus $\sigma_{TA} = (TA_{max} - TA_{min})/2$.

The **total actin density** was calculated by dividing the total amount of the actin by the cell area. This parameter is interesting because it does not depend on the number of

cells, as the number of cells divides both parameters used to calculate the density, so it is canceled. Nevertheless, the value obtained for each image was attributed to all cells present in that image.

The number of filaments and total branch length were analyzed based on the AF488 channel. A series of tools and plugins available in *ImageJ* were used for the analysis of these parameters. The procedures used were:

1. To apply an enhancement filter to the image, using an *ImageJ* tool. Table 4.3 represents the matrix used in this filter. The application of this filter replaces each pixel value by an average between the grey level values of surrounding pixels, with the weights represented in the matrix. This filter was applied in each optical section individually. Figure 4.6, on the left, shows the image after the filter application, for a central optical section.
2. To set the threshold to 90 and converting the image into a black and white image. This threshold value was determined by testing a few different values. The resulting image after this process is shown in Figure 4.6, on the right.
3. To use the *Skeletonize 3D* plugin, which finds the center lines of the image object [123]; it usually marks the object geometrical characteristics. Figure 4.7, on the left, shows the image following this plugin application.
4. To analyze the generated skeleton with the plugin *Analyze skeleton 3D* [124]. This plugin evaluates the twenty-six surrounding pixels (a three-pixel-wide cube, centered on the pixel that is being tagged), and finds its neighbors that are not background pixels (black pixels are neighbors, and white pixels are background). Then, the plugin tags each image pixel based on the neighbors found. The central pixel is classified as *end-point*, when there are less than two neighbors, and is represented in blue; *slab*, when there are exactly two neighbors, represented in orange; or *junction*, when there are more than two neighbors, represented in purple. Figure 4.7, on the right, shows the image after the skeleton analysis. The plugin also identifies the ramifications of each branch and calculates the average branch length.

Table 4.3 – Matrix that represents the enhancement filter applied to the image for the number of filaments and total branch length analysis.

-1	-1	-1	-1	-1
-1	-1	-1	-1	-1
-1	-1	24	-1	-1
-1	-1	-1	-1	-1
-1	-1	-1	-1	-1

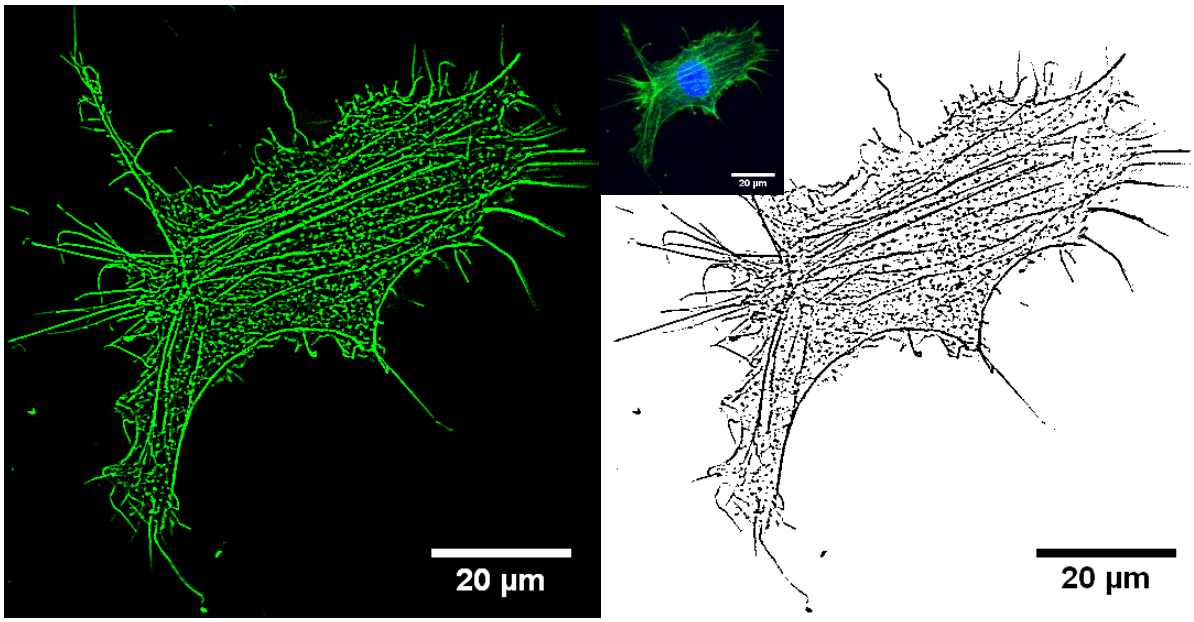

Figure 4.6: Example of filament analysis. On the left, the image after the filter application used only in the AF488 channel. On the right, the same image after threshold and conversion to black and white. Both images are from a central optical section of the image. The small inlet image on the top center is the MIP presented in Figure 4.4.

The average branch length was used to determine the **total branch length** (TBL) that is the total length of a branch, including all ramifications. The multiplication of the average branch length by the number of ramifications in a branch is the TBL. The number of cells in the image was not considered for this parameter. That means that the TBL is for the image, not for the cell.

The sum of all ramifications, from all branches, independent on the branch length, is the **number of filaments**. The number of filaments per cell was also determined, through the division of the number of filaments by the number of cells.

The uncertainty of the number of filaments was also calculated varying the threshold value. In this case, the threshold was changed in 5 grey levels up and down. The uncertainty was determined as the half of the difference between the maximum (NF_{max}) and the minimum (NF_{min}) number of filaments, thus $\sigma_{NF} = (NF_{max} - NF_{min})/2$.

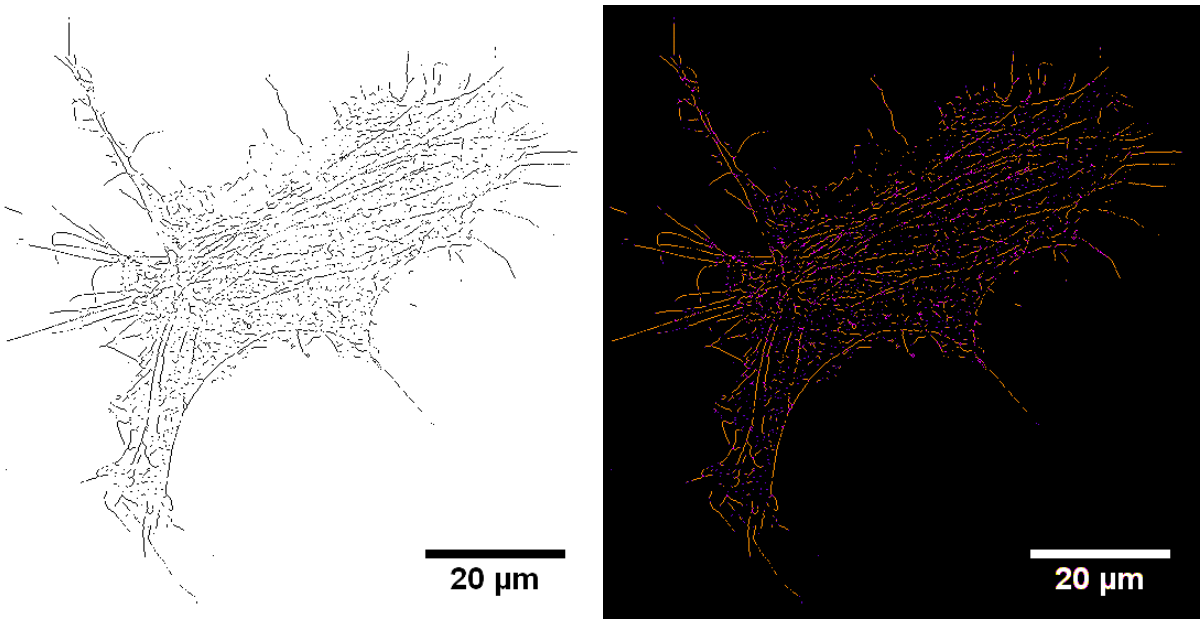

Figure 4.7: Example of filament analysis. On the left, the image after the application of the *ImageJ Skeletonize 3D* plugin. On the right, the same image after the application of the *ImageJ Analyze skeleton 3D* plugin. Blue pixels represent *end-point*s, which are pixels with less than two neighbors; orange pixels represent *slab*s, which are pixels with exactly two neighbors; and purple pixels represent *junction*s, which are pixels with more than two neighbors. Both images are from a central optical section of the image.

Once obtained these parameters, a comparison between the effect of different treatments (cytochalasin D or PBMT) was done, comparing the distribution and median of control and treated groups. The distribution comparison was completed using boxplots of all data. Each experiment (as shown in Table 4.2) resulted in one boxplot. For the PBMT experiments, the results of all experiments were compared using relative parameters and relative variation between the control and photo-treated groups. The relative parameter was defined as the ratio between the photo-treated and control group medians. The relative variation is defined as the difference between the photo-treated and control medians, divided by the control median.

The two-sample rank sum test [84] was used to compare photo-treated and control groups, for all cell parameters, for all experiments, (for more details regarding the two-sample rank sum test, see Appendix B). This test was chosen because it can be used for any data distribution. As the following section shows, some of our data do not seem

to have a normal distribution, so this test was more adequate. Moreover, the test was used because it is almost unaffected by outliers [84]. The Student's *t*-test was used to determine if the relative variation of each cell parameter was different from zero, which means to evaluate if the PBMT caused changes in that parameter. Furthermore, the Kruskal-Wallis test was used to compare the relative variation for each cell parameter and determine the influence of the photo-treatment parameters (wavelength, time after treatment and gel stiffness) in the results. This test is the extension of the two-sample rank sum test for more than two samples and was applied three times – one for each PBMT parameter. The first time, all relative cell parameters from the samples that were photo-treated with the same wavelength were considered as one sample, independent of the time after treatment or the gel stiffness; thus, there were two samples one for $625\ \mathrm{nm}$ and the other for $808\ \mathrm{nm}$. The second time, the same was executed with the time after treatment, resulting in three samples, for $5\ \mathrm{min}$, $1\ \mathrm{h}$, and $24\ \mathrm{h}$; and the third time, for gel stiffness, resulting in two samples, for $4\ \mathrm{kPa}$ and $16\ \mathrm{kPa}$. The samples were considered to be different when $p < 5\%$, for all tests.

Besides that, for some parameters (cell area, total actin, total branch length and the number of filaments), the correlation was tested for each pair of parameters, which resulted in six comparisons. Instead of the more traditional Pearson's correlation coefficient, the Spearman's coefficient was chosen for the analysis. The Spearman's correlation coefficient [125] was used due to its lower sensitivity to outliers, as it uses ranks to determine the correlation between data. Moreover, this coefficient was used because it detects monotonic relationships, not just linear correlations, as for the Pearson's correlation coefficient. The coefficient of determination (that is the correlation coefficient squared) was also calculated; it can be interpreted as the percentage of variation in one variable that might be explained by the variation in the other variable [126]. At last, for the pairs with high correlation coefficient, a linear regression was fitted in the correlation graph using the least square method. Both coefficients and the slopes were compared between photo-treated and control groups.

To calculate the correlation coefficient, data from all images from a same group were used. Most of the parameters have an average or a median value for the image and, in this case, the value used for the analysis was this average or median value. As the number of fibroblasts per image vary too much between images, the average/median value of the parameter in the image was repeated as many times as the number of

fibroblasts in that image. This way, the correlation analysis is weighted by the number of fibroblasts measured.

4.2 Results

The coverslips of each experiment replication were imaged on day one or two in the confocal microscope. The confocal parameters used were the same, for all images. Ideally, data from each imaging day, from the same experiment replication could be analyzed together. That is because the samples were equivalent and manipulated together. When data from different imaging days were compared they were incompatible for many cases. Some attempts were made to try to assemble these data. The first one was to use the threshold to make data compatible between days: by using slightly different thresholds for images from different days. Unfortunately, this was ineffective. The other approach was to use the DAPI channel histogram to normalize the AF488 channel data. Again, this was ineffective, because the DAPI channel histograms vary between images, within the same imaging day. In conclusion, there are factors that change between different imaging days and that are not controllable. Thus, only data from one imaging day was analyzed together. Images, graphs or tables that have one replication appearing twice refer to these different confocal imaging days. In most of these situations, the imaging day or the imaging month and day are shown. For other situations, the letters *A* and *B* are used to denominate the first and second imaging days, respectively.

To determine the best threshold to be used for each parameter analyzed (cell area, total actin, the number of filaments and total branch length), a study was performed with the cytochalasin experiments. One threshold level was determined for cell area and total actin parameters and another level for the filament parameters. Five different thresholds were tested for the control group of the experiment 14.1. For the cell area and total actin, the thresholds tested were grey levels 2, 4, 6, 8 and 10, with the results shown in Figure 4.8. Note that the data distribution is similar, comparing the different thresholds used, which occurred for both parameters analyzed. Furthermore, the values of the measured parameter decrease as the threshold increases, as expected. That means that the threshold choice is almost arbitrary. Thus, with these graphs and analyzing the original images, after the application of each of these thresholds, we decided to use the threshold of 4 to the images when analyzing cell area and total

actin, with uncertainty of 2. For the number of filaments and total branch length, the threshold values tested were 75, 80, 85, 90 and 95, with the results shown in Figure 4.9. Note that here, again, the data distribution is similar, comparing the different thresholds used, and for both parameters analyzed. Furthermore, the values of the measured parameters decrease as the threshold increases. In this case, we decided to use the threshold of 90 to the images when analyzing the number of filaments and total branch length, with an uncertainty of 5.

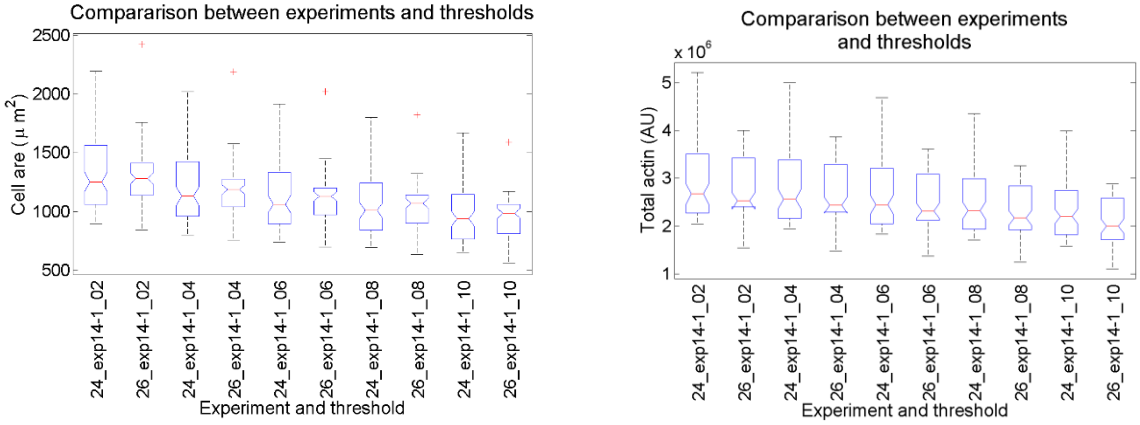

Figure 4.8: Threshold study for cell area, on the left, and total actin, on the right. Just control groups were tested, from two different imaging days of experiment 14.1. The names in the horizontal axis represent the confocal imaging *day*, the *experiment* and, the last two digits, the *threshold used* (2, 4, 6, 8 and 10).

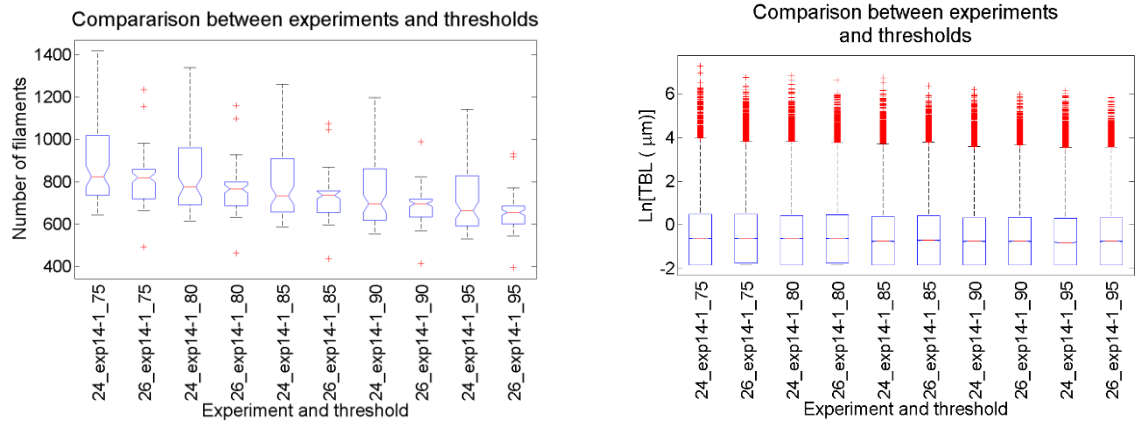

Figure 4.9: Threshold study for the number of filaments, on the left, and total branch length, on the right. Just control groups were tested, from two different imaging days of experiment 14.1. The names in the horizontal axis represent the confocal imaging *day*, the *experiment* and the *threshold used* (last two digits: 75, 80, 85, 90 and 95).

4.2.1 Cytochalasin D positive control experiments

As the use of cytochalasin D changes the cytoskeleton sharply, the group (positive or negative control) to which the fibroblast belongs is easily identifiable visually. Figure 4.10 shows typical images of a control sample, on the top left, a DMSO "$10\ \mu mol/dm^3$" sample, on the top right, and a cytochalasin D $10\ \mu mol/dm^3$ sample, on the bottom. The cytochalasin action is clear, even just visually: the fibroblasts have not filopodia; the fibroblast edges are not as clear as they are in the fibroblasts not treated with cytochalasin; the connection with the neighbor fibroblasts is reduced, and the actin is concentrated just in some fibroblast areas, instead of being distributed along the whole fibroblast.

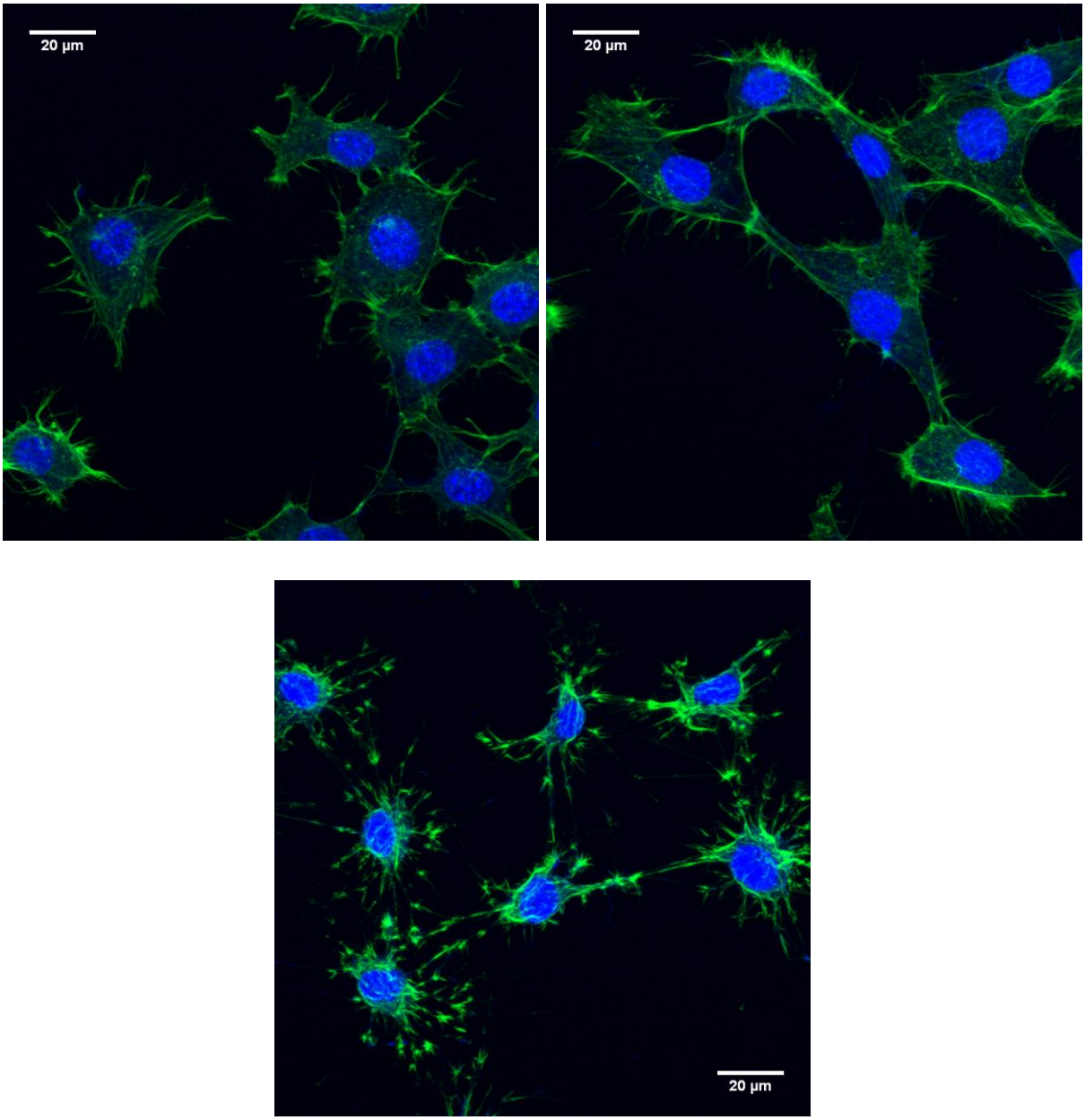

Figure 4.10: Example of images obtained with confocal microscopy. Fibroblasts from the negative control group are on the top left, DMSO "$10\ \mu mol/dm^3$" group, on the top right and cytochalasin D $10\ \mu mol/dm^3$ on the bottom. All images are MIP for both channels, from experiment 14.1, first confocal imaging day.

The following graphs show the results for the parameters analyzed for the positive control experiments. Figure 4.11 shows the results for nucleus area on the left and cell area on the right. Figure 4.12 shows the results for total actin on the left, and total actin density on the right. At last, Figure 4.13 shows the results for total branch length on the top, and number of filaments on the bottom. Table 4.4 shows the results for the two-sample rank sum test, for all parameters analyzed. The comparison was always performed with the negative control sample, which appears as *con_00uM* in the graph labels. For all parameters, the cytochalasin D sample data are incompatible with the

negative control sample data, except for the number of filaments of one of the $30\ \mu mol/dm^3$ sample. Regarding the total actin, for the cytochalasin D $30\ \mu mol/dm^3$ sample, although both samples are incompatible with the control sample, one of them has its median increasing when compared with the control median, while the other has its median decreasing when compared with the control median. This might indicate that there are other factors acting in the fibroblasts, besides the factors that we controlled. This means that we have to be careful with the interpretation of the results, because some modifications might be due to unknown factors, rather than to the factors we are interested in. As far as the DMSO sample data are concerned, some are compatible and some are not. Most of them have data from one confocal imaging day compatible and for the other day not. The three exceptions are: DMSO "$10\ \mu mol/dm^3$" for total actin density (data from both days incompatible) and for total branch length (data from both days compatible); and DMSO "$30\ \mu mol/dm^3$" for nucleus area (data from both days compatible). Therefore, we can conclude that the changes in the cytoskeleton are mainly caused by the cytochalasin D.

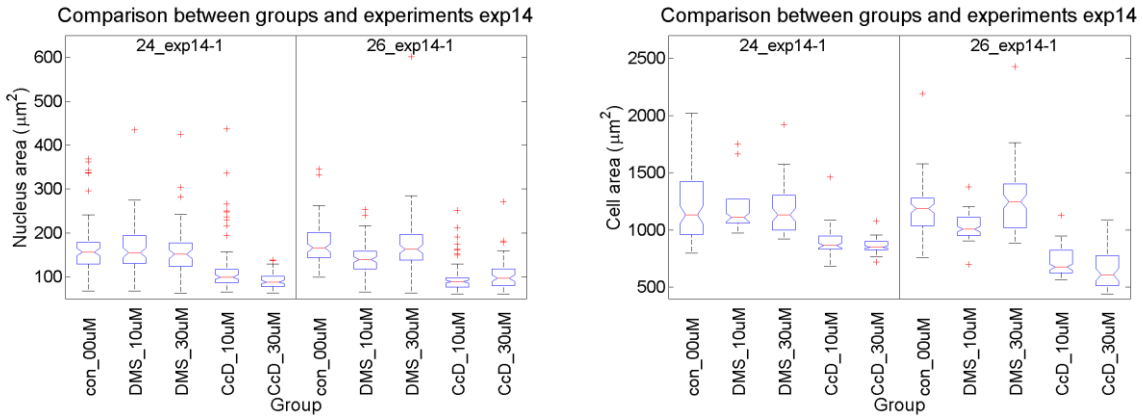

Figure 4.11: Boxplot for the nucleus area, on the left, and cell area, on the right, for the experiment 14.1. Experimental parameters are shown in Table 4.2. Data represented in the graph are data of fibroblasts from different images. Each graph was divided into regions that represent different imaging days. The label on top of each region describes the only replication 14.1 and the numbers before it represent the confocal imaging day. In the horizontal axis label, *con_00uM* refers to the negative control group; *DMS_10uM* refers to the DMSO "$10\ \mu mol/dm^3$" group; *DMS_30uM* refers to the DMSO "$30\ \mu mol/dm^3$" group; *CcD_10uM* refers to the cytochalasin D $10\ \mu mol/dm^3$ group; and *CcD_30uM* refers to the cytochalasin D $30\ \mu mol/dm^3$ group.

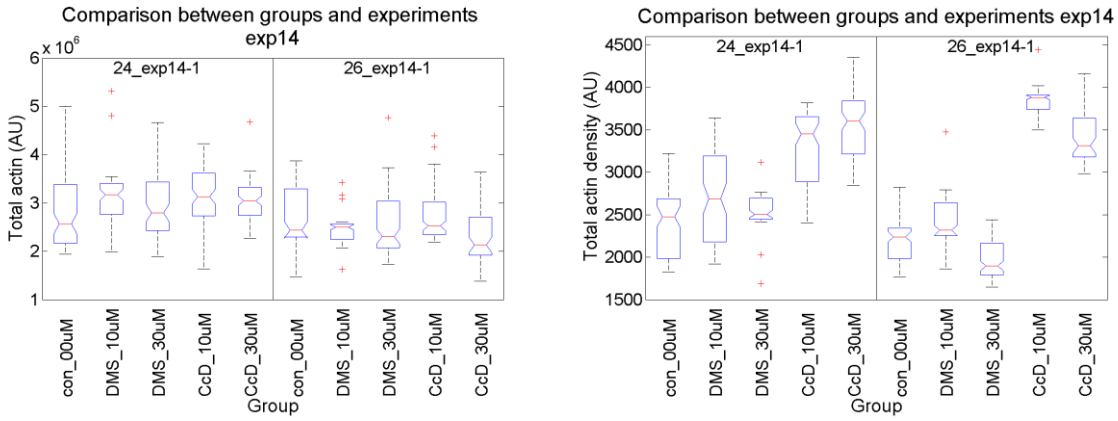

Figure 4.12: Boxplot for the total actin, on the left, and total actin density, on the right, for the experiment 14.1. Experimental parameters are shown in Table 4.2. Data represented in the graph are data of fibroblasts from different images. Each graph was divided into regions that represent different imaging days. The label on top of each region describes the only replication 14.1 and the numbers before it represent the confocal imaging day. In the horizontal axis label, *con_00uM* refers to the negative control group; *DMS_10uM* refers to the DMSO "10 μmol/dm^3" group; *DMS_30uM* refers to the DMSO "30 μmol/dm^3" group; *CcD_10uM* refers to the cytochalasin D 10 μmol/dm^3 group; and *CcD_30uM* refers to the cytochalasin D 30 μmol/dm^3 group.

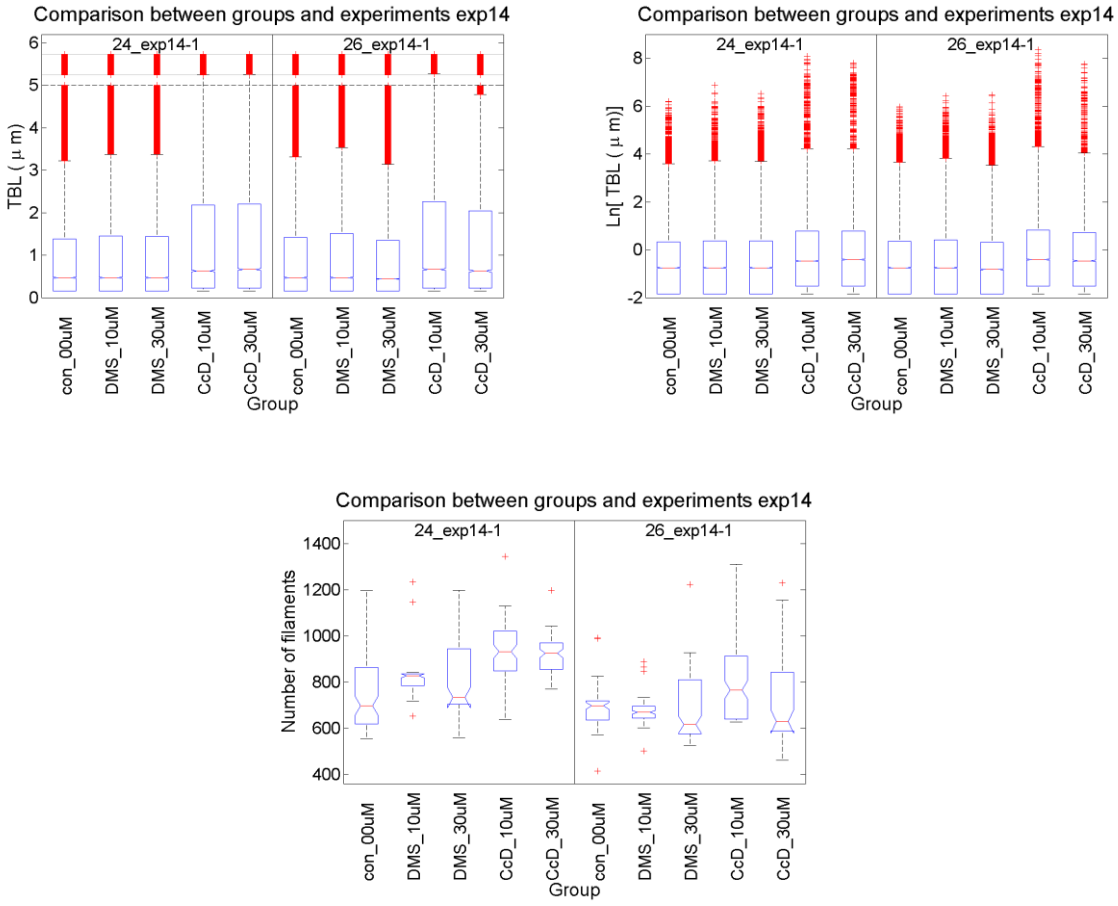

Figure 4.13: Boxplot for the experiment 14.1, for the total branch length (TBL) on the top, and the number of filaments, on the bottom. Experimental parameters are shown in Table 4.2. Data represented in the graph are data of multiple images, for total branch length and for fibroblasts from different images, for the number of filaments. On the top left graph, the vertical axis was compressed after $5\ \mu m$ to facilitate the visualization of the boxes. Thus, data above $5\ \mu m$ are compressed and not in scale. On the top right graph, the vertical axis has a logarithmic scale. Each graph was divided into regions that represent different imaging days, the label on top of each region describes the only replication 14.1 and the numbers before it represents the confocal imaging day. In the horizontal axis label, *con_00uM* refers to the negative control group; *DMS_10uM* refers to the DMSO "$10\ \mu mol/dm^3$" group; *DMS_30uM* refers to the DMSO "$30\ \mu mol/dm^3$" group; *CcD_10uM* refers to the cytochalasin D $10\ \mu mol/dm^3$ group; and *CcD_30uM* refers to the cytochalasin D $30\ \mu mol/dm^3$ group.

Table 4.4 – Results of the comparison between the negative and positive control groups with the two-sample rank sum test, for all parameters analyzed. The symbols "+", "=" and "-" indicate that the positive control group median is larger, equal or smaller when compared to the negative control group median, respectively. The numbers represent the p-values, in percentage, the sample data were considered incompatible when $p < 5\%$. Incompatibility is represented in red, and compatibility in green.

	DMSO "10 μmol/dm^3"		DMSO "30 μmol/dm^3"		Cytochalasin D 10 μmol/dm^3		Cytochalasin D 30 μmol/dm^3	
Nucleus area	52-	0-	57-	35-	0-	0-	0-	0-
Cell area	42-	0-	77-	2.8+	0-	0-	0-	0-
Total actin	0.06+	18+	7+	2.4-	0.51+	3.3+	0.17+	0.06-
Total actin density	0.09+	0.05+	25+	0-	0+	0+	0+	0+
Number of filaments	0+	52-	0.94+	24-	0+	0+	0+	85-
Total branch length	40=	17=	25=	0-	0+	0+	0+	0+

4.2.1.1 Correlation analysis

Figure 4.14 shows the correlation coefficients, on the left, and the coefficients of determination, on the right, for experiment 14.1. A linear regression was fitted for the graphs with a coefficient of determination above 0.5. This means that, for the pair of parameters that have most of the coefficients of determination of the different groups above 0.5, the linear regression was fitted. Therefore, the linear regression was fitted to the graphs of cell area versus total actin (noted as TA/Ar or Ar vs TA), cell area versus the number of filaments (NF/Ar or Ar vs NF) and the number of filaments versus total actin (TA/NF or NF vs TA).

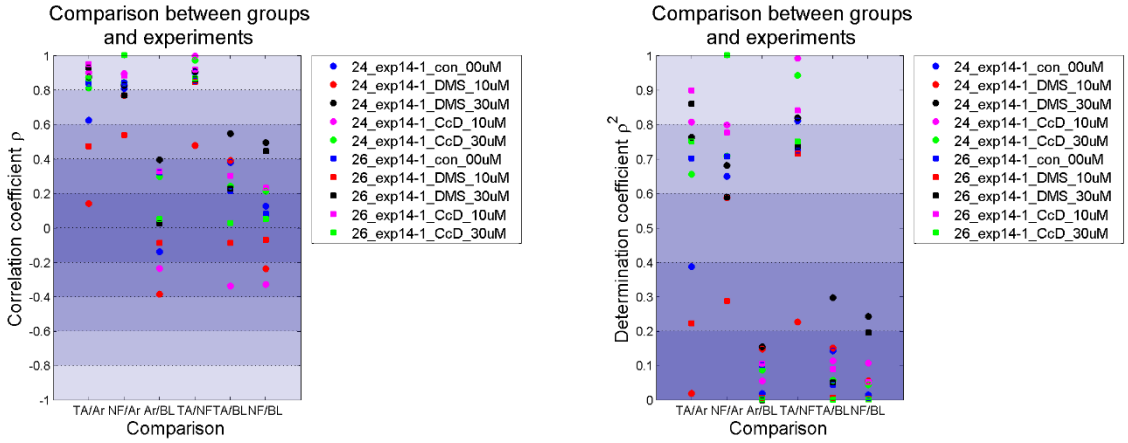

Figure 4.14: Correlation coefficient, on the left, and coefficient of determination, on the right, for experiment 14.1. In the horizontal axis, the initials refer to the parameters correlated, so, TA means total actin, Ar means cell area, NF means the number of filaments and BL means total branch length. In the legend, *con_00uM* refers to the negative control group; *DMS_10uM* refers to the DMSO "10 $\mu mol/dm^3$" group; *DMS_30uM* refers to the DMSO "30 $\mu mol/dm^3$" group; *CcD_10uM* refers to the cytochalasin D 10 $\mu mol/dm^3$ group; and *CcD_30uM* refers to the cytochalasin D 30 $\mu mol/dm^3$ group. The numbers before the experiment replication refers to the confocal imaging day.

Figure 4.15 shows the results for the slope of the linear regression fit for the correlation graphs. The cell area versus total actin slopes are on the top left, the cell area versus the number of filaments slopes are on the top right, and the number of filaments versus total actin slopes are on the bottom. If the error bars do not overlap, the slopes were considered incompatible, otherwise, they were considered as compatible. The slopes for the correlation between cell area and the number of filaments show a systematic behavior: for the cytochalasin D groups, the slopes are smaller than for the control group. Furthermore, for this correlation, the coefficients (correlation and determination) for cytochalasin D groups are higher than for the control groups. Indeed, both effects (higher correlation coefficient and smaller slope) can be seen in the correlation graph, shown in Figure 4.16. For this case, cytochalasin D slopes from the two concentrations are compatible and almost all DMSO sample and control slopes are compatible. It is worth mentioning that slopes from similar samples should be compatible, however, this is not always observed. This might indicate that there are other factors acting in the fibroblasts, not just the factors that we controlled. This means, again, that we have to be careful with the interpretation of the results, as modifications might be caused by unknown factors instead of the factors we are interested in.

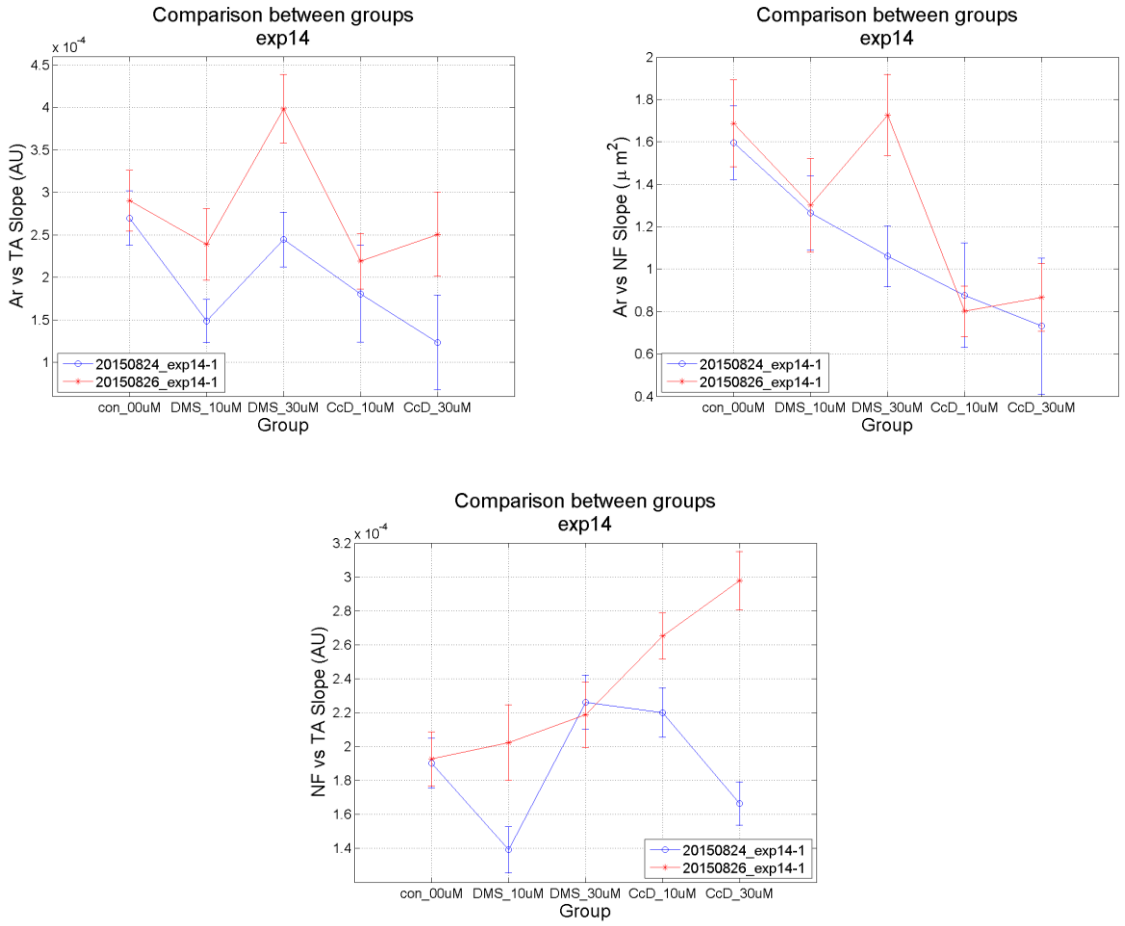

Figure 4.15: Graphs of the slopes of linear fittings for experiment 14.1. On the top left, cell area versus total actin correlation; on the top right, cell area versus the number of filaments; and on the bottom, the number of filaments versus total actin. The legend describes the confocal imaging date (year, month and day). In the horizontal axis label, *con_00uM* refers to the negative control group; *DMS_10uM* refers to the DMSO "$10\ \mu mol/dm^3$" group; *DMS_30uM* refers to the DMSO "$30\ \mu mol/dm^3$" group; *CcD_10uM* refers to the cytochalasin D $10\ \mu mol/dm^3$ group; and *CcD_30uM* refers to the cytochalasin D $30\ \mu mol/dm^3$ group. The error bars represent two times the slope uncertainty, thus, if the error bars overlap, the slopes were considered as compatible. Otherwise, they were considered incompatible. The lines are drawn just as a guide for the eyes.

For the total branch length measurements, we found no tendencies within groups or correlations with other parameters. It seems that the total branch length is an independent parameter. Because of that, some analysis were tested for this parameter, such as the group histogram. For a specific group (control or treatment) all data from all images were used to do a histogram of the total branch length. Histograms were plotted either on linear or logarithmic scales. These histograms are very similar between groups and data do not seem to have a lognormal distribution. Some distribution parameters were calculated for these image data, such as median, interquartile range, maximum branch length, among others, but they were also very similar between groups and images. Boxplots were also done to compare the different images within the same group, with data from each image. These boxplots are also

very similar to each other. Therefore, the TBL distribution was not further analyzed for the cytochalasin D positive control experiments.

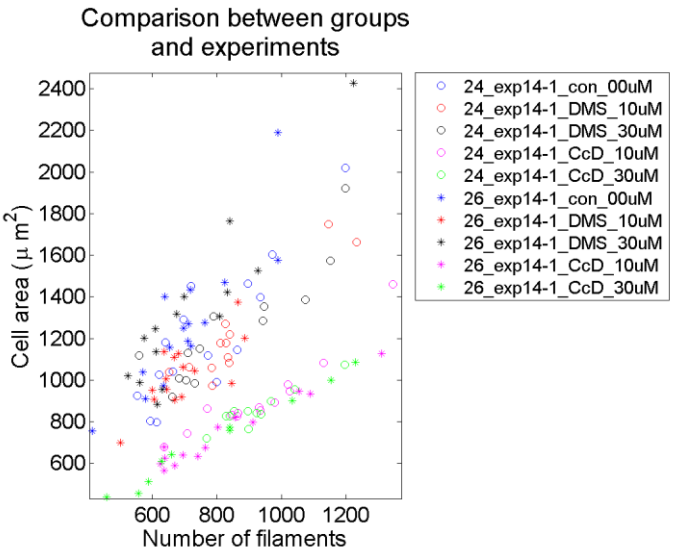

Figure 4.16: Correlation graph between cell area and the number of filaments. In the legend, *con_00uM* refers to the negative control group; *DMS_10uM* refers to the DMSO "10 μmol/dm³" group; *DMS_30uM* refers to the DMSO "30 μmol/dm³" group; *CcD_10uM* refers to the cytochalasin D 10 μmol/dm³ group; and *CcD_30uM* refers to the cytochalasin D 30 μmol/dm³ group. The numbers before the experiment replication refers to the confocal imaging day.

Through the analysis of the graphs and tables, it is possible to conclude that the methodology is sensitive to changes in the cytoskeleton. Furthermore, it is possible that there are other factors acting in the fibroblasts, besides the factors that we have controlled. Thus, the analysis and conclusions have to be careful.

The cytochalasin results were not used as a guide for analyzing the PBMT experiments because it is only a positive control, which changes the cytoskeleton in a specific way that is not necessarily the same way that the PBMT could modify the cytoskeleton. Thus, a fresh analysis of all parameters was carried out for the photo-treatment experiments.

4.2.2 PBMT experiments

For the PBMT experiments, the results were presented in various forms, as an attempt to facilitate the identification of systematic behaviors and differences between control and photo-treated groups. Boxplots were used to visualize all data, from each group. Relative values and relative variations were used to compare results from different experiments.

For the PBMT experiments, the differentiation between photo-treated and non-treated samples is not as easy as for the cytochalasin positive control samples. Figure 4.17 shows typical images of a control sample, on the left, and a photo-treated sample, on the right. The images are from experiment 1.1. The differentiation between samples cannot be carried out visually.

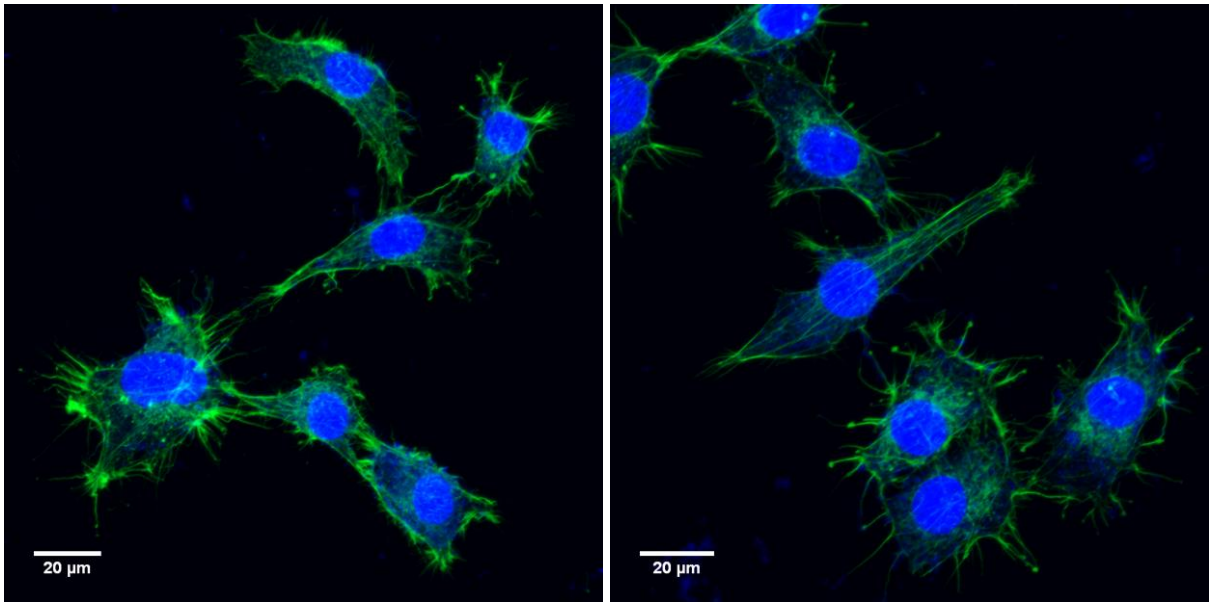

Figure 4.17: Example of images obtained with the confocal microscopy. Fibroblasts from the control group are on the left, and from the photo-treated group are on the right. All images are MIP for both channels, from experiment 1.1.

Here, just some graphs with the results for the PBMT experiments are presented. Because all graphs are similar, and there are too many of them, to let the text more fluent, just some were included in this chapter, and all graphs are in Appendix E. Figure 4.18 shows one example of a boxplot comparing results for the replications of experiment 1, for the nucleus area. For this experiment, the fibroblasts were grown in $4\,\mathrm{kPa}$ gels, photo-treated with $625\,\mathrm{nm}$ and fixed $5\,\mathrm{min}$ after photo-treatment. In the graph, the symbol "+" indicates that the photo-treated group median is higher than the control group median. The red symbols indicate that the control and photo-treated group data are incompatible according to the two-sample rank sum test and $p < 5\%$, on the other hand, the green symbols indicate compatible data. Graphs show data from fibroblasts, from all images of the specific groups and experiments.

Figure 4.19 shows the same example, but for the total branch length (TBL). In this case, data represented are from the whole image, for all images from the specific group, as there is not an individual value for each fibroblast. The symbols have the

same meaning; additionally "=" symbols mean that the photo-treated and control group medians are equal, and the "-" symbol means that the photo-treated group median is smaller than the control group median. The difference between the two graphs in Figure 4.19 is that the vertical axis has a compressed scale on the left and a logarithmic scale on the right.

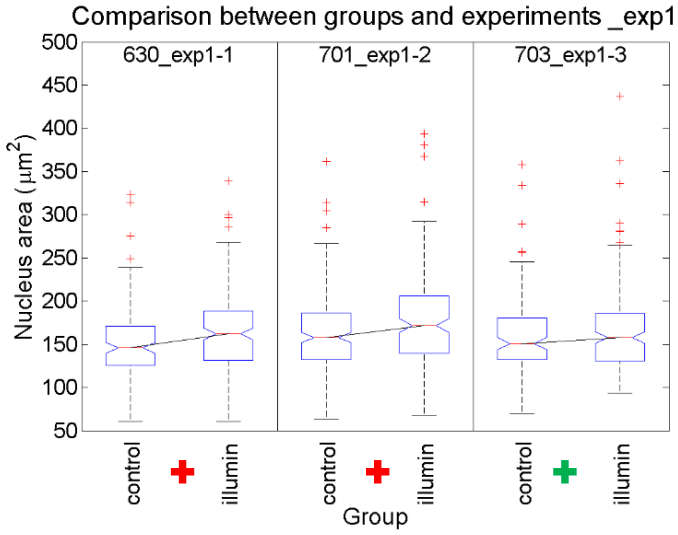

Figure 4.18: Boxplot of the nucleus area for the three replications of experiment 1. Experimental parameters for this experiment are shown in Table 4.2. Data represented in the graph are from fibroblasts, from different images. The graph was divided into regions that represent different imaging days, the label on top of each region describes the three replications 1.1, 1.2 and 1.3, and the numbers before it represent the confocal imaging date (month and day). In the horizontal axis label, *control* refers to the control group, and *illumin* refers to the photo-treated group, the "+" signal indicates that the photo-treated group median is larger than the control group median. The red color indicates that the control and photo-treated sample data are not compatible according to the two-sample rank sum test and $p < 5\%$, otherwise, the green color indicate that the control and photo-treated sample data are compatible according to the two-sample rank sum test. Graphs from others experiments are in Appendix E.

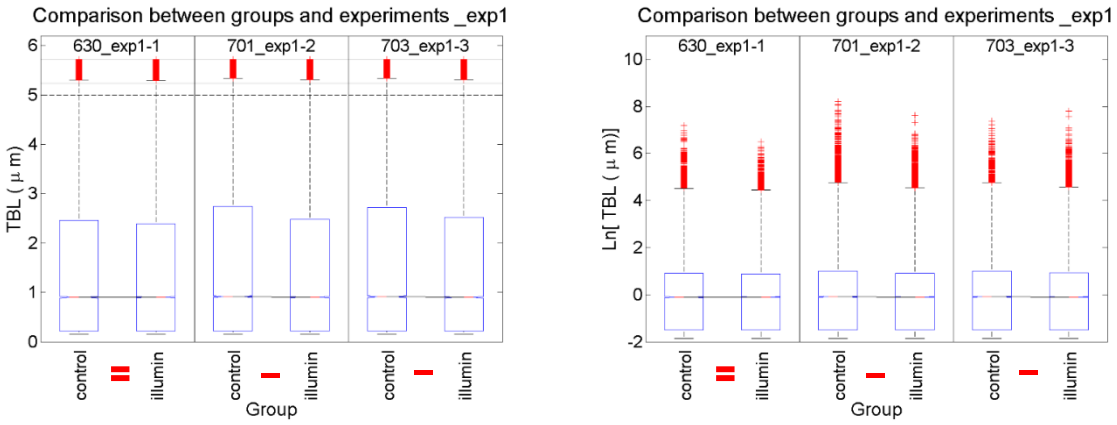

Figure 4.19: Boxplot of the total branch length for the three replications of experiment 1. Experimental parameters for this experiment are shown in Table 4.2. Data represented in the graph are data of each image, for all images of the specific group and experiment, because for this parameter there is not one value for each fibroblast. Each graph was divided into regions that represent different imaging days, the label on top of each region describes the three replications 1.1, 1.2 and 1.3, and the numbers before it represent the confocal imaging date (month and day). In the horizontal axis label, *control* refers to the control group, and *illumin* refers to the photo-treated group, the "-" signal indicates that the photo-treated group median is smaller than the control group median. The "=" signal indicates that the medians from both groups are equal. The red color indicates that the control and photo-treated sample data are not compatible according to the two-sample rank sum test and $p < 5\%$. On the left, the vertical axis was compressed after 5 μm to facilitate the visualization of the boxes, thus, data above 5 μm are compressed and not in scale. On the right, the vertical axis has a logarithmic scale. Graphs from others experiments are in Appendix E.

4.2.2.1 Relative parameter and relative variation analysis

Relative parameters were used to compare all experiments; they were defined as the ratio between the photo-treated group median and the control group median, for each imaging day, of each experiment replication. As the data distribution is not known, the relative parameters and relative variations were calculated using the median values, not the average values. Figure 4.20 shows a 3D graph comparing the nucleus area for all experiments, considering all experimental variables: photo-treatment wavelength, gel stiffness and time after treatment. This graph is just illustrative, as this 3D representation does not help the visualization. Therefore, two projections of this graph were plotted and are shown in Figure 4.21. On the left, the projection is in the *time after treatment* axis, so the symbol's shape represents the gel stiffness, and the color represents the wavelength. On the right, the projection is in the *gel stiffness* axis, so the symbol's shape represents the time after treatment, and the color represents the wavelength. For both graphs, the symbols outlined in green represent experiments where the control and photo-treated group data were compatible according to the two-

sample rank sum test and $p > 0.05$. Appendix E presents this kind of graph, for the other parameters analyzed.

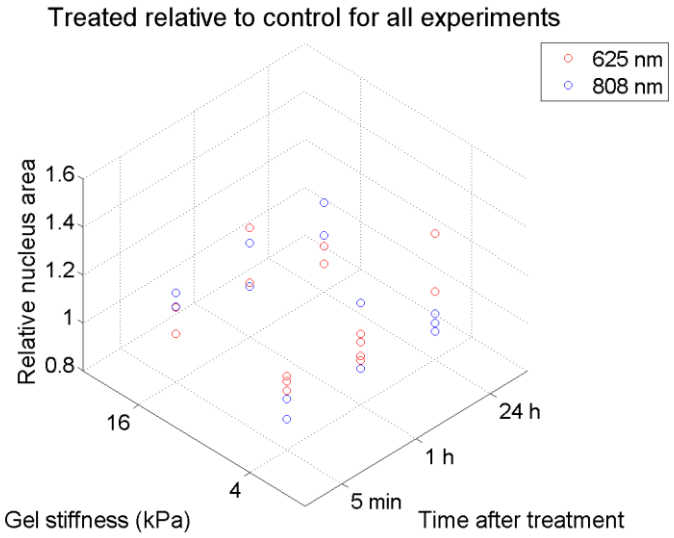

Figure 4.20: Comparison between all experiments in a 3D graph, for the relative nucleus area. The relative nucleus area is the ratio between the photo-treated group median and the control group median for the nucleus area. The axis *time after treatment* is not in scale.

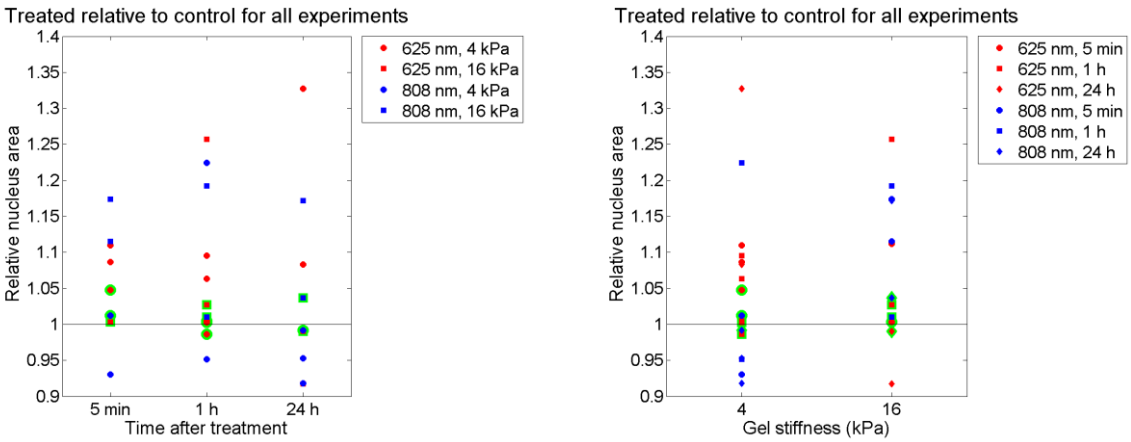

Figure 4.21: Comparison between all experiments in projections of the 3D graph shown in Figure 4.20, for the relative nucleus area. The relative nucleus area is the ratio between the photo-treated group median and the control group median, for the nucleus area. On the left, the horizontal axis shows the *time after treatment* (not in scale), the symbols represent the different gel stiffness, and the color represents the photo-treatment wavelength. On the right, the horizontal axis shows the *gel stiffness:* the symbols represent the different times after treatment, and the color represents the photo-treatment wavelength. Green outlined symbols represent samples in which the photo-treated and control group data were compatible according to the two-sample rank sum test and a confidence interval of 95%.

The results for the two-sample rank sum test, for all experiments and replications, are presented in Table 4.6 for the nucleus area, Table 4.7 for cell area, Table 4.9 for total actin, Table 4.10 for total actin density, Table 4.12 for the number of filaments and Table 4.13 for total branch length. Table 4.5 is the interpretation map for these tables

and shows the experiment replications corresponding to each p-value shown in the result tables. The symbols indicate the median behavior, so, “+” symbols indicate that the photo-treated group median increases related to the control group median, while the “-” symbols indicate that the median decreases, and “=” symbols indicate that both medians are equal. The numbers shown indicate the p-value, in percentage. The sample data were considered incompatible if $p < 5\%$. A summary of these data is presented in Table 4.8, Table 4.11 and Table 4.14. In these summary tables, all replications were collapsed in a single position of the table. If all replications present photo-treated group medians larger than the control group medians a “+” symbol is shown. The opposite situation is represented by a “-” symbol (for photo-treated medians smaller than control medians, for all replications). If the symbol is “+-“, for some replications, the photo-treated median is larger while for other replications it is smaller. For the total branch length summary table (Table 4.14) there is also the “=” symbol when the photo-treated and control medians are equal and the combinations “+=”, “-=” and “+=-”, with similar interpretation as the “+-” symbol. The colors in these tables are related to the compatibility, according to the two-sample rank sum test and confidence interval of 95%. Green was used when all experiments have control and photo-treated group data compatible; red when all experiments have control and photo-treated group data incompatible; and yellow when some experiments have control and photo-treated group data compatible but other experiments have control and photo-treated group data incompatible.

Furthermore, Figure 4.22, Figure 4.23 and Figure 4.24 show bar graphs with the relative variation, which is the difference between the photo-treated group median and the control group median divided by the control group median, for the parameter analyzed. In this kind of graph, the plot area was divided into three regions related to the time after treatment, the color represents the photo-treatment wavelength, and the horizontal axis and color shade represent the gel stiffness. Bars going above zero means that the photo-treated group median is larger than the control group median; on the other hand, bars going below zero means that the photo-treated group median is lower than the control group median. The higher the bar in the graph, the larger the variation between photo-treated and control group medians. Figure 4.22 shows the relative variation graph for nucleus area, on the left, and cell area, on the right. Figure 4.23 shows the relative variation graph for total actin, on the left, and total actin

density, on the right. At last, Figure 4.24 shows the relative variation graph for the number of filaments, on the left, and total branch length, on the right.

Here, as in the cytochalasin D positive control experiments, there are some cases where the median of one sample increases when compared with the control median while the median of other sample decreases when compared with the control median, for the same analyzed parameter and the same experiment variables. These cases may be seen in Table 4.8, Table 4.11 and Table 4.14, for positions where there are the "+-" symbol and red color. It is worth mentioning that for all parameters this configuration occurs at least once. This is another situation where there are indications that other factors, besides the factors we controlled, might be acting in the fibroblasts. Therefore, we have to be careful with the interpretation of these results, as modifications might be caused by unknown factors instead of the factors we are interested in.

Table 4.5 – Interpretation map for Table 4.6, Table 4.7, Table 4.9, Table 4.10, Table 4.12 and Table 4.13. Experiments are represented in each table position. The letters *A* and *B* after the experiment replication represent the imaging day, *A* refers to the first confocal imaging day of that replication and *B* the second. Experiments that do not have a letter were imaged in only one day.

Analyzed parameter		5 min			1 h					24 h		
625 nm	4 kPa	1.1	1.2	1.3	2.1A	2.2A	2.3A	2.2B	2.3B	3.1A	3.1B	
	16 kPa	4.1A	4.1B		5.1A		5.1B			6.1A	6.1B	
808 nm	4 kPa	7.1A	7.1B		8.1A		8.1B			9.1A	9.2A	9.2B
	16 kPa	10.1A	10.1B		11.1A		11.1B			12.1A	12.1B	

Table 4.6 – Results of the comparison between the control and photo-treated groups with the two-sample rank sum test, for the nucleus area. The symbols "+" and "-" indicate that the photo-treated group median is larger or smaller than the control group median, respectively. The numbers represent the p-values, in percentage, sample data were considered incompatible when $p < 5\%$ and are represented in red, compatible sample data are represented in green. The experiment replication of each table position is shown in the equivalent position in Table 4.5.

Nucleus area		5 min			1 h					24 h			
625 nm	4 kPa	2.4+	0.7+	45+	35+	87+	0.4+	0.3+	43-	0+		2.1+	
	16 kPa	1.4+		42+	11+		0+			7.5-		1.4-	
808 nm	4 kPa	1.8-		62+	4.2-		0+			0.5-	88-		2.7-
	16 kPa	0+		0+	0+		89+			0+		17+	

Table 4.7 – Results of the comparison between the control and photo-treated groups with the two-sample rank sum test, for the cell area. The symbols "+" and "-" indicate that the photo-treated group median is larger or smaller than the control group median, respectively. The numbers represent the p-values, in percentage, sample data were considered incompatible when $p < 5\%$ and are represented in red, compatible sample data are represented in green. The experiment replication of each table position is shown in the equivalent position in Table 4.5.

Cell area		5 min			1 h					24 h			
625 nm	4 kPa	5.3+	0+	31-	11-	17-	1.3+	0-	0-	0+		82-	
	16 kPa	0+		18+	8.1+		0.2-			0.2-		1.6-	
808 nm	4 kPa	23+		2.8+	0-		0+			0-	9.1-		0-
	16 kPa	0+		36+	0.3+		0.2-			0+		2.0+	

Table 4.8 – Summary table with the results of the two-sample rank sum test for nucleus area and cell area. The symbols “+” and “-” indicate that for all experiments with that specific configuration, the photo-treated group median was larger or smaller, respectively, than the control group median. The symbol “+-“ indicates that for some experiments the photo-treated group median was larger than the control group median, but for other experiments, it was smaller. The red and green colors indicate that for all experiments with that specific configuration, the photo-treated and control group data were incompatible or compatible, respectively, according to the two-sample rank sum test and confidence interval of 95%. The yellow color indicates that, for some experiments, sample data were compatible, but for others they were incompatible.

		Nucleus area			Cell area		
		5 min	1 h	24 h	5 min	1 h	24 h
625 nm	4 kPa	+	+-	+	+-	+-	+-
	16 kPa	+	+	-	+	+-	-
808 nm	4 kPa	+-	+-	-	+	+-	-
	16 kPa	+	+	+	+	+-	+

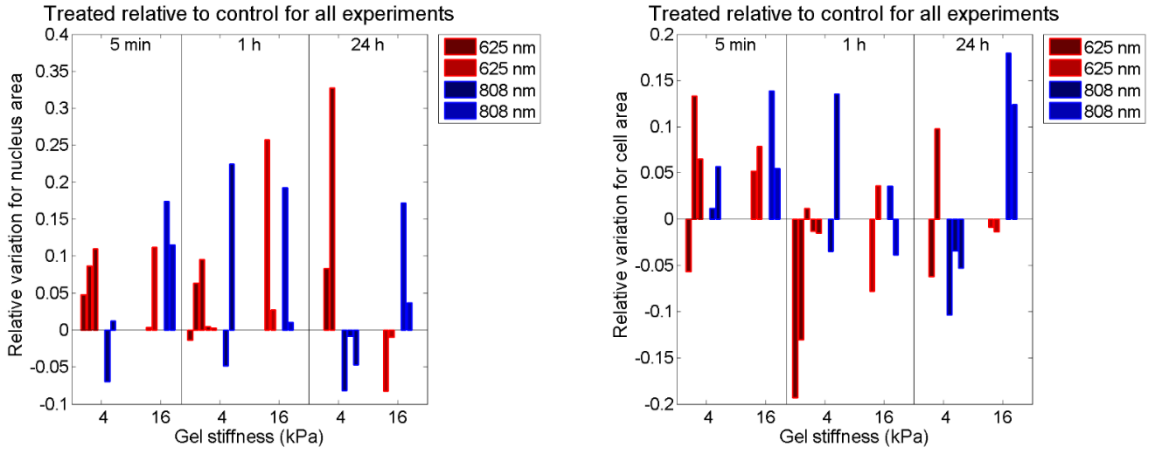

Figure 4.22: Comparison between all experiments. Nucleus area is on the left, and cell area on the right. Each graph was separated into three regions, related to the time after treatment. The colors represent the photo-treatment wavelengths. The horizontal axis and color shades represent the gel stiffness. The parameter represented is the difference between the photo-treated group median and the control group median, divided by the control group median.

Table 4.9 – Results of the comparison between the control and photo-treated groups with the two-sample rank sum test, for the total actin. The symbols “+” and “-” indicate that the photo-treated group median is larger or smaller than the control group median, respectively. The numbers represent the p-values, in percentage, sample data were considered incompatible when $p < 5\%$ and are represented in red, compatible sample data are represented in green. The experiment replication of each table position is shown in the equivalent position in Table 4.5.

Total actin		5 min			1 h					24 h	
625 nm	4 kPa	0-	0-	0-	0.6-	0-	0-	0-	0-	0.5+	41-
	16 kPa	0-	0-		0-		23-			0-	3.2+
808 nm	4 kPa	0-	0-		0-		33+			0-	4.3-	6.6-
	16 kPa	87+	0-		0-		0-			99-	29+

Table 4.10 – Results of the comparison between the control and photo-treated groups with the two-sample rank sum test, for the total actin density. The symbols “+” and “-” indicate that the photo-treated group median is larger or smaller than the control group median, respectively. The numbers represent the p-values, in percentage, sample data were considered incompatible when $p < 5\%$ and are represented in red, compatible sample data are represented in green. The experiment replication of each table position is shown in the equivalent position in Table 4.5.

Total actin density		5 min			1 h					24 h	
625 nm	4 kPa	0-	0-	0-	0.7-	0-	0-	67+	0-	0.4-	44-
	16 kPa	0-	0-		0-		8.1+			0-	0+
808 nm	4 kPa	0-	0-		0-		0-			0-	0-	0.3+
	16 kPa	0-	0-		0-		0-			0-	0.4-

Table 4.11 – Summary table with the results of the two-sample rank sum test for total actin and total actin density. The symbols “+” and “-” indicate that for all experiments with that specific configuration, the photo-treated group median was larger or smaller, respectively, than the control group median. The symbol “+-“ indicates that for some experiments the photo-treated group median was larger than the control group median, but for other experiments, it was smaller. The red and green colors indicate that for all experiments with that specific configuration, the photo-treated and control group data were incompatible or compatible, respectively, according to the two-sample rank sum test and confidence interval of 95%. The yellow color indicates that, for some experiments, sample data were compatible, but for others they were incompatible.

		Total actin			Total actin density		
		5 min	1 h	24 h	5 min	1 h	24 h
625 nm	4 kPa	-	-	+-	-	+-	-
	16 kPa	-	-	+-	-	+-	+-
808 nm	4 kPa	-	+-	-	-	-	+-
	16 kPa	+-	-	+-	-	-	-

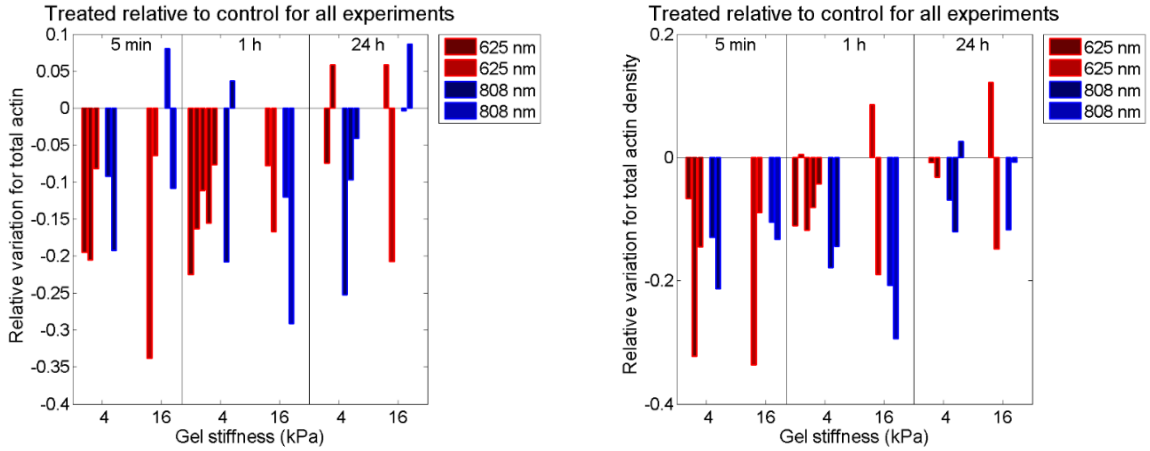

Figure 4.23: Comparison between all experiments. Total actin is on the left and total actin density on the right. Each graph was separated into three regions, related to the time after treatment. The colors represent the photo-treatment wavelengths. The horizontal axis and color shades represent the gel stiffness. The parameter represented is the difference between the photo-treated group median and the control group median, divided by the control group median.

Table 4.12 – Results of the comparison between the control and photo-treated groups with the two-sample rank sum test, for the number of filaments. The symbols “+” and “-” indicate that the photo-treated group median is larger or smaller than the control group median, respectively. The numbers represent the p-values, in percentage, sample data were considered incompatible when $p < 5\%$ and are represented in red, compatible sample data are represented in green. The experiment replication of each table position is shown in the equivalent position in Table 4.5.

Number of filaments		5 min			1 h					24 h		
625 nm	4 kPa	0-	0-	16-	0-	0-	0-	0-	0-	0-	0.5-	
	16 kPa	0-	0-		0-	5.9+				0-	0+	
808 nm	4 kPa	0-	0-		0-	2.7-				0-	84+	51-
	16 kPa	23-	0-		0-	0-				81+	9.6+	

Table 4.13 – Results of the comparison between the control and photo-treated groups with the two-sample rank sum test, for the total branch length. The symbols “+”, “=” and “-” indicate that the photo-treated group median is larger, equal or smaller when compared to the control group median, respectively. The numbers represent the p-values, in percentage, sample data were considered incompatible when $p < 5\%$ and are represented in red, compatible sample data are represented in green. The experiment replication of each table position is shown in the equivalent position in Table 4.5.

Total branch length		5 min			1 h					24 h		
625 nm	4 kPa	0=	0-	0-	0+	55=	41=	0.7=	0-	0-	0+	
	16 kPa	0-	0-		0=	0+				74=	0+	
808 nm	4 kPa	48=	0+		0+	0=				81+	0-	57=
	16 kPa	0-	0-		3.0-	0.2-				3.0=	69-	

Table 4.14 – Summary table with the results of the two-sample rank sum test for the number of filaments and total branch length. The symbols “+”, “=” and “-” indicate that for all experiments with that specific configuration, the photo-treated group median was larger, or equal, or smaller, respectively, than the control group median. The symbol “+-“ indicates that for some experiments the photo-treated group median was larger than the control group median, but for other experiments, it was smaller. Analogous interpretation can be used for the other symbol combinations “+=”, “=-“ and “+=-“. The red and green colors indicate that for all experiments with that specific configuration, the photo-treated and control group data are incompatible or compatible, respectively, according to the two-sample rank sum test and confidence interval of 95%. The yellow color indicates that, for some experiments, sample data were compatible, but for others they were incompatible.

		Number of filaments			Total branch length		
		5 min	1 h	24 h	5 min	1 h	24 h
625 nm	4 kPa	-	-	-	=-	+=-	+-
	16 kPa	-	+-	+-	-	+=	+=
808 nm	4 kPa	-	-	+-	+=	+=	+=-
	16 kPa	-	-	+	-	-	=-

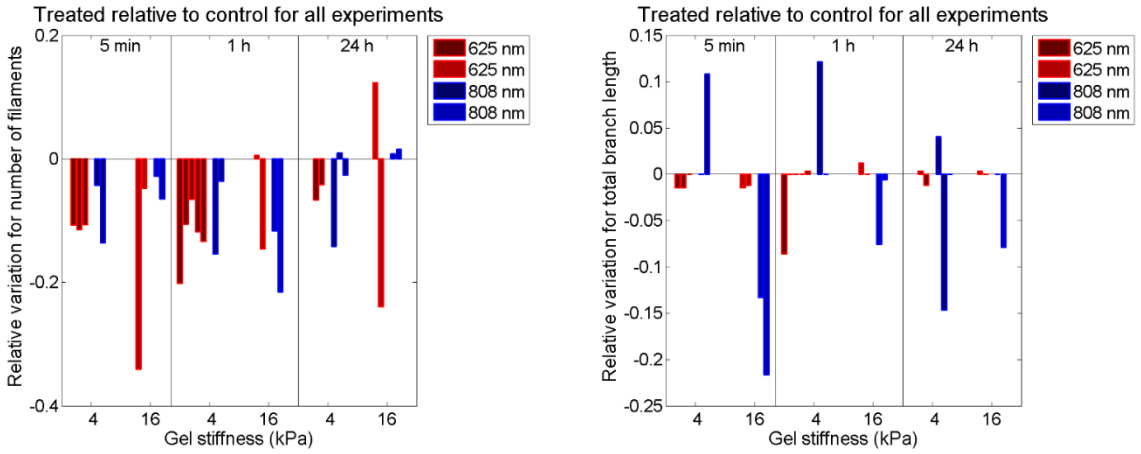

Figure 4.24: Comparison between all experiments. The number of filaments is on the left and total branch length on the right. Each graph was separated into three regions, related to the time after treatment. The colors represent the photo-treatment wavelengths. The horizontal axis and color shades represent the gel stiffness. The parameter represented is the difference between the photo-treated group median and the control group median, divided by the control group median.

A Student’s *t*-test was performed to test whether the photo-treatment cause changes in the relative variation of a specific parameter. Although no statistical tests were performed to verify the data distribution, data seem to have normal distribution. The only exception is the total branch length; thus data of this parameter was not tested. The test results are shown in Table 4.15. Sample data were considered different from

zero when $p < 5\%$, meaning that the photo-treatment cause changes in that parameter. It is worth to remember that for this test, all relative parameters from samples that were photo-treated with the same wavelength were considered as one sample, independent of the time after treatment or gel stiffness, thus, there were two samples one for $625\ \text{nm}$ and the other for $808\ \text{nm}$. The same was completed with the time after treatment, resulting in three samples, for $5\ \text{min}$, $1\ \text{h}$ and $24\ \text{h}$; and for gel stiffness, resulting in two samples, for $4\ \text{kPa}$ and $16\ \text{kPa}$. According to the results, we can notice that for the $24\ \text{h}$ after treatment, none of the parameters can be considered different from zero, what probably means that whatever is the change that PBMT causes in the fibroblasts, it disappears after $24\ \text{h}$.

Table 4.15 – Results of the Student's *t*-test, for comparison between the relative variation data with zero, for all parameters. The numbers represent the p-values, in percentage, sample data were considered incompatible when $p < 5\%$ and are represented in red, compatible data are represented in green.

	Wavelength		Time after treatment			Gel stiffness	
	625 nm	808 nm	5 min	1 h	24 h	4 kPa	16 kPa
Nucleus area	1.6	11	2.9	4.1	36	9	1.5
Cell area	78	16	1.7	35	67	62	5.6
Total actin	0.02	1.8	0.9	0.03	22	0.004	3.6
Total actin density	0.9	0.01	0.08	0.5	20	0.02	1.2
Number of filaments	0.09	0.4	0.8	0.02	28	0.0003	4.0

The results of the Kruskal-Wallis test are shown in Table 4.16. According to this test, only for the total actin density in the PBMT parameter time after treatment, it is possible to differentiate the groups. This means that despite the fact that the PBMT causes differences in the cell parameters, as shown with the Student's *t*-test, it is not possible to differentiate between the experimental variables, such as wavelength and gel stiffness.

Table 4.16 – Results of the Kruskal-Wallis test, for comparison between the relative variation data for each experimental variable: wavelength, time after treatment and gel stiffness, for all parameters. The numbers represent the p-values, in percentage, sample data were considered incompatible when $p < 5\%$ and are represented in red, compatible data are represented in green.

	Wavelength	Time after treatment	Gel stiffness
Nucleus area	73	45	23
Cell area	27	7	10
Total actin	54	15	51
Total actin density	25	4.4	53
Number of filaments	24	8	62
Total branch length	59	25	14

Through the analysis of all graphs and tables, it is possible to determine whether the PBMT causes changes in the parameters analyzed. Here, the *increase* means that the photo-treated group median is larger than the control group median, on the other hand, *decrease* means that the photo-treated group median is smaller than the control group median.

- Most of the results indicate that the **nucleus area** increases, mainly for short times after treatment ($5\,\mathrm{min}$ and $1\,\mathrm{h}$). That could indicate a change in configuration related to cell division or migration, for example.
- The **cell area** does not show any strong systematic behavior. In the $5\,\mathrm{min}$ experiments, there are more indications of cell area increasing than decreasing, while in the $1\,\mathrm{h}$ and the $24\,\mathrm{h}$ experiments the opposite happens. In fact, the $5\,\mathrm{min}$ sample is the only group of cell area data whose variation with PBMT might be considered different from zero according to the Student's *t*-test.
- The analyses indicate that the **total actin** decreases. There are exceptions for all the time intervals after treatment, but the $24\,\mathrm{h}$ experiments have more exceptions. Most of them refer to compatible sample data (no changes due to photo-treatment).

- The analyses indicate that the **total actin density** decreases. Exceptions are for the experiments with the longer times after treatment. Some of the exceptions refer to compatible sample data.
- The analyses indicate that the **number of filaments** decreases. Exceptions are in the longer times after treatment. Most of the exceptions refer to compatible sample data.
- The **total branch length** does not seem to have any strong systematic behavior. The infrared photo-treated samples change more than the red photo-treated samples, but all the changes are small.

Hence, the PBMT changes the fibroblasts and their cytoskeleton. However, those changes are subtle, not as strong as the cytochalasin changes in the cytoskeleton.

4.2.2.2 Correlation analysis

Figure 4.25 shows the correlation coefficients, on the left, and the coefficients of determination, on the right, for experiment 1 replications. Similar graphs for the other experiments are presented in Appendix E. The linear regression was fitted for the graphs with coefficient of determination above 0.5. This means that for the pair of parameters that have most of the coefficients of determination of the different groups above 0.5, the linear regression was fitted. Therefore, the linear regression was fitted to the graphs of cell area versus total actin (noted as TA/Ar or Ar vs TA), cell area versus the number of filaments (NF/Ar or Ar vs NF) and the number of filaments versus total actin (TA/NF or NF vs TA).

Figure 4.26 shows the results of the slope of the linear regression fit for the cell area versus total actin correlation graph, for experiment 1 replications. As before, if the error bars do not overlap, the slopes were considered incompatible, otherwise, they were considered as compatible. Graphs for the other experiments and correlations can be found in Appendix E. Here again, there are situations where slopes that should be compatible are not. This is an indication that the modifications in the slopes might be caused by unknown factors, which we did not control. Therefore, the interpretation of the results should be done carefully.

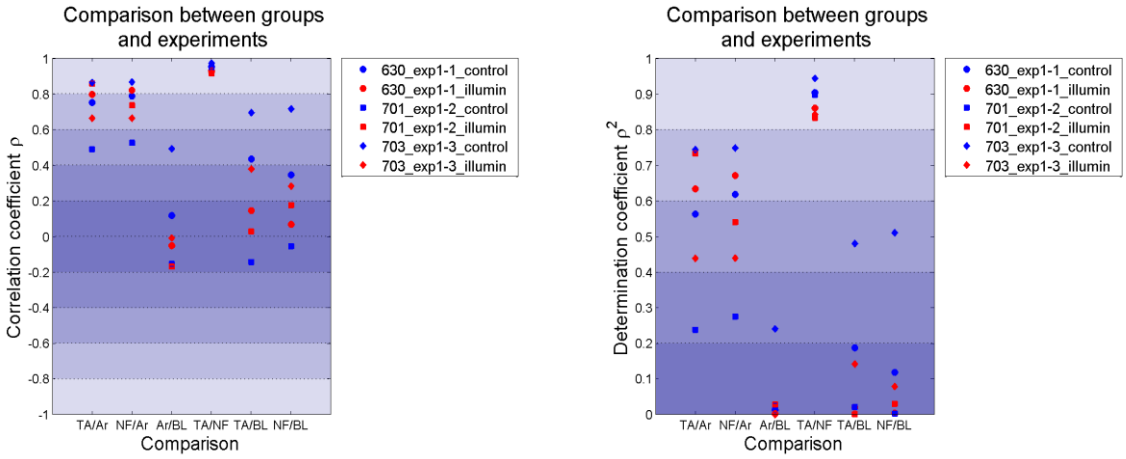

Figure 4.25: Correlation coefficient, on the left, and coefficient of determination, on the right, for experiment 1 replications. Experimental parameters, for this experiment, are shown in Table 4.2. In the horizontal axis, the initials refer to the parameters correlated, so, TA means total actin, Ar means cell area, NF means the number of filaments and BL means total branch length. In the legend, *control* refers to the control group, and *illumin* refers to the photo-treated group, the numbers before the experiment replication refers to the imaging day (month and day).

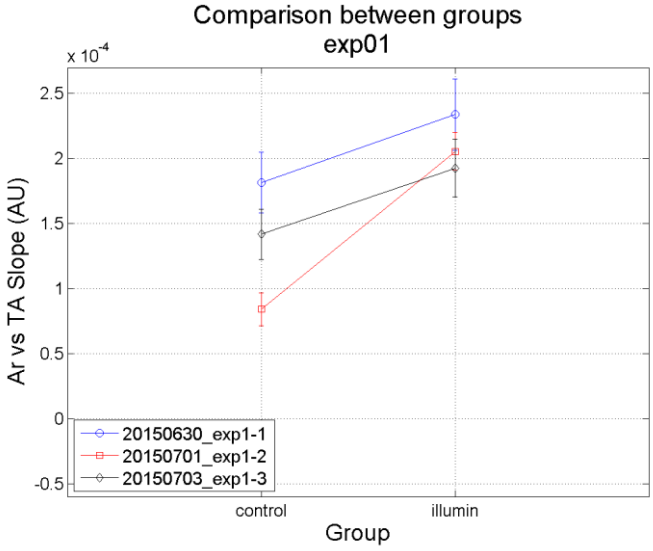

Figure 4.26: Graph of the cell area versus total actin slope for the three replications of experiment 1. Experimental parameters, for this experiment, are shown in Table 4.2. The legend represents the three replications 1.1, 1.2 and 1.3, and the numbers before it represent the confocal imaging date (month and day). The error bars represent two times the slope uncertainty, thus, if the error bars overlap, the slopes were considered as compatible. Otherwise, they were considered as incompatible. The lines are guides for the eyes.

Figure 4.27 show the bar graphs with the relative variation (the difference between the photo-treated group parameter and control group parameter, divided by the control group parameter) for the correlation between cell area and total actin. On the top left, the correlation coefficient, on the top right, the coefficient of determination and on the bottom, the slope of the linear regression fit. Figure 4.28 and Figure 4.29 show the

same data, but for the correlations between cell area versus the number of filaments and the number of filaments versus total actin, respectively.

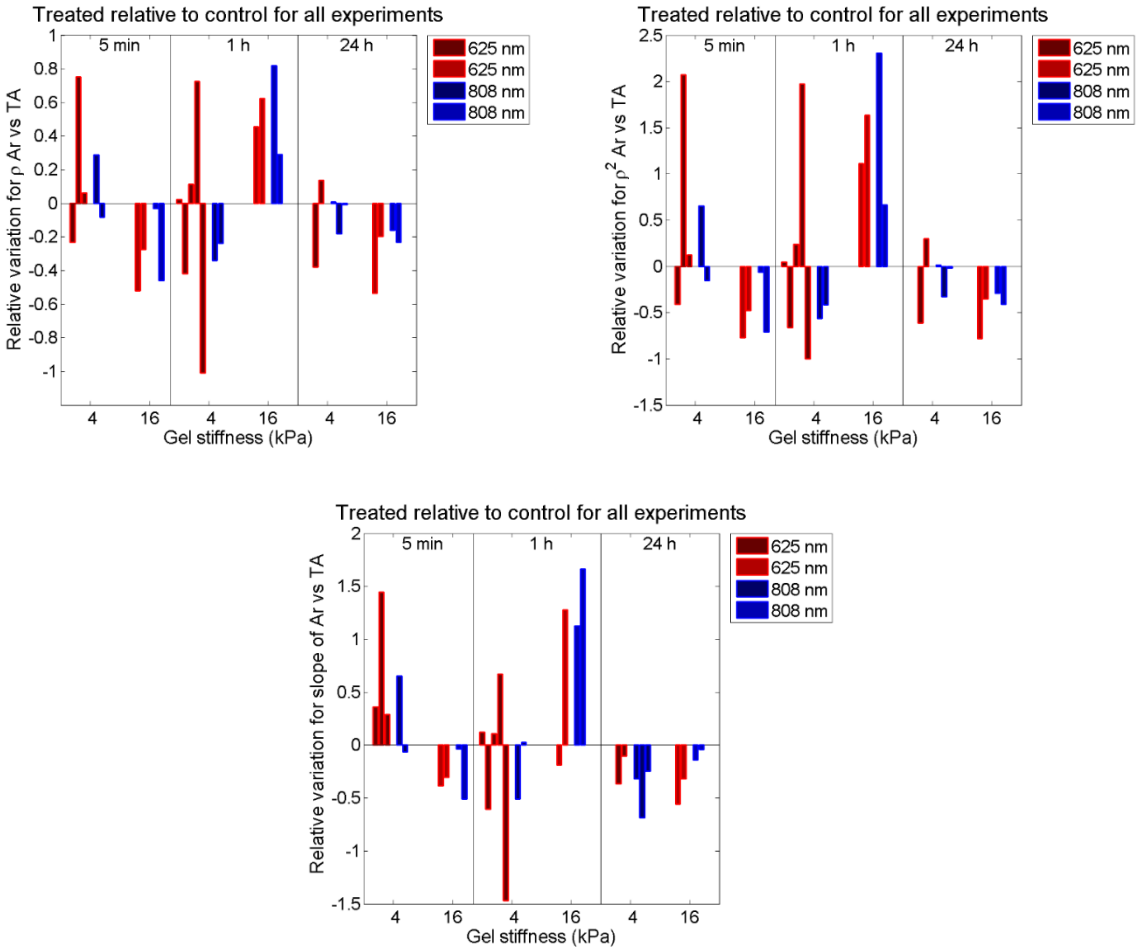

Figure 4.27: Comparison between all experiments. On the top left, the comparison for the correlation coefficient of the cell area versus total actin graph. On the top right, for the coefficient of determination, and on the bottom, for the linear fit slope. Each graph was separated into three regions, related to the time after treatment. The colors represent the photo-treatment wavelengths. The horizontal axis and color shades represent the gel stiffness. The parameter represented is the difference between the photo-treated group value and the control group value, divided by the control group value.

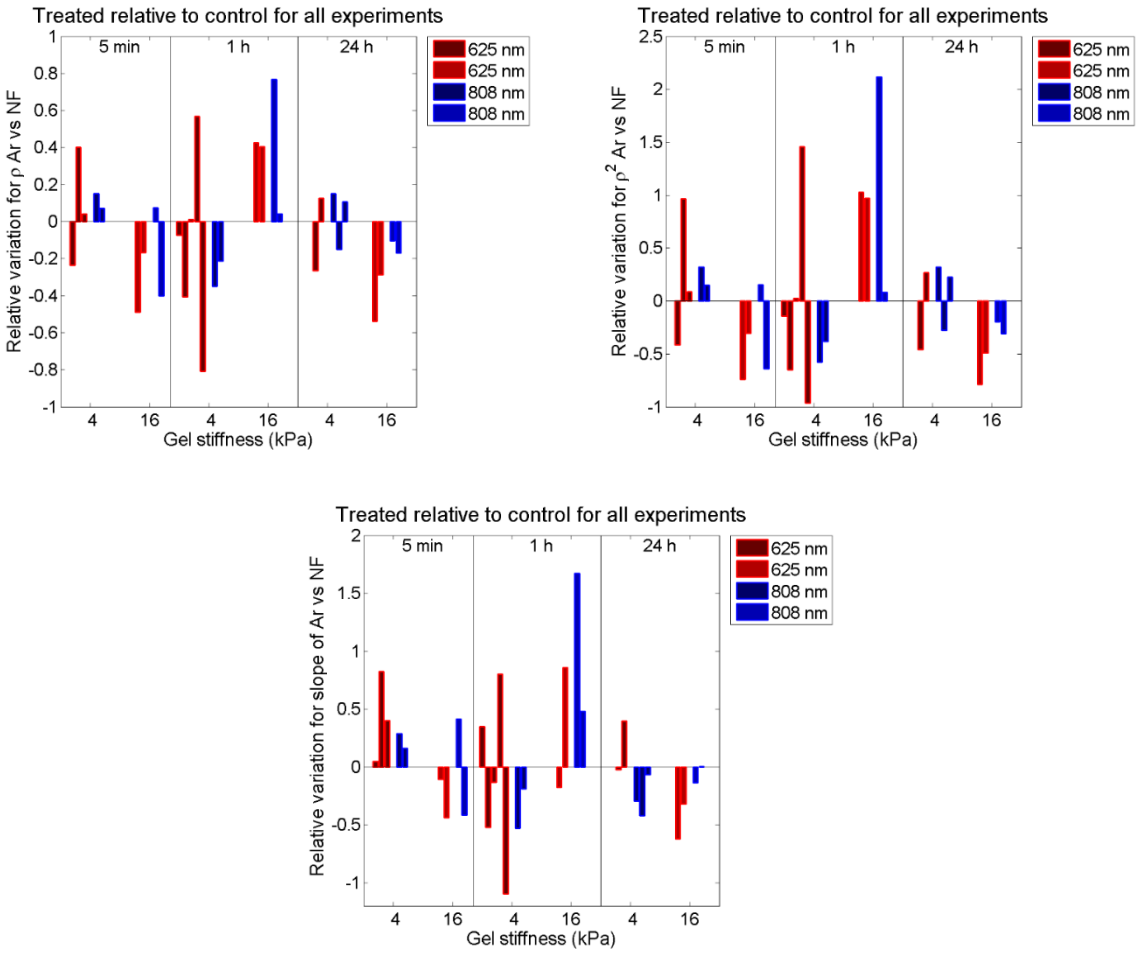

Figure 4.28: Comparison between all experiments. On the top left, the comparison for the correlation coefficient of the cell area versus the number of filaments graph. On the top right, for the coefficient of determination, and on the bottom, for the linear fit slope. Each graph was separated into three regions, related to the time after treatment. The colors represent the photo-treatment wavelengths. The horizontal axis and color shades represent the gel stiffness. The parameter represented is the difference between the photo-treated group value and the control group value, divided by the control group value.

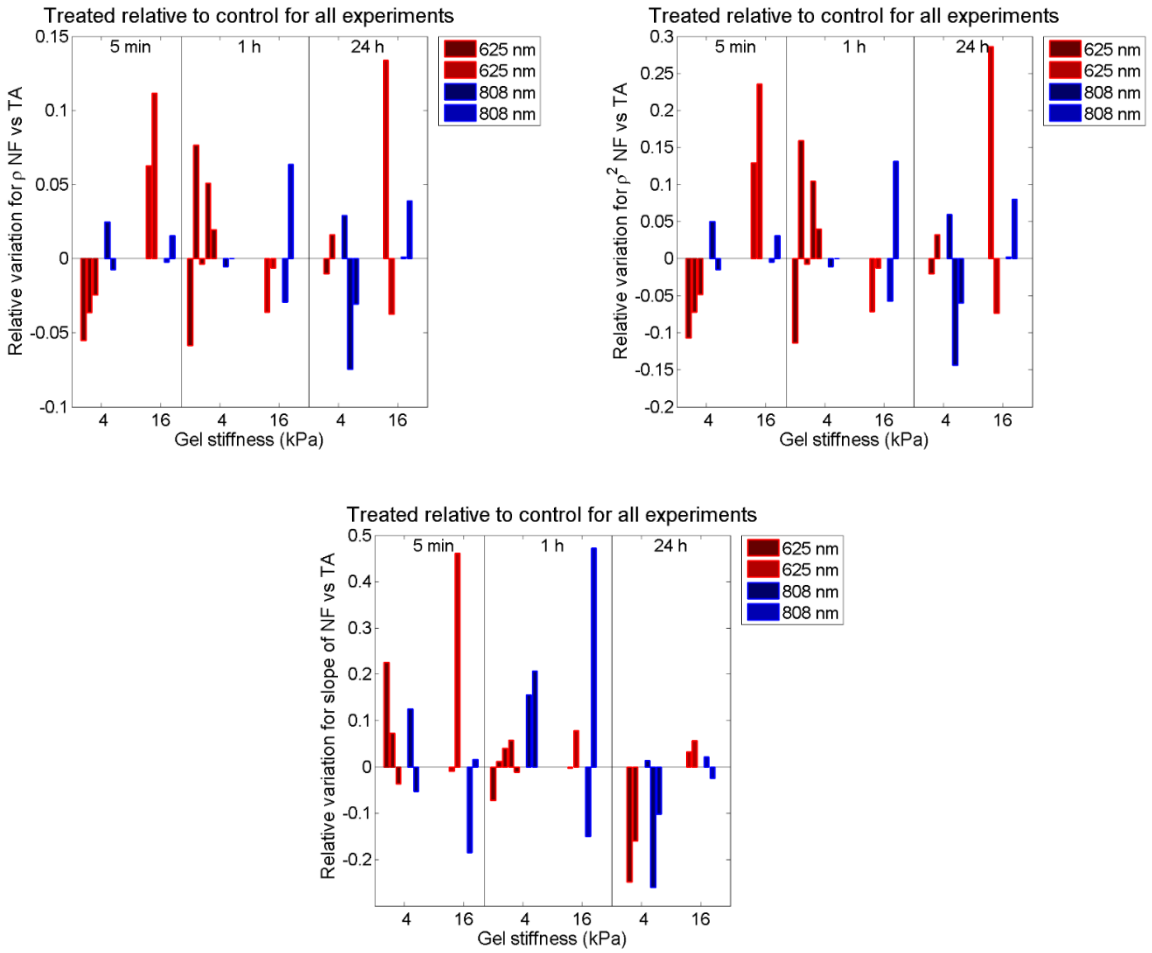

Figure 4.29: Comparison between all experiments. On the top left, the comparison for the correlation coefficient of the number of filaments versus total actin graph. On the top right, for the coefficient of determination, and on the bottom, for the linear fit slope. Each graph was separated into three regions, related to the time after treatment. The colors represent the photo-treatment wavelengths. The horizontal axis and color shades represent the gel stiffness. The parameter represented is the difference between the photo-treated group value and the control group value, divided by the control group value.

The Student's *t*-test was performed to test whether the photo-treatment cause changes in the relative variation of the correlation coefficient, coefficient of determination and slope. The results are shown in Table 4.17. Sample data were considered different from zero when $p < 5\%$, meaning that the photo-treatment cause changes in that parameter. For this test, all relative parameters from samples that were photo-treated with the same wavelength were considered as one sample, independent of the time after treatment or gel stiffness. Thus, there were two samples one for $625\ \mathrm{nm}$ and the other for $808\ \mathrm{nm}$. The same was completed with the time after treatment, resulting in three samples, for $5\ \mathrm{min}$, $1\ \mathrm{h}$ and $24\ \mathrm{h}$; and for gel stiffness, resulting in two samples, for $4\ \mathrm{kPa}$ and $16\ \mathrm{kPa}$. For the correlation between total actin and cell area, for the $24\ \mathrm{h}$ after treatment, the relative variation of the coefficients might be considered different from zero. In this case, all these coefficients decreased when comparing the photo-

treated with the control samples, which means that the samples were correlated, but they lost the correlation after the photo-treatment.

Table 4.17 – Results of the Student's *t*-test, for comparison between the relative variation data with zero, for the correlation coefficients, coefficients of determination and slopes. The numbers represent the p-values, in percentage, sample data were considered incompatible when $p < 5\%$ and are represented in red, compatible data are represented in green.

		Wavelength		Time after treatment			Gel stiffness	
		625 nm	808 nm	5 min	1 h	24 h	4 kPa	16 kPa
TA/Ar	ρ	74	79	68	59	3.6	66	89
	ρ^2	56	82	92	19	3.7	72	61
	Slope	99	72	46	48	0.23	80	56
NF/Ar	ρ	42	98	53	82	14	52	75
	ρ^2	96	70	80	38	18	98	78
	Slope	92	66	37	57	13	99	61
TA/NF	ρ	40	85	59	62	72	59	14
	ρ^2	36	81	55	58	67	65	13
	Slope	44	74	30	18	11	95	30

The results of the Kruskal-Wallis test are shown in Table 4.18. No differences can be noticed between the experimental variables, such as wavelength, time after treatment and gel stiffness.

Through the analysis of all graphs and tables, it is possible to determine whether the photo-treatment causes changes in the correlations analyzed. It seems that there are not systematic behaviors. Something that worth to be noted is that usually the correlation coefficient and the slope have the same behavior, if the correlation coefficient increases (comparing photo-treated to control groups), the slope also increase. Nevertheless, there are some exceptions to this behavior. Furthermore, higher values of coefficient of determination usually means higher values of the slope.

Table 4.18 – Results of the Kruskal-Wallis test, for comparison between the relative variation data for each experiment variable: wavelength, time after treatment and gel stiffness, for the correlation coefficients, coefficients of determination and slopes. The numbers represent the p-values, in percentage, sample data were considered incompatible when $p < 5\%$, compatible data are represented in green.

		Wavelength	Time after treatment	Gel stiffness
TA/Ar	ρ	86	42	76
	ρ^2	86	42	76
	Slope	90	12	96
NF/Ar	ρ	46	76	76
	ρ^2	46	76	76
	Slope	97	37	93
TA/NF	ρ	90	99	17
	ρ^2	90	99	17
	Slope	66	14	54

4.2.3 Summary

For the fibroblast cells analyzed with the confocal laser-scanning microcopy, it was possible to observe changes in the cytoskeleton of photo-treated fibroblasts. The total amount of actin, the total actin density and the number of filaments decreased for photo-treated samples when compared to control samples. On the other hand, the nucleus and cell area of photo-treated samples increased when compared to control samples, for short times after treatment, until $1\ \mathrm{h}$. All those changes detected disappear for long times after photo-treatment, thus after $24\ \mathrm{h}$ they are not detectable anymore. The total branch length of the actin filaments does not seem to suffer any changes.

It was not possible to detect differences between the red and the infrared wavelengths in the effects found in fibroblasts. It was neither possible to detect differences in the gel stiffness in the effects found in fibroblasts. Related to the time after treatment, for the total actin density, the time after treatment was an important factor, and this

parameter might be used for analyzing the mechanical properties of fibroblasts and the effects of the PBMT.

However, there are indications that, in some cases, the observable modifications might be caused by unknown factors, or statistical fluctuation.

5. Final Discussion

In this study, we experimentally evaluated several mechanical and morphological properties of some cells and their modifications by photobiomodulation therapy (PBMT), in the red or infrared spectral ranges. The characteristics and limitations of the techniques used – optical magnetic twisting cytometry (OMTC), defocusing and confocal microscopies – resulted in narrow intersection between the experiments. However, this does not invalidate the work, because all the experiments intended to assess the effects in cells that are subjected to light during clinical treatments with PBMT. Table 5.1 presents a summary of all experiments and its respective conditions and parameters.

The defocusing microscopy experiments could not detect changes in the evaluated characteristics of human red blood cells (RBCs) related to the photo-treatment with red light, for the doses used. A few factors could cause this result. First, it is possible that the changes depend on the interaction between the RBCs and other blood elements. In our case, this interaction might not have happened because the blood sample was highly diluted. Furthermore, the substances used for dilution might change the effects, compared to a photo-treatment in another kind of sample, such as whole blood, for example. Another possibility is that the doses used might be inadequate to cause changes in the RBCs. Thus, the photobiomodulation did not occur probably due to a small dose, which would not be enough to trigger the biological effect.

A subtle trend was observed for the volume and for the thickness of the RBC edge as a function of the accumulated photo-treatment time. For the $30\,\mathrm{mW}$ photo-treated sample, there was a decrease behavior in the volume and thickness of the RBC edge. On the other hand, for the $100\,\mathrm{mW}$ photo-treated sample, there was an increasing behavior. Two interpretations could be given to this result. First, this could indicate a modulation effect of the RBC volume. Thus, for the $30\,\mathrm{mW}$ photo-treated samples, which presented volumes slightly higher than the volumes found in the literature, the PBMT caused the volume to decrease. For the $100\,\mathrm{mW}$ photo-treated samples, the volume increased. Another possible interpretation is a biphasic effect: for lower doses, the effect is stimulatory, and for higher doses, the effect is inhibitory, inducing the RBCs to increase the volume. However, it is important to note that these trends could be

produced by statistical fluctuation, as for the $30\ \mathrm{mW}$ neither the linear and the constant fit are adequate to data, according to the χ^2 goodness of fit analysis.

Table 5.1 – Summary of the experiments used in this work and their respective conditions and parameters.

Experimental parameters	OMTC	Defocusing microscopy	Confocal microscopy	
Wavelength (nm)	660	660	625	808
Source	Laser	Laser	LED	LED
Area (cm^2)	0.196	0.196	1.13	1.13
Radiant power (mW)	30	Variable 0 to 100	113 to 147	124 to 158
Power density (mW/cm^2)	153	Variable 0 to 510	100 to 130	110 to 140
Time (s)	300	Variable 0 to 180	300	300
Radiant energy (J)	9	Variable 0 to 18	34 to 44	37 to 47
Energy density (J/cm^2)	46	Variable 0 to 92	30 to 39	33 to 42
Sample type	Human epithelial cell culture (BEAS-2B)	Human RBCs	Mouse fibroblast cell culture (3T3)	
Sample condition	Healthy cells in 96 well plate	Highly diluted (0.002% to 0.005%) in a BSA solution in PBS at 0.1%	Healthy cells in 24 well plate with substrates with different stiffness	
Type of photo-treatment	One photo-treatment section	One photo-treatment section or 6 fractions with 30 s interval	One photo-treatment section	
Time Interval treatment-measurement	Immediate	Immediate to 1 h	5 min, 1 h or 24 h	
Parameters analyzed	Cell hysteresivity η	Volume, radial profile of cell thickness, lateral and vertical membrane fluctuations	Nucleus area, cell area, total actin, total actin density, the number of filaments, total branch length	
What did change?	No changes detected	No changes detected	Possible decrease of the total actin and its density. Possible slightly increase in cell and nucleus areas. Indications that after 24 h, all changes disappeared.	
What does that mean?	PBMT has no effect, or the technique is not sensitive enough	PBMT has no effect, or the technique is not sensitive enough	Possible reduction of the polymerized actin filaments with PBMT	

The RBCs are predominantly responsible for blood viscosity. However, the rheological changes observed in the previous pilot study, which was our motivation, might be related to the interaction of light with other blood components. Possibly, in the samples used for the defocusing microscopy experiments, those components were not present in sufficient number to trigger an effect. Therefore, those components might be the primary target of PBMT and could be responsible for the effects in blood and RBCs.

If we assume that PBMT does not cause modifications in the RBCs, we can consider that the outcomes are consistent with the PBMT mechanism of action most accepted in literature: the photons are absorbed and cause changes in the cytochrome C oxidase inside mitochondria, causing variations in the respiratory chain [14]. It is known that healthy RBCs in circulation, do not have internal organelles like mitochondria, neither they have a nucleus [24]. Therefore, it would be expected that the PBMT does not cause changes in the RBCs. Nevertheless, there are other PBMT mechanisms, which are not related to the mitochondria, such as the direct action in the cell membrane. Thus, if the RBCs are the light target in blood, the action mechanism should not be related to the mitochondria.

The other possible mechanism of action of PBMT discussed in the literature is the action directly on the cytoskeleton. It is reported that possibly PBMT has effect in two types of the cytoskeleton: the actin filaments [63], [64] and microtubules [62]. As the RBC cytoskeleton is composed by spectrin, with some actin filaments [24], it is possible that the PBMT cannot cause changes in RBC cytoskeleton.

For the OMTC experiments with human epithelial cells photo-treated with red light, neither was possible to detect changes due to the photo-treatment in the parameters evaluated. In this case, this result can also be caused by various factors.

Cell cultures do not mimic all characteristics of living tissues, such as the interactions between different types of cells that are found in a tissue. This fact could lead to the result for the OMTC experiments: in this case, there is no interaction between epithelial cells with other types of cells, also present in epithelial tissue, such as fibroblasts. This interaction could trigger a local effect, which typically would not occur in *in vitro* cultures because usually cell cultures have just one type of cell. Therefore, the PBMT effect might depend on the complex environment of a living tissue, which is not easy to reproduce in a cell culture.

Regarding the PBMT mechanism of action, which was cited previously as the most accepted mechanism, there is no reason to believe that it cannot occur in epithelial cells. That is because epithelial cells have the regular organelles found in cells in general. In particular, they have mitochondria, where cytochrome C oxidase, which is the main photoacceptor for PBMT, is found. This mechanism is accepted as a general mechanism for a wide variety of cells [12], and it also was observed in epithelial cells [127]. Regarding the cytoskeleton, there is also no reason to assume that the PBMT cannot act on the actin filaments or in microtubules present in epithelial cells, as changes in actin filaments due to PBMT were found in other types of cells [63], [64], [67].

For both techniques, the defocusing microscopy and OMTC, the sensibility might be an important factor. It is possible that those techniques are not sensitive enough to detect the changes caused by PBMT in the cell mechanical properties evaluated. If there are changes caused by PBMT in the cells, they might be subtle and each method is not quite sensitive to detect the cell modifications. Thus, the changes might be hidden by other variations of each method (covered by the uncertainties) or in the cells (natural metabolic variations, for example). On the other hand, it is also possible that the number of cells evaluated was too small, so the natural variation of the cells masks the photo-treatment changes in those cells. Thus, it is possible that each technique is sensitive to detect the changes caused by the PBMT, but a larger number of cells should be analyzed to evidence those changes. These considerations are valid for both techniques: OMTC, with epithelial cells, for which just eight samples were used in each group; and defocusing microscopy, with RBCs, for which a few cells were evaluated (tenths of cells for each group).

A preliminary study was done to evaluate the uncertainties for the OMTC experiments. The results indicate that, if the differences between the control and photo-treated groups were greater than 7%, it would be possible to differentiate the groups with 95% of confidence level. This analysis is valid for the configuration used in this experiment.

For the confocal experiments with mouse fibroblast cells that were photo-treated with either red or infrared light, a few parameters were modified by PBMT. The total actin, the total actin density and the number of filaments decreased when comparing the photo-treated with the control samples. The total branch length does not seem to

change in any case. The phalloidin, which was the fluorescent probe used to detect the actin filaments, only binds to actin filaments, not to actin monomers [128]. This suggests that PBMT might have an effect in the actin filaments that may induce a slight depolymerization of the actin filaments. This depolymerization is milder than the one caused by cytochalasin D, as we can see in the confocal images. The actin filaments depolimerization might be related to the cytoskeleton reorganization that occur prior to cell division or cell migration, for example, or other actin filament functions. Regarding the nucleus and cell areas, it seems that the areas increase when comparing the photo-treated and control samples, mainly for the observations at short times after treatment. Specifically, the cell area increases were observed only for $5\ \mathrm{min}$ after treatment, while the nucleus area growth lasts a little longer and could be observed even $1\ \mathrm{h}$ after treatment. No changes were observed at $24\ \mathrm{h}$ post treatment, thus, after this period, the fibroblasts return to their natural characteristics. The increased area is consistent with the reduction of the actin filaments because these filaments are responsible for maintaining the membrane shape and rigidity. With the reduction of the actin filaments, the membrane might be more pliable than it is normally thus increasing the observed area.

A few experimental factors were compared in the confocal microscopy experiments: wavelength ($625\ \mathrm{nm}$ and $808\ \mathrm{nm}$), time after treatment ($5\ \mathrm{min}$, $1\ \mathrm{h}$ and $24\ \mathrm{h}$) and gel stiffness ($4\ \mathrm{kPa}$ and $16\ \mathrm{kPa}$). Among those, just the time after treatment appears to have significance, the choices of light wavelength and gel stiffness did not produce observable differences in the outcomes. Furthermore, the only analyzed parameter that has an influence of the time after treatment is the total actin density. Because of that, this parameter might be the most important in this experiment. The total actin density might be related to the mechanical properties of cells. Two papers from Chang and colleagues, [129], [130], correlate the actin fluorescence intensity with the apparent Young's modulus of actin fibers in cells, which is related to the mechanical properties and stiffness. In both papers, experiments with AFM and confocal microscopy were compared. In the first case, [129], for PC-12 rat neuron cells, they found a positive correlation between the actin apparent Young's modulus and the grey-scale intensity, but did not find any correlation between the apparent Young's modulus of microtubules and the grey-scale intensity. In the second case, [130], for RSC rat neuron cells, the authors compared two regions in the cells: one on top of an actin

stress fiber and the other in the cytosol, along the stress fiber. The stress fiber region presents higher apparent Young's modulus and actin concentration, also indicated by the higher actin fluorescence intensity, in the image. On the other hand, the cytosol region presents lower apparent Young's modulus and lower actin concentration. Guo and colleagues [131] used AFM experiments to show that stress fiber regions present lower elasticity when compared to regions without stress fibers. At last, Wang and Sun [132] showed that optical tweezers cause stronger deformations in hematopoietic cells with lower actin concentration than in hematopoietic cells with higher actin concentration. Considering this, it is reasonable to state that the total actin density is a promising indicator of mechanical properties and that the PBMT alters the cell mechanical properties and the cytoskeleton.

We cannot rule out that many of those changes, accessed with the confocal microscopy in fibroblast cells, could be explained by statistical fluctuation or could be caused by unknown factors other than the photo-treatment. This alternative is relevant because many groups that should be compatible, as they are equivalent, are not. Facts that corroborate this explanation are the cases where the parameter analyzed was incompatible when comparing photo-treated and control samples, but the median increased for some samples and decreased for others. For both cases, the modification might be related to other experimental factors that we do not have control, instead of being caused by the photo-treatment.

One could argue that the timescale of the experiments, with observations soon after photo-treatment, could explain the absence of modifications in the RBCs and epithelial cells with defocusing microscopy and OMTC techniques, respectively. Although the light energy is delivered and absorbed during the photo-treatment, effects observed in clinical trials might be noticed immediately after the therapeutic section until days after the photo-treatment. The primary effects of photo-treatment are short term, but the secondary effects are not. Thus, it would be possible that the effects that can be assessed by the methods used here are late effects, which did not yet happened by the time of the quantification of the cell's modifications were performed. The comparison between the three experiments (OMTC, defocusing and confocal microscopies) are not direct, because the techniques and the cell types used are different and additionally not the same PBMT doses were used. Despite that, in the confocal microscopy experiments, with fibroblasts, it was seen that, after $24\,\mathrm{h}$ of the

photo-treatment, the changes detected had disappeared. This suggests that the variations in the cytoskeleton are possibly related to primary effects, and might be observed at short intervals between the photo-treatment and the measurement. Therefore, the absence of observable effects of PBMT in the cells for the other experiments (OMTC and defocusing microscopy) might not be related to the timescale in which the experiments were performed, if the changes to be observed are related to cytoskeleton modifications.

Another factor that might cause the absence of changes in the photo-treated cells is the homeostasis. PBMT leads cells to homeostasis [13]. Thus, it is possible to argue that cell injury is necessary for PBMT action. It was shown that nutrient-deprived endothelial cells present regular actin filaments when photo-treated in comparison with nutrient deprived control endothelial cells [64]. The determination of homeostasis in cells in vitro is not easy; however, none of the cells used in this work were intentionally submitted to stress. Thus, they were probably in homeostasis. The RBCs did not pass through any process that could cause injury, except for the procedures necessary to the experiment. The epithelial cells were kept outside the incubator for around $20\ \mathrm{min}$. However, it was not possible to notice differences between the two groups of control epithelial cells, the ones that were kept in the incubator all the time and the ones that were held outside the incubator during the photo-treatment. This means that the period that the epithelial cells took outside the incubator was not "enough" to cause damage to epithelial cells and to remove them from homeostasis. At last, in the experiments with fibroblasts, some changes in the cytoskeleton were detected, but the fibroblasts were also not under stress conditions. Considering the three experiments and their characteristics regarding cell stress conditions, we could conclude that the PBMT might also have effect in cells in homeostasis and that cell injury is not strictly necessary to the PBMT effects.

Regarding the OMTC experiments, the exact process by which the beads bind to cells is unknown [80], but it is believed that the beads bind to the cytoskeleton through integrins [76], which are transmembrane receptors. As the integrin is a protein found in the cell membrane, probably, the most relevant type of cytoskeleton that beads interact is the actin filaments, because they are the most abundant cytoskeleton near the membrane. However, it is possible that the beads bind in regions with a different concentration of actin filaments, being more or less rigid. This would influence the bead

displacement and the parameters measured, such as the hysteresivity. As the analysis is performed in the entire image, considering the movement of many beads, the parameters assessed probably refer to a collective behavior of the cells. On the other hand, the confocal experiments looked specifically for the actin filaments, using a much smaller number of fibroblasts per image. This could refer to an individual behavior of the fibroblasts. Comparing the results of those two experiments, we could argue that the PBMT might have an individual effect on cells, which was evidenced by the confocal experiments. However, these effects do not reflect a cumulative effect on cells, which was quantified by the OMTC experiments.

At last, there are some considerations regarding the methodology used for the analysis of data from the confocal microscopy experiments. An automatic and reproducible analysis method was developed, using the *ImageJ* and *MATLAB* software. The methodology proved to be a good analysis routine, as it is automated, so it is objective and independent from the operator, which are essential characteristics for methods of analysis of large sets of data. Besides, it can access quantitative data from the confocal images. However, this method still has to be improved, to access the uncertainties related to the measurements, giving more reliability to the results. Therefore, the methodology developed here has potential to be used for other experimental configurations, which use actin filament staining and confocal images, or even adapted to experiments that use fluorescent markers for other cell structures, such as the microtubules, for example.

6. Conclusion

Concerning the optical magnetic twisting cytometry experiments (OMTC), as no modifications were observed in the ratio between the loss and elastic shear moduli (cell hysteresivity η) of epithelial cells, we conclude that the photobiomodulation therapy (PBMT) does not cause changes in epithelial cell hysteresivity, in the studied conditions.

For the experiments performed, bead displacement and hysteresivity usually did not present a lognormal distribution. Therefore, we conclude that possibly these parameters do not have a lognormal distribution.

Regarding the red blood cells analyzed with the defocusing microscopy, it is possible to determine that the PBMT does not cause significant changes in red blood cells, about the parameters evaluated: volume, radial profile, lateral and vertical fluctuation.

Alternatively, for both techniques, it is possible that the technique does not have sufficient sensitivity to detect changes in the analyzed variables, in the studied conditions. Furthermore, as the number of samples analyzed might be considered small, the changes caused by the photo-treatment could be hidden by cellular natural variations.

For the fibroblast cells analyzed with the confocal laser-scanning microcopy, it was possible to determine that the technique seems to be sensitive to detect changes in the cytoskeleton of photo-treated fibroblast cells. The total amount of actin, the total actin density and the number of filaments decreased for photo-treated samples when compared to control samples. This might suggest that the PBMT induce the depolymerization of the actin filaments. On the other hand, the nucleus and cell area of photo-treated samples increased when compared to control samples, for short times after treatment, until $1\ \mathrm{h}$, which is consistent with the actin filament reduction. All those detected changes disappear for longer times after photo-treatment, thus after $24\ \mathrm{h}$ they are not anymore detectable. The total branch length of the actin filaments does not suffer any changes.

It was not possible to detect differences between the red and the infrared wavelengths in the effects found in fibroblasts. It was neither possible to identify differences in the

gel stiffness in the effects found in fibroblasts. Related to the time after treatment, for the total actin density, this was an important factor, and the total actin density might be used to analyze the mechanical properties of cells and the effects of the PBMT.

There are indications that the modifications of some parameters of the fibroblasts might be a result of unknown factors or caused by statistical fluctuation. Thus, the uncertainties should be better estimated, in order to turn the results more reliable and the experimental conditions better understood and controlled.

At last, the methodology developed for the analysis of the confocal images has potential to be used for other experimental configurations, as it is automated and reproducible.

In summary, from data acquired with the three techniques used, it was found that the PBMT, in the red range, with the powers and energies used, could not cause noticeable modifications in red blood cells and epithelial cells *in vitro*. Nevertheless, for the fibroblast cells *in vitro* there are indications that PBMT, in the red and near-infrared ranges, causes small variations in the actin filaments, specifically in the total actin density. Furthermore, the methodology of analysis developed in this work might be used in other experimental configurations.

References

[1] R. Jin, X. Huang, H. Li, Y. Yuan, B. Li, C. Cheng, and Q. Li, “Laser therapy for prevention and treatment of pathologic excessive scars,” *Plast. Reconstr. Surg.*, vol. 132, no. 6, pp. 1747–1758, Dec. 2013.

[2] U. H. Mitchell and G. L. Mack, “Low-level laser treatment with near-infrared light increases venous nitric oxide levels acutely: a single-blind, randomized clinical trial of efficacy,” *Am. J. Phys. Med. Rehabil.*, vol. 92, no. 2, pp. 151–156, Feb. 2013.

[3] D. B. Höfling, M. C. Chavantes, A. G. Juliano, G. G. Cerri, M. Knobel, E. M. Yoshimura, and M. C. Chammas, “Low-level laser in the treatment of patients with hypothyroidism induced by chronic autoimmune thyroiditis: a randomized, placebo-controlled clinical trial,” *Lasers Med. Sci.*, vol. 28, no. 3, pp. 743–753, May 2013.

[4] M. Saglam, A. Kantarci, N. Dundar, and S. S. Hakki, “Clinical and biochemical effects of diode laser as an adjunct to nonsurgical treatment of chronic periodontitis: a randomized, controlled clinical trial,” *Lasers Med. Sci.*, vol. 29, no. 1, pp. 37–46, Jan. 2014.

[5] N. N. F. Lopes, H. Plapler, R. V Lalla, M. C. Chavantes, E. M. Yoshimura, M. A. B. da Silva, and M. T. S. Alves, “Effects of low-level laser therapy on collagen expression and neutrophil infiltrate in 5-fluorouracil-induced oral mucositis in hamsters,” *Lasers Surg. Med.*, vol. 42, no. 6, pp. 546–552, Aug. 2010.

[6] A. Cafaro, P. G. Arduino, G. Massolini, E. Romagnoli, and R. Broccoletti, “Clinical evaluation of the efficiency of low-level laser therapy for oral lichen planus: a prospective case series,” *Lasers Med. Sci.*, vol. 29, no. 1, pp. 185–190, Jan. 2014.

[7] J. F. L. de Castro, E. G. F. Abreu, A. V. L. Correia, C. da M. V. Brasil, D. E. da C. Perez, and F. de P. R. Pedrosa, “Low-level laser in prevention and treatment of oral mucositis in pediatric patients with acute lymphoblastic leukemia,” *Photomed. Laser Surg.*, vol. 31, no. 12, pp. 613–618, Dec. 2013.

[8] M. H. C. Pereira, N. C. Pinto, M. Okada, S. Tomimura, N. A. G. Stolf, E. M. Yoshimura, and M. C. Chavantes, “Post traumatic neuropatic pain non-responsive to conventional treatment: a clinical trial applying low level laser therapy,” in *29th Annual Conference of the American Society for Laser Medicine and Surgery*, 2009, p. 64.

[9] R. A. B. Lopes-Martins, S. C. Penna, J. Joensen, V. Vereid Iversen, and J. Magnus Bjordal, “Low Level Laser Therapy [LLLT] in Inflammatory and Rheumatic Diseases: A Review of Therapeutic Mechanisms,” *Curr. Rheumatol. Rev.*, vol. 3, no. 2, pp. 147–154, May 2007.

[10] N. C. Pinto, N. Shoji, M. Favoretto Junior, M. Muramatso, M. C. Chavantes, and N. A. G. Stolf, “New treatment applying Low Level Laser Therapy for acute dehiscence saphenectomy in post myocardial revascularization,” in *AIP*

CONFERENCE PROCEEDINGS, 2008, vol. 992, pp. 92–97.

[11] M. V. Pires de Sousa, C. Ferraresi, M. Kawakubo, B. Kaippert, E. M. Yoshimura, and M. R. Hamblin, “Transcranial low-level laser therapy (810 nm) temporarily inhibits peripheral nociception: photoneuromodulation of glutamate receptors, prostatic acid phophatase, and adenosine triphosphate,” *Neurophotonics*, vol. 3, no. 1, p. 15003, 2016.

[12] H. Chung, T. Dai, S. K. Sharma, Y.-Y. Huang, J. D. Carroll, and M. R. Hamblin, “The nuts and bolts of low-level laser (light) therapy,” *Ann. Biomed. Eng.*, vol. 40, no. 2, pp. 516–533, Feb. 2012.

[13] M. C. Chavantes, *Laser em Bio-Medicina - Princípios e Práticas*. São Paulo: Atheneu, 2009.

[14] T. Karu, “Primary and secondary mechanisms of action of visible to near-IR radiation on cells,” *J. Photochem. Photobiol. B.*, vol. 49, pp. 1–17, Mar. 1999.

[15] T. I. Karu, L. V Pyatibrat, and N. I. Afanasyeva, “Cellular effects of low power laser therapy can be mediated by nitric oxide.,” *Lasers Surg. Med.*, vol. 36, no. 4, pp. 307–14, Apr. 2005.

[16] D. B. Tata and R. W. Waynant, “Laser therapy: A review of its mechanism of action and potential medical applications,” *Laser Photon. Rev.*, vol. 5, no. 1, pp. 1–12, Jan. 2011.

[17] Y. Sakurai, M. Yamaguchi, and Y. Abiko, “Inhibitory effect of low-level laser irradiation on LPS-stimulated prostaglandin E2 production and cyclooxygenase-2 in human gingival fibroblasts,” *Eur. J. Oral Sci.*, vol. 108, pp. 29–34, 2000.

[18] M. R. Hamblin, T. Agrawal, and M. de Sousa, *Handbook of low level laser therapy*. Pan Stanford, 2016.

[19] A. C. de Magalhães, “Estudo da distribuição de luz vermelha e infravermelha em sangue humano diluído para circulação extracorpórea,” Dissertação de Mestrado - Instituto de Física da Universidade de São Paulo, 2011.

[20] M. H. L. Souza and D. O. Elias, *Fundamentos da circulação extracorpórea*, 2a. ed. Rio de Janeiro: Centro Editorial Alfa Rio, 2006.

[21] J. Butler, G. M. Rocker, and S. Westaby, “Inflammatory Response to Cardiopulmonary Bypass,” *Ann. Thorac. Surg.*, vol. 55, no. 2, pp. 552–559, 1993.

[22] G. F. Teixeira Filho (org.), *Temas atuais em circulação extracorpórea*. Porto Alegre, 1997.

[23] C. Blacher and J. P. Ribeiro, “Cirurgia de revascularização miocárdica sem circulação extracorpórea: uma técnica em busca de evidências,” *Arq. Bras. Cardiol.*, vol. 80, no. 6, pp. 656–662, Jun. 2003.

[24] B. Alberts, A. Johnson, L. Julian, M. Raff, K. Roberts, and P. Walter, *Biologia*

Molecular da Célula, 5ª Ed. Porto Alegre: Artes Médicas, 2010.

[25] L. Deng, X. Trepat, J. P. Butler, E. Millet, K. G. Morgan, D. A. Weitz, and J. J. Fredberg, “Fast and slow dynamics of the cytoskeleton,” *Nat. Mater.*, vol. 5, no. August, pp. 636–640, 2006.

[26] A. C. Guyton, *Fisiologia humana*. Rio de Janeiro: Interamericana, 1974.

[27] J. A. M. e Silva, “Reologia do sangue - Importância da deformabilidade eritrocitária,” in *Biopatologia Sanguínea e Vascular*, vol. 105, 1982, pp. 195–228.

[28] F. Gittes, B. Mickey, J. Nettleton, and J. Howard, “Flexural Rigidity of Microtubules and Actin Filaments Measured from Thermal Fluctuations in Shape,” *J. Cell Biol.*, vol. 120, no. 4, pp. 923–934, 1993.

[29] J. Zurlo, D. Rudacille, and A. M. Goldberg, *Animals and Alternatives in Testing: History, Science, and Ethics*. Mary Ann Liebert, 1994.

[30] H. Landecker, “New times for biology: nerve cultures and the advent of cellular life in vitro,” *Stud. Hist. Philos. Biol. Biomed. Sci.*, vol. 33, no. 4, pp. 667–694, 2002.

[31] B. Alberts, A. Johnson, L. Julian, M. Raff, K. Roberts, and P. Walter, *Molecular Biology of the Cell*, 4th ed. New York: Garland Science, 2002.

[32] J. R. Masters, “HeLa cells 50 years on: the good, the bad and the ugly,” *Nat. Rev. Cancer*, vol. 2, no. 4, pp. 315–319, Apr. 2002.

[33] R. Skloot, *The immortal life of Henrietta Lacks*. Crown Publishing Group, 2010.

[34] E. Molinaro, L. Caputo, and R. Amendoeira, *Conceitos e Métodos para a Formação de profissionais em Laboratórios de Saúde*. 2010.

[35] R. I. Freshney, M. G. Freshney, J. Wiley, and Sons, *Culture of Epithelial Cells*, 2nd ed. Glasgow: Wiley-Liss, 2002.

[36] H. Y. Chang, J.-T. Chi, S. Dudoit, C. Bondre, M. van de Rijn, D. Botstein, and P. O. Brown, “Diversity, topographic differentiation, and positional memory in human fibroblasts,” *Proc. Natl. Acad. Sci.*, vol. 99, no. 20, pp. 12877–12882, 2002.

[37] P. Rieske, B. Krynska, and S. A. Azizi, “Human fibroblast-derived cell lines have characteristics of embryonic stem cells and cells of neuro-ectodermal origin,” *Differentiation*, vol. 73, pp. 474–483, 2005.

[38] L. I. Grossweiner, *The Science of Phototherapy: an introduction*. Springer, 2005.

[39] R. Roelandts, “The history of phototherapy: Something new under the sun?,” *J. Am. Acad. Dermatol.*, vol. 46, no. 6, pp. 926–930, Jun. 2002.

[40] M. H. Niemz, *Laser-Tissue Interactions: Fundamentals and Applications*. Springer, 2004.

[41] K. C. Smith, “The first law of photochemistry and lasers,” *Off. J. World Assoc. Laser Ther.*, vol. 11, no. 4, pp. 162–163, 1999.

[42] N. N. Houreld, R. T. Masha, and H. Abrahamse, “Low-intensity laser irradiation at 660 nm stimulates cytochrome c oxidase in stressed fibroblast cells,” *Lasers Surg. Med.*, vol. 44, no. 5, pp. 429–434, 2012.

[43] C. M. M. Carnevalli, C. P. Soares, R. A. Zângaro, A. L. B. Pinheiro, and N. S. Silva, “Laser Light Prevents Apoptosis on Cho K-1 Cell Line,” *J. Clin. Laser Med. Surg.*, vol. 21, no. 4, pp. 193–196, 2003.

[44] R. A. B. Lopes-Martins, R. Albertini, P. S. L. L. Martins, J. M. Bjordal, and H. C. C. Faria Neto, “Spontaneous effects of low-level laser therapy (650 nm) in acute inflammatory mouse pleurisy induced by carrageenan,” *Photomed. Laser Surg.*, vol. 23, no. 4, pp. 377–381, Aug. 2005.

[45] I. Khan, E. Tang, and P. Arany, “Molecular pathway of near-infrared laser phototoxicity involves ATF-4 orchestrated ER stress,” *Sci. Rep.*, vol. 5, p. 10581, 2015.

[46] A. Amat, J. Rigau, R. W. Waynant, I. K. Ilev, and J. . Anders, “The electric field induced by light can explain cellular responses to electromagnetic energy: A hypothesis of mechanism,” *J. Photochem. Photobiol. B Biol.*, vol. 82, pp. 152–160, 2006.

[47] T. I. Karu, L. V Pyatibrat, and N. I. Afanasyeva, “A novel mitochondrial signaling pathway activated by visible-to-near infrared radiation.,” *Photochem. Photobiol.*, vol. 80, no. 2, pp. 366–72, 2004.

[48] N. N. Houreld, “Shedding Light on a New Treatment for Diabetic Wound Healing: A Review on Phototherapy,” *Sci. World J.*, vol. 2014, pp. 1–13, Jan. 2014.

[49] X. Luo, P. Duan, L. Li, S. Gao, X. Ni, J. Xu, H. Liu, Y. Yan, J. Liu, J. Ma, and J. Shen, “Influence of Low-level laser Radiation on Erythrocyte Membranes,” *Proccedings SPIE*, vol. 4916, pp. 140–142, 2002.

[50] J. Kujawa, L. Zavodnik, I. Zavodnik, V. Buko, A. Lapshyna, and M. Bryszewska, “Effect of Low-Intensity (3.75–25 J/cm2) Near-Infrared (810 nm) Laser Radiation on Red Blood Cell ATPase Activities and Membrane Structure,” *J. Clin. Laser Med. Surg.*, vol. 22, no. 2, pp. 111–117, 2004.

[51] J. Kujawa, K. Pasternak, I. Zavodnik, R. Irzmanski, D. Wróbel, and M. Bryszewska, “The effect of near-infrared MLS laser radiation on cell membrane structure and radical generation,” *Lasers Med. Sci.*, pp. 1663–1668, 2014.

[52] D. G. Siposan and A. Lukacs, “Effect of low-level laser radiation on some rheological factors in human blood: an in vitro study,” *J. Clin. Laser Med. Surg.*, vol. 18, no. 4, pp. 185–95, Aug. 2000.

[53] D. G. Siposan and A. Lukacs, “An in vitro study of the effects of low level laser radiation on human blood,” in *Proceedings of SPIE*, 2003, vol. 5287, pp. 108–119.

[54] M. S. Al Musawi, M. S. Jafar, B. T. Al-Gailani, N. M. Ahmed, F. M. Suhaimi, and N. Suardi, “In Vitro Mean Red Blood Cell Volume Change Induced by Diode Pump Solid State Low-Level Laser of 405nm,” *Photomed. Laser Surg.*, vol. 34, no. 5, pp. 1–4, 2016.

[55] T. Itoh, H. Murakami, K. Orihashi, T. Sueda, Y. Kusumoto, M. Kakehashi, and Y. Matsuura, “Low power laser protects human erythrocytes in an in vitro model of artificial heart-lung machines,” *Artif. Organs*, vol. 24, no. 11, pp. 870–873, 2000.

[56] K. Iijima, N. Shimoyama, M. Shimoyama, and T. Mizuguchi, “Effect of low-power He-Ne laser on deformability of stored human erythrocytes,” *J. Clin. Laser Med. Surg.*, vol. 11, no. 4, pp. 185–9, 1993.

[57] G. Y. Luo, L. Sun, and T. C. Y. Liu, “Aquaporin-1-Mediated Effects of Low Level He-Ne Laser Irradiation on Human Erythrocytes,” *Int. J. Photoenergy*, vol. 2012, pp. 1–5, 2012.

[58] Y. Cen and J. Y. Chen, “Photohemolysis of erythrocytes by He-Ne laser irradiation: the effect of power density,” *Lasers Med. Sci.*, vol. 19, no. 3, pp. 161–164, Jan. 2004.

[59] X. Q. Mi, J. Y. Chen, Y. Cen, Z. J. Liang, and L. W. Zhou, “A comparative study of 632.8 and 532 nm laser irradiation on some rheological factors in human blood in vitro,” *J. Photochem. Photobiol. B.*, vol. 74, no. 1, pp. 7–12, Mar. 2004.

[60] W. G. Zijlstra and A. Buursma, “Spectrophotometry of Hemoglobin: Absorption Spectra of Bovine Oxyhemoglobin, Deoxyhemoglobin, Carboxyhemoglobin, and Methemoglobin,” vol. 118, no. 4, pp. 743–749, 1997.

[61] Y. H. Liu, C. C. Ho, C. C. Cheng, Y. H. Hsu, and Y. S. Lai, “Photoradiation could influence the cytoskeleton organization and inhibit the survival of human hepatoma cells in vitro,” *Lasers Med. Sci.*, vol. 21, no. 1, pp. 42–8, Apr. 2006.

[62] R. T. Chow, M. A. David, and P. J. Armati, “830 nm laser irradiation induces varicosity formation, reduces mitochondrial membrane potential and blocks fast axonal flow in small and medium diameter rat dorsal root ganglion neurons: implications for the analgesic effects of 830 nm laser,” *J. Peripher. Nerv. Syst.*, vol. 12, no. 1, pp. 28–39, Mar. 2007.

[63] D. A. A. P. Oliveira, R. F. De Oliveira, M. Magini, R. A. Zangaro, C. P. Soares, and R. F. De Oliveira, “Assessment of cytoskeleton and endoplasmic reticulum of fibroblast cells subjected to low-level laser therapy and low-intensity pulsed ultrasound,” *Photomed. Laser Surg.*, vol. 27, no. 3, pp. 461–466, Jun. 2009.

[64] R. Ricci, M. C. Pazos, R. E. Borges, and C. Pacheco-Soares, “Biomodulation with low-level laser radiation induces changes in endothelial cell actin filaments and cytoskeletal organization,” *J. Photochem. Photobiol. B.*, vol. 95, no. 1, pp. 6–8, Apr. 2009.

[65] M. Monici, F. Cialdai, F. Ranaldi, P. Paoli, F. Boscaro, G. Moneti, and A. Caselli, “Effect of IR laser on myoblasts: a proteomic study,” *Mol. Biosyst.*, vol. 9, no. 6, pp. 1147–61, Jun. 2013.

[66] N. N. Houreld, S. M. Ayuk, and H. Abrahamse, “Expression of genes in normal fibroblast cells (WS1) in response to irradiation at 660nm,” *J. Photochem. Photobiol. B.*, vol. 130, pp. 146–52, Jan. 2014.

[67] H. J. Lim, M. S. Bang, H. M. Jung, J. I. Shin, G. S. Chun, and C. H. Oh, “A 635-nm light-emitting diode (LED) therapy inhibits bone resorptive osteoclast formation by regulating the actin cytoskeleton,” *Lasers Med. Sci.*, vol. 29, no. 2, pp. 659–670, 2014.

[68] P. Berntsen, C. Y. Park, B. Rothen-Rutishauser, A. Tsuda, T. M. Sager, R. M. Molina, T. C. Donaghey, A. M. Alencar, D. I. Kasahara, T. Ericsson, E. J. Millet, J. Swenson, D. J. Tschumperlin, J. P. Butler, J. D. Brain, J. J. Fredberg, P. Gehr, and E. H. Zhou, “Biomechanical effects of environmental and engineered particles on human airway smooth muscle cells,” *J. R. Soc. Interface*, vol. 7, pp. S331–S340, Jun. 2010.

[69] A. C. de Magalhães, D. Martinez, M. Z. J. Ferreira, E. M. Yoshimura, A. M. Alencar, and M. C. Chavantes, “How low-level laser therapy can change mechanical properties of cells,” in *Proccedings SPIE*, 2013, vol. 8569, p. 856909/1-6.

[70] B. Fabry, G. Maksym, J. Butler, M. Glogauer, D. Navajas, and J. Fredberg, “Scaling the Microrheology of Living Cells,” *Phys. Rev. Lett.*, vol. 87, no. 14, pp. 1–4, Sep. 2001.

[71] X. Trepat, M. Grabulosa, F. Puig, G. N. Maksym, D. Navajas, and R. Farré, “Viscoelasticity of human alveolar epithelial cells subjected to stretch,” *Am. J. Physiol. Lung Cell. Mol. Physiol.*, vol. 287, no. 5, pp. L1025–L1034, Nov. 2004.

[72] X. Trepat, L. Deng, S. S. An, D. Navajas, D. J. Tschumperlin, W. T. Gerthoffer, J. P. Butler, and J. J. Fredberg, “Universal physical responses to stretch in the living cell,” *Nature*, vol. 447, no. 7144, pp. 592–595, May 2007.

[73] K. K. Mandadapu, S. Govindjee, and M. R. K. Mofrad, “On the cytoskeleton and soft glassy rheology,” *J. Biomech.*, vol. 41, no. 7, pp. 1467–1478, Jan. 2008.

[74] M. Puig-de-Morales-Marinkovic, K. T. Turner, J. P. Butler, J. J. Fredberg, and S. Suresh, “Viscoelasticity of the human red blood cell,” *Am. J. Physiol. Cell Physiol.*, vol. 293, no. 2, pp. C597–C605, Aug. 2007.

[75] G. N. Maksym, B. Fabry, J. P. Butler, D. Navajas, D. J. Tschumperlin, J. D. Laporte, and J. J. Fredberg, “Mechanical properties of cultured human airway smooth muscle cells from 0.05 to 0.4 Hz,” *J. Appl. Physiol.*, vol. 89, no. 4, pp. 1619–1632, 2000.

[76] M. R. K. Mofrad and R. D. Kamm, *Cytoskeletal Mechanics Models and Measurements*. Cambridge University Press, 2006.

[77] J. M. Maloney, E. Lehnhardt, A. F. Long, and K. J. Van Vliet, “Mechanical fluidity of fully suspended biological cells,” *Biophys. J.*, vol. 105, no. 8, pp. 1767–1777, 2013.

[78] C. L. Dinardo, G. Venturini, E. H. Zhou, I. S. Watanabe, L. C. G. Campos, R. Dariolli, J. M. da Motta-Leal-Filho, V. M. Carvalho, K. H. M. Cardozo, J. E. Krieger, A. M. Alencar, and A. C. Pereira, “Variation of mechanical properties and quantitative proteomics of VSMC along the arterial tree,” *Am. J. Physiol. Heart Circ. Physiol.*, vol. 306, no. 4, pp. H505–H516, Feb. 2014.

[79] C. L. Dinardo, G. Venturini, S. V. Omae, E. H. Zhou, J. M. da Motta-Leal-Filho, R. Dariolli, J. E. Krieger, A. M. Alencar, and A. C. Pereira, “Vascular smooth muscle cells exhibit a progressive loss of rigidity with serial culture passaging,” *Biorheology*, vol. 49, pp. 365–373, 2012.

[80] X. Trepat, L. Deng, S. S. An, D. Navajas, D. J. Tschumperlin, W. T. Gerthoffer, J. P. Butler, and J. J. Fredberg, “Universal physical responses to stretch in the living cell - Supplementary information,” *Nature*, vol. 447, pp. 1–27, 2007.

[81] B. Fabry, G. N. Maksym, S. A. Shore, P. E. Moore, R. A. Panettieri Jr., J. P. Butler, and J. J. Fredberg, “Signal transduction in smooth muscle,” *J. Applyed Physiol.*, vol. 91, pp. 986–994, 2001.

[82] H. W. Lilliefors, “On the Kolmogorov-Smirnov test for normality with mean and variance unknown,” *J. Am. Stat. Assoc.*, vol. 62, no. 318, pp. 399–402, 1967.

[83] F. J. Massey Jr., “The Kolmogorov-Smirnov test for goodness of fit,” *J. Am. Stat. Assoc.*, vol. 46, no. 253, pp. 68–78, 1951.

[84] S. M. Ross, *Simulation*, 4th ed. San Diego: Elsevier Academic Press, 2006.

[85] U. Agero, C. Monken, C. Ropert, R. Gazzinelli, and O. Mesquita, “Cell surface fluctuations studied with defocusing microscopy,” *Phys. Rev. E*, vol. 67, no. 5, pp. 1–9, May 2003.

[86] U. Agero, L. G. Mesquita, B. R. A. Neves, R. T. Gazzinelli, and O. N. Mesquita, “Defocusing microscopy,” *Microsc. Res. Tech.*, vol. 65, no. 3, pp. 159–165, Oct. 2004.

[87] L. G. Mesquita, U. Agero, and O. N. Mesquita, “Defocusing microscopy: An approach for red blood cell optics,” *Appl. Phys. Lett.*, vol. 88, no. 13, p. 133901/1-3, 2006.

[88] J. Coelho Neto and O. N. Mesquita, “Living cell motility,” *Philos. Trans. A. Math. Phys. Eng. Sci.*, vol. 366, no. 1864, pp. 319–328, Feb. 2008.

[89] G. Glionna, C. K. Oliveira, L. G. Siman, H. W. Moyses, D. M. U. Prado, C. H. Monken, and O. N. Mesquita, “Tomography of fluctuating biological interfaces using defocusing microscopy,” *Appl. Phys. Lett.*, vol. 94, no. 19, p. 193701/1-3, 2009.

[90] G. Glionna, “Tomografia de Hemácias,” Tese de Doutorado - Instituto de Ciências Exatas da Universidade Federal de Minas Gerais, 2009.

[91] L. S. Gomes, “Desenvolvimento de métodos em microscopia óptica para obtenção de parâmetros biomecânicos de células e moléculas únicas,” Tese de

Doutorado - Instituto de Ciências Exatas da Universidade Federal de Minas Gerais, 2013.

[92] P. M. R. da Lapa, “Caracterização de parâmetros biomecânicos de hemácias via Microscopia de Desfocalização : Imagem tridimensional total e elasticidade da membrana,” Tese de Doutorado - Instituto de Ciências Exatas da Universidade Federal de Minas Gerais, 2014.

[93] B. Rappaz, A. Barbul, Y. Emery, R. Korenstein, C. Depeursinge, P. J. Magistretti, and P. Marquet, “Comparative study of human erythrocytes by digital holographic microscopy, confocal microscopy, and impedance volume analyzer,” *Cytometry. A*, vol. 73, no. 10, pp. 895–903, Oct. 2008.

[94] G. Tomaiuolo, “Biomechanical properties of red blood cells in health and disease towards microfluidics,” *Biomicrofluidics*, vol. 8, no. 5, 2014.

[95] M. Musielak, “Red blood cell-deformability measurement: review of techniques,” *Clin. Hemorheol. Microcirc.*, vol. 42, no. 1, pp. 47–64, Jan. 2009.

[96] Y. Park, C. Best, T. Kuriabova, M. Henle, M. Feld, A. Levine, and G. Popescu, “Measurement of the nonlinear elasticity of red blood cell membranes,” *Phys. Rev. E*, vol. 83, no. 5, pp. 1–6, May 2011.

[97] Y. Park, C. Best, K. Badizadegan, R. R. Dasari, M. S. Feld, T. Kuriabova, M. L. Henle, A. J. Levine, and G. Popescu, “Measurement of red blood cell mechanics during morphological changes,” *Proc. Natl. Acad. Sci. USA*, vol. 107, no. 15, pp. 6731–6736, Apr. 2010.

[98] James B. Pawley, *Handbook of Biological Confocal Microscopy*, 2nd ed. New York, 1995.

[99] M. Minsky, “Microscopy apparatus,” US 3013467 A, 1961.

[100] A. Nwaneshiudu, C. Kuschal, F. H. Sakamoto, R. R. Anderson, K. Schwarzenberger, and R. C. Young, “Introduction to confocal microscopy,” *J. Invest. Dermatol.*, vol. 132, no. 12, pp. 1–5, Dec. 2012.

[101] C. J. Niu, C. Fisher, K. Scheffler, R. Wan, H. Maleki, H. Liu, Y. Sun, C. A. Simmons, R. Birngruber, and L. Lilge, “Polyacrylamide gel substrates that simulate the mechanical stiffness of normal and malignant neuronal tissues increase protoporphyin IX synthesis in glioma cells,” *J. Biomed. Opt.*, vol. 20, no. 9, pp. 98002-1–7, 2015.

[102] R. S. Fischer, K. A. Myers, M. L. Gardel, and C. M. Waterman, “Stiffness-controlled three-dimensional extracellular matrices for high-resolution imaging of cell behavior,” *Nat. Protoc.*, vol. 7, no. 11, pp. 2056–66, Nov. 2012.

[103] C. Rotsch, K. Jacobson, and M. Radmacher, “Dimensional and mechanical dynamics of active and stable edges in motile fibroblasts investigated by using atomic force microscopy,” *PNAS Cell Biol.*, vol. 96, no. February, pp. 921–926, 1999.

[104] I. Yahara, F. Harada, S. Sekita, and K. Yoshihira, “Correlation between effects of 24 different cytochalasins on cellular structures and cellular events and those on actin in vitro immunofluorescence observations of cellular actin decoration with heavy eromyosin (HMM),” *J. Cell Biol.*, pp. 69–78, 1982.

[105] J. A. Cooper, “Effects of Cytochalasin and Phalloidin on Actin,” *J. Cell Biol.*, vol. 105, pp. 1473–1478, 1987.

[106] Sigma-Aldrich, “Product Information: Cytochalasins,” 2013.

[107] C. Rotsch and M. Radmacher, “Drug-induced changes of cytoskeletal structure and mechanics in fibroblasts: an atomic force microscopy study,” *Biophys. J.*, vol. 78, no. 1, pp. 520–535, 2000.

[108] M. Y. Shen, J. Michaelson, and H. Huang, “Rheological responses of cardiac fibroblasts to mechanical stretch,” *Biochem. Biophys. Res. Commun.*, vol. 430, no. 3, pp. 1028–1033, 2013.

[109] LifeTechnologies, “Cytochalasin D manual.” 2011.

[110] ThermoFisher-Scientific, “Actin Staining Protocol,” 2006. [Online]. Available: https://www.lifetechnologies.com/ca/en/home/references/protocols/cell-and-tissue-analysis/microscopy-protocol/actin-staining-protocol.html. [Accessed: 04-May-2015].

[111] J. E. Bear, T. M. Svitkina, M. Krause, D. A. Schafer, J. J. Loureiro, G. A. Strasser, I. V Maly, O. Y. Chaga, J. A. Cooper, G. G. Borisy, and F. B. Gertler, “Antagonism between Ena/VASP Proteins and Actin Filament Capping Regulates Fibroblast Motility,” *Cell*, vol. 109, pp. 509–521, 2002.

[112] K. E. Kasza, C. P. Broedersz, G. H. Koenderink, Y. C. Lin, W. Messner, E. A. Millman, F. Nakamura, T. P. Stossel, F. C. MacKintosh, and D. A. Weitz, “Actin Filament Length Tunes Elasticity of Flexibly Cross-Linked Actin Networks,” *Biophys. J.*, vol. 99, no. 4, pp. 1091–1100, 2010.

[113] I. Martin, A. Leitner, P. Walther, H. Herrmann, and O. Marti, “Model-based analysis of keratin intermediate filament assembly,” *J. Phys. D. Appl. Phys.*, vol. 48, pp. 1–11, 2015.

[114] D. Sturm, A. Alonso, C. Corbo, I. Osores, and C. Murillo, “Quantitative analysis of the effect of phosphorylated tau on cellular microfilament networks,” *Proc. SPIE*, vol. 8672, p. 86721U/1-6, 2013.

[115] A. M. Al-Jumaily, P. Mbikou, and P. R. Redey, “Effect of length oscillations on airway smooth muscle reactivity and cross-bridge cycling,” *AJP Lung Cell. Mol. Physiol.*, vol. 303, pp. L286–L294, 2012.

[116] NIH, “ImageJ - Image Processing and Analysis in Java.” [Online]. Available: http://imagej.nih.gov/ij/.

[117] M. B. Smith, H. Li, T. Shen, X. Huang, E. Yusuf, and D. Vavylonis, “Segmentation and tracking of cytoskeletal filaments using open active contours,” *Cytoskeleton*,

vol. 67, no. 11, pp. 693–705, 2010.

[118] A. Boudaoud, A. Burian, D. Borowska-Wykręt, M. Uyttewaal, R. Wrzalik, D. Kwiatkowska, and O. Hamant, “FibrilTool, an ImageJ plug-in to quantify fibrillar structures in raw microscopy images,” *Nat. Protoc.*, vol. 9, no. 2, pp. 457–463, 2014.

[119] D. F. T. da Silva, B. C. Vidal, D. M. Zezell, T. M. T. Zorn, S. C. Núñez, and M. S. Ribeiro, “Collagen birefringence in skin repair in response to red polarized-laser therapy,” *J. Biomed. Opt.*, vol. 11, no. 2, p. 024002/1-6, 2006.

[120] S. Nilufar, A. A. Morrow, J. M. Lee, and T. J. Perkins, “FiloDetect: automatic detection of filopodia from fluorescence microscopy images,” *BMC Syst. Biol.*, vol. 7, no. 66, pp. 1–12, 2013.

[121] D. Sage and D. Prodanov, “Miji.” 2011.

[122] T. W. Ridler and S. Calvard, “Picture thresholding using an iterative selection method,” *IEEE Trans. Syst. Man. Cybern.*, no. 8, pp. 630–632, 1978.

[123] T. C. Lee, R. L. Kashyap, and C. N. Chu, “Building Skeleton Models via 3-D Medial Surface Axis Thinning Algorithms,” *CVGIP: Graphical Models and Image Processing*, vol. 56, no. 6. pp. 462–478, 1994.

[124] I. Arganda-Carreras, R. Fernández-González, A. Muñoz-Barrutia, and C. Ortiz-De-Solorzano, “3D reconstruction of histological sections: Application to mammary gland tissue,” *Microsc. Res. Tech.*, vol. 73, no. 11, pp. 1019–1029, 2010.

[125] T. D. Gautheir, “Detecting Trends Using Spearman’s Rank Correlation Coefficient,” *Environ. Forensics*, vol. 2, no. 4, pp. 359–362, 2001.

[126] R. Taylor, “Interpretation of the Correlation Coefficient: A Basic Review,” *J. Diagnostic Med. Sonogr.*, vol. 6, pp. 35–39, 1990.

[127] W. P. Hu, J. J. Wang, C. L. Yu, C. C. E. Lan, G. S. Chen, and H. S. Yu, “Helium-neon laser irradiation stimulates cell proliferation through photostimulatory effects in mitochondria.,” *J. Invest. Dermatol.*, vol. 127, no. 8, pp. 2048–2057, 2007.

[128] J. E. Estes, L. A. Selden, and L. C. Gershman, “Mechanism of action of phalloidin on the polymerization of muscle actin,” *Biochemistry*, vol. 20, no. 4, pp. 708–712, 1981.

[129] C. T. Chang, C. C. K. Lin, and M. S. Ju, “Morphology and Ultrastructure-Related Local Mechanical Properties of Pc-12 Cells Studied By Integrating Atomic Force Microscopy and Immunofluorescence Imaging,” *J. Mech. Med. Biol.*, vol. 12, no. 5, p. 1250032/1-21, 2012.

[130] C. T. Chang, C. C. K. Lin, and M. Ju, “Combined atomic force microscopy and fluorescence microscopies to measure subcellular mechanical properties of live cells,” *J. Mech. Med. Biol.*, vol. 13, no. 4, p. 1350057/1-15, 2013.

[131] Q. Guo, Y. Xia, M. Sandig, and J. Yang, “Characterization of cell elasticity correlated with cell morphology by atomic force microscope,” *J. Biomech.*, vol. 45, no. 2, pp. 304–309, 2012.

[132] K. Wang and D. Sun, “Influence of semiflexible structural features of actin cytoskeleton on cell stiffness based on actin microstructural modeling,” *J. Biomech.*, vol. 45, no. 11, pp. 1900–1908, 2012.

[133] R&DSystems, “Protocol for Making a 4% Formaldehyde Solution in PBS.” [Online]. Available: https://www.rndsystems.com/resources/protocols/protocol-making-4-formaldehyde-solution-pbs. [Accessed: 20-Apr-2015].

[134] ThermoFisher-Scientific, “DAPI Protocol for Fluorescence Imaging.” [Online]. Available: https://www.lifetechnologies.com/ca/en/home/references/protocols/cell-and-tissue-analysis/protocols/dapi-imaging-protocol.html. [Accessed: 04-May-2015].

Appendix A – Kolmogorov-Smirnov test and Lilliefors test

The Kolmogorov-Smirnov test for one sample is widely used to test whether a statistical sample is described by a specific distribution. The test compares the experimental cumulative distribution function with the reference cumulative distribution function. Furthermore, the null hypothesis is that the reference function describes the experimental function. The reference cumulative distribution function will be called as $F_0(x)$, and represents the probability of finding a sample element smaller than or equal to *x*. If the experimental function is close to the reference function, we can assure that the reference represents the sample. The greatest distance between the reference function $F_0(x)$ and the experimental function $F_e(x)$ is the test value *KS*. Thus, $KS = max|F_0(x) - F_e(x)|$, where $F_e(x) = m/M$, *m* is the number of observations smaller than *x* and *M* is the total number of observations. The value *KS* is compared with values on a specific table, which means that it is compared with the critical values for different significance levels. The graph in Figure A.1 shows the test graphically. [83]

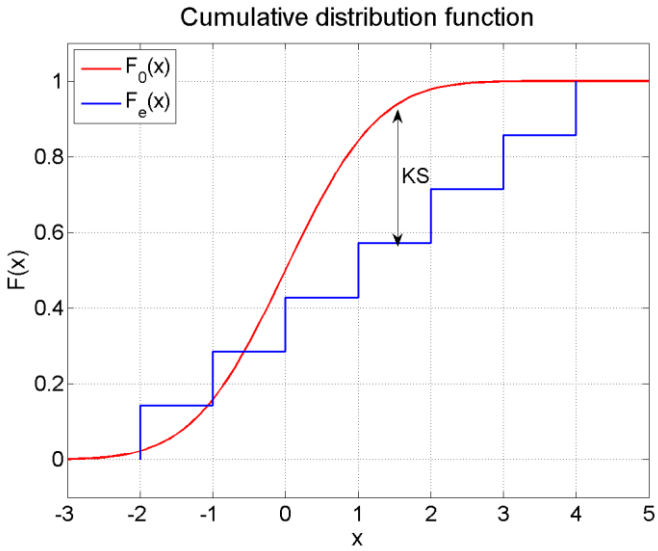

Figure A.1: Graph of the cumulative distribution functions. The reference cumulative distribution function is $F_0(x)$ and the experimental is $F_e(x)$. The largest distance between the two curves represents the Kolmogorov-Smirnov test value (*KS*).

Often the Kolmogorov-Smirnov test appears as a more accurate alternative compared to the χ^2 test, for samples of any size [83]. However, to use such testing it is necessary to know the distribution parameters. If any parameter has to be estimated, this test is not adequate. For those cases, in which the parameters are not known, the Lilliefors

test should be used instead, in particular whether the tested distribution is normal, and any parameter has to be estimated through the statistical sample. The statistical test value is the same in both cases, the difference is the table used, which means the critical values for the different significance levels, this happens because the probability distribution of the test value is different when the parameters are either known or estimated. [82]

Appendix B – Two-sample rank sum test

The two-sample rank sum test, also known as Wilcoxon two-sample test or Mann-Whitney two-sample test [84] is a non-parametric test, which can be used to check whether two independent data sets originate from the same distribution. The hypothesis to be tested (null hypothesis) is that data from the two samples are independent and equally distributed. The test is done as follows: all values are sorted together and ranked, all ranks are considered to be different and the order unique[§].The test value will be the rank sum of the first statistical sample, called as standard sample, which can be any one of the two samples. The null hypothesis will be rejected, if the probability of finding statistical samples with test values greater or lower than the standard sample test value is too small. Actually, here, greater and lower are inclusive, so ≥ or ≤, respectively.

A computer simulation by hit or miss Monte Carlo method was used to estimate the p-value. For that, all rank settings were considered as equiprobable. As the null hypothesis says that data are identically distributed, the ranks of the standard sample data (size *n*) can be assumed to have the same distribution of a random drawing of *n* ranks, among all the possible ranks for the two statistical samples. Therefore, the simulation is done drawing these ranks and summing them. The $P_{H_0}\{R \leq r\}$ value is estimated by counting how many simulations have the test value lower or equal to the standard sample test value, where *r* is the standard sample rank sum and *R* is the drawn sample rank sum. The same thing is done for $P_{H_0}\{R \geq r\}$. The p-value is given by

$$\text{p-value} = 2\ min\left(P_{H_0}\{R \leq r\}, P_{H_0}\{R \geq r\}\right)$$

because too large or too small test values are rejected. It is important to remember that the p-value is the probability of obtaining statistical samples more extreme than the initial statistical sample. The scheme of Figure B.1 shows two examples of this test that help to understand it.

[§] When there are equal values, their ranks are considered the same and corresponds to the average of the ranks they occupy.

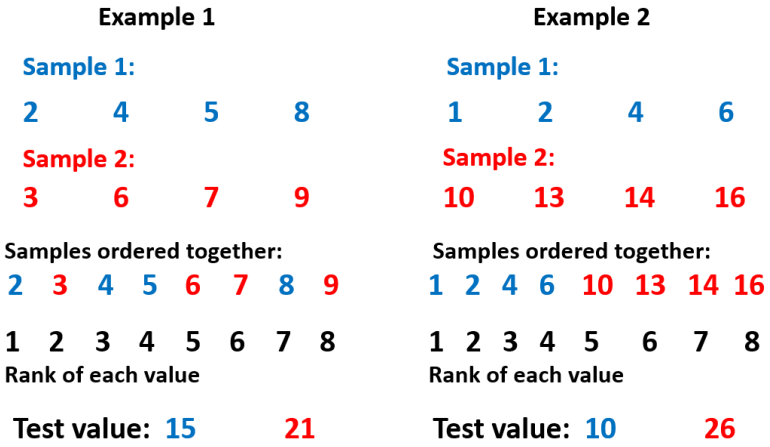

Figure B.1: Two examples of the two-sample rank sum test. To perform the test, the two samples are sorted together and then ranked. The test value is the sample rank sum. Example 1 shows the case that data from the two samples are merged. On the other hand, for example 2, samples are separated. The probability that the two samples from example 1 come from the same distribution is much larger than the probability that the two samples from example 2 come from the same distribution. Indeed, the p-values are 49% for example 1 and 2,9% for example 2.

Any of the two statistical samples can be considered as the standard sample. However, the sample with the smallest test value was considered the standard sample. This is because through the simulation the p-value obtained for the sample with the smallest test value is, on average, larger than the p-value obtained for the largest test value sample. Hence, the smallest test value sample is chosen as the standard sample because actually, the test is done to show that the two statistical samples are not from the same distribution, which means, to reject the null hypothesis. If the largest p-value is used, and it is still small, thus, the chance of the null hypothesis being false is larger.

Appendix C – Polyacrylamide gel substrate full protocol

Piranha acid cleaning

To do in the clean room. It takes less than $1\ \mathrm{h}$.

Wear goggles, face shield, protective gloves and cover.

Prepare 3:1 ratio sulfuric acid and H_2O_2 (peroxide) respectively. $150\ \mathrm{mL}$ H_2SO_4 + $50\ \mathrm{mL}$ H_2O_2 is the right amount for our Pyrex dish volume.

Pour each in separate beakers cleaned and dried with clean room paper.

Pour sulfuric acid first slowly. Pour peroxide after sulfuric acid. Add hydrogen peroxide to sulfuric acid very slowly, never vice versa.

Put the coverslips in the mixture.

Time your timer to $5\ \mathrm{min}$.

Prepare one large beaker filled with distilled water and one small beaker with ethanol.

When $5\ \mathrm{min}$ is up take, fish the coverslips, dip them in the water beaker and put in the ethanol beaker.

Once all coverslips are done, cover the beaker with parafilm. They might be used after at least one hour.

Leave Pyrex dish at the bottom of hood with a note with “Piranha + *X* water, your name, date”

Return the next day and pour it into the sink. Otherwise, $10\times$ volume of water can also neutralize it to throw into the sink.

Activation

It takes around $2.5\ \mathrm{h}$ to $3\ \mathrm{h}$.

Materials:

- Coverslips in ethanol;
- Glass dishes (glass petri dishes);
- Bunsen burner and lighter;
- $25\ \mathrm{mL}$ pipette tip, $5\ \mathrm{mL}$ pipette tip and P1000 pipette;
- (3-aminopropyl)triethoxysilane;
- Tweezers and metal spatula;
- 2 of $50\ \mathrm{mL}$ graduated cylinders;
- 2 of $500\ \mathrm{mL}$ beaker;
- Gluteraldehyde;
- PBS;
- Stir bar, stir plate (same as hot plate) and timer;
- $\sim 500\ \mathrm{mL}$ distilled water and $\sim 100\ \mathrm{mL}$ deionized water;
- Kimwipes;
- Dry glass dishes.

Pry open (3-aminopropyl)triethoxysilane bottle and make a solution with

- $49.74\ \mathrm{mL}$ deionized water
- $0.26\ \mathrm{mL}$ (3-aminopropyl)triethoxysilane

Turn on the Bunsen burner and flame ethanol off by passing coverslips through flame as many times as needed (do not let the coverslips on flame, otherwise they will pop).

Put dry coverslips on glass dish, on the edges, letting the middle open.

Place glass dish on stir plate, place stir bar on dish, pour the (3-aminopropyl)triethoxysilane solution in and stir at the lowest setting for $30\ \mathrm{min}$.

Check if oven is on ($50\ ^{\circ}\mathrm{C}$, setting right before 7) and if not, preheat it.

After stirring, wash $6\times$ ($\sim 50\ \mathrm{mL}$ each) with distilled water, blot off water with Kimwipe and place in oven for $\sim 30\ \mathrm{min}$ (or until everything is dry).

When dry, remove coverslips from oven.

Make gluteraldehyde-PBS solution:

- $44\ \mathrm{mL}$ deionized water;

- 5 mL PBS;
- 1 mL glutaraldehyde.

When the coverslips were cool, place them on the stir plate, put the stir bar in and pour in the gluteraldehyde-PBS solution, stir for 30 min.

After stirring, wash the coverslips 3× (~50 mL each) with distilled water.

Air-dry on a bench.

They can be stored for up to two months in a desiccator.

Making polyacrylamide gel substrate

It takes around 1.5 h for around 20 coverslips.

Materials:

- Ammonium persulfate (APS) powder;
- Petri dishes for the coverslips (usually we put 8 in each dish);
- Rain-X (substance usually used in car windows to make glass hydrophobic);
- Test tubes;
- Glass slides;
- Kimwipes;
- 1 mol/dm^3 HEPES;
- 50 $mmol/dm^3$ HEPES;
- 40% acrylamide;
- 2% bis-acrylamide;
- TEMED (N, N, N, N - tetramethylethylenediamine);
- ~5 mL deionized water for each gel;
- P1000, P200 and 3 of P20 pipettes;
- 25 mL and 5 mL pipette tips;
- Beaker;

As early as possible, Rain-X the test tubes by spraying once into each, rinse them with distilled water.

Polish glass slides with Rain-X soaked Kimwipe, rinse them with distilled water, air dry if possible, but Kimwipe if necessary.

Prepare APS in a 1.5 mL microtube (Eppendorf tube), it is a 10% (weight/volume) solution.

- 0.1 g APS
- 1 mL deionized water

To mix, flick, invert tube.

Place glass slides in glass dishes and let the coverslips near.

Mix gels thoroughly:

- 4 kPa (total 5 mL)
    - 3.6375 mL deionized water (3.6 mL+37.5 μL);
    - 937.5 μL 40% acrylamide (930 μL+7.5 μL);
    - 375 μL 2% bis-acrylamide;
    - 50 μL HEPES (1 mol/dm^3).
- 16 kPa (total 5 mL)
    - 3.0875 mL deionized water (3 mL + 87.5 μL);
    - 1.5 mL 40% acrylamide;
    - 362.5 μL 2% bis-acrylamide (360 μL + 2.5 μL);
    - 50 μL HEPES (1 mol/dm^3).

Use a 5 mL pipette to mix gel thoroughly and separate each into 2 of 2.5 mL aliquots.

Add 10 μL of TEMED to test tube, swirl. Can pipette solution up and down to mix TEMED properly.

Add 15 μL of APS. Can pipette solution up and down to mix APS properly.

Quickly pipet 3 μL onto each glass slide and invert coverslips onto them. You will likely only be able to do 2 to 3 glass slides before the gel polymerize.

Let gel polymerize for 20 min to 30 min. The gel will have polymerized in the test tube also, though there may be a thin layer of liquid at the top. Heat is emitted.

During polymerization, check if you have $500\ \mathrm{mL}$ or more of $50\ \mathrm{mmol/dm^3}$ HEPES. If not, make some:

- $475\ \mathrm{mL}$ deionized water
- $25\ \mathrm{mL}$ $1\ \mathrm{mol/dm^3}$ HEPES

Flood glass slides, with coverslips with $50\ \mathrm{mmol/dm^3}$ HEPES ($\sim 75\ \mathrm{mL}$) after they have polymerized.

Take out petri dishes and fill each with $10\ \mathrm{mL}$ of $50\ \mathrm{mmol/dm^3}$ HEPES.

Using tweezers gently push coverslip sideway until an edge is hanging off the glass slide, lift and place gel side-up in a petri dish. Repeat for each coverslip.

Rinse $5\times$ with $50\ \mathrm{mmol/dm^3}$ HEPES. Let in the 6th change of HEPES.

Wrap petri dish edges with parafilm.

Can be stored in $50\ \mathrm{mmol/dm^3}$ HEPES at $4\ ^\circ\mathrm{C}$ for 2 or 3 weeks.

Cross-linking gels

To do in the clean room. It takes around $1.5\ \mathrm{h}$ for around 40 coverslips.

Put in an ice bucket:

- Sulfo-SANPAH ($100\ \mu\mathrm{L}$ for each coverslip; each sulfo-SANPAH is $1\ \mathrm{mL}$; bring as many + 1);
- Deionized water ($1\ \mathrm{mL}$ for each sulfo-SANPAH);
- Coverslips with gels;
- Collagen or matrigel solution at $100\ \mu\mathrm{g/mL}$ concetration;

Also get:

- P1000, P200, P20 pipettes;
- New petri dishes ;
- PBS.

Sterile packages should be opened only in the clean room, if it was opened anywhere else, cannot be used in the clean room. So, petri dishes, PBS and pipette tips, might be left on the clean room to be used there.

Once in the clean room, gather:

- Glass dish;
- Parafilm and scissors;
- Tweezers (clean them with ethanol);
- Paper towel.

Fill glass dish with PBS, $\sim 100\ \mathrm{mL}$.

Place a folded paper towel on the table.

Mix the sulfo-SANPAH by adding $960\ \mu\mathrm{L}$ of deionized water (protect sulfo-SANPAH from light with the hands).

Unwrap old petri dish and place parafilm on lid of old dish.

Lift coverslip, blot off excess HEPES and place coverslip, gel side up, on parafilm covered lid. Put a maximum of 4 coverslips each time.

Add $50\ \mu\mathrm{L}$ of sulfo-SANPAH to each gel and put in UV cross-linker for $30\ \mathrm{s}$.

Place parafilm on new dish bottom.

Take coverslip out of UV cross-linker. Blot off excess sulfo-SANPAH and rinse in PBS, blot off excess PBS and put it back on old lid. Do it for each coverslip.

Add $50\ \mu\mathrm{L}$ more sulfo-SANPAH in each coverslip and place in UV cross-linker for more $30\ \mathrm{s}$.

Add a $20\ \mu\mathrm{L}$ collagen/matrigel drop for each coverslip, on the new dish bottom with parafilm.

Take coverslip out of UV cross-linker. Blot off excess sulfo-SANPAH and rinse in PBS, blot off excess PBS and invert onto collagen/matrigel drops. Do it for each coverslip. Cover with lid.

Once done with all the gels, use parafilm to seal the edges of the new petri dishes.

Throw garbage out, use RO water to pour PBS down the sink.

Wipe down lab area with ethanol.

Allow gels to cross-link overnight at 4 °C.

On the other day, in a sterile hood, place gel side up into a new petri dish in sterile PBS. Rinse 4× to 6× with PBS and let it in the last PBS change.

Can be stored in PBS at 4 °C for up to 2 weeks.

Matrigel solution

Take Matrigel from the freezer and put in the fridge for a few hours (to thaw).

Aliquot PBS (990 µL for 1 mL final volume, or 1485 µL for 1.5 mL final volume) and put it on ice to cool down.

When Matrigel is liquid, put in a container with ice (it might be a glass container).

Dissolve 1:100, so for 1 mL that is the 990 µL of PBS and 10 µL of Matrigel; for 1.5 mL that is the 1485 µL PBS and 15 µL Matrigel.

Vortex for 5 s.

Return stuff for freezer or fridge (in case of the Matrigel solution that will be used soon).

Appendix D – Cell fixation, permeabilization and staining

All quantities were set for 24 well plate.

Cell fixation with formaldehyde

It takes around $40\ \mathrm{min}$.

Materials:

- 4% formaldehyde solution in PBS;
- PBS;
- Pasteur pipette;
- Automatic pipette +2 polystyrene pipettes (size depends on the number of wells).

For all substances use $1\ \mathrm{mL}$ per well.

Take media off.

Wash the cells $3\times$ with PBS.

Put formaldehyde in each well and let $20\ \mathrm{min}$ at room temperature.

Wash the cells $3\times$ with PBS.

Put PBS in each well to maintain hydrated and put on the fridge for the time needed.

The first pipette is for the first 3 washes and for the formaldehyde, the second is for the last 3 washes.

Use the Pasteur pipette to take off liquids.

Permeabilization

It takes around $20\ \mathrm{min}$.

This step is done after all cells were fixed.

Materials:

- 0.1% solution of Triton X-100 in PBS;
- PBS;
- Pasteur pipette;
- Automatic pipette + 2 polystyrene pipettes (size depends on the number of wells);
- Rotator plate.

For all substances use $1\ \mathrm{mL}$ per well.

Take PBS off the wells using the vacuum and Pasteur pipette.

Add Triton X-100 solution in each well.

Put it on the rotator plate in low rotation for $5\ \mathrm{min}$.

Wash $3\times$ with PBS

Staining with fluorescence markers (AF488 and DAPI) and slide mounting

It takes around $1\ \mathrm{h}$.

This step is done after all cells were fixed and permeabilized.

Materials:

- 1% solution of BSA in PBS;
- AF488 stock solution;
- DAPI stock solution (stock solution is $14.3\ \mathrm{mmol/dm^3}$ and intermediate solution is $300\ \mu\mathrm{mol/dm^3}$; it will be probably frozen, so, it has to be taken from the freezer a few minutes before using);
- Aluminum foil;
- PBS;
- Deionized water;
- Pasteur pipette;
- Automatic pipette + 2 polystyrene pipettes (size depends on the number of wells);
- P1000, P200, P20 pipettes and tips;

- Eppendorf tube;
- Glass slides;
- Pencil;
- ProLong Gold;
- Rotator plate.

Make AF488 solution: add $5\ \mu L$ of AF488 in $200\ \mu L$ of 1% BSA in PBS, for each well (consider one more well when using up to 20 wells). Protect from light.

Take PBS off the wells.

Add $200\ \mu L$ per well of AF488 solution.

Wrap the plate with aluminum foil.

Put it on the rotator plate for $20\ min$.

Meanwhile, check if there is DAPI intermediate solution, otherwise, do it: add $97.9\ \mu L$ of PBS and $2.1\ \mu L$ of DAPI stock solution in an eppendorf tube. Protect from light.

Make $300\ nmol/dm^3$ DAPI solution: dissolve 1:1000 the intermediate solution in 1% BSA in PBS. Protect from light.

After the $20\ min$, wash $3\times$ with PBS ($1\ mL$ per well).

Add $300\ \mu L$ per well of DAPI $300\ nmol/dm^3$ solution.

Wrap the wells in aluminum foil.

Put it on the rotator plate for $5\ min$.

Wash $2\times$ with PBS ($1\ mL$ per well) and once with deionized water.

Let it air dry protected from light.

Get ProLong Gold and discard the first drop in case it has air bubbles.

Put one drop of ProLong Gold for each coverslip on a clean glass slide (maximum of 3 coverslips at each glass slide).

Take each coverslip from the well using tweezers and put them on top of the drop. The cells must be face down on the glass slide. To avoid air bubbles, put the coverslip by the drop edge.

Let it at least $24\ \mathrm{h}$ at room temperature in a flat surface, in dark, to dry. Then put it on fridge, in the dark.

Obs 1: Always use pencil to write on the glass slide. Put important information, like: light or no light; fixing time; fluorescent markers.

Obs 2: Keep DAPI intermediate solution on the fridge, protected from light.

Formaldehyde 4%

Adapted from [133].

Caution: Formaldehyde is toxic. Please read the MSDS before working with this chemical. Gloves and safety glasses should be worn and solutions made inside a fume hood.

Please read the protocol in its entirety before starting.

Materials:

- Deionized water (or RO water);
- HCl (Dilute);
- NaOH ($1\ \mathrm{N}$) (around $2.5\ \mathrm{mL}$) (our stock solution is $6\ \mathrm{N}$, so add $166.7\ \mu\mathrm{L}$ of this in $833.3\ \mu\mathrm{L}$ of RO water to make $1\ \mathrm{N}$);
- Paraformaldehyde (PFA) powder (metals to avoid: brass, steel of all types and surface treatments, cooper);
- PBS;
- Filter units;
- Glassware and stir bar (dedicated for formaldehyde solution);
- Gloves and eye protection;
- Hot plate with magnetic stirrer;
- Thermometer;
- Ventilated hood.

For $1\ \mathrm{L}$ of 4% formaldehyde, add $800\ \mathrm{mL}$ of PBS to a glass beaker on a stir plate in a ventilated hood. Heat while stirring to approximately $60\ °\mathrm{C}$. Take care because the solution cannot boil.

Add $40\ \mathrm{g}$ of PFA powder to the heated PBS solution.

The powder will not immediately dissolve into solution. Slowly raise the pH by adding $1\ \mathrm{mol/dm^3}$ NaOH dropwise from a pipette until the solution clears.

Once the PFA is dissolved, the solution should be cooled and filtered.

Adjust the volume of the solution to $1\ \mathrm{L}$ with PBS.

Recheck the pH, and adjust it with small amounts of dilute HCl to approximately 6.9.

The solution can be aliquoted and either frozen or stored at $2\ °\mathrm{C}$ to $8\ °\mathrm{C}$ for up to one month.

AF488 stock solution

Adapted from [110].

Materials:

- AF488 phalloidin vial;
- $1.5\ \mathrm{mL}$ methanol.

Dissolve the vial contents in the methanol. The final concentration is $200\ \mathrm{units/mL}$, which is equivalent to approximately $6.6\ \mathrm{\mu mol/dm^3}$.

One unit of phallotoxin is the amount of material used to stain one microscope slide of fixed cells, and is equivalent to $5\ \mathrm{\mu L}$ of methanolic stock solution for the fluorescent phallotoxins.

The stock solution should be stored at $-20\ °\mathrm{C}$ in the dark.

DAPI stock solution

Adapted from [134].

Materials:

- DAPI vial;
- $2\ \mathrm{mL}$ deionized water or dimethylformamide (DMF).

Dissolve the vial contents in the water or DMF. The final concentration is $14.3\ \mathrm{mmol/dm^3}$ ($5\ \mathrm{mg/mL}$). As DAPI is poorly dissolved in water, to sonicate might be necessary to dissolve it properly.

The stock solution should be stored at $2\ ^{\circ}\mathrm{C}$ to $6\ ^{\circ}\mathrm{C}$ up to 6 months or at $-20\ ^{\circ}\mathrm{C}$ for longer periods, always in the dark.

Appendix E – Result graphs

All graphs with the results for all the parameters analyzed, for all experiments are presented here. The first graphs show the absolute parameters, comparing photo-treated and control groups, for nucleus area, cell area, total actin, total actin density, the number of filaments and total branch length. The following graphs show the correlation coefficients and coefficients of determination, for the combinations between the parameters cell area (Ar), total actin (TA), the number of filaments (NF) and total branch length (BL). After that, there are the slopes for the correlation graphs, for the parameters with high correlation coefficient (Ar vs TA, Ar vs NF and NF vs TA). For these, each page shows the graphs with the experiments with one wavelength, either $625\ \mathrm{nm}$ or $808\ \mathrm{nm}$, both gel stiffness, $4\ \mathrm{kPa}$ (graphs on the left side) and $16\ \mathrm{kPa}$ (on the right side), and the three fixation times after treatment, $5\ \mathrm{min}$ (first row of graphs), $1\ \mathrm{h}$ (second row) and $24\ \mathrm{h}$ (third row). At last, there are the graphs comparing the relative parameters, with all experiments in the same graph. The relative parameter is defined as the ratio of the photo-treated median and the control median, for that specific parameter. For these last graphs, there are two projections, the first projection has the time after treatment in the horizontal axis and different symbols representing different gel stiffness; the second projection has the gel stiffness in the horizontal axis and the different symbols representing the different times after treatment. The relative parameters shown are nucleus area, cell area, total actin, total actin density, the number of filaments, total branch length and the slopes for the correlation graphs, for the parameters with high correlation coefficient (Ar vs TA, Ar vs NF and NF vs TA).

For some graphs, the vertical scale is zoomed, to facilitate the visualization and, because of that, some outliers are missing. For those cases, the graphs are repeated with the full vertical scale, after the graphs comparing that parameter for all the experiments, with the standardized vertical scale. The graphs with zoomed scale are outlined in black.

Some graphs have a “+”, “-” or “=” signal in the horizontal axis. These represent the comparison between the control and photo-treated median. For the “+” signal, the median of the parameter shown in the graph for the photo-treated sample is higher than for the control group, for the “-“ signal the median is smaller in photo-treated group than in the control and for the “=” signal the photo-treated median is equal to the control

median. The colors represent the compatibility according to the two-sample rank sum test and $p < 5\%$, red color means that the two sample data are incompatible, while the green color means that the sample data are compatible.

Each graph was divided into regions that represent different imaging days, the label on top of each region describes the replications of that experiment and the numbers before it represent the confocal imaging date (day or month and day).

In the graphs with the correlation slopes, the error bars represent two times the slope uncertainty. Thus, if the error bars do not overlap, the slopes were considered incompatible, otherwise, they were considered compatible.

For the graphs with the comparison between all experiments, the relative parameter is represented. It is defined as the ratio of the photo-treated median and the control median. The green outlined symbols represent samples in which the photo-treated and control group data were compatible according to the two-sample rank sum test and confidence interval of 95%.

Nucleus area

625 nm

4 kPa

16 kPa

5 min

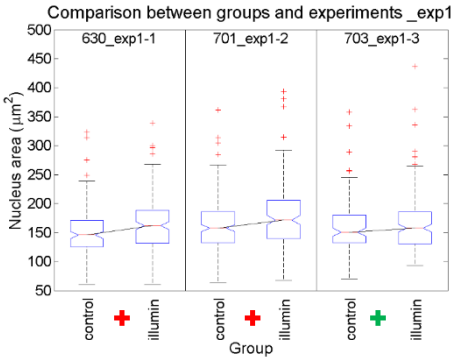

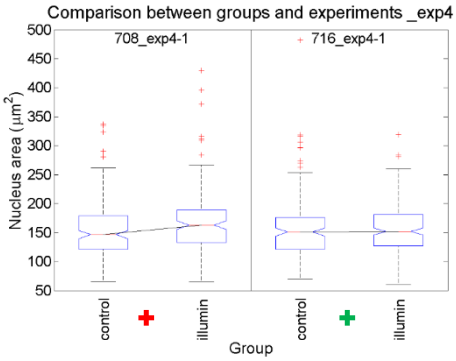

1 h

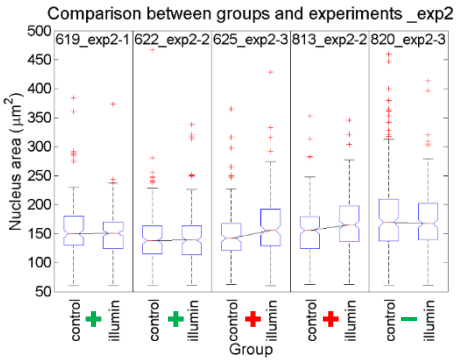

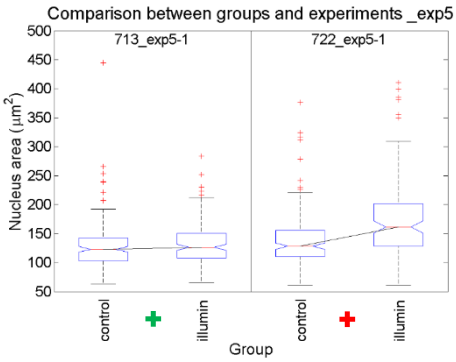

24 h

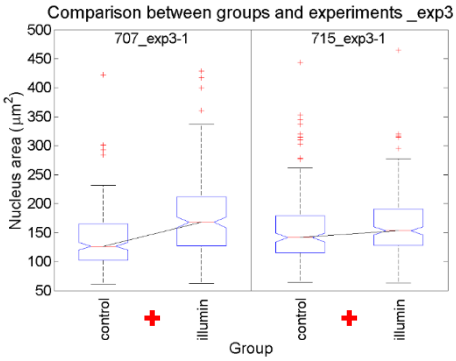

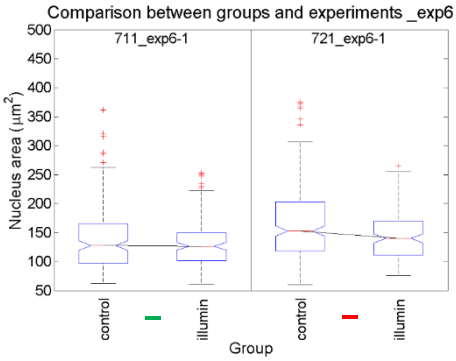

808 nm

	4 kPa	16 kPa
5 min	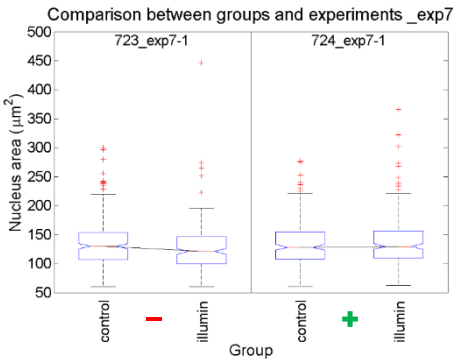	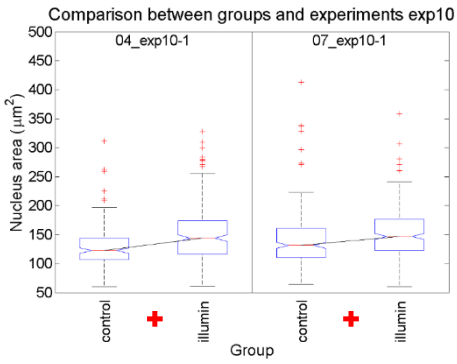
1 h	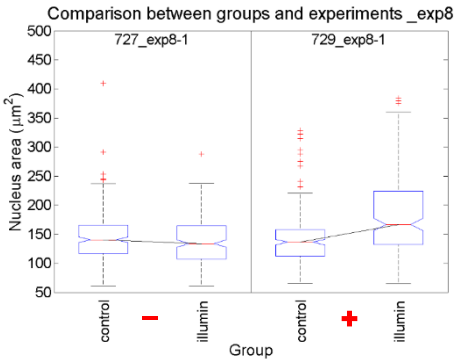	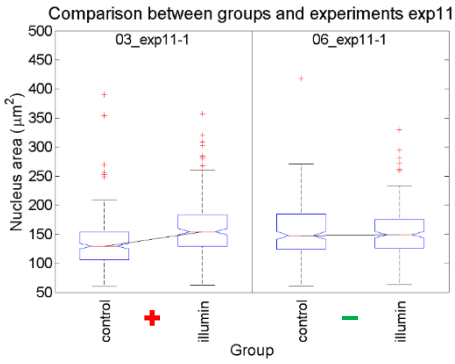
24 h	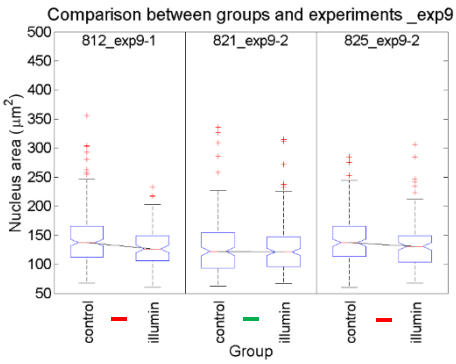	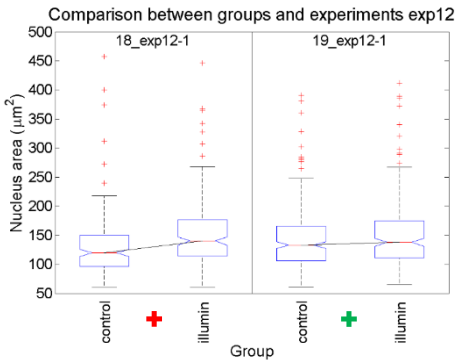

Graphs with the complete vertical scale, including all outliers.

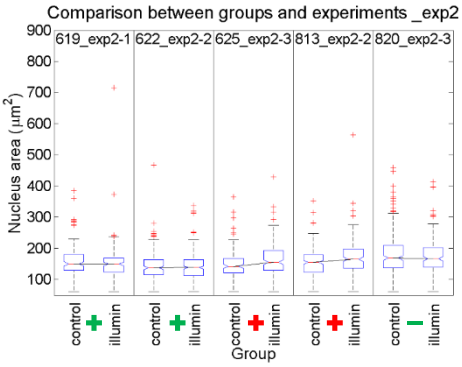

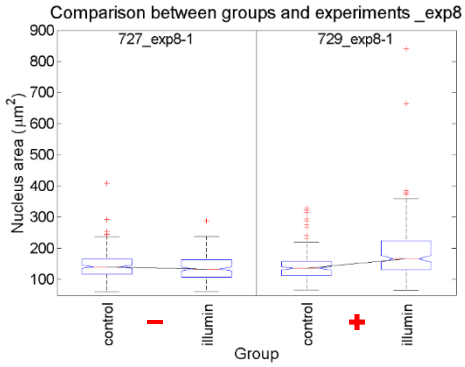

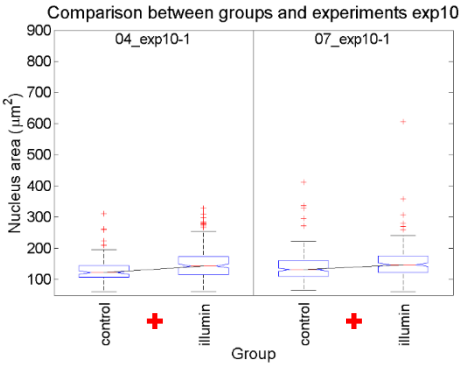

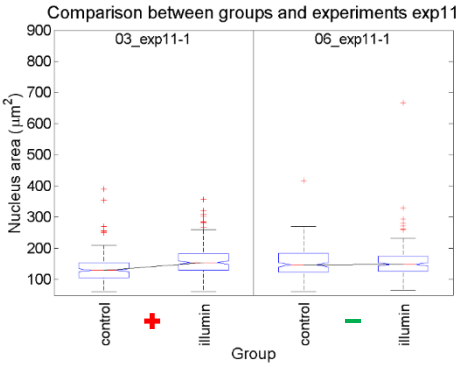

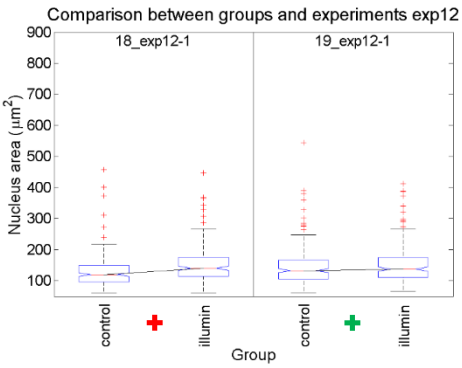

Cell area

625 nm

4 kPa

16 kPa

5 min

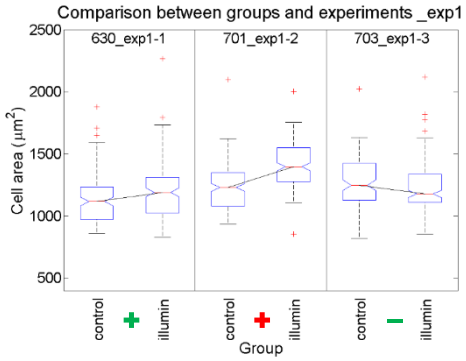

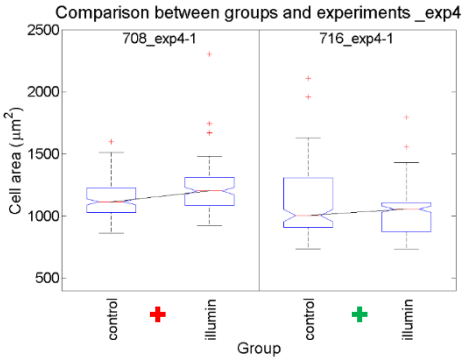

1 h

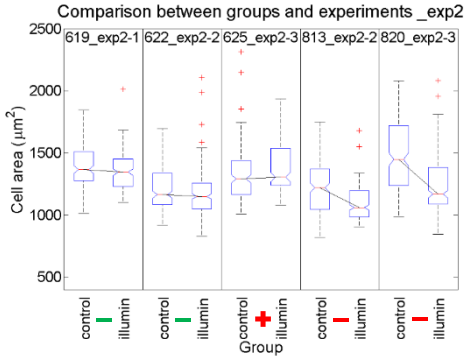

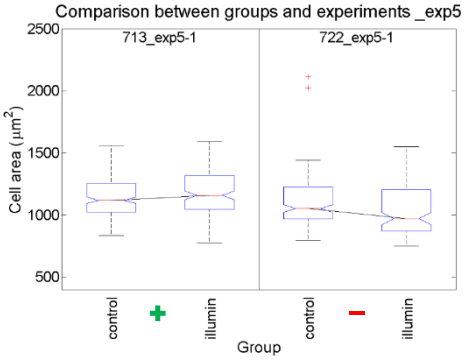

24 h

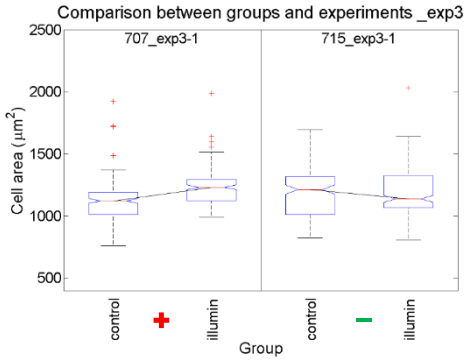

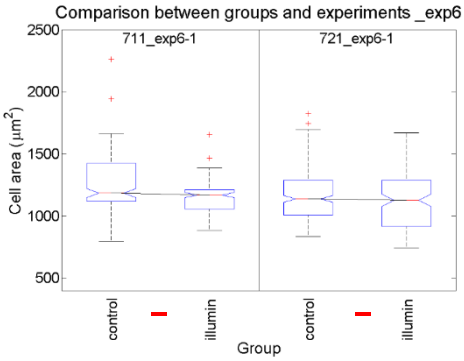

808 nm

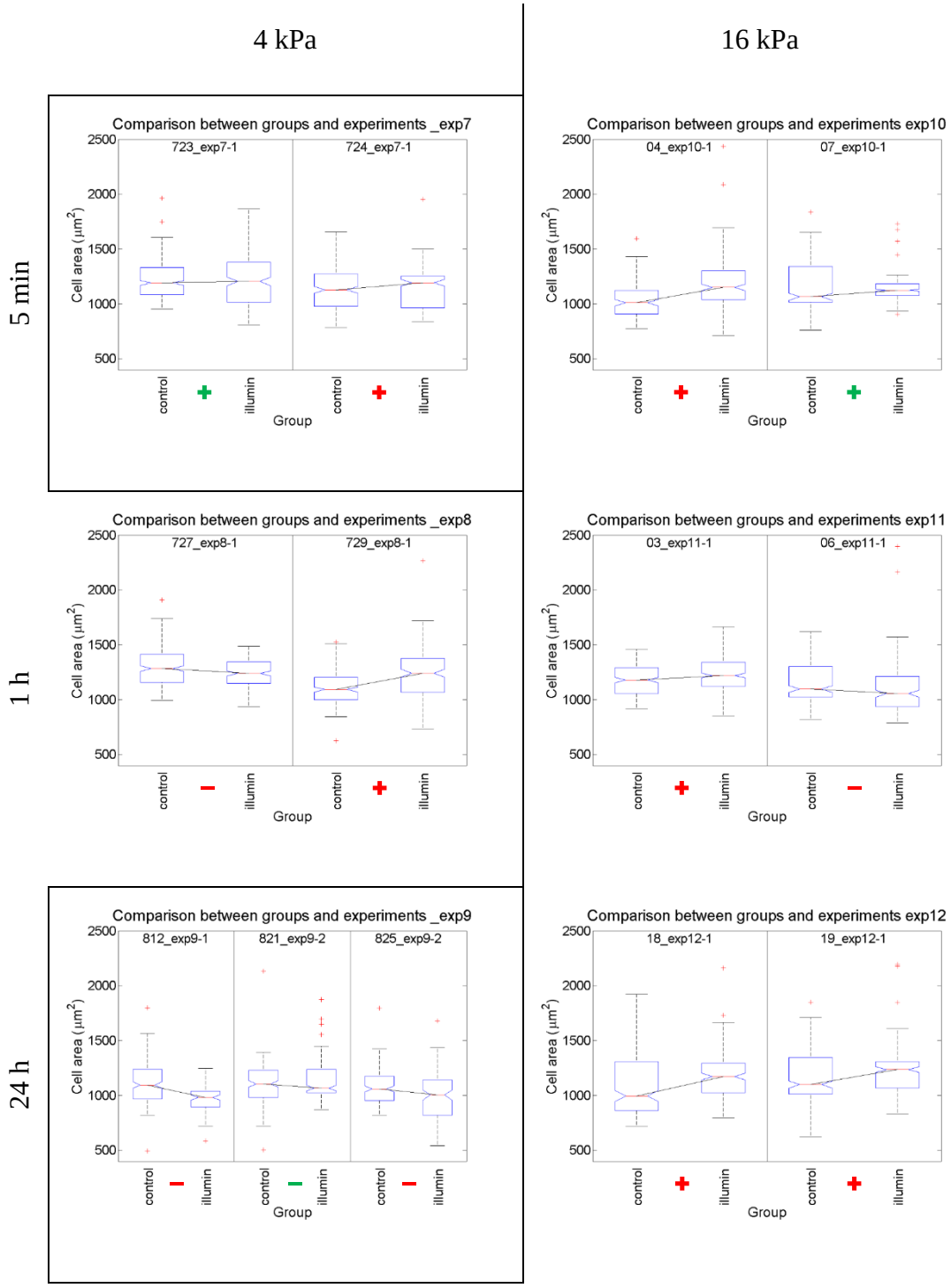
4 kPa
16 kPa
5 min
1 h
24 h
Comparison between groups and experiments _exp7
723_exp7-1
724_exp7-1
Comparison between groups and experiments exp10
04_exp10-1
07_exp10-1
Comparison between groups and experiments _exp8
727_exp8-1
729_exp8-1
Comparison between groups and experiments exp11
03_exp11-1
06_exp11-1
Comparison between groups and experiments _exp9
812_exp9-1
821_exp9-2
825_exp9-2
Comparison between groups and experiments exp12
18_exp12-1
19_exp12-1
Cell area (µm²)
Group
control
illumin

Graphs with the complete vertical scale, including all outliers.

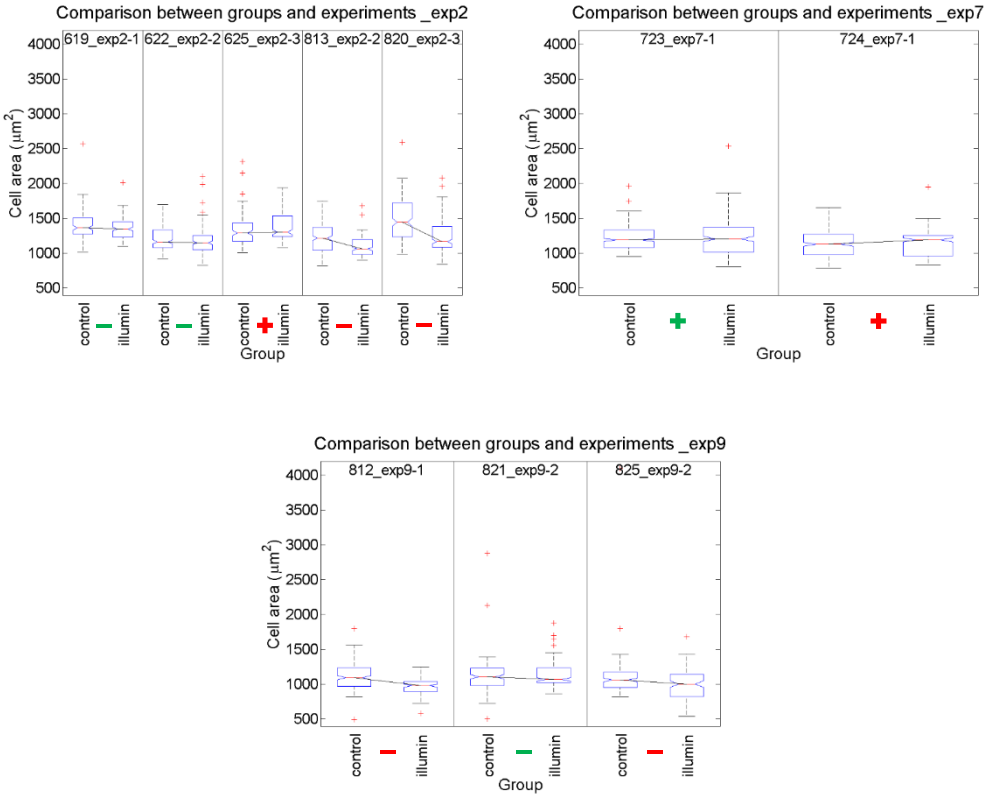

Total actin

625 nm

	4 kPa	16 kPa
5 min	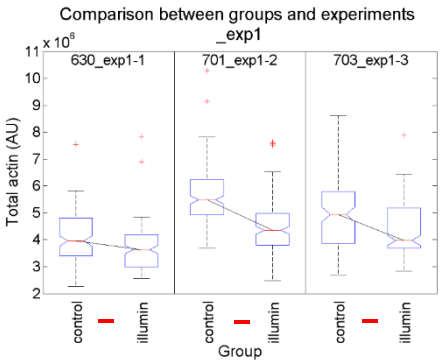	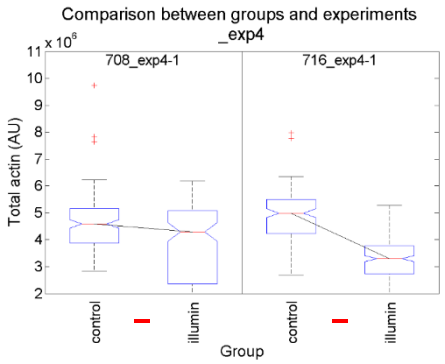
1 h	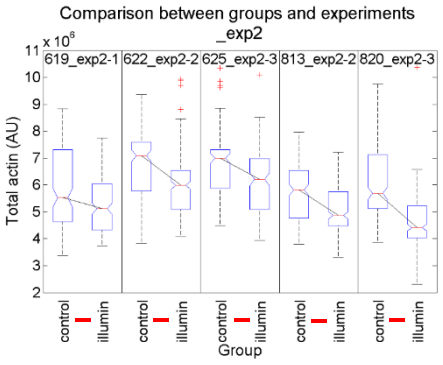	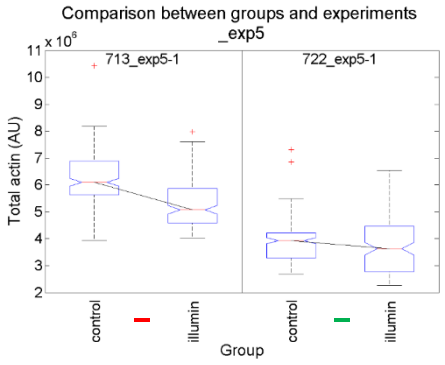
24 h	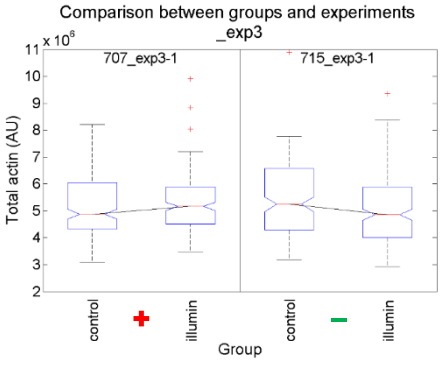	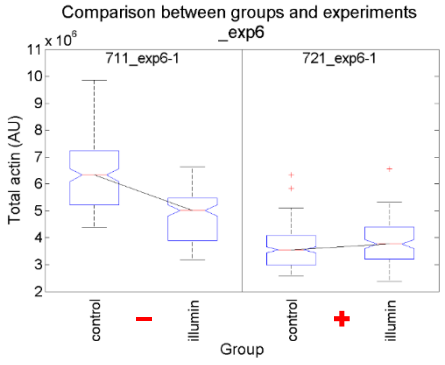

808 nm

	4 kPa	16 kPa
5 min	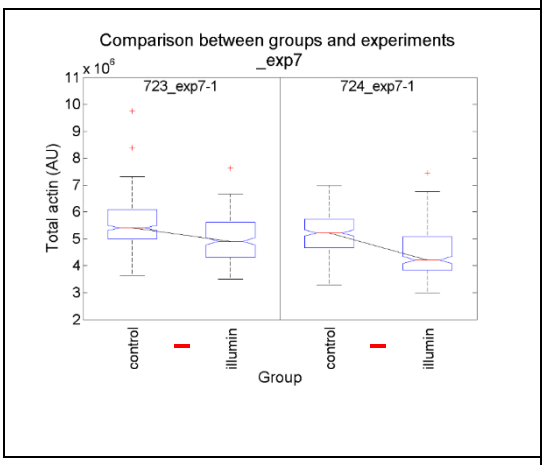	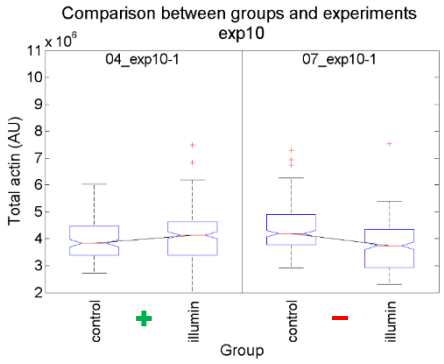
1 h	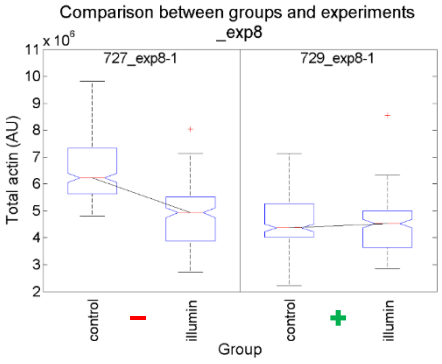	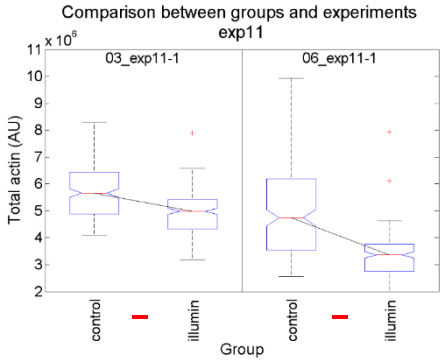
24 h	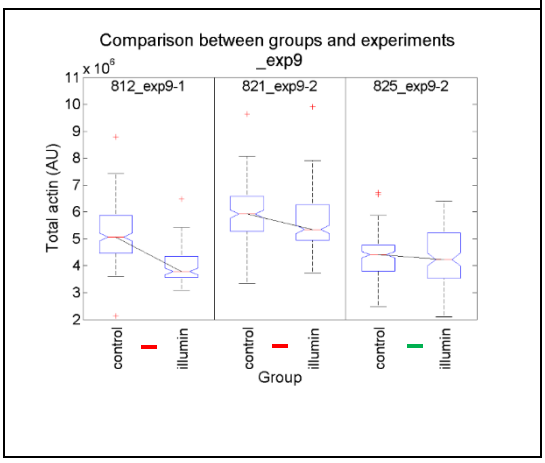	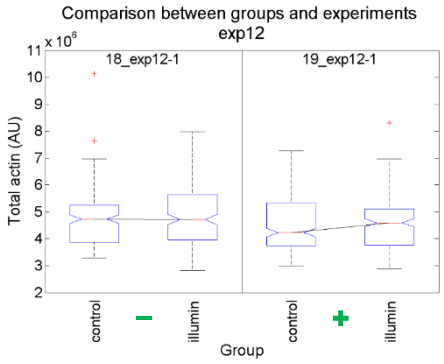

Graphs with the complete vertical scale, including all outliers.

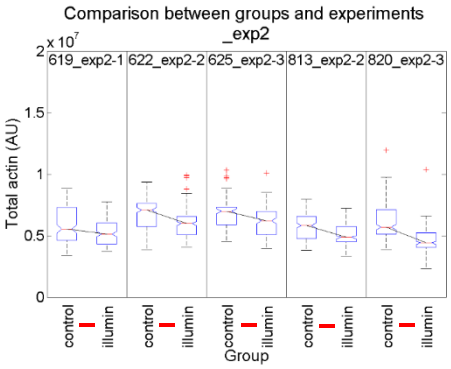

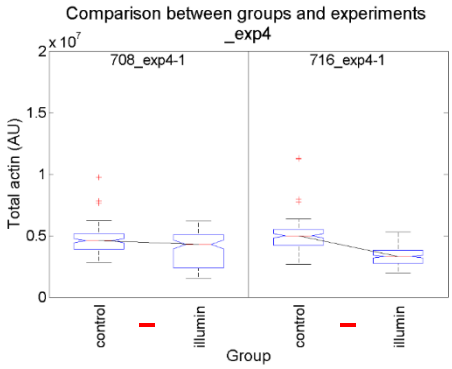

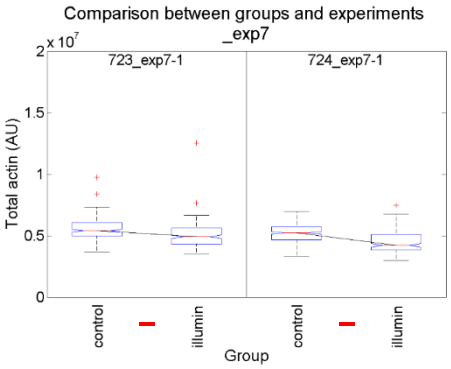

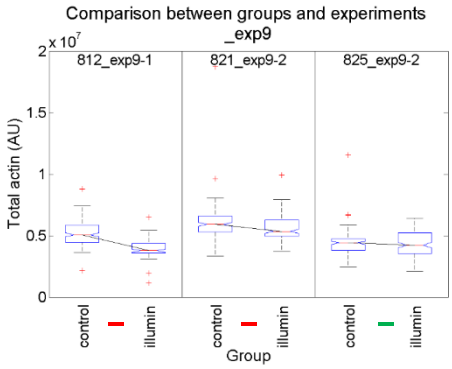

Total actin density

625 nm

4 kPa

16 kPa

5 min

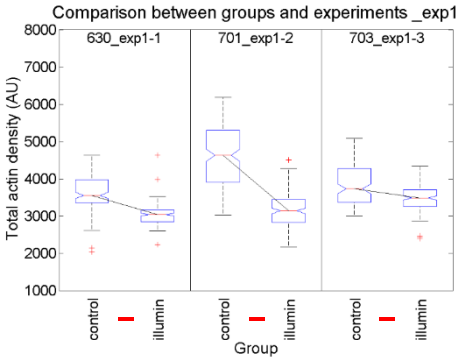

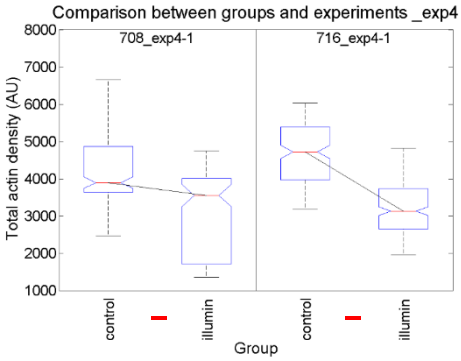

1 h

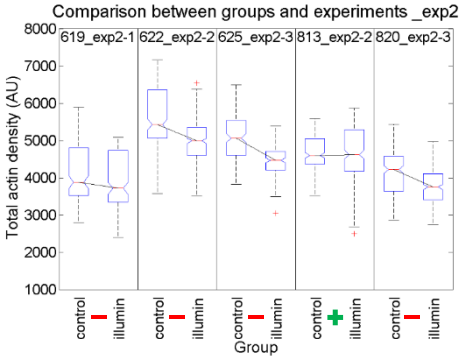

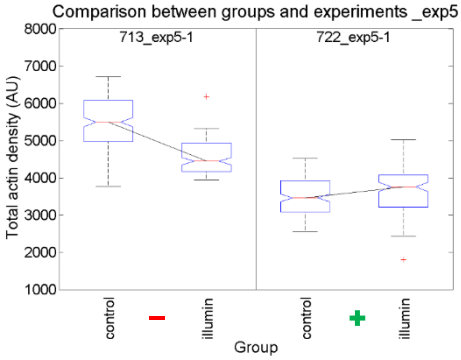

24 h

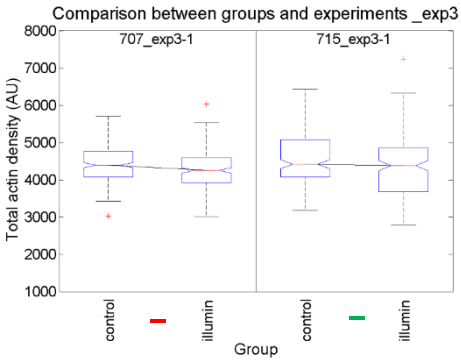

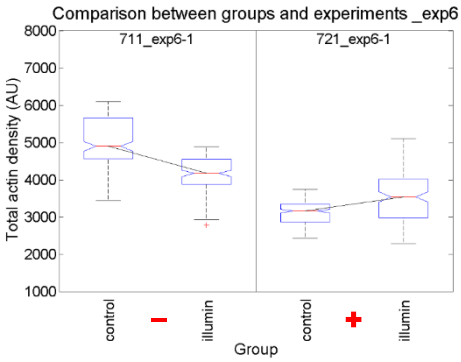

808 nm

	4 kPa	16 kPa
5 min	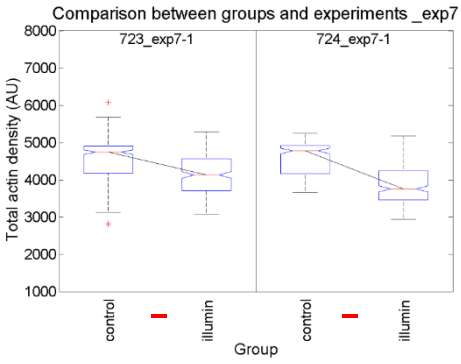	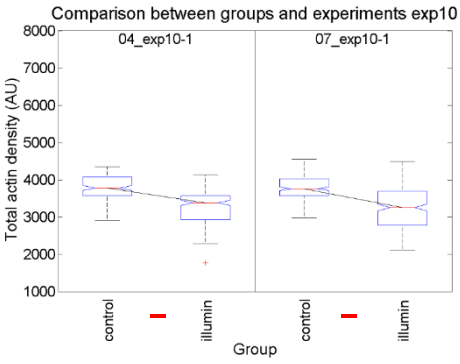
1 h	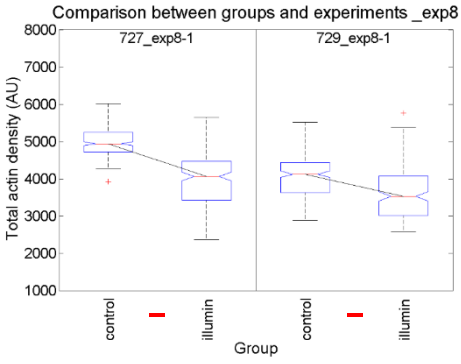	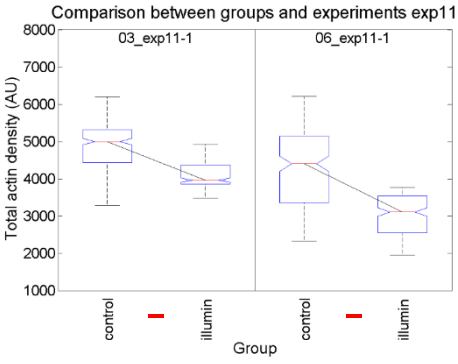
24 h	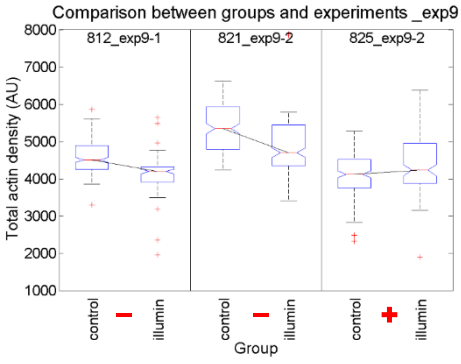	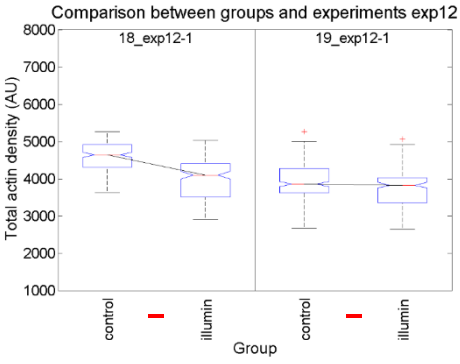

Number of filaments

625 nm

	4 kPa	16 kPa
5 min	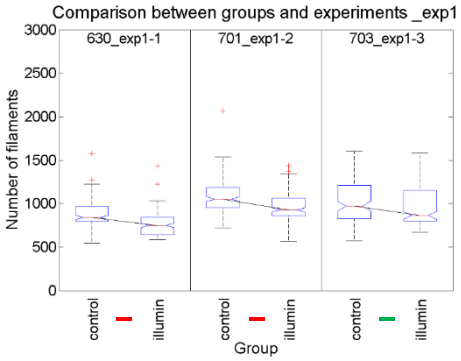	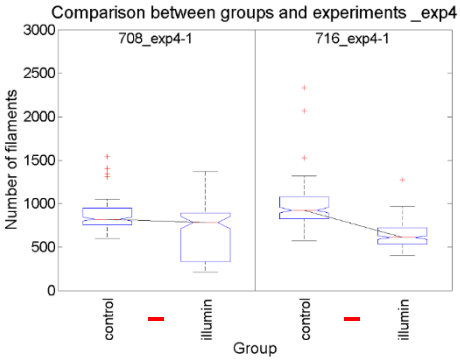
1 h	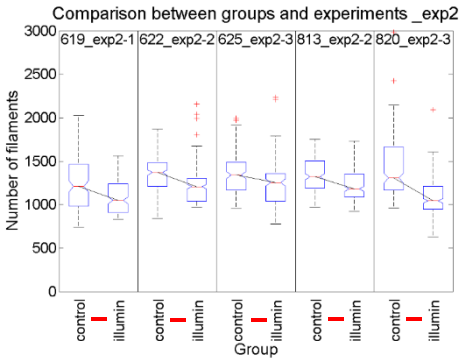	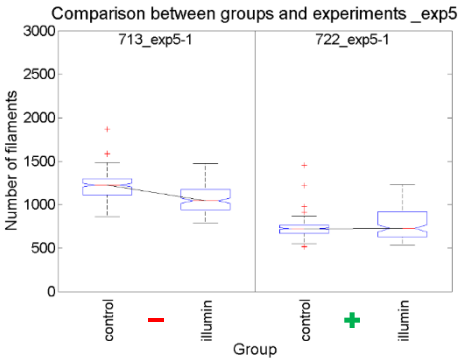
24 h	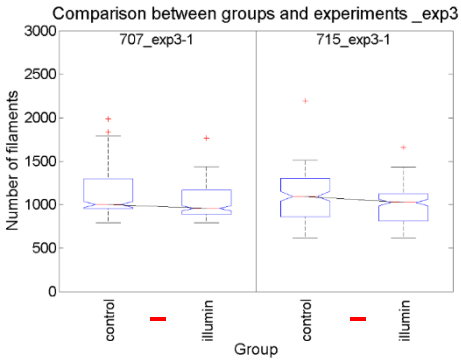	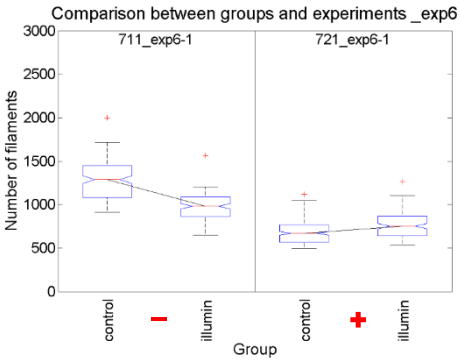

808 nm

	4 kPa	16 kPa
5 min	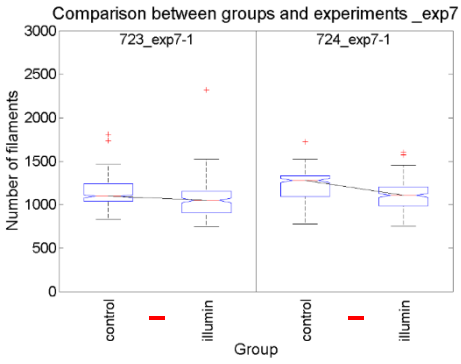	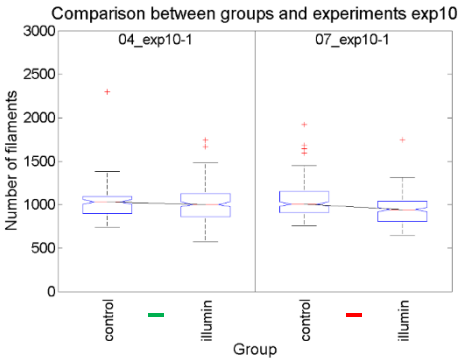
1 h	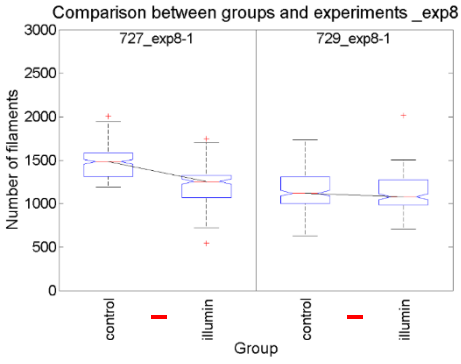	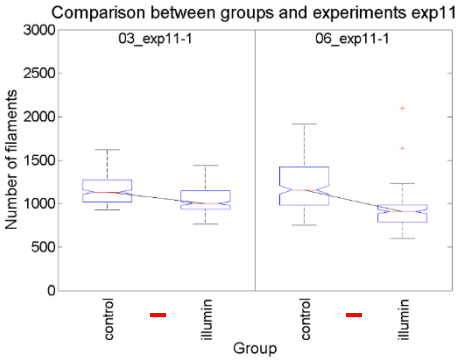
24 h	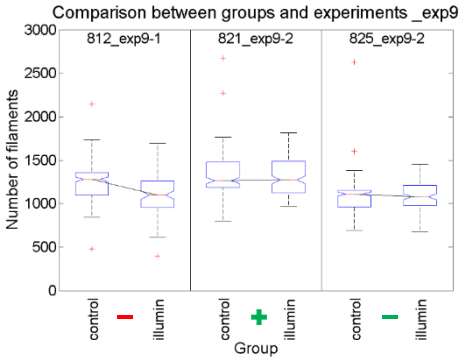	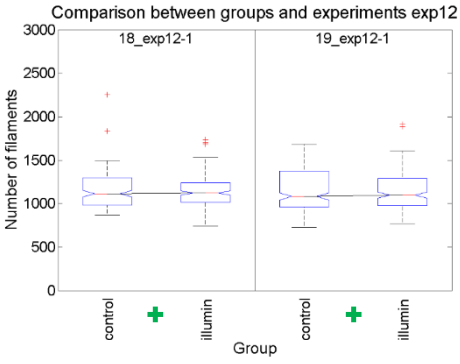

Total branch length

625 nm, compressed scale. Data above 5 μm are compressed and not in scale.

	4 kPa	16 kPa
5 min	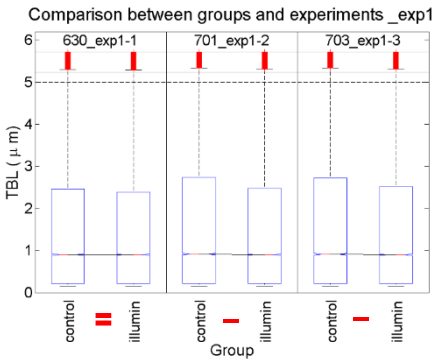	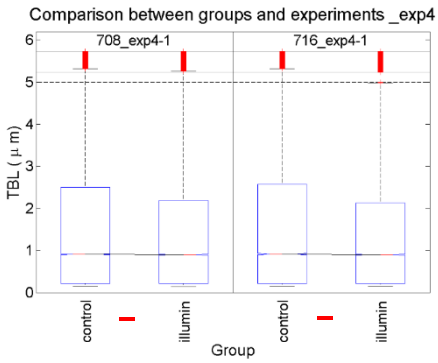
1 h	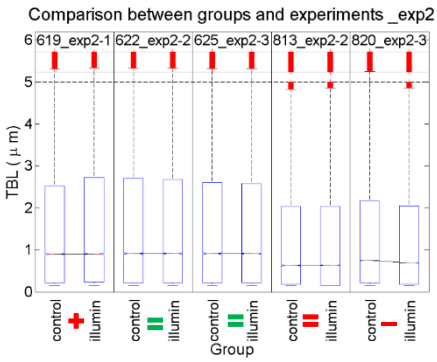	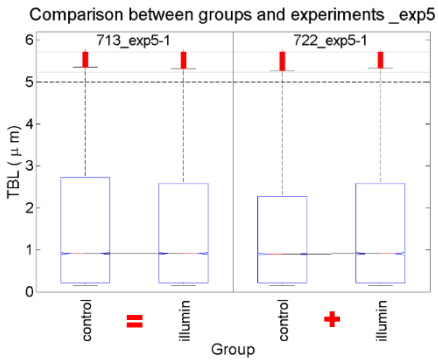
24 h	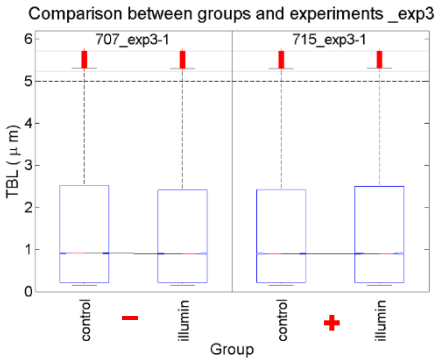	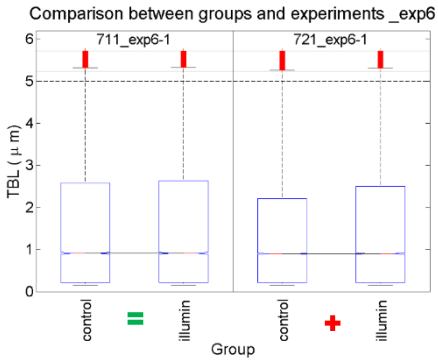

808 nm, compressed scale. Data above 5 μm are compressed and not in scale.

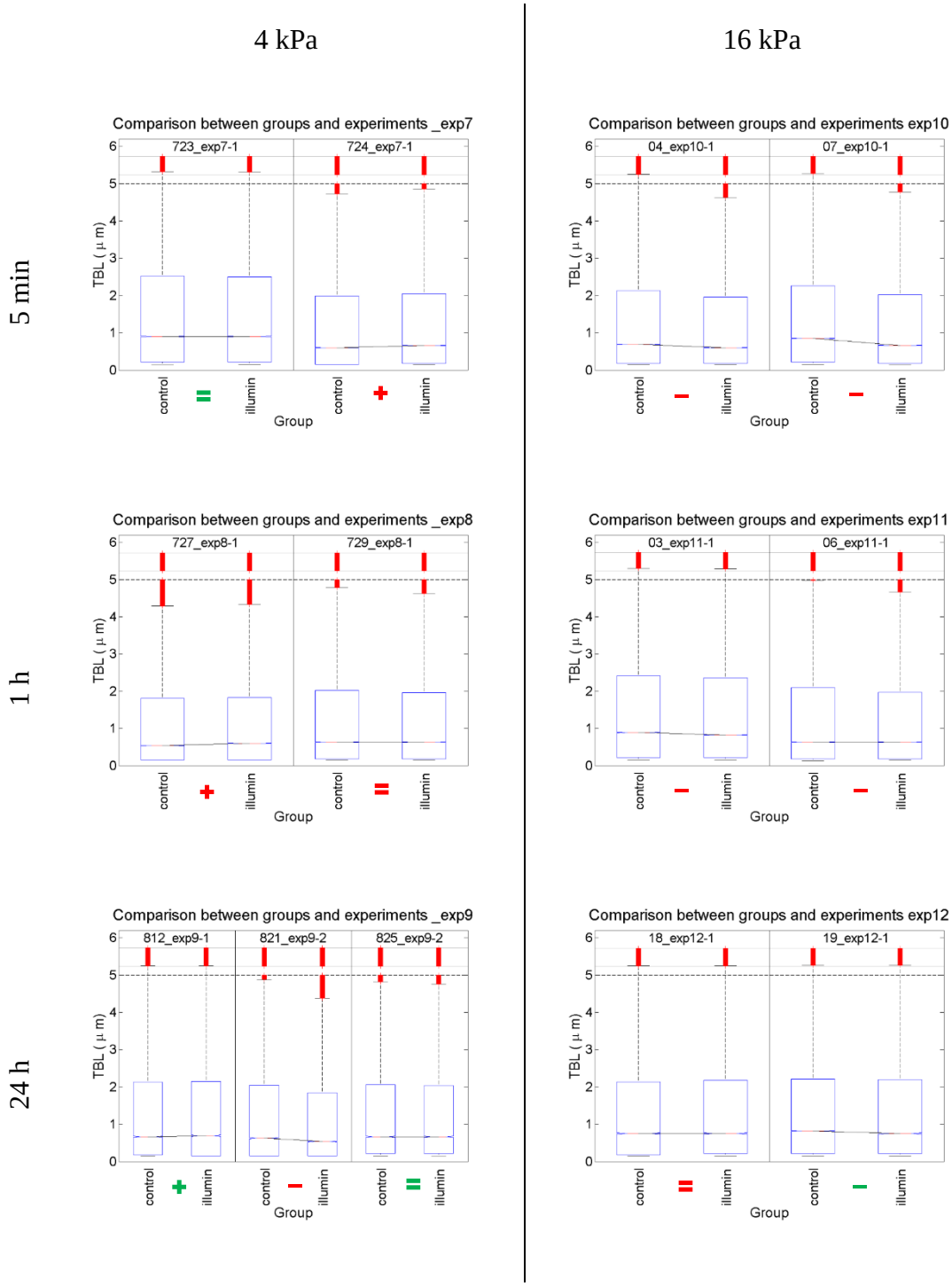

625 nm, logarithmic scale.

	4 kPa	16 kPa
5 min	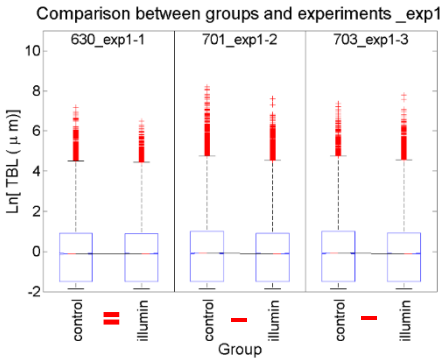	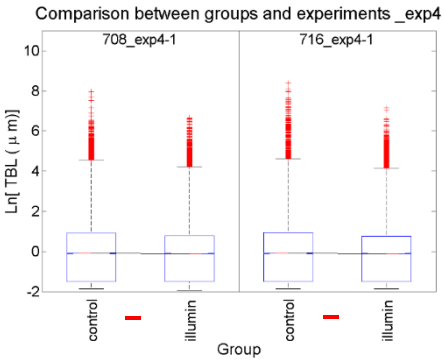
1 h	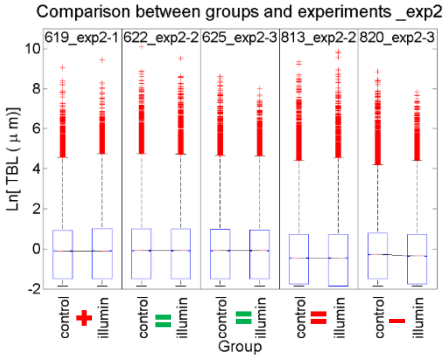	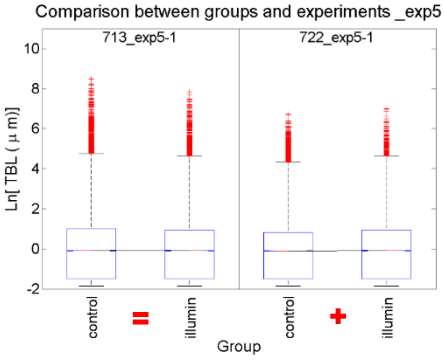
24 h	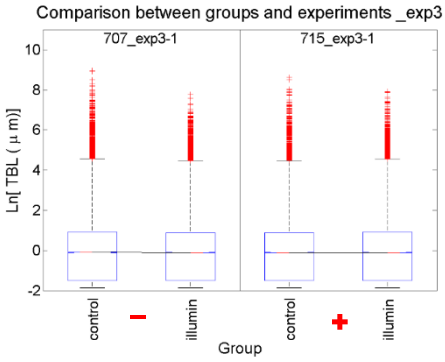	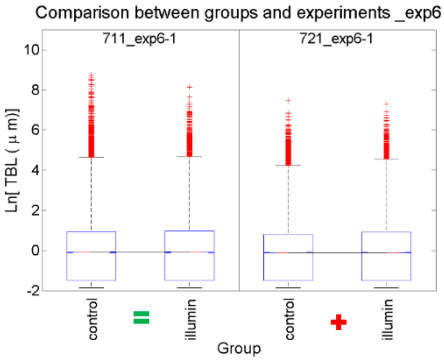

808 nm, logarithmic scale.

	4 kPa	16 kPa
5 min	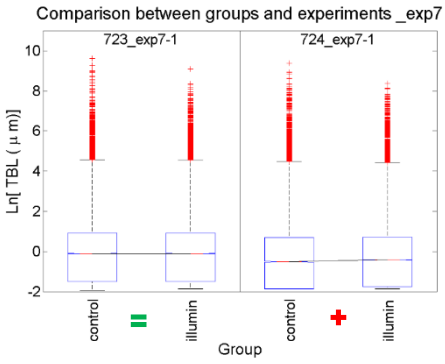	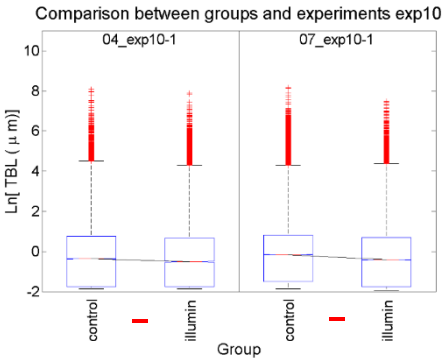
1 h	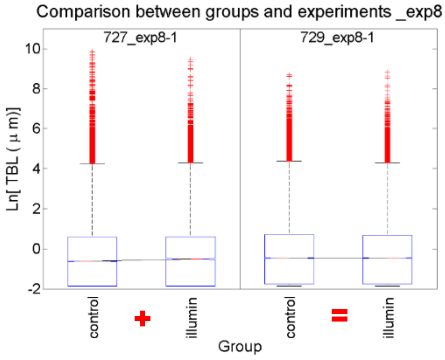	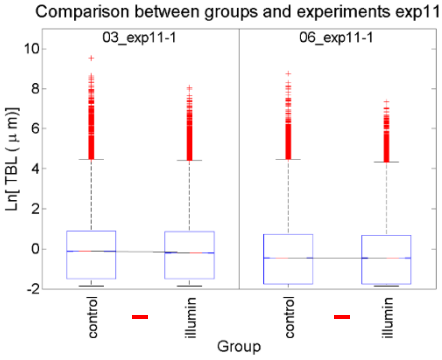
24 h	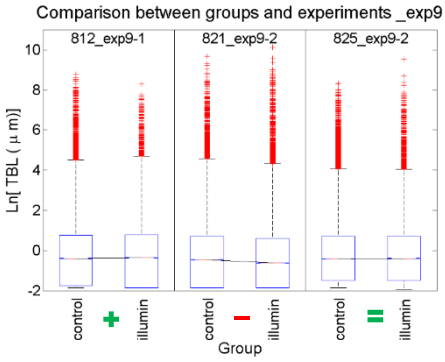	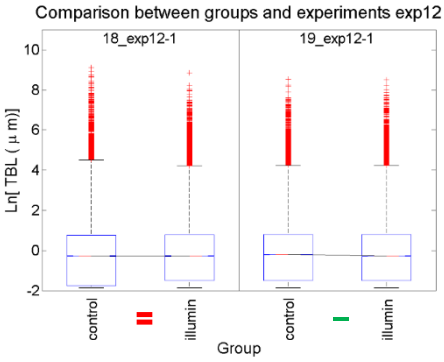

Correlation coefficients between the parameters total actin, cell area, the number of filaments and total branch length

625 nm

	4 kPa	16 kPa
5 min	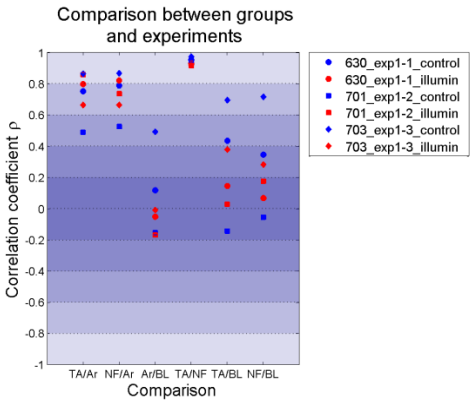	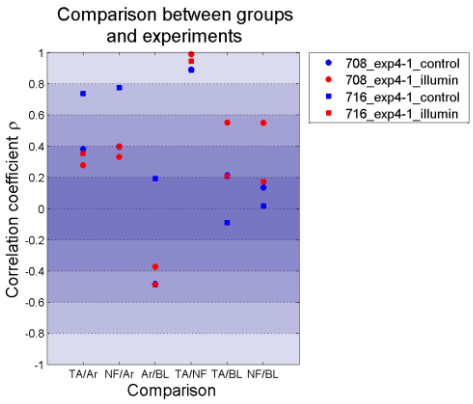
1 h	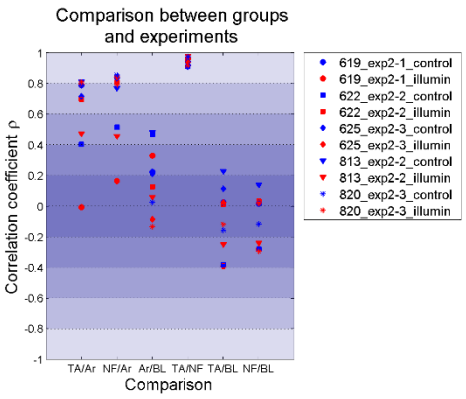	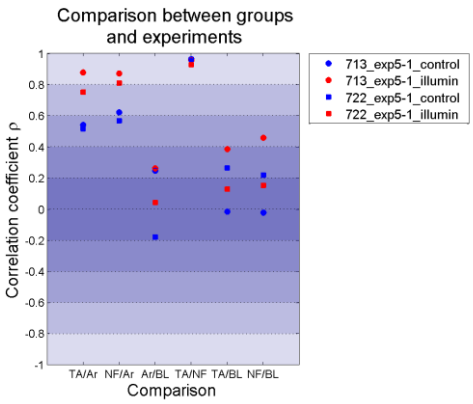
24 h	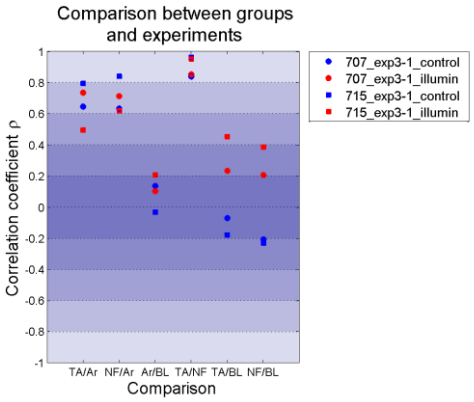	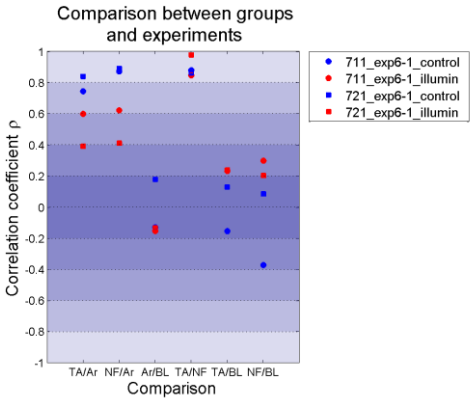

808 nm

	4 kPa	16 kPa
5 min	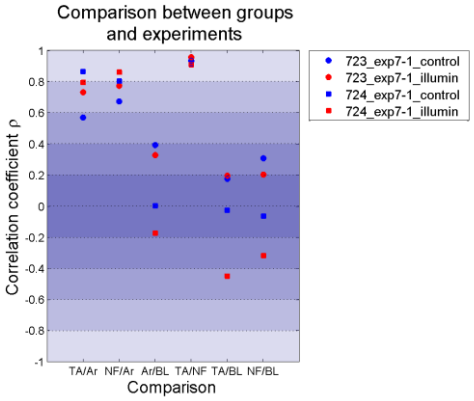	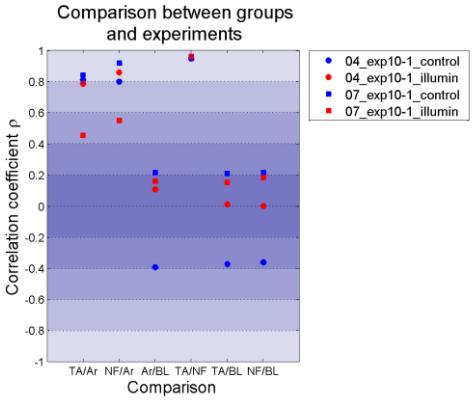
1 h	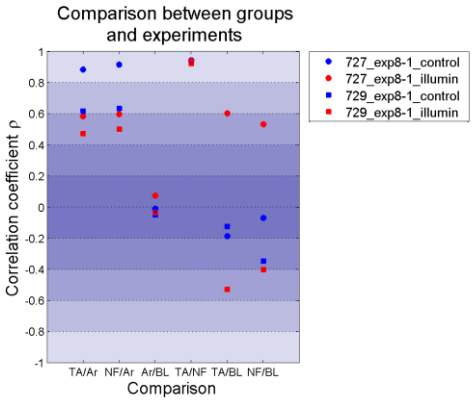	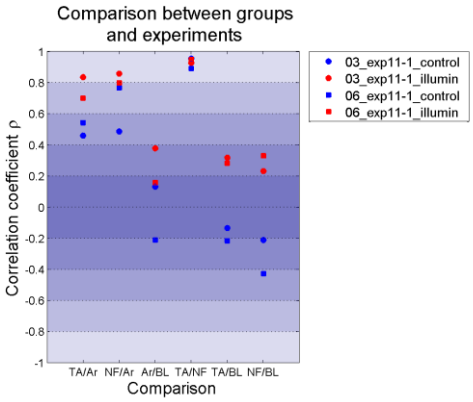
24 h	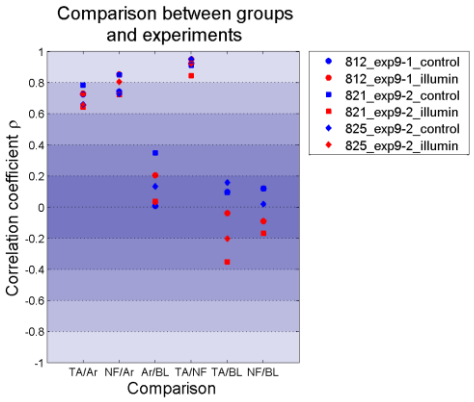	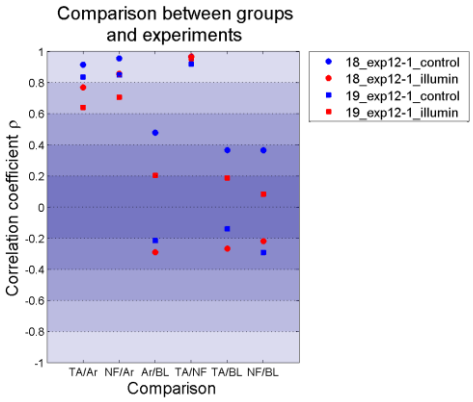

Coefficients of determination between the parameters total actin, cell area, the number of filaments and total branch length

625 nm

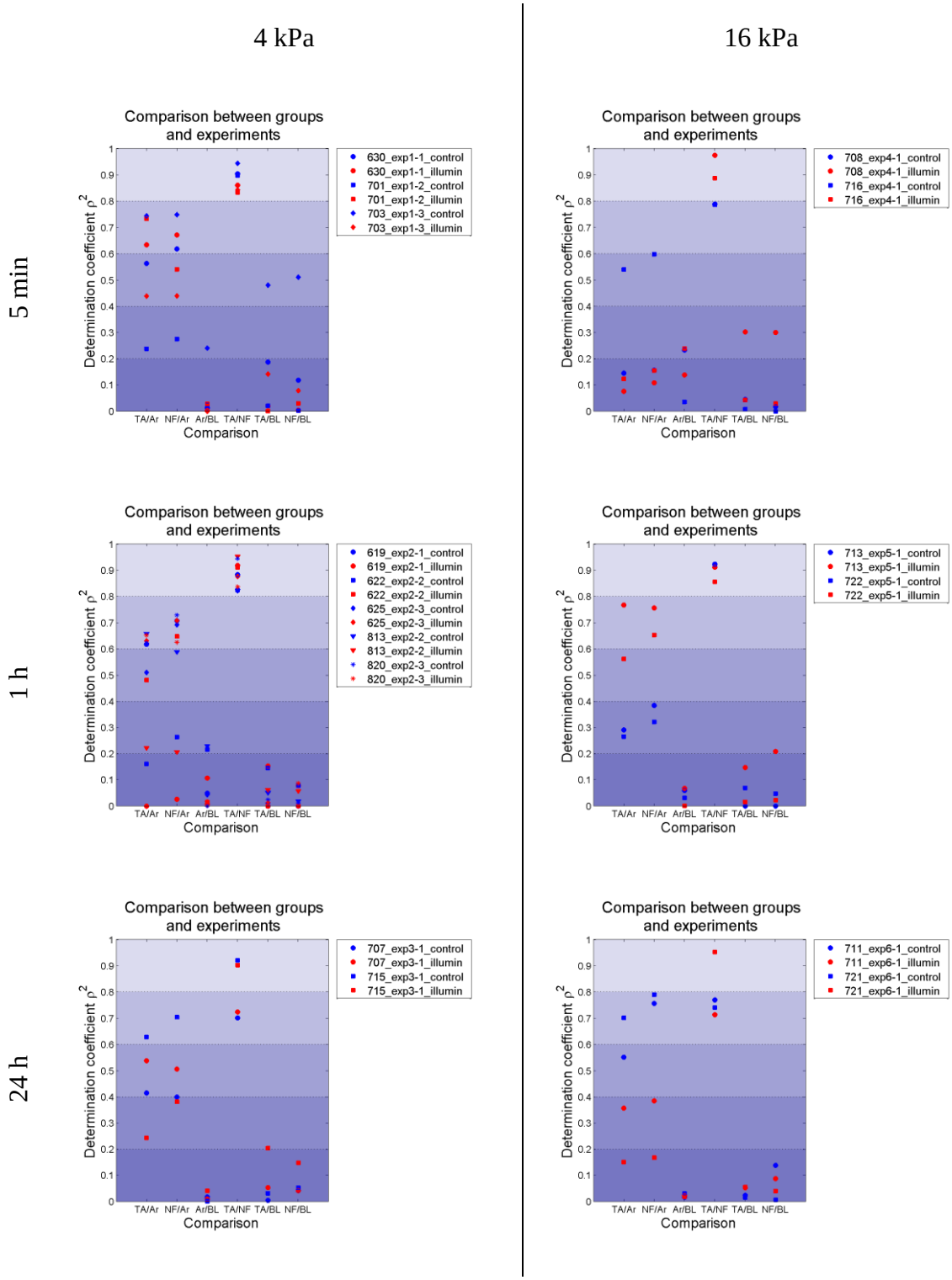

808 nm

	4 kPa	16 kPa
5 min	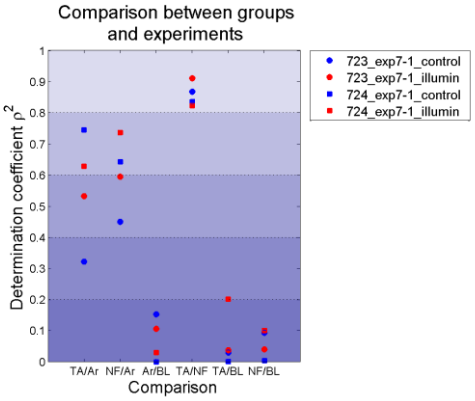	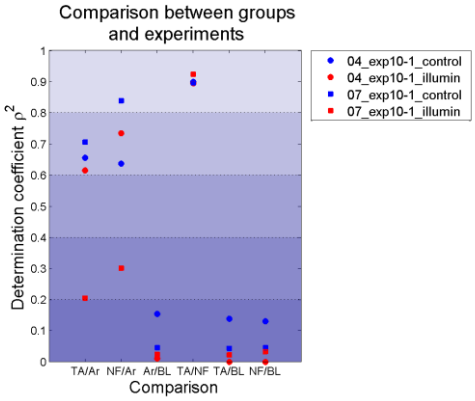
1 h	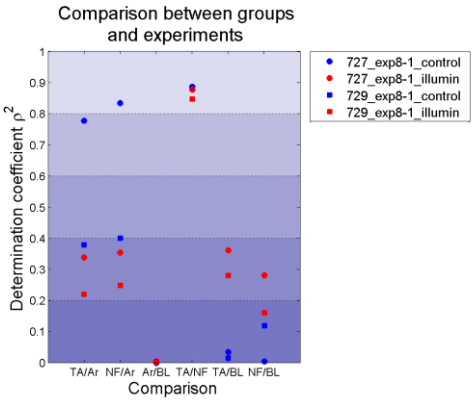	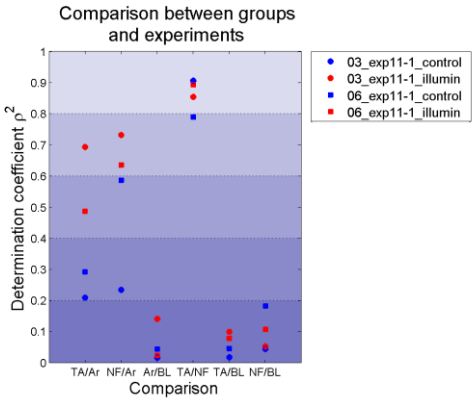
24 h	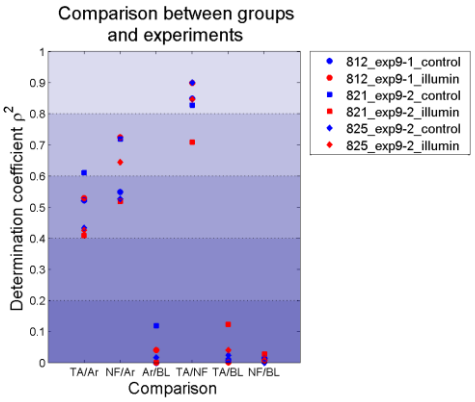	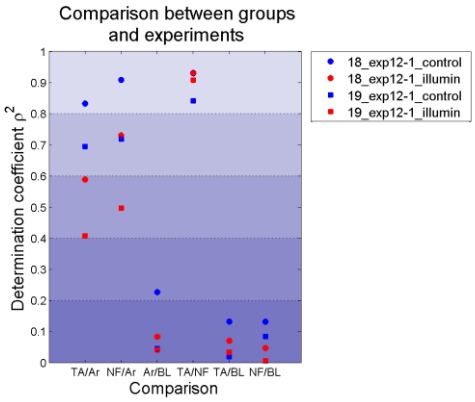

Ar vs TA slope

625 nm

	4 kPa	16 kPa
5 min	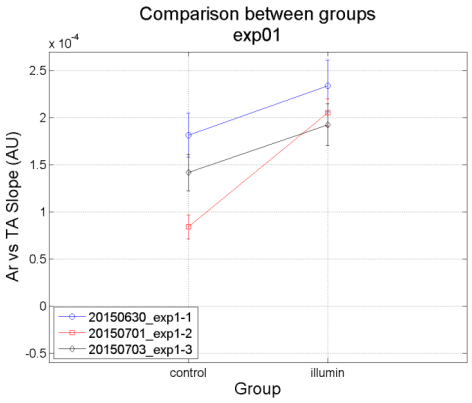	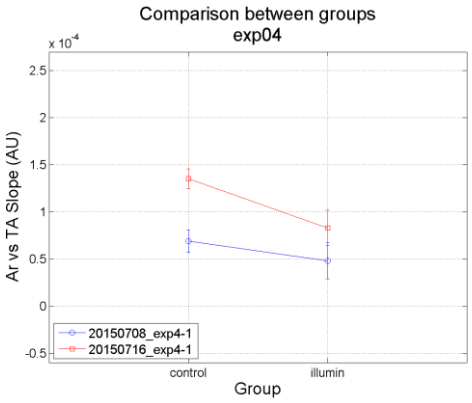
1 h	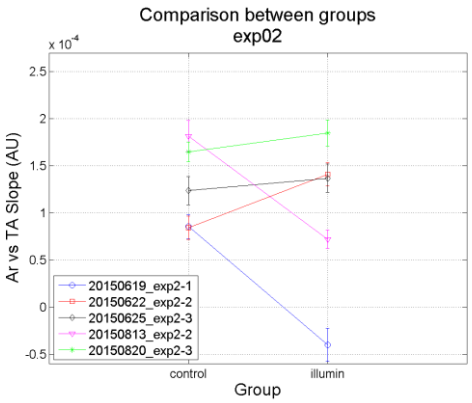	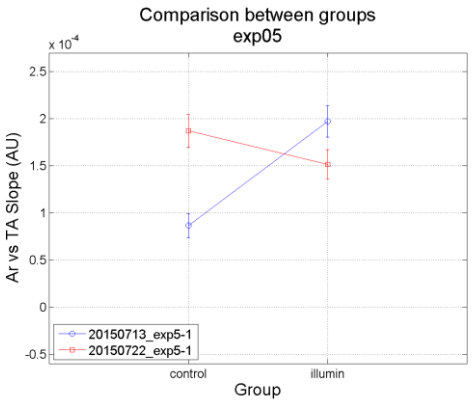
24 h	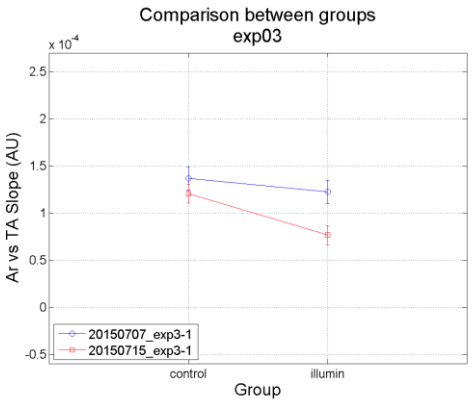	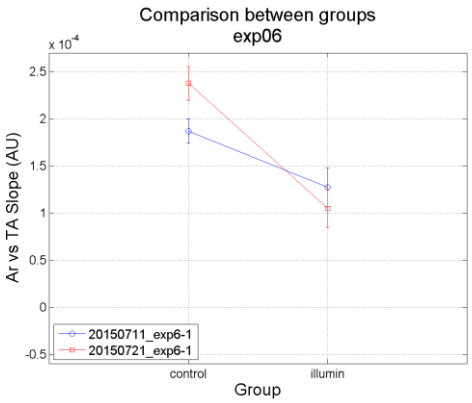

808 nm

	4 kPa	16 kPa
5 min	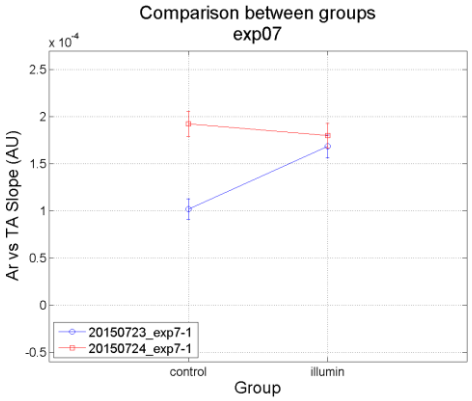	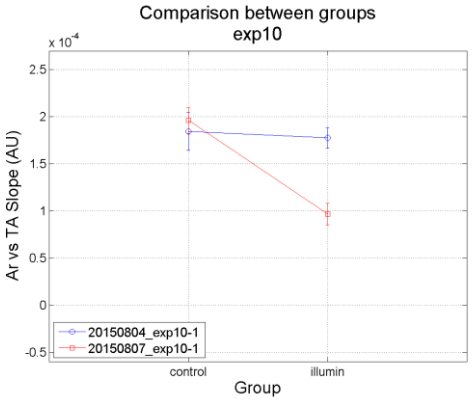
1 h	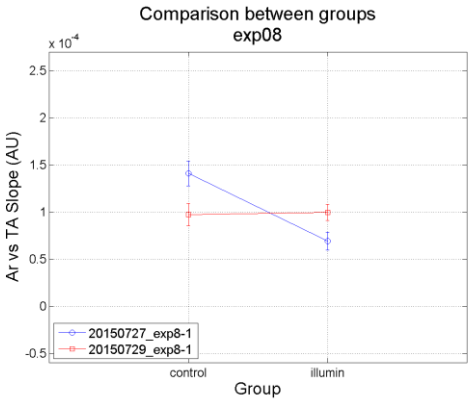	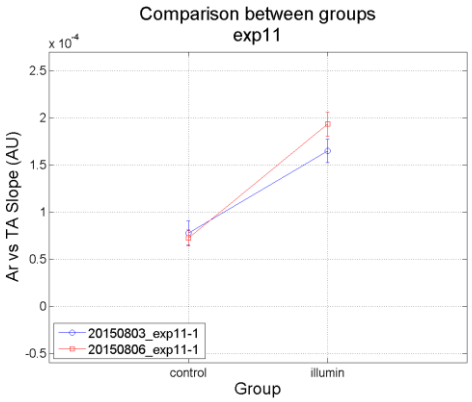
24 h	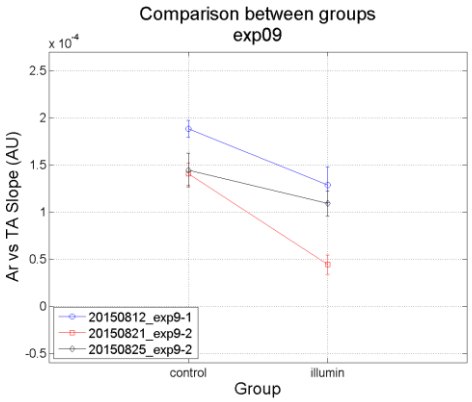	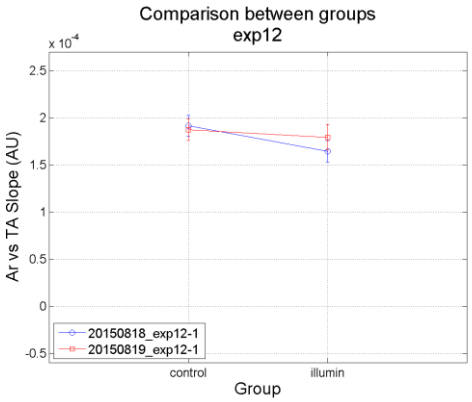

Ar vs NF slope

625 nm

	4 kPa	16 kPa
5 min	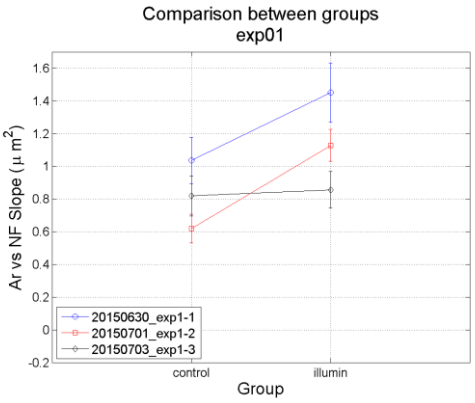	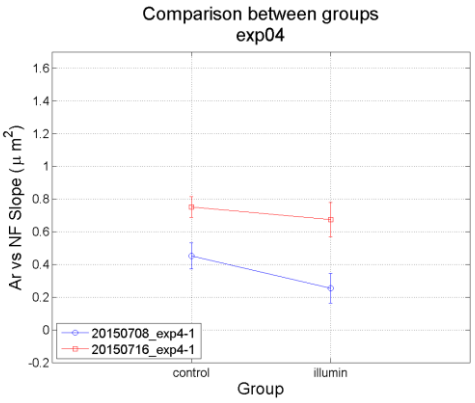
1 h	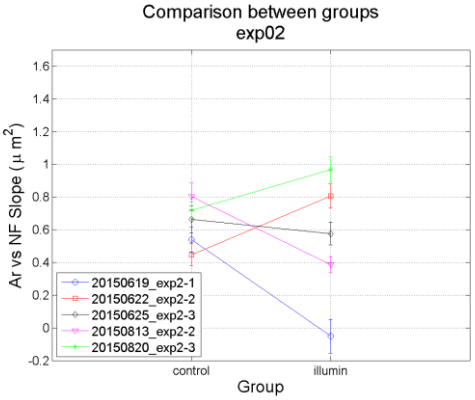	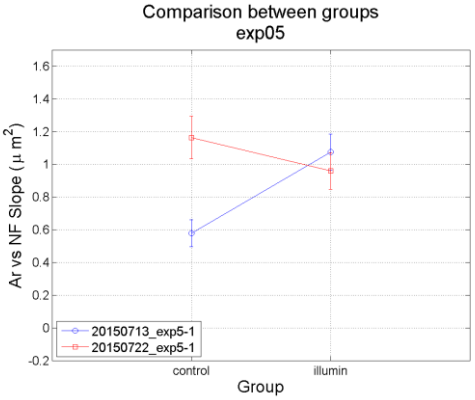
24 h	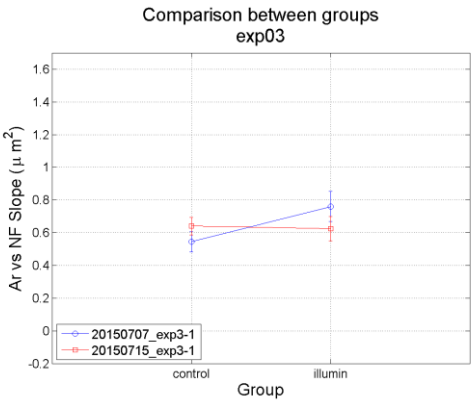	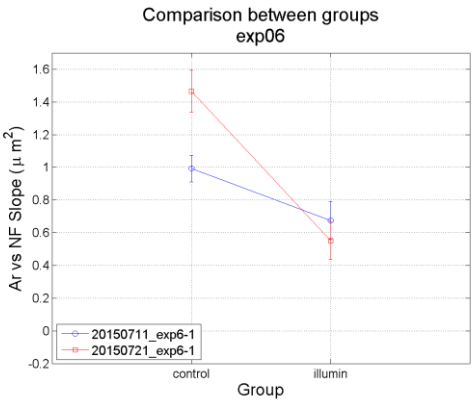

808 nm

	4 kPa	16 kPa
5 min	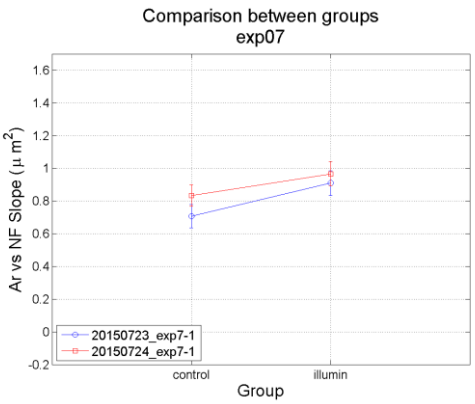	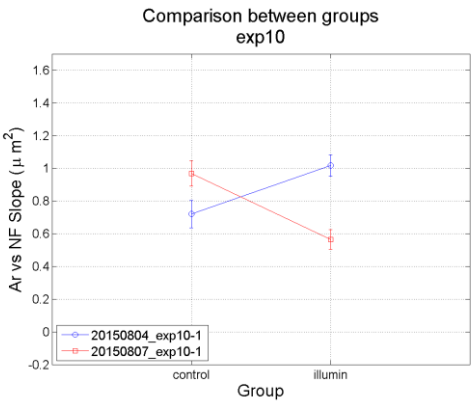
1 h	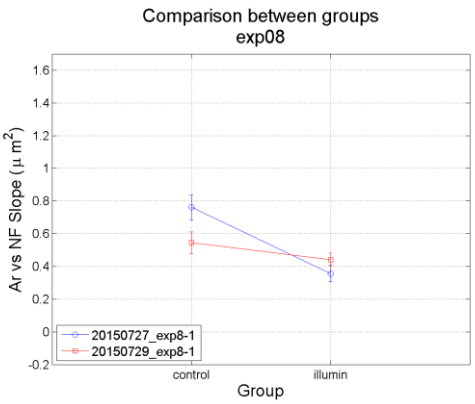	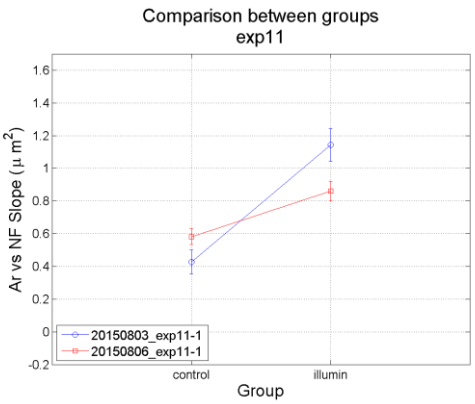
24 h	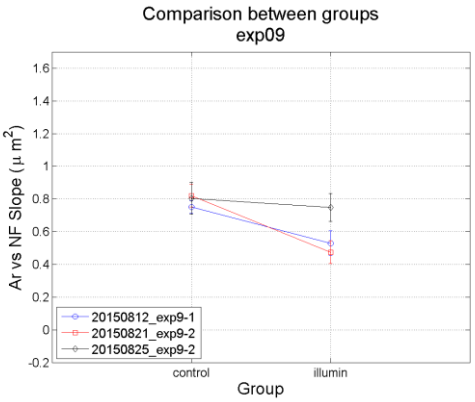	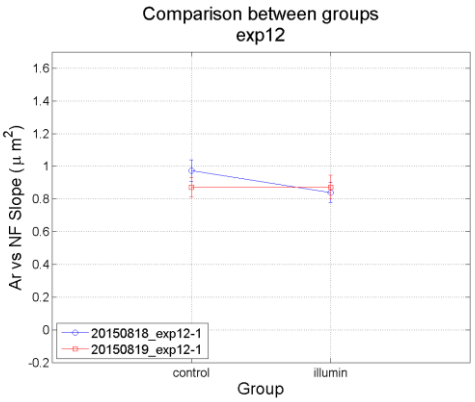

NF vs TA slope

625 nm

	4 kPa	16 kPa
5 min	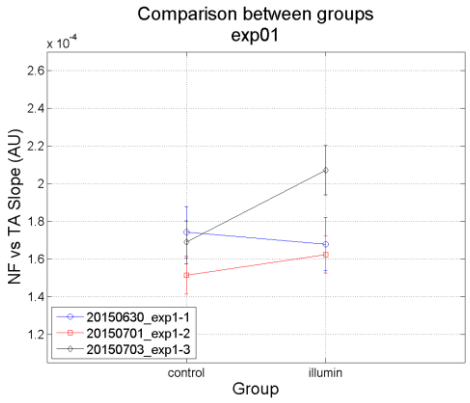	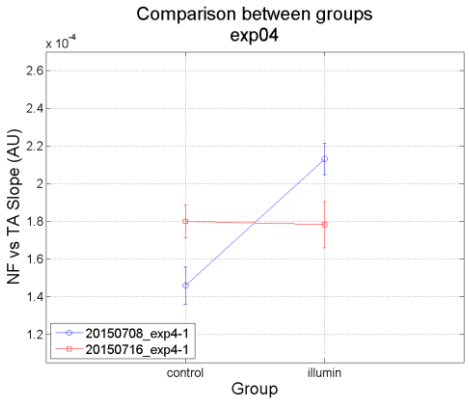
1 h	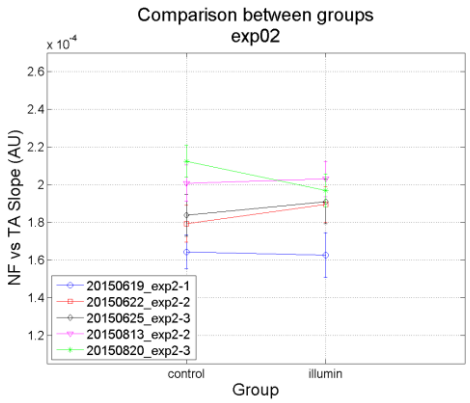	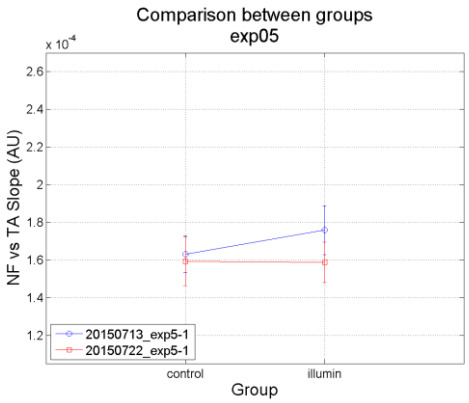
24 h	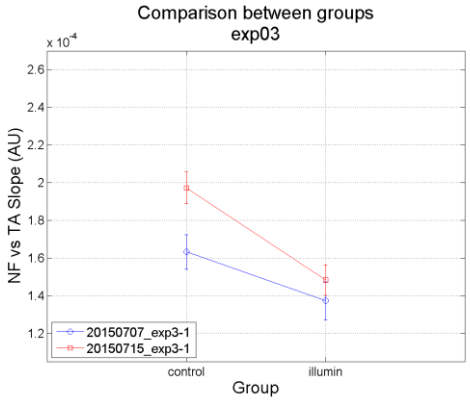	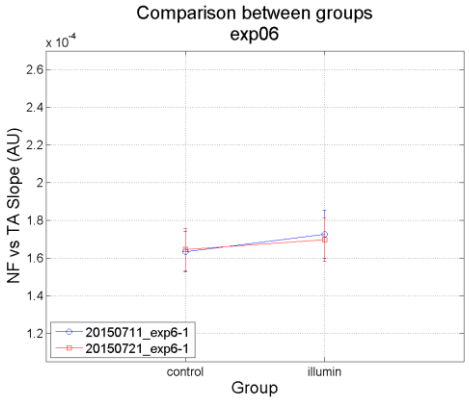

808 nm

	4 kPa	16 kPa
5 min	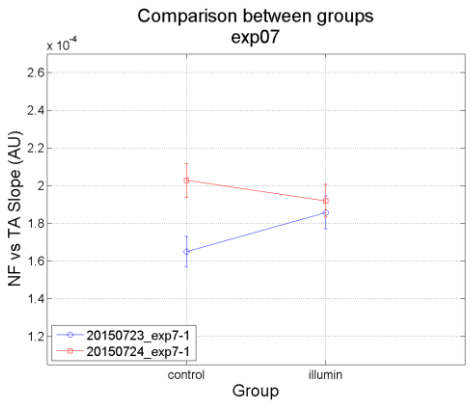	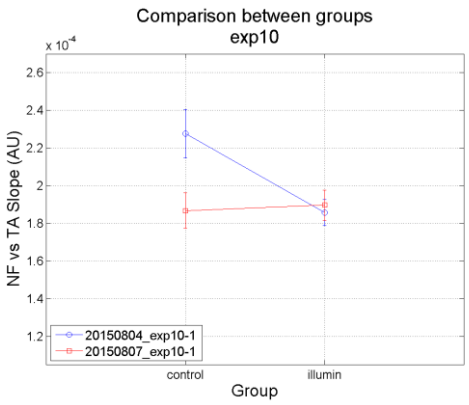
1 h	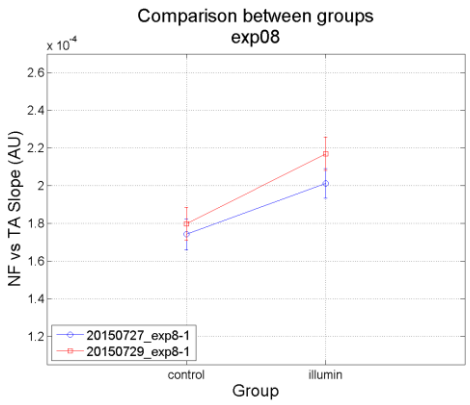	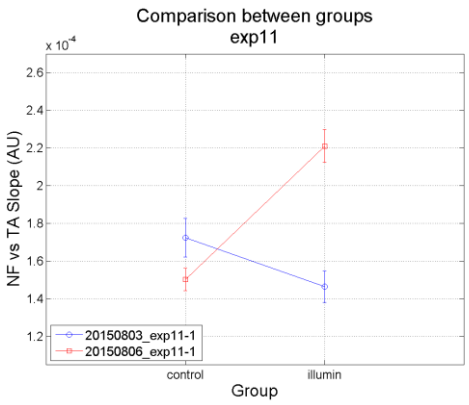
24 h	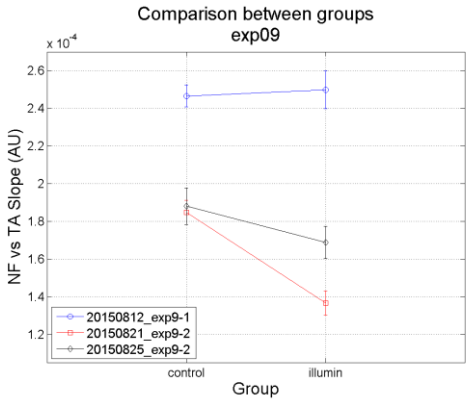	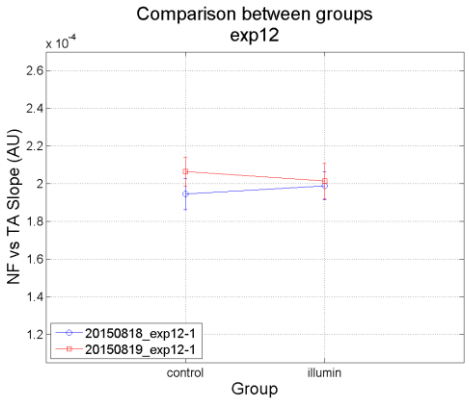

Comparison between relative parameters for all experiments

Nucleus area

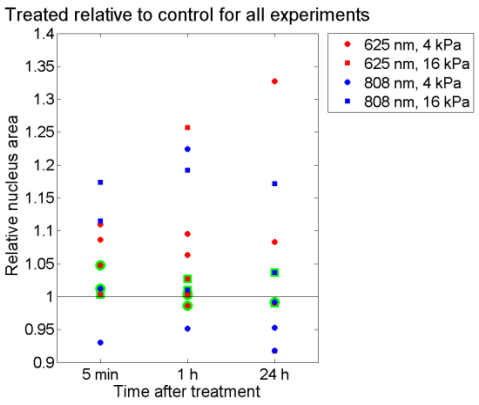

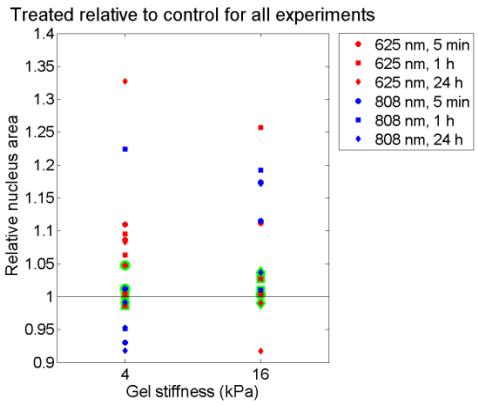

Cell area

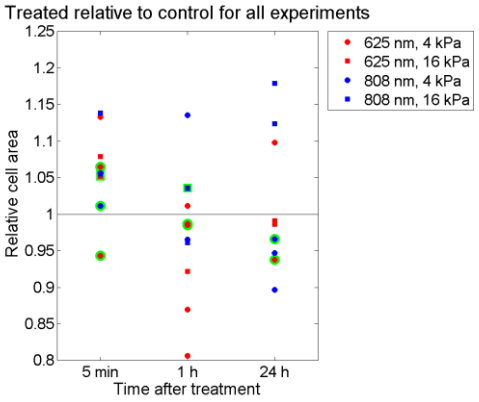

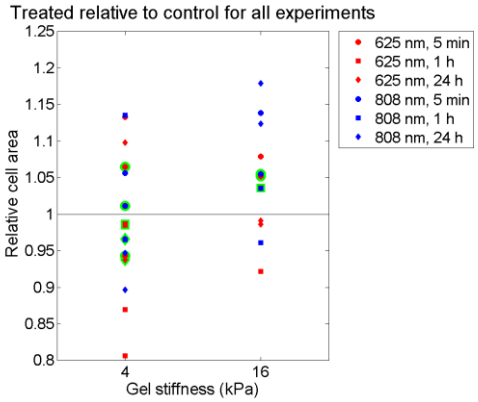

Total actin

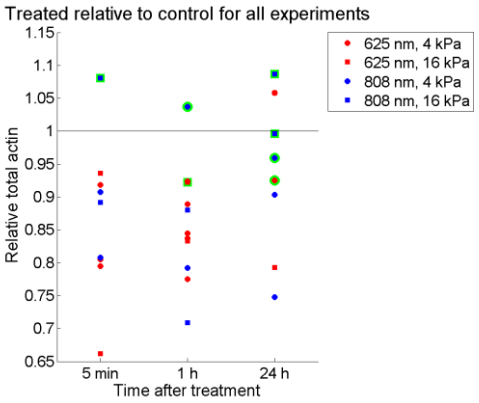

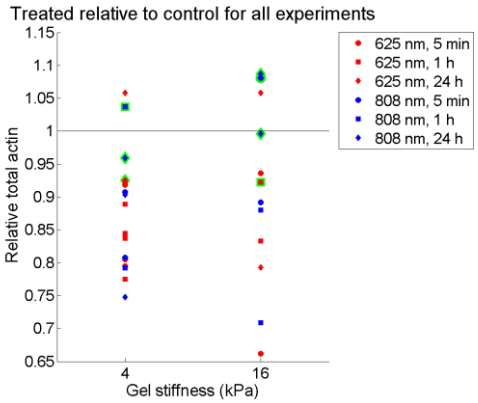

Total actin density

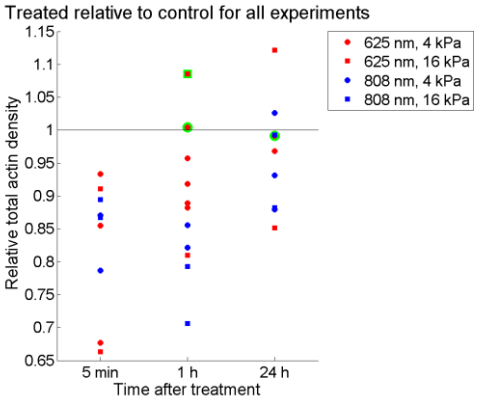

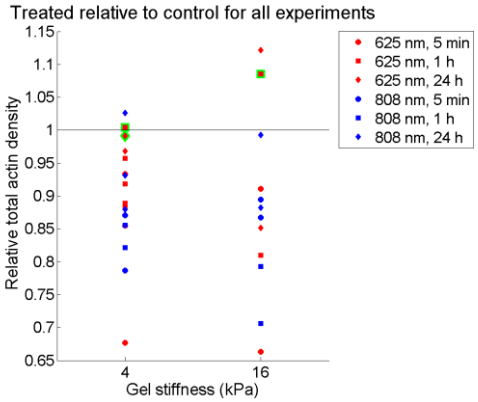

Number of filaments

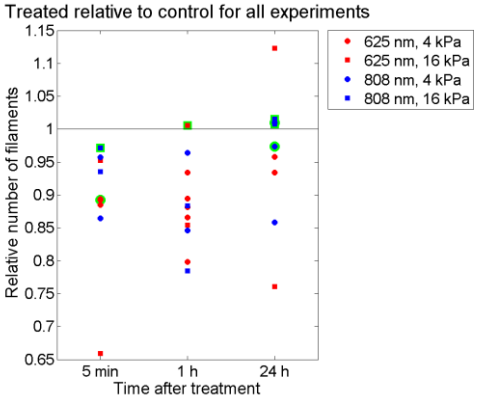

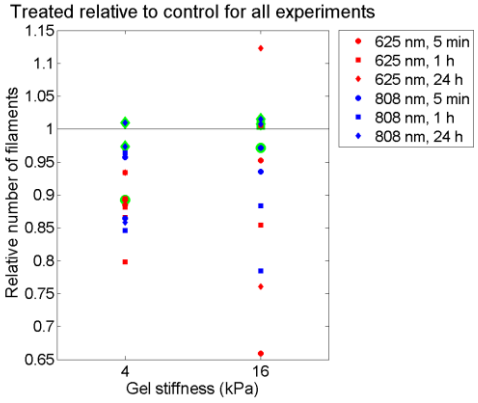

Total branch length

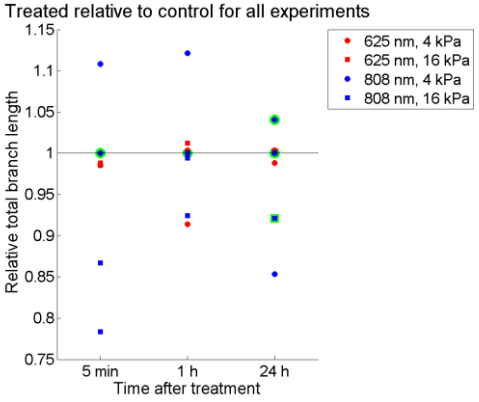

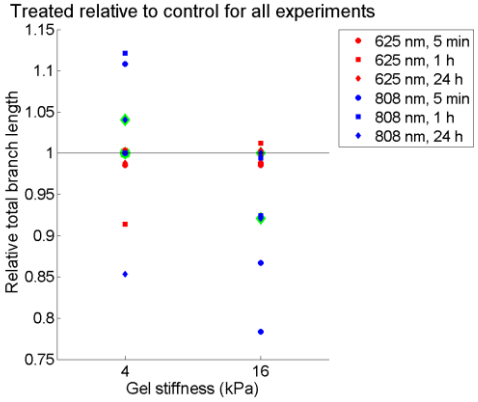

These graphs do not show whether there is compatibility between photo-treated and control group data.

Ar vs TA

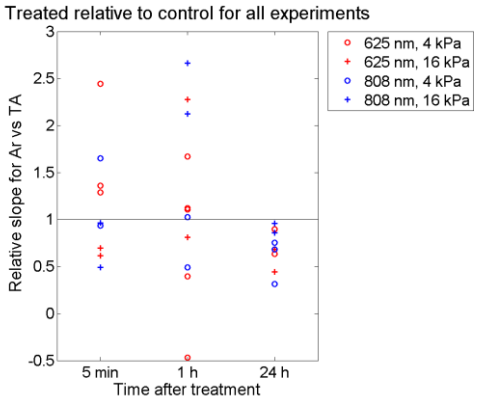

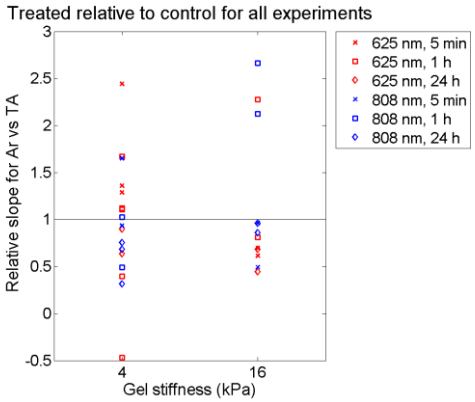

Ar vs NF

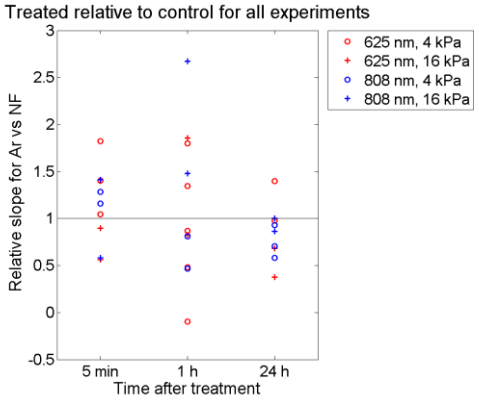

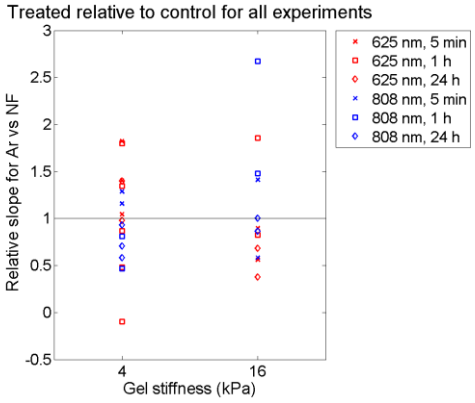

NF vs TA